

Structural and functional characterization of proteins: Bovine visual rhodopsin and PaMTH1, a SAM dependent O-methyltransferase

Dissertation
zur Erlangung des Doktorgrades
der Naturwissenschaften

vorgelegt beim Fachbereich Biochemie, Chemie und Pharmazie
der Johann Wolfgang Goethe -Universität
in Frankfurt am Main

von
DEEP CHATTERJEE
aus Kolkata, Indien

Frankfurt 2016

(D 30)

Vom Fachbereich Biochemie, Chemie und Pharmazie

Der Johann Wolfgang Goethe - Universität als Dissertation angenommen.

Dekan: Prof. Dr. Michael Karas

Gutachter : Prof. Dr. Harald Schwalbe

Prof. Dr. Josef Wachtveitl

Datum der Disputation: TBD

To my parents and wife

Table of Contents

List of abbreviations	iii
1 Overview and Summary	1
2 General Introduction.....	7
2.1 The druggable genome.....	8
2.2 Membrane proteins	10
2.3 GPCRs: G-protein coupled receptors	12
2.3.1 <i>The GPCR superfamily</i>	13
2.3.2 <i>Structural and functional insight from GPCRs</i>	16
2.3.3 <i>Signal transductions of GPCRs</i>	19
2.3.4 <i>Therapeutic relevance of GPCR</i>	23
2.4 Enzymes	24
2.4.1 <i>Enzyme classification</i>	25
2.5 Methyltransferase	27
2.5.1 <i>Biological functions of methyltransferases</i>	28
2.5.2 <i>Functional diversity of methyltransferase</i>	30
2.5.3 <i>Structural diversity of methyltransferases</i>	32
2.5.4 <i>Clinical significance of methyltransferase</i>	35
2.6 Structural biology of proteins	36
2.6.1 <i>Biophysical techniques: X-ray crystallography and NMR</i>	37
2.6.2 <i>Protein dynamics studied using NMR spectroscopy</i>	41
2.6.3 <i>Real-time NMR</i>	44
2.6.4 <i>SOFAST-HMQC</i>	45
2.6.5 <i>In-situ illumination set up</i>	48
3 NMR-spectroscopic Characterization of the Transiently Populated Photointermediates of Bovine Rhodopsin and it's interaction with Arrestin	49
3.1 The role of light in biology	49
3.2 The retina - a complex neural network	50
3.3 Rods and cones - the photoreceptor cells	51
3.4 Signal transduction of the visual process	54
3.5 Rhodopsin - a G-protein coupled receptor	56
3.5.1 <i>Rhodopsin structure</i>	56
3.5.2 <i>Rhodopsin photocycle</i>	60
3.5.3 <i>The meta II / meta III pathway</i>	62
3.5.4 <i>Retinal regeneration pathway: Visual cycle</i>	64
3.5.5 <i>Rate limiting steps in photo cycle and visual cycle</i>	66
3.6 Arrestin - a GPCR desensitizer.....	68
3.6.1 <i>Arrestin structure</i>	68
3.6.2 <i>Down regulation of rhodopsin by arrestin</i>	70
3.7 Motivation.....	71
3.8 Research article 1: Characterization of the Simultaneous Decay Kinetics of Metarhodopsin States II and III in Rhodopsin by Solution-State NMR Spectroscopy.....	73
3.9 Research article 2: Influence of Arrestin on the Photodecay of Bovine Rhodopsin.	75

4	Structural and Biophysical Characterization of PaMTH1, a putative SAM dependent O-Methyltransferase from filamentous fungi <i>Podospora anserina</i>.....	77
4.1	Aging and Molecular Aging Research.....	77
4.2	Formation and effects of reactive oxygen species.....	78
4.3	ROS formation in the mitochondrial respiratory chain	80
4.4	ROS formation by catechol-containing compounds.....	82
4.5	The filamentous ascomycete <i>Podospora anserina</i>	84
4.5.1	<i>Proteome analysis in P. anserina during aging</i>	84
4.6	PaMTH1- SAM dependent O-methyltransferases	85
4.6.1	<i>Sequence homology of PaMTH1 with other SAM O-MTs</i>	86
4.6.2	<i>Structural diversity in SAM O-MTs</i>	88
4.7	Motivation.....	89
4.8	Research article 3: Structure and Biophysical Characterization of the S-Adenosylmethionine-dependent O-Methyltransferase PaMTH1, a Putative Enzyme Accumulating during Senescence of <i>Podospora anserina</i>	91
	German summary	93
	References	99
	Acknowledgments	109
	Curriculum vitae.....	113

List of abbreviations

°C	temperature in degrees Celsius
1D, 2D,..., nD	one-, two-dimensional, ..., n-dimensional
7TM	seven transmembrane
A _{2A} R	human adenosine A _{2A} receptor
Ar ⁺	argon ion
BisTris	2-[bis(2-hydroxyethyl)amino]-2-(hydroxymethyl)propane-1,3-diol
C1,2 and 3	Interhelical loops on the cytoplasmic side
Ca ²⁺	calcium ions
CAM	calmodulin
cAMP	cyclic adenosine monophosphate
cGMP	cyclic guanosine monophosphate
CCoAOMT	caffoyl-CoA- O-methyltransferase
CNBr	cyanogen bromide
COMT	catechol- O-methyltransferase
LiOMT	L. interrogans O-methyltransferase;
CSP	chemical shift perturbation
D ₂ O	deuterated water
DAG	diacyl glycerol
DDM	n-dodecyl-β-maltoside
DHPC	1,2-diheptanoyl- <i>sn</i> -glycero-3-phosphate
DMEM	Dulbecco's modified eagle medium
DNA	desoxyribonucleic acid
DSS	3-(trimethylsilyl)-1-propanesulfonic acid
EDTA	ethylenediaminetetraacetic acid
<i>e.g.</i>	<i>exempli gratia</i> , for example
EM	electron microscopy
<i>et al.</i>	<i>et alia</i> , and others
FBS	fetal bovine serum
FTIR	fourier transform infrared spectroscopy
GARP	globally optimized alternating phase rectangular pulse
GDP	guanosine diphosphate
GPCRs	G-protein coupled receptors
GTP	guanosine-5'-triphosphate
h	hour
HEK293	Human embryonic kidney 293 cells
HMQC	heteronuclear multi-quantum correlation spectroscopy
H ₂ O	water
H ₂ O ₂	hydrogen superoxide
HPLC	high performance liquid chromatography
<i>H. sapiens</i>	<i>Homo sapiens</i>
HSQC	heteronuclear single-quantum correlation spectroscopy
<i>i.e.</i>	<i>id est</i> , that is
IP ₃	inositol 1,4,5-triphosphate
IPM	interphotoreceptor matrix
IPTG	isopropyl β-D-1-thiogalactopyranoside
IRBP	interphotoreceptor retinoid-binding protein
LRAT	lecithin retinol acyl transferase
K	temperature in degrees Kelvin
K ⁺	potassium cation
kb	kilobase
KCl	potassium chloride
M	molar
m	meter
MAD	multiple-wavelength anomalous dispersion

MALS	multiangle laser light scattering
Mg ²⁺	magnesium cation
MHz	Megahertz
min	minute
mRNA	messenger RNA
MT	methyltransferase
mtDNA	mitochondrial DNA
Na ⁺	sodium cation
NADPH	nicotinamide adenine dinucleotide phosphate
NiNTA	Nitrilotriacetic acid complexed with nickel
NMR	nuclear magnetic resonance
NOE	nuclear Overhauser effect
PaMTH1	<i>P. anserina</i> O-methyltransferase
PCR	polymerase chain reaction
PDB	protein data bank
pDNA	plasmid DNA
PEG	polyethylene glycol
pH	the negative of the logarithm to base 10 of the hydrogen ion activity (M)
PIP ₂	phosphatidylinositol 4,5-bisphosphate
PKC	protein kinase C
PLC	phospholipase C
ppm	parts per million
R1	spin-lattice relaxation rate
R2	lattice-lattice relaxation rate
R _{1ρ}	rotating frame relaxation rate
RDC	residual coupling constants
RDH	retinol dehydrogenase
RMSD	rootmeansquare deviation
RNA	ribonucleic acid
RPE	retinal pigment epithelium
s	second
SAM	S-adenosyl-L-methionine
SAM-MT	SAM-dependentmethyltransferase
SAM O-MT	SAM-dependent O-methyltransferase
SAH	S-adenosyl homocysteine
SDS-PAGE	sodium dodecyl sulfate polyacrylamide gel electrophoresis
SEC	size exclusion chromatography
S/N	signal-to-noise ratio
SOFAST	band-selective optimized flip-angle short-transient
TCEP	tris(2-carboxyethyl)phosphine
TM	transmembrane
TROSY	transverse relaxation optimized spectroscopy
TSP-d4	3-(trimethylsilyl)-2,2,3,3-tetradeuteropropionic acid
UV	ultraviolet
UV/Vis	ultraviolet/visible
%	percent
β ₂ AR	human beta 2 adrenergic receptor

1 *Overview and Summary*

Cells perform a wide range of functions such as signalling, transportation, immuno-protection and metabolism. Unravelling the molecular mechanism behind those processes will provide a platform for more targeted and rational drug design. This is achieved by discerning the structural and functional aspects of the biological macromolecules involved. This thesis discusses about the biophysical characterization of protein structures and the biological importance of protein dynamics. Membrane receptors and enzymes which are ubiquitously present in our biological systems and regulate wide variety of functions are excellent choice for such study. From a pharmaceutical point of view, receptor and enzymes are exceptionally important drug targets as they represent the major share (receptor, 30% and enzymes, 47%) of all marketed drugs. Therefore, apart from biological insights, the detailed study of receptors and enzymes will provide the basis for new pharmaceutical applications. Most information about receptor activation and enzyme activity come from the structural and functional analysis of target members of the above mentioned systems.

In “**Chapter 1 – General Introduction**” the readers are introduced to the world of proteins with special focus on G-protein coupled receptors (GPCRs) and methyltransferases. The first part of this chapter discusses about GPCRs with emphasis on their classification, structural features and functions. GPCRs are the most abundant membrane receptors present in mammalian cells, accounting for almost 15% of all membrane proteins. The GPCR superfamily consists of ~800 members and can be subdivided into six classes (A-F). Class A containing rhodopsin, peptide hormones, olfactory GPCRs, is the most abundant with a large share of 85% of GPCR protein family. GPCRs share a common architecture of 7 transmembrane α -helices, with different ligand binding sites. Although a variety of ligands ranging from subatomic particles (a photon) to large proteins can activate a GPCR, their mechanism of signal transduction is almost similar. There are two major signal transduction pathways identified for GPCRs: the cAMP pathway and the phosphatidylinositol pathway. The therapeutic relevance of GPCRs has also been pointed out here since a large share (30%) of modern marketed drugs target GPCRs. In the second part of this chapter, the structural and functional characterizations of methyltransferases (MTs) are discussed in detail. Several important biological processes in cells e.g. drug metabolism, gene transcription, epigenetic

regulations are modulated by methylation of targets ranging from small biomolecules to large proteins. MTs are the proteins which catalyze this methylation reaction and transfer the methyl group to an acceptor molecule through SN2 like nucleophilic substitution reaction. The MTs can be classified on the basis of the substrate atoms they methylate: O (54% of all MTs), N (23%), C (18%), S (3%) and other acceptors (such as halides; 2%). They can also be categorized into five different classes (Class I-V) depending upon distinctive structural features facilitating substrate binding or catalytic activity. Rossmann fold and SET (acronym acquired from the *Drosophila* Su(var)3-9 and 'Enhancer of zeste' proteins) domain are the two characteristic structural motifs commonly found in MTs. Similar to GPCRs, MTs dysfunction has been shown to be involved in various diseases including neuropsychiatric diseases and cancer. Therefore they are also interesting targets for drug development. The final part of this chapter discusses the importance of structural biology in gathering information related to structure and conformational dynamics of proteins. The two prominent biophysical techniques used in structural biology, X-ray crystallography and NMR, are discussed with focus on their advantages and limitation. The importance of NMR spectroscopic techniques to investigate different dynamic processes of protein at atomic resolution under physiological conditions is also discussed. Real time NMR spectroscopy required for the analysis of slow protein dynamic processes (protein folding, enzyme catalysis, domain rearrangement) has been explained in detail.

The second part of the thesis (Chapters 3-4), which is the cumulative part, comprises the original publications grouped into 2 chapters according to their topic:

- *NMR-spectroscopic characterization of the transiently populated photointermediates of bovine rhodopsin and its interaction with arrestin (Chapter 3)*
- *Structural and biophysical characterization of PaMTH1, a putative SAM dependent O-methyltransferase from filamentous fungi *Podospora anserina* (Chapter 4)*

Each chapter is initiated by a detailed introduction to the topic, providing the framework for the following papers. The personal contribution of this thesis' author to each publication is stated in the introduction to the respective article.

Chapter 2 focuses on bovine visual rhodopsin, the model system for GPCRs, which plays an important role in the visual signal transduction present in the mammalian rod cells. The structure, activation and deactivation pathways of rhodopsin are extensively discussed with special emphasis on the rhodopsin photocycle. Photomediated isomerization of the retinal chromophore in rhodopsin from its 11-*cis* to all-*trans*

configuration leads to major conformational changes and subsequent formation of several transiently populated intermediate states.

Among these intermediates, the metarhodopsin II (meta II) and meta rhodopsin III (meta III) states are of special interest since they are considered as the rate limiting steps due to their slower decay kinetics. The publication presented in **Chapter 3.8** comprises the kinetic investigation of the meta II and meta III photointermediate states of rhodopsin via real time NMR spectroscopy (Figure 1.1). This is achieved by using the selectively labeled five tryptophans (W35, W126, W161, W175, and W265) present in rhodopsin as reporter groups. The kinetic properties of rhodopsin are crucial for the understanding of the regulation processes (activation, signalling and inactivation) of GPCRs.

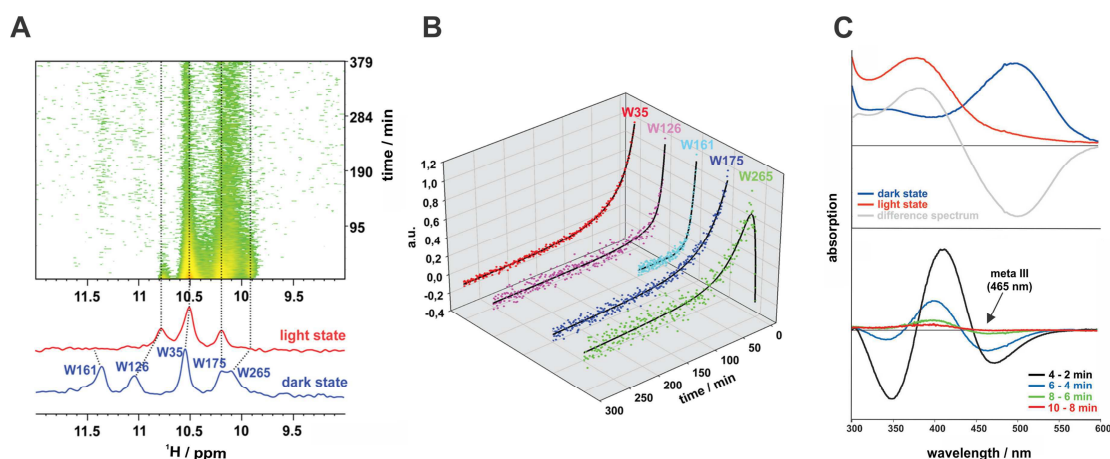


Figure 1.1: Photodynamics of bovine rhodopsin. A) A series of 1D ^1H NMR spectra of α, ϵ - ^{15}N -tryptophan-labeled rhodopsin recorded after illumination. B) Extracted signal intensities from the NMR spectra were normalized and plotted as a function of time. Each of these plots was fitted using exponential functions. C) Upper panel: absorption spectra of the rhodopsin dark (blue) and illuminated state (red). The corresponding difference spectrum is depicted in gray. Lower panel: double difference spectra of rhodopsin after photoexcitation at different time points.

Achievements

- High quantities of rhodopsin enriched with stable isotopes for NMR study were acquired through recombinant expression in mammalian cell line HEK293 to accommodate post translation modifications.
- NMR kinetic analysis of meta II and meta III states of visual rhodopsin were performed under physiological condition.
- Spatially resolved kinetic information augmented the structural information obtained for the rhodopsin photointermediates by X-ray crystallography.

Chapter 3 also focusses on the interaction of bovine visual rhodopsin with visual arrestin, belonging to a protein super family responsible for down regulation of GPCRs signal cascade. The structure of visual arrestin and its role in rhodopsin deactivation have been discussed in **chapter 3.6**. The article presented in **Chapter 3.9**, reveals the effect of a truncated form of bovine visual arrestin (Arr^{Tr}) on the photodecay dynamics of meta II and meta III states of rhodopsin (Figure 1.2).

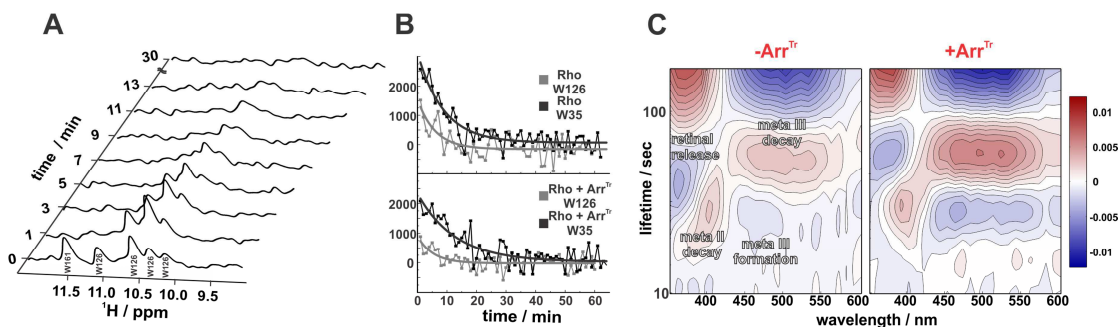


Figure 1.2: Interaction of bovine visual rhodopsin and arrestin. A) A series of 1D ^1H NMR spectra of $\alpha,\epsilon\text{-}^{15}\text{N}$ -tryptophan-labeled rhodopsin recorded at different time intervals after illumination in presence and absence of arrestin (Arr^{Tr}). B) Extracted signal intensities from the NMR spectra of rhodopsin in presence and absence of Arr^{Tr} . A mono-exponential fit was applied for the signal intensities of W35 (black curve) and W126 (gray curve). C) Lifetime density analysis (LDM) of the transient absorption data of rhodopsin (25 μM) samples without and with Arr^{Tr} (100 μM).

Achievements

- Insight into the role of arrestin in rhodopsin deactivation and the retinal regeneration process was provided using two biophysical techniques – NMR and flash photolysis absorption spectroscopy.
- Effect of arrestin on stabilizing the meta III state of visual rhodopsin necessary for the regulation of the free all-*trans* retinal concentration in rod outer segment was unravelled.

Chapter 4 focusses on PaMTH1, a putative SAM dependent O-methyltransferase from filamentous fungi *Podospora anserina* which has been suggested to be involved in age-related methylation reactions protecting aging cultures of *P. anserina* against increasing oxidative stress. The article presented in **Chapter 4.8** describes the structure of PaMTH1 and biophysical characterization of its enzymatic mechanism (Figure 1.3).

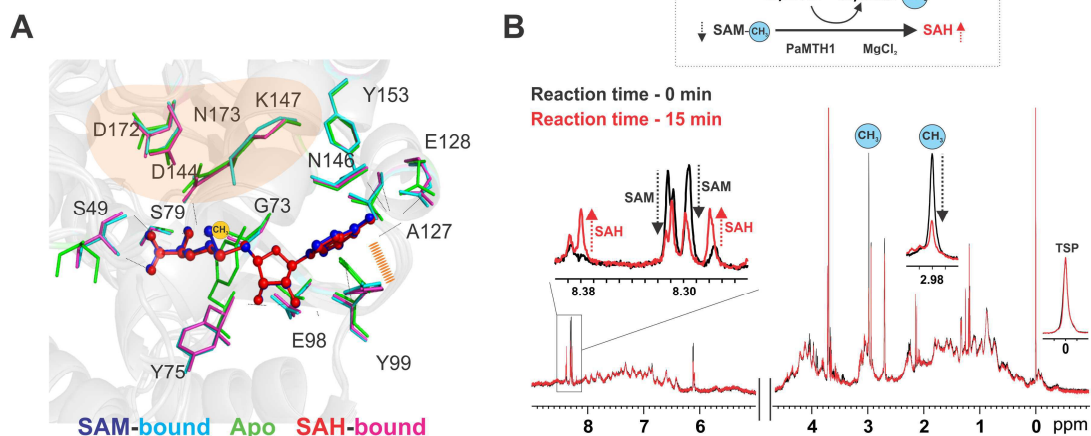


Figure 1.3: Biophysical characterization of PaMTH1. A. Crystal structures of PaMTH1 apo-state (green) and SAM (blue) / SAH (red) co-complexes with a close-up view of the catalytic pocket. B. PaMTH1-catalyzed methyl group transfer reaction as monitored by 1D ^1H NMR.

Achievements

- Crystal structures of PaMTH1 and PaMTH1-SAM/SAH co-complexes were determined.
- PaMTH1 catalyzed enzymatic methylation of its substrate, myricetin was characterized by NMR and other biophysical techniques.

List of publications presented in the cumulative part

- **Research article 1:**
Characterization of the Simultaneous Decay Kinetics of Metarhodopsin States II and III in Rhodopsin by Solution-State NMR Spectroscopy.
Stehle J, Silvers R, Werner K, Chatterjee D, Gande S, Scholz F, Dutta A, Wachtveitl J, Klein-Seetharaman J, Schwalbe H. *Angew Chem Intl Ed Engl.* **2014**, 53, 2078-2084.
- **Research article 2:**
Influence of Arrestin on the Photodecay of Bovine Rhodopsin.
Chatterjee D*, Eckert CE*, Slavov C, Saxena K, Fürtig B, Sanders CR, Gurevich VV, Wachtveitl J, Schwalbe H. *Angew Chem Intl Ed Engl.* **2015**, 54, 13555-13560. *Equal contribution
- **Research article 3:**
Structure and Biophysical Characterization of the S-Adenosylmethionine-dependent O-Methyltransferase PaMTH1, a Putative Enzyme Accumulating during Senescence of *Podospora anserina*.
Chatterjee D, Kudlinzki D, Linhard V, Saxena K, Schieberr U, Gande SL, Wurm JP, Wöhnert J, Abele R, Rogov VV, Dötsch V, Osiewacz HD, Sreeramulu S, Schwalbe H. *J Biol Chem.* **2015**, 290, 16415-16430.

The personal contribution of the author of this thesis to each paper is stated in the cumulative part.

2 *General Introduction*

Life on earth revolves around the key players of the central dogma – nucleic acids and protein. The nucleic acids, DNA and its close relative RNA are considered as store house of genetic information, which determines the characteristics of the offspring through reproduction. But mere reproduction is not enough, living system need an executioner which will perform the functions necessary for sustenance of life. And that's where the most remarkable molecular device, protein comes into picture. They are the driving force of various cellular functions that control practically all major biological processes. And that's why its terminology following the Greek word "proteios" meaning "of first importance", stands out to be perfect.

Protein, the most abundant macromolecule in cell, is built up from a pool of 20 amino acids which polymerized in a sequence following the genetic codes implanted in DNA. These long chain polypeptide folds into an unique three dimensional structures which governs the function performed by that particular protein. Protein function may range from modulating cellular signaling (receptors), accelerating metabolic processes (enzymes) to providing mechanical support (actin). These wide varieties of function make protein the major choice for most of the biological research.

The role of protein in a healthy living system has been optimized through a long process of evolution. Any changes initiated either by complex interactions with the environment (exposure to allergen or toxin) or through mutation of the genes can be deleterious, impairing protein function and causing disease. Thus identification of the protein associated with particular physiological state or disease is of prime importance.

The genetic disorders can be attributed to abnormalities in wide range of proteins including enzymes, transport proteins, structural proteins and other functional classes of proteins. With the discovery of alkaptonuria by Sir Archibald Edward Garrod in 1902, it became evident that several other unknown disease phenotypes could be linked to genetic disorders. Some of those genetic diseases involve single mutation in a gene which leads to malfunctioning of a particular protein. A classic example of such monogenic disorders is cystic fibrosis, in which a deletion of single amino acid (phenylalanine) at position 508 of the protein cystic fibrosis transmembrane conductance regulator (CFTR) results in a buildup of thick, sticky mucus that can damage many of the

body's organs most commonly the respiratory and digestive system. Other common examples of single gene defects are sickle cell disease, Huntington's disease which are usually inherited but sometimes caused by spontaneous mutations. In addition, a complex interplay between several genes and environmental factors can lead to some multifactorial genetic diseases such as obesity, Alzheimer's disease, diabetes and some cancers.

2.1 The druggable genome

The development of therapeutic initiative in pharmaceutical industry depends on proper assessment of the number of molecular targets. There are four groups of molecular targets in biological system: protein, DNA, RNA and lipids but the vast majority of successful drugs are produced against the proteins. The successful completion of whole human genome sequencing under the Human Genome Project ^[1] in 2001 has made it easier to genetically map mutant genes related to a particular disease. It has also helped to identify protein members of crucial signal transduction involved with manifestation of certain diseases for example cancer. Although it is long way to go before potentially useful medical information could be extracted from such a huge genomic map, this has marked the beginning of era of personalized human genomics.

Human genome consists of approximately 30,000 genes and subset of these genes express proteins that are able to bind drug like small molecule therapeutic agents. The extensive analysis of different drugs database (Investigational Drugs Database, Pharmaprojects Database) and physio-chemical properties of drugs developed in pharmaceutical industry has identified 400-500 potential drug targets ^[2,3]. Several studies have suggested that the number of druggable targets can be extended to ~3000 by properly assessing the protein family members and the drug binding sites or domains of existing drug targets ^[4,5]. Among these known drug targets the pharmaceutical industry exploits those which are involved with disease modifying genes. The overall distribution of the marketed drug targets shows enzymes represent the major share (47%), whereas GPCRs account for 30%. The rest of the drug targets belong to protein classes such as ion channels, transporters and nuclear hormone receptors (Figure 2.1). The limited number of drug targets belonging to large gene-family size suggests that druggable gene families are still under-exploited. This can be overcome by complete structural and functional investigation of the prototype representatives of these gene families.

The focus of this PhD work is the biophysical characterization of the two most important subclasses of proteins targeted by the pharma industry: GPCR and enzymes. In chapter 2, the details about the bovine visual rhodopsin, the archetypal class A GPCR has been discussed. The focus of chapter 3 is a representative from the enzyme superfamily: a putative SAM O-MT, PaMTH1.

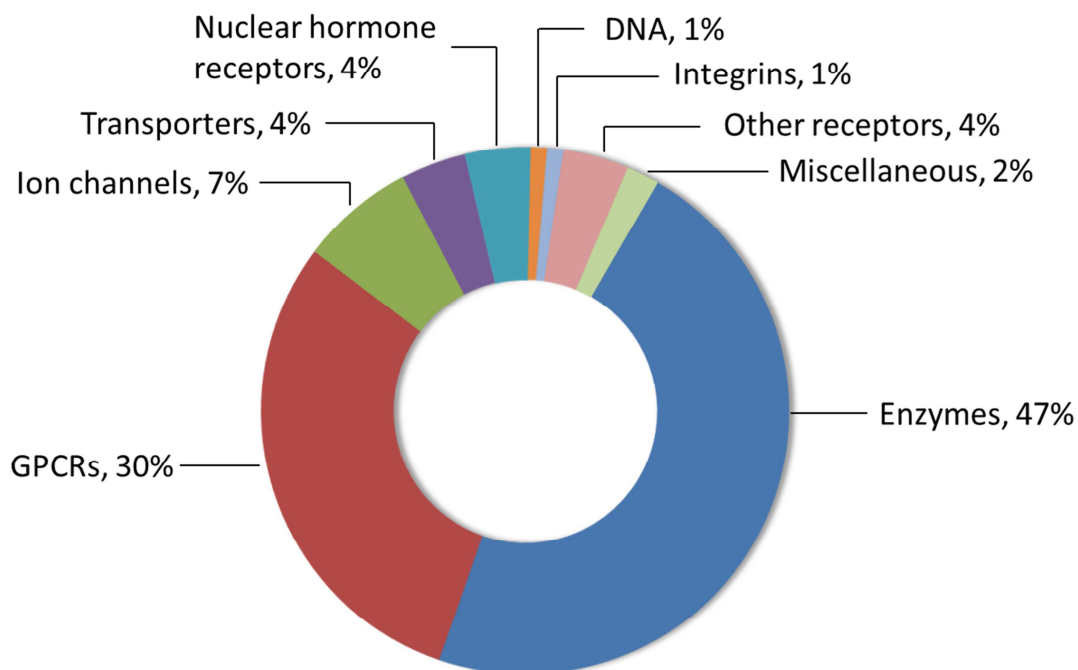


Figure 2.1: Marketed small-molecule drug targets by biochemical class. Adapted from Hopkins et al., 2002 ^[5].

2.2 Membrane proteins

Biological membranes, a protective envelope found on cells of all living organism, function as an effective insulators and selective filters between the cytoplasm and the extracellular medium. Composed of a phospholipid double layer, each membrane houses particular set of proteins or protein complexes that are important for cellular communications and transport. Approximately one-third of all genes present in eukaryotic, prokaryotic as well as human genomes encode for membrane proteins ^[6]. Some of the important functions performed by membrane proteins includes transporting diverse molecules including ions, metabolites, proteins, and RNA across the cell membrane, sending and receiving chemical signals, propagating electrical impulses, ensuring the attachment to neighboring cells, regulating intracellular vesicle transportation, converting light energy to chemical energy, and guiding proteins to specific locations on the cell ^[7] (Figure 2.2). Such a broad functional spectrum of this protein class has made it a prime choice for pharmaceutical industries, with targets of over 30% of all modern medicinal drugs.

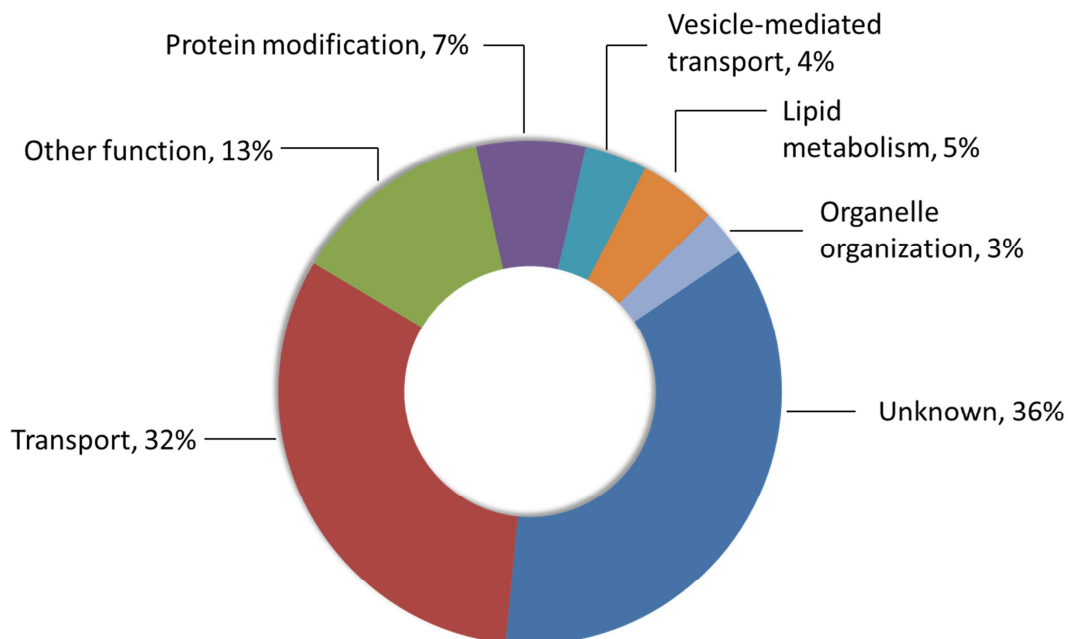


Figure 2.2: Overview of membrane protein functions in the eukaryote *Saccharomyces cerevisiae*. Adapted from Hejine, 2007 ^[7].

Membrane proteins can be categorized into 2 major groups depending upon their localization in membrane. They are either found to be bound only to the membrane surface, peripheral membrane proteins or have one or more segments that are

embedded in the phospholipid bilayer, integral membrane proteins. Peripheral membrane proteins or extrinsic proteins are found on both the cytosolic and the extracellular side and do not interact directly with the hydrophobic core of the phospholipid bilayer. Instead they have covalently attached hydrocarbon chain or moieties that help them to be anchored on the membrane. Integral membrane proteins, on the other hand, have distinct structural organization due to its localization in largely hydrophobic phospholipid bilayers. They generally have hydrophobic surface to facilitate their incorporation into a lipid bilayer through hydrophobic-hydrophobic interaction. The two typical architectural features found in integral membrane proteins are α -helix bundles and β -barrels, which accommodate for this anisotropic environment (Figure 2.3). The α -helix structural element is most abundant among these two architectures and exists in almost all cellular membrane locations. Moreover in comparison to β -barrel proteins, the α -helical integral membrane proteins perform variety of functions, which includes transport and cell signaling. One of the major classes of integral membrane proteins consists of seven membrane-spanning α helical proteins that includes many cell-surface receptors involved in signaling pathways. Seven transmembrane receptors (7TM receptor), the most abundant cell surface receptors, make up a significant portion of approximately 5% of the overall proteins found in human cells, and 15% of membrane proteins [8].

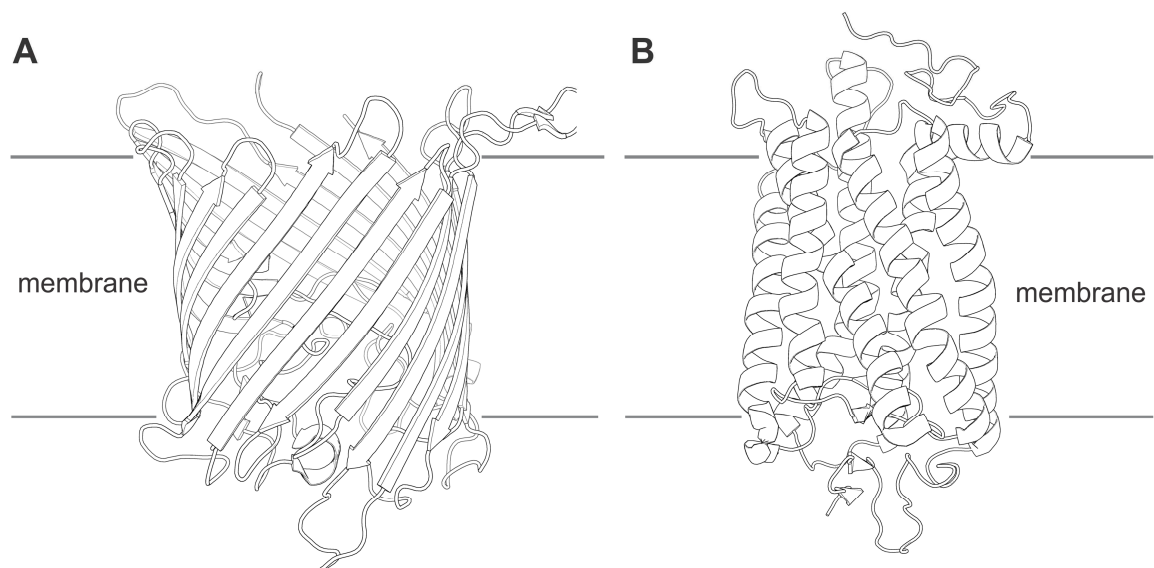


Figure 2.3: The two motifs found in membrane proteins: (A) β -barrel motif of the outer membrane carboxylate channel OCCAB3 (PDB: 5DL7) and (B) α -helical motif of bovine visual rhodopsin (PDB: 1U19). The figure was created using the PyMOL.

Despite being such important drug targets, our understanding of membrane proteins is limited because of their highly hydrophobic nature, their intricate subunit structure, and their resistance to assemble into three-dimensional crystals suitable for X-ray analysis. This is evident by the fact that only 127 unique GPCR structures are available as of today (early 2016). Moreover due to their insolubility in aqueous media, the functional analysis of membrane proteins using other biophysical methods like NMR is extremely difficult. As a solution, detergent treatment is applied for solubilization and purification of the membrane proteins, which may often leads to instability and aggregation. In spite of all these difficulties involved in membrane proteins studies, the functional and structural knowledge of GPCRs has to be extended as they play a key role in the treatment of diseases as indicated by the fact that approximately 30% of all modern drugs targets GPCRs ^[9].

2.3 GPCRs: G-protein coupled receptors

The eukaryotic cell surface is populated by a plethora of distinct G-protein coupled receptors (GPCRs) that control important physiological processes by generating signal inside the cells. In response to external stimuli, GPCRs regulate a myriad of inter- and intra-cellular signaling systems that includes the sensory mechanism of taste, smell, and vision. The human genome contains 720 to 800 GPCRs which accounts for approximately 5% of the human genome and 15% of all membrane proteins. Based on the GRAFS classification ^[8], the human GPCR superfamily can be divided into at least five subfamilies: i) the Glutamate family (15 members), ii) the Rhodopsin family (701 members), iii) the Adhesion family (24 members), iv) the Frizzled/taste family (24 members), and v) the Secretin family (15 members). The physiologic function of most of the GPCRs still remains unknown, which are referred to as orphan GPCRs. The deorphanization of these GPCRs with unknown function is an ongoing process ^[10], as they are a promising group of targets for the pharmaceutical industry. A graphical representation summarizing the division of the GPCR superfamily and their numeric distribution is shown in Figure 2.4.

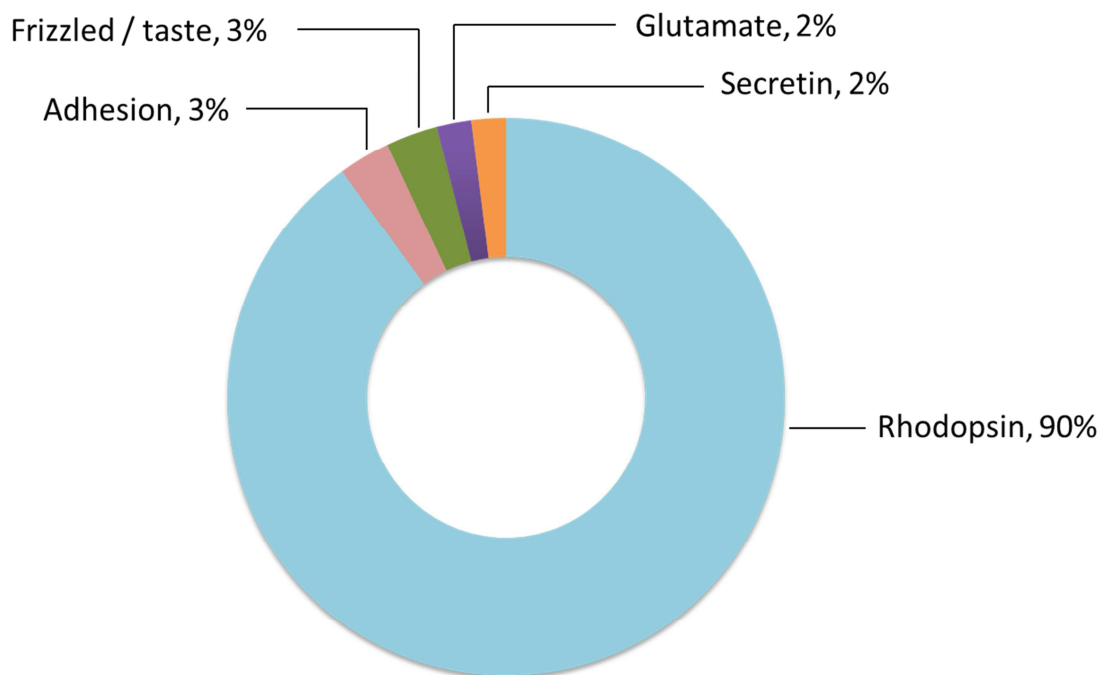


Figure 2.4: Pie chart of the numeric distribution of the subclasses of the GPCR superfamily^[11]. Class A comprises by far the largest subclass.

2.3.1 The GPCR superfamily

Over the years, many classification systems have been used to group GPCRs into several families. Among those, the most frequently used classification system categorized GPCRs into 6 classes on the basis of sequence homology: Class A (rhodopsin-like), Class B (secretin receptor family), Class C (metabotropic glutamate), Class D (fungal mating pheromone receptors), Class E (cyclic AMP receptors) and Class F (frizzled/smoothened)^[12,13]. This A–F classification system is designed from known GPCRs from both vertebrates and invertebrates. An overview of known GPCR structure and their corresponding protein family branch is shown in Figure 2.5.

The class A (Rhodopsin-like) is the largest GPCR subfamily consisting of 85% of all GPCRs. The member of this class ranges from (Rhod)opsins, peptide hormones, olfactory, nucleotide-like, cannabinoid, to glycoprotein hormone receptors^[12–14] which can be further categorized into the 19 subclasses on the basis of phylogenetic analysis^[15]. In spite of such diversity, this receptor class is characterized by several highly conserved amino acids and a disulfide bridge connecting loop I and loops III. Another common feature among Class A GPCRs is palmitoylation at C-terminal tail which helps in its

insertion into the cytoplasmic leaflet of the plasma membrane ^[16]. This posttranslational modification not only modulates the structural properties of the GPCR ^[17] but also affects its regulation and signaling mechanism ^[18,19]. The desensitization of Class A GPCRs also proceeds via a common mechanism, which is initiated by phosphorylation of certain residues (serine or threonine) of the C-terminal tail. This phosphorylation enhances the affinity of the receptor to a family of protein called arrestin ^[20] which deactivate the receptors by competing with G-proteins ^[21].

Class B GPCRs also known as the secretin receptor family, are found only in prokaryotes, fungi, and plants. They interact mainly with peptide hormones such as secretin, calcitonin, and the parathyroid hormone and are further subdivided into the three subfamilies B1-B3 ^[22]. They are characterized by similar 7 TM helix motifs, but the transmembrane architecture is different from other GPCRs. Moreover, Class B GPCRs have a long extracellular N-terminus which forms a globular complex involving three highly conserved disulfide bridges with the extracellular loop segments.

Class C GPCRs, also referred to as metabotropic receptors, are mainly involved in the central and peripheral nervous system ^[23]. Most prominent members of this class are metabotropic glutamate receptors (mGluR), pheromone, calcium sensing-like, GABA-B, and taste (T1R) receptors. The main structural features include very large C- and N-terminal tails and the disulfide bridge connecting the two extracellular loops II and IV. The N-terminal domain containing the ligand binding site is connected to the 7TM domains through cysteine-rich segment.

Class D GPCRs found in *Saccharomyces cerevisiae* consist of fungal mating pheromone receptors such as STE2, STE3 (fungal pheromone A-Factor-like), BAR, BBR, RCB, PRA (fungal pheromone B-Factor-like). They play a role in the response of mating factors on the cell membrane ^[24–26]. The lack of sequence similarity with the other classes, accounts for a distinct 7TM signatures for GPCRs of this class.

Class E GPCRs, also known as cyclic AMP receptors, are involved in the development of the soil-living amoeba *Dictyostelium discoideum*. The transmembrane signature present in this class is also distinct in nature ^[11,27,28]. The adhesion GPCRs are believed to be evolved for cAMP receptors.

The last GPCR subfamily, Class F or frizzled and smoothed receptors, plays significant roles in the Wnt ^[28] and the hedgehog signaling pathway ^[27].

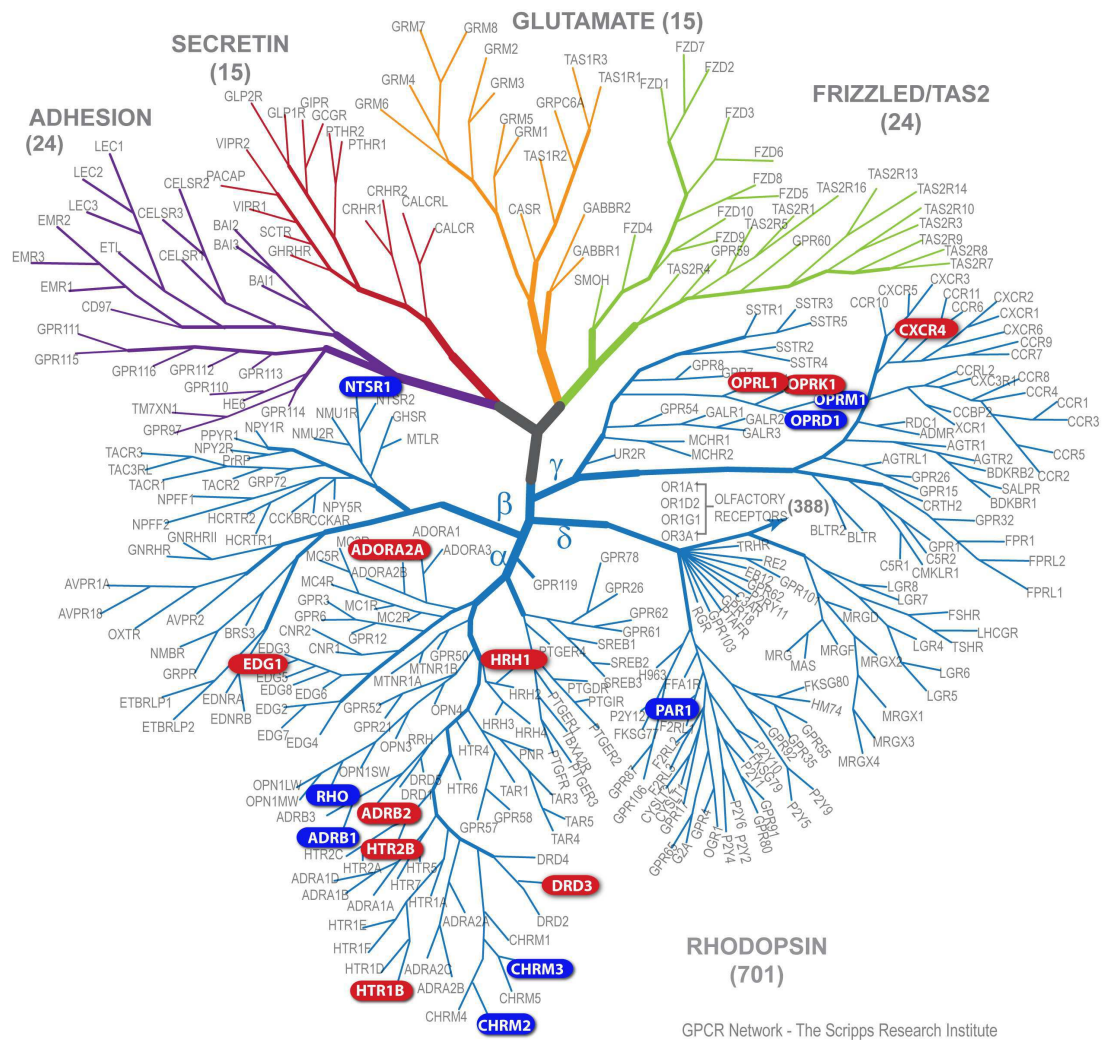


Figure 2.5: Overview of the GPCR family tree. The solved GPCR structures are displayed. Reprinted with permission from GPCR Network [29], © The Scripps Research Institute 2013.

2.3.2 Structural and functional insight from GPCRs

Structural studies of GPCR are important for understanding the molecular mechanisms of GPCR signal transduction, which is necessary for developing new therapeutics against many human diseases. But the structural studies of GPCR face several challenges including difficulties in its large scale recombinant expression, conformational flexibility in solutions, and non-availability of polar surface for forming crystal lattice contacts. In spite of such difficulties, Palczewski and colleagues solved the first GPCR structure of bovine rhodopsin in 2000 ^[30]. It took another seven year of extensive research and major technological development for the next GPCR structure of the human β 2-adrenergic receptor (β 2AR) ^[17]. This is soon followed by the first active-state GPCR structure of ligand free rhodopsin (opsin) in 2008 ^[31]. Breakthroughs in membrane protein engineering and crystallography in next few years show an exponential growth of GPCR structure determination (Figure 2.6). The total number of GPCR structures has grown to 133 including 127 structures from 28 different class A GPCRs and 5 structures of the transmembrane domain of receptors from classes B, C and F ^[32]. These structures shed light on structural similarity and diversity of the GPCR superfamily, and molecular basis of GPCR ligand recognition, activation, allosteric modulation and dimerization.

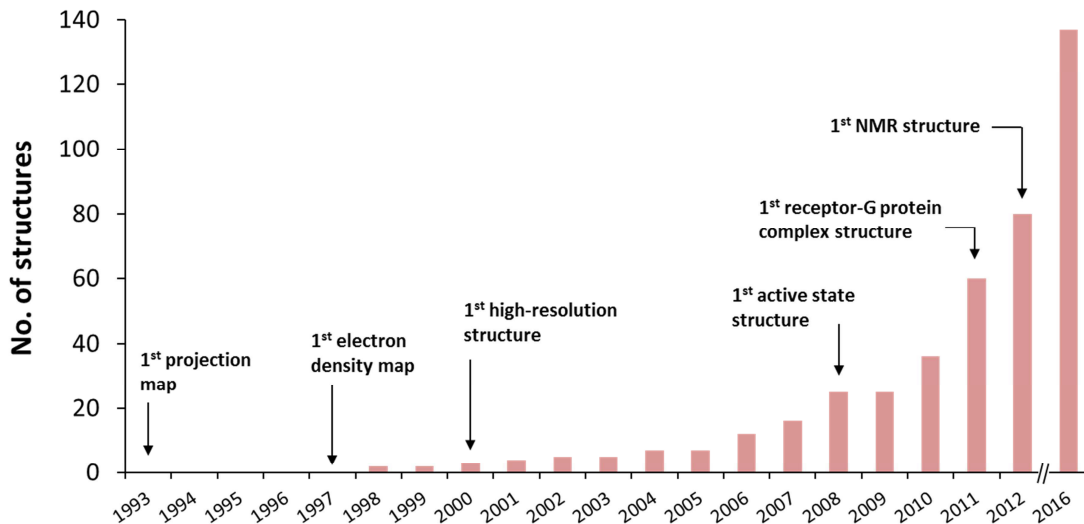


Figure 2.6: Timeline of GPCR structures. Bar chart showing the increase in the number of GPCR structures with time. Adapted from Venkatakrishnan et al., 2013 ^[33].

The GPCR subfamilies with a very little sequence homology surprisingly share a common structural motif of 7TM α -helices (Figure 2.7). The 7TM bundle region forms the structural core transducing extracellular signals to the intracellular region through conformational

changes. They have a serpentine-like topology connecting the helices via three extracellular (ECL1-3) and three intracellular loops (ICL1-3) with the amino-terminal facing the extracellular side and the carboxyl-terminal end in the cytosol. The extracellular region is involved mostly in ligand binding and the intracellular (IC) region interacts with cytosolic G-proteins, arrestins, G protein coupled receptor kinases (GRKs) and other downstream signaling partners.

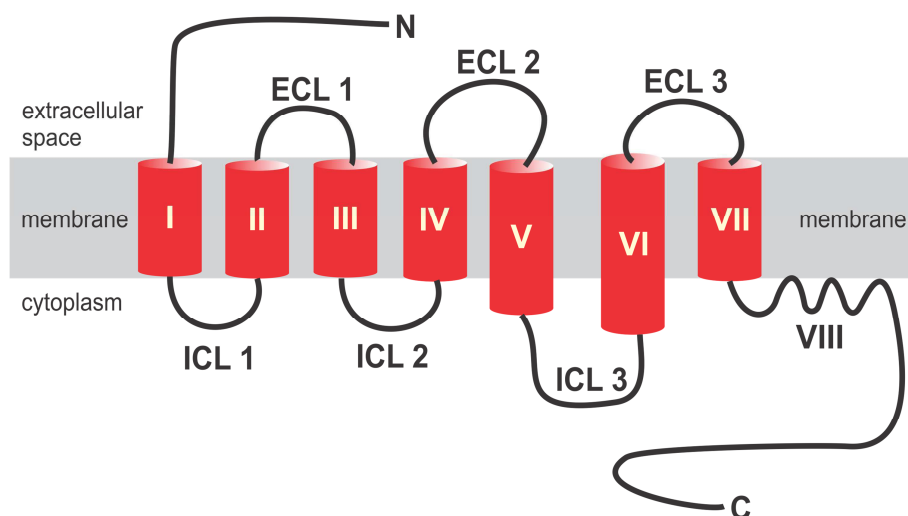


Figure 2.7: Secondary structure common to GPCRs.

The GPCR structures share some similar structural motifs in conserved regions. The D[E]RY motif in helix III, is one such conserved motifs which forms salt bridge with D/E in helix VI. This interaction is called “ionic lock” which is observed in the inactive conformation of GPCRs and prevents its binding with the G-protein at the cytoplasmic region. Another conserved motif NPxxY located in helix VII has also been suggested to play an important role in GPCR activation. Apart from these conserved motifs in the transmembrane domain, GPCR structures also show some similarities in the extracellular loop regions. Most GPCR structures comprise of a highly conserved disulfide bond between the cysteine residues in helix III and ECL2, which stabilize the conformation of the extracellular region. The intracellular region of GPCRs is also relatively conserved, containing a C-terminus with 3-4 turn α -helix and helix VIII with a common [F(RK)xx(FL)xxx] amphiphilic motif, running parallel to the membrane.

The greatest homology in GPCRs structures are found within the TM segments, but they can sometimes display different tilts and rotations, which may contribute to the difference in size and shape of the ligand-binding pockets among GPCRs. The most variable regions in GPCRs are the carboxyl terminus, the intracellular loop spanning TM5 and

TM6, and the amino terminus (Figure 2.8) ^[34–36]. Remarkable structural diversity is also observed in the dynamic extracellular loop region. For example, ECL2 exhibits an α -helical structure in adrenergic receptor structures, and a hairpin structure in all the peptide receptor structures. Another structurally diverse region in GPCR is the amino terminus which can range from relatively short stretch of 10–50 amino acids for monoamine and peptide receptors, to much larger domain of 350–600 amino acids for glycoprotein hormone receptors, and the glutamate family receptors. The largest amino terminal domains are observed in the adhesion family receptors.

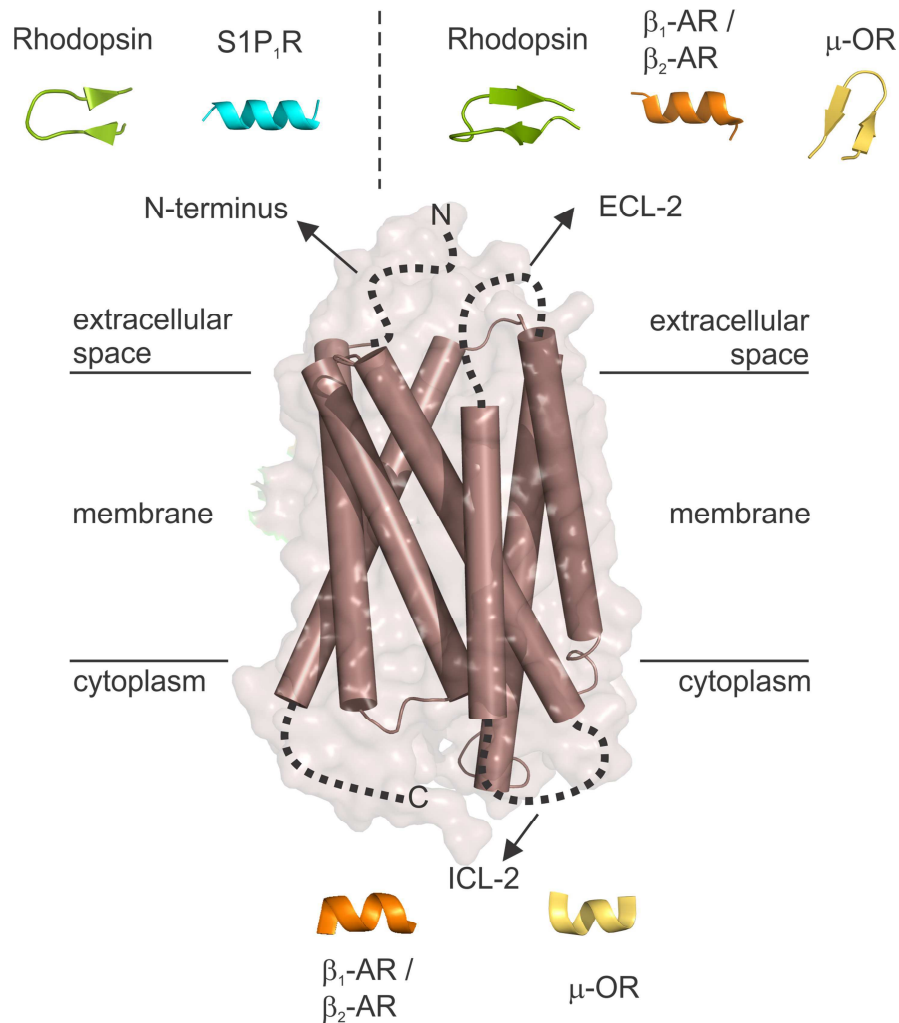


Figure 2.8: Diversity in the secondary structure elements of GPCRs in the extracellular and intracellular regions. TM helices (TM1–TM7) are displayed as cartoon (colored in a spectrum of green) and surface representation. N and C termini and the segments containing defined secondary structure in the extracellular (EC) and intracellular (IC) region are indicated as dotted lines. Type of secondary structure element for the different representative GPCRs are shown in the upper and lower panel. Adapted from Venkatakrisnan et al., 2013 ^[33].

Despite of having structural similarity, GPCRs bind to a wide variety of natural ligands with huge structural diversity (Figure 2.9) ^[37]. These range from subatomic particles (a photon), to ions (H^+ and Ca^{++}), to small organic molecules, to peptides and proteins. The ligand binding domains of GPCRs can also vary depending upon the ligands ^[37]. For instance, the TM region is the binding site for many small organic agonists, while peptide hormones and proteins mainly interact with the amino terminus and extracellular sequences joining the TM domains. But the binding site for the ligands does not always correlate with their size. Small ligands like glycoprotein hormones, glutamate, and Ca^{2+} bind to relatively large amino terminal domains, to activate their respective neurotransmitter receptors ^[37,38].

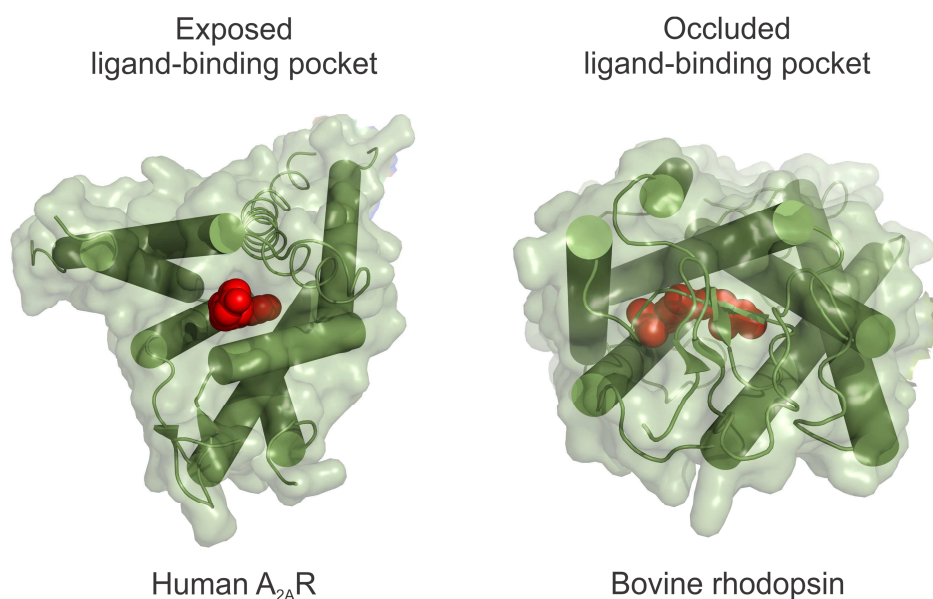


Figure 2.9: The occluded or exposed ligand-binding pocket of GPCRs as seen from the extracellular side (top view). Adapted from Venkatakrishnan et al., 2013 ^[33].

2.3.3 Signal transductions of GPCRs

GPCRs show a common mode of signal transduction mechanism, in which an extracellular signal influences structural and dynamic changes in GPCRs and thus modulating its interaction with guanosine-5'-triphosphate (GTP) binding proteins. These so called G proteins are the interacting partners of the GPCRs and responsible for the signal transduction initiated by the activated GPCR (Figure 2.10). In the inactive state, the receptor interacts with the heterotrimeric subunits ($G\alpha$ and $G\beta\gamma$) of G-proteins with a bound guanosine diphosphate (GDP) on the alpha subunit. GPCR activation by an

effector is followed by the exchange of the GDP for guanosine triphosphate (GTP) which results in the dissociation of the $G\alpha$ subunit from the G protein complex [39]. The dissociated $G\alpha$ and $G\beta\gamma$ subunits activate a signal cascade within the cell by interacting with other intracellular proteins. The freed GPCR in turn interacts with another G protein and continues the signal transduction resulting in significant signal amplification. Finally GPCRs are inactivated by the conversion of GTP to GDP by an enzyme called GTPase [40].

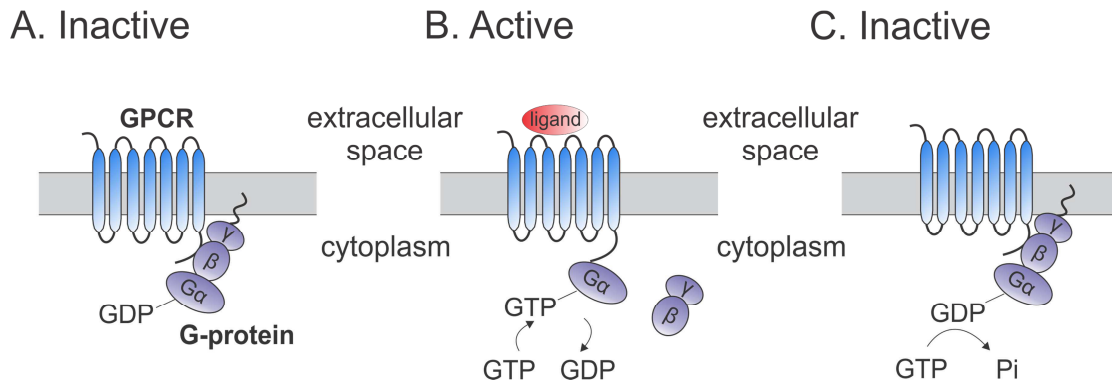


Figure 2.10: Schematic overview of the general signal transduction of GPCRs. (A) In the inactive state the G protein is bound to the GPCR and GDP interacts with the $G\alpha$ subunit of the G protein. (B) In the active state, induced by an effector, GDP is exchanged by GTP and the $G\alpha$ subunit dissociates from the $G\beta$ and $G\gamma$ subunits of the G protein. (C) The inactivation of the active state is achieved by $G\alpha$ -GTPase that catalyzes GTP to GDP and P_i . GDP binds to the $G\alpha$ subunit of the G protein once again resulting in the inactivation of the GPCR signaling. Adapted from Tuteja, 2009 [40].

The signal transduction by the dissociated $G\alpha$ subunit can proceed through either the cAMP pathway (Figure 2.11) or the phosphatidylinositol pathway (Figure 2.12) [41]. In the cAMP-dependent pathway, the α -subunit activates the enzyme adenylyl cyclase which in turn converts adenosine triphosphate (ATP) to cyclic adenosine monophosphate (cAMP). Increased level of cytosolic cAMP within the cell triggers several cellular responses by activating downstream proteins for example Protein kinase A. Thus cAMP is considered as a second messenger and PKA as a secondary effector. This signaling process is deactivated by reducing the cAMP concentration via a dephosphorylation reaction catalyzed by the enzyme phosphodiesterase that converts cAMP into AMP. In the absence of cAMP, the downstream enzyme activity reduces which results in the deactivation of the cAMP-dependent pathway.

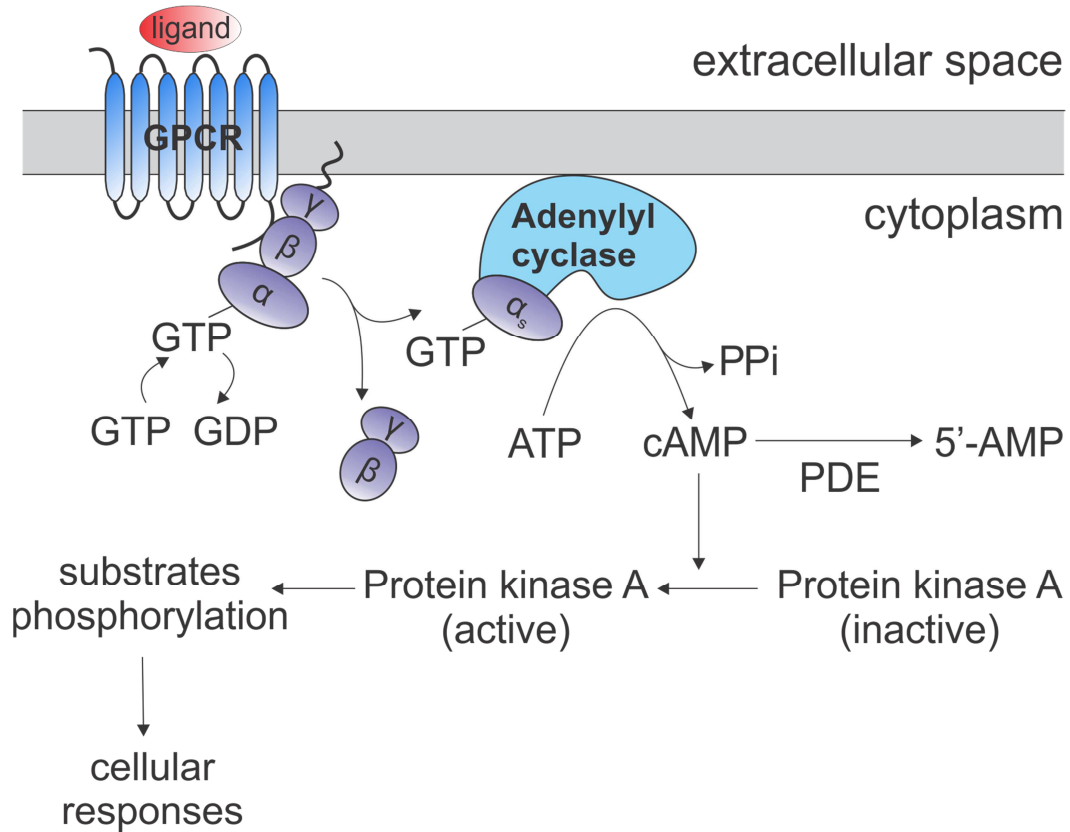


Figure 2.11: Schematic overview of the cAMP-dependent pathway. Adapted from Horton et al., 2006 ^[42].

In the phosphatidylinositol pathway, the α -subunit of the G protein activates the enzyme phospholipase C (PLC) located on the plasma membrane. The lipase in turn hydrolyzes the phosphatidylinositol 4,5-bisphosphate (PIP₂) into two second messengers: inositol 1,4,5-trisphosphate (IP₃) and diacylglycerol (DAG). The IP₃ interacts with IP₃-gated Ca²⁺ transport channel and promotes the release of Ca²⁺ from the endoplasmic reticulum. The increase of the Ca²⁺ concentration in the cytosol results in an activation of calmodulin and subsequent stimulation of various cellular processes. The DAG, on the other hand, remains in the lipid bilayer and activate the protein kinase C (PKC) in the presence of Ca²⁺ which in turn modulates cellular responses by phosphorylating several proteins.

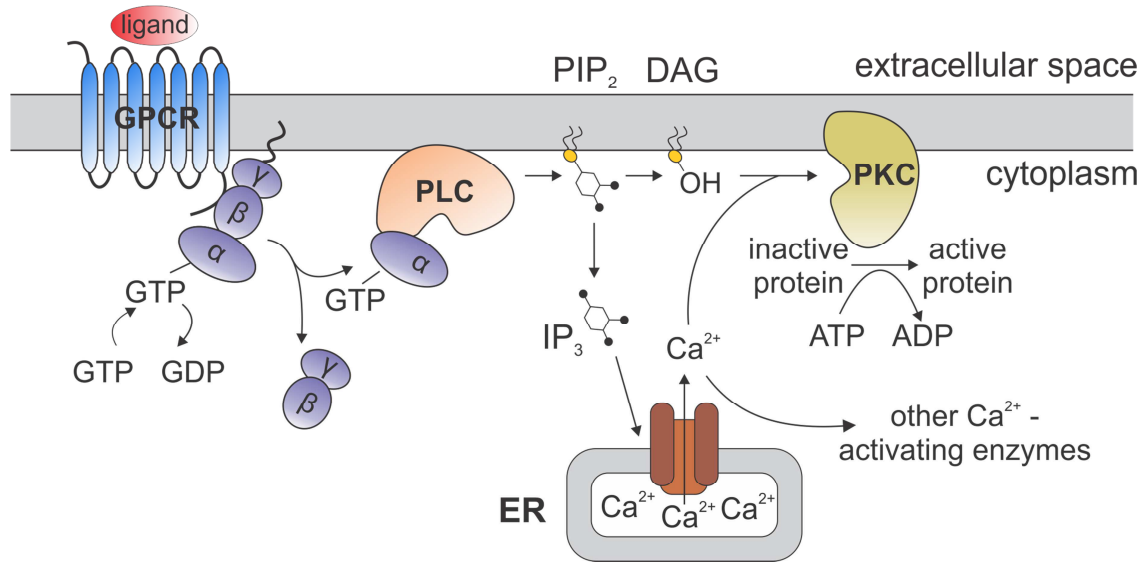


Figure 2.12: Schematic overview of the phosphatidylinositol pathway. Adapted from Voet et al., 2002 ^[43].

In fact, there are many different regulatory mechanisms that involve a large variety of effectors leading to very diverse signaling cascades and feedback mechanisms ^[44–46]. This huge variety of GPCR receptors and their corresponding signaling cascades explains why GPCRs represent major drug targets. For this reason, we have investigated the functional dynamics of a model GPCR, bovine visual rhodopsin which is the archetype of the largest subfamily of GPCRs, class A. Our study will provide insights into the activation and deactivation pathways of GPCRs.

2.3.4 Therapeutic relevance of GPCR

GPCRs are distributed among different organs and tissues in the human body. They function as key signal transducers converting extracellular messages into intracellular responses and act as regulators of broad range of normal and pathological processes. The typical physiological processes attributed to GPCRs includes modulation of neuronal firing, regulation of ion transport across the membrane, modulation of homeostasis, control of cell division/proliferation, and modification of cell morphology. The dysfunction of these crucial biological functions may cause acute or chronic human diseases comprising of cardiovascular disease (β 1-adrenergic receptor) ^[47], asthma (β 2-adrenergic receptor) ^[48], and strokes and cerebral hypoperfusion (A2a-adenosine receptor) ^[49,50]. Mutations in GPCRs also cause diverse diseases like retinitis pigmentosa (rhodopsin), female infertility (follicle stimulating hormone receptor), nephrogenic diabetes insipidus (vasopressin receptor), familial exudative vitreoretinopathy (frizzled receptors), and dominant and recessive obesity (melanocortin receptors) (for review, see ^[51]). Some GPCRs have also played pivotal role in the development of cancer and cancer metastasis ^[52] and are overexpressed in primary and metastatic tumor cells of head and neck squamous cell carcinoma (HNSCC) (Bradykinin receptor, CXC chemokine receptor 2), non-small cell lung cancer (Prostaglandin E2 receptors), breast, prostate and gastric tumors (G protein coupled estrogen receptor), melanoma (CXC chemokine receptor 4) and diffused large B cell lymphoma (Smoothed receptor). Apart from human GPCRs, there are also certain viral GPCR which are involved in viral replication and pathogenesis, as well as virally induced oncogenesis through constitutive activity GPCRs ^[53]. For example human herpes virus 8 (HHv8), which encodes the viral GPCR oRF74 (also known as vGPCR) that is implicated in the pathogenesis of Kaposi's sarcoma ^[54,55]. The involvement of GPCRs in such a wide variety of disease makes GPCRs an important target for drug discovery ^[56,57]. Although, 30% of the current marketed drugs target the GPCR superfamily, only a few GPCR members (20 of the 750 known GPCR subtypes) are affected by these drugs ^[58,59]. Therefore, huge efforts are currently underway to develop new GPCR-based drugs.

2.4 Enzymes

Enzymes are biological macromolecules that act as catalysts in living organisms, regulating the rate of different chemical reactions necessary for various physiological functions. The processes catalyzed by enzymes are mainly involved in metabolic pathways which range from degradation of nutrient molecules, transformation and conservation of chemical energy to conversion of simple biological precursors to macromolecules. The concerted interplay of these different metabolic activities regulated by a system of enzymes has been critical for proper functioning of different living organisms. This is evident by the fact that certain inheritable genetic disorders are caused by either deficiency/absence of one or more enzymes in the tissues or excessive activity of a specific enzyme. Diagnoses of those diseases are performed by measuring the level or activity of those enzymes in tissue sample or blood collected from patients. Apart from medical field, the study of enzymes as practical tools for chemical industry, food processing and agriculture has provided immense effect on our daily lives.

In 1926, James B. Sumner crystallized the enzyme urease and showed that it consisted entirely of protein ^[60]. This led to the popular belief that enzymes can be biochemically characterized as proteins. But with the discovery of catalytic nucleic acid called ribozymes (or catalytic RNAs) in 1980s, the axiom “all enzymes are proteins” was proved wrong. Since most of the enzymes are protein in nature, the primary focus of this discussion will be on protein enzymes.

An enzyme's function including its substrate binding, catalysis and regulation is intrinsically based on its three dimensional structure. In 1965, lysozyme became the first enzyme whose structure was solved at an atomic resolution (2 Å) ^[61]. During that time, structure determination was an extremely time consuming process, and only a few structures were solved each year. However, since 1990 with the development of high throughput methods the number of solved enzyme structures increased exponentially. As of February, 2016 the total number of PDB-enzyme entries is approximately ~63,000 ^[62], though many of these structures are different forms of the same protein (Figure 2.13). Although most enzymes structure shows a common globular form, they are vastly complex in their quaternary structure. They vary from being small and simple, formed of a single domain (e.g. dihydrofolate reductase, ~18 kDa in molecular mass) to large and complex (e.g. plant ribulose-1,5-bisphosphate carboxylase oxygenase, consisting of eight large protein chains and eight small chains assembling into a larger complex of ~540 kDa).

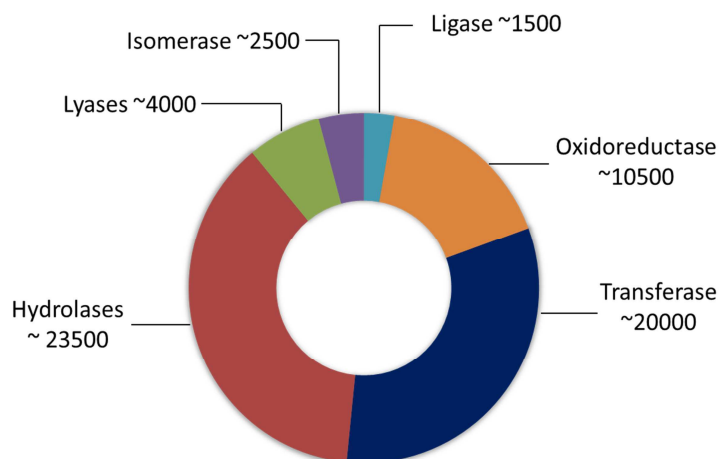


Figure 2.13: Enzyme structure entries in the PDB (as of February, 2016). Statistics obtained from enzyme structures database, the European Bioinformatics Institute ^[62].

Most enzymes are large molecules comprising of hundreds of amino acids, but the functional regions of an enzyme are generally restricted to a small part of ten to twelve amino acids. The most important of these regions is the active site which binds the substrate and performs the catalytic mechanism. Generally, there are three or four amino acids in the active site which are directly involved in the catalysis of the biochemical reaction and thus known as catalytic amino acids. Most of the catalytic residues are shown to be conserved and their properties depend on the specific chemical reaction they perform. The chemical properties of the active site residues also determine the specificity of the enzyme towards its substrate. The enzymatic catalysis of certain biochemical reaction may also require the presence of a cofactor or coenzyme or inhibitor, which binds to the active site or to another region. These regulatory molecules can range from small inorganic metal ions to organic molecules. Some of these molecules also transfer a chemical group to the substrate during the catalysis. For example, Phosphofructokinase catalyzes the phosphorylation of D- fructose 6-phosphate in the presence of ATP, which itself is converted to ADP during the reaction. The regulatory molecules binding to a different region from the active site are shown to allosterically regulate the reaction taking part in the active site by changing the conformation or dynamics of the enzyme.

2.4.1 Enzyme classification

In the early days, enzymes were given trivial names in order to uniquely identify and distinguish them from the rest. But with remarkable increase in the number of newly

discovered enzymes, it was required to set up a system for proper nomenclature and classification for. In 1956, the Nomenclature Committee of the International Union of Biochemistry and Molecular Biology (NC-IUBMB) developed a unified system, the Enzyme Commission (EC) classification ^[63]. On the basis of EC classification system, enzymes are named and identified systematically using an EC number; which depends upon the overall chemical transformation of substrates into products ^[64]. EC classification consists of four level of description; the first level corresponds to the general chemistry involved in the reaction: Oxidoreductases catalyze oxidation/reduction reactions (EC 1), transferases transfer a chemical group (EC 2), for example, a methyl or glycosyl moiety from one compound to another; hydrolases perform hydrolysis of chemical bonds (EC 3), lyases also cleave chemical bonds by other means than by oxidation or hydrolysis (EC 4), isomerases catalyze geometric and structural changes between isomers (EC 5) and lastly, ligases join two compounds with associated hydrolysis of a nucleoside triphosphate molecule (EC 6). These EC classes are further divided in subclasses and sub-subclasses (second, third and fourth level) depending upon the properties of the reaction such as the chemical bond cleaved or formed, the reaction center, the transferred chemical group and the cofactor used for catalysis and the substrate specificity of the enzymes. For example transferase (EC 2) class of enzyme is further subdivided to 10 subclasses depending upon the group they transfer (Table 1).

Classification of transferases into subclasses:		
EC number	Examples	Group(s) transferred
EC 2.1	methyltransferase and formyltransferase	single-carbon groups
EC 2.2	transketolase and transaldolase	aldehyde or ketone groups
EC 2.3	acyltransferase	acyl groups or groups that become alkyl groups during transfer
EC 2.4	glycosyltransferase, hexosyltransferase, and pentosyltransferase	glycosyl groups, as well as hexoses and pentoses
EC 2.5	riboflavin synthase and chlorophyll synthase	alkyl or aryl groups, other than methyl groups
EC 2.6	transaminase, and oximinotransferase	nitrogenous groups
EC 2.7	phosphotransferase, polymerase, and kinase	phosphorus-containing groups; subclasses are based on the acceptor (e.g. alcohol, carboxyl, etc.)
EC 2.8	sulfurtransferase and sulfotransferase	sulfur-containing groups
EC 2.9	selenotransferase	selenium-containing groups
EC 2.10	molybdenumtransferase and tungstenttransferase	molybdenum or tungsten

Table 1: Subclasses of transferase class of enzyme

The following sections of this chapter contains a detail discussion on the methyltransferase enzyme belonging to EC class 2, transferase.

2.5 Methyltransferase

Methylation of myriad molecules ranging from small biological molecules to proteins is a key process for the regulation of numerous cellular processes, including signal transduction, biosynthesis, protein repair, and gene silencing and chromatin regulation. Methyltransferases are abundant, highly conserved across phylogeny and mutation of their gene product has been linked to several diseases and genetic disorders such as pernicious anemia, ICF, Rett syndrome, and Fragile X syndrome ^[65]. Hypo- and hypermethylation of DNA has been found to inactivate tumor-suppressor genes and thus cause cancer. This motivates many scientists to characterize the structural and functional features of methyltransferase enzymes.

Methyltransferases (EC 2.1.1) belonging to the enzyme class of Transferases, help in transferring a methyl group from a donor molecule to various acceptor molecules. There are several biological methyl group donors such as S-adenosyl-L-methionine (SAM or AdoMet), methanol, methyl tetrahydrofolate, mono-, di-, and trimethylamine, methanethiol, methyltetrahydromethanopterin, and chloromethane. But SAM or AdoMet being used by 95% of methyltransferase is the second most commonly used enzymatic cofactor after ATP. The reason behind the preference of SAM as a methyl donor is due to favorable energetic of the charged methylsulfonium center ^[66]. SAM is naturally produced in our body by a reaction between methionine and ATP which is catalyzed by S-adenosylmethionine synthetase (Figure 2.14). SAM serves as precursors for numerous methyl transfer reactions and methyltransferase enzyme involved in those reactions are called the SAM-dependent methyltransferases. Many methyltransferase related diseases such as Alzheimer's, depression, Parkinson's, multiple sclerosis, liver failure and cancer ^[67] can also be linked to aberrant levels of SAM.

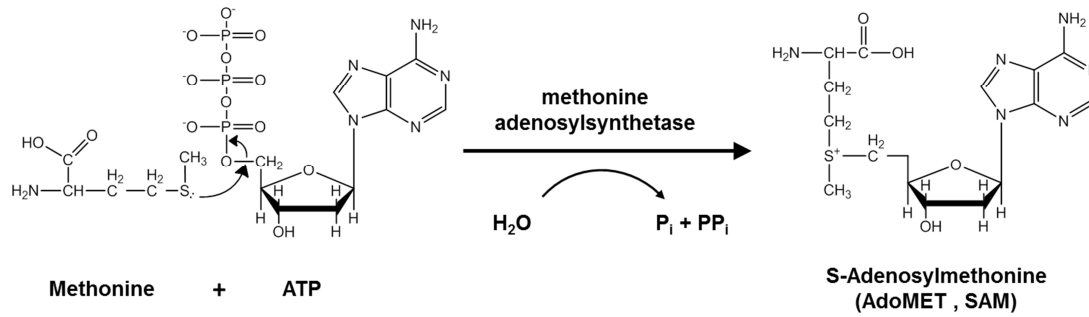


Figure 2.14: Biosynthesis reaction of SAM or AdoMet. A reaction between ATP and methionine catalyzed by methionine adenosyltransferase yields SAM or AdoMet. Adapted from Lu, 2002 ^[68].

The general mechanism behind the methyl group transfer from SAM involves a catalytic attack of a nucleophile (carbon, oxygen, nitrogen, sulfur or even halides) from the acceptor molecules in an SN₂ like mechanism on the reactive methionine-sulfur group in SAM which functions as the methyl donor (Figure 2.15). This reaction also involves a removal of a proton before or after methyl transfer ^[69]. The transfer of the methyl group to an acceptor molecule results in the formation of a methylated product and S-adenosylhomocysteine (AdoHcy or SAH) as by-product. The enzyme responsible for catalyzing this transfer reaction is called SAM-dependent methyltransferase, which methylates a whole range of molecular targets (methyl group acceptor), such as DNA, RNA, proteins, hormones, neurotransmitters and small molecules and thus regulates important cellular and metabolic processes.

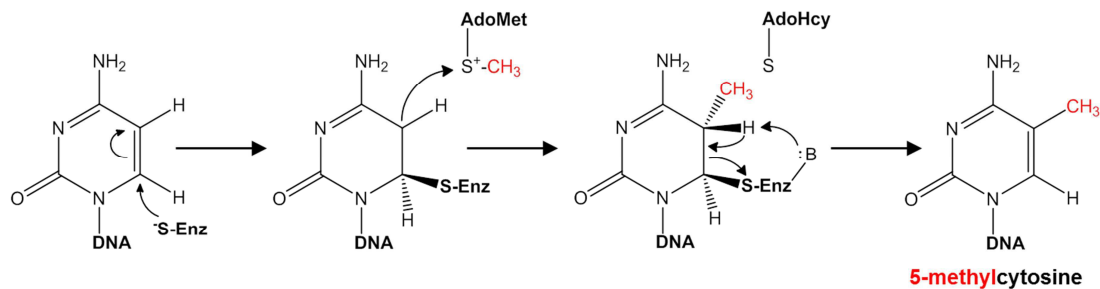


Figure 2.15: General methylation reaction mechanism catalyzed by methyltransferase. Adapted from Wu et al., 1987 ^[70].

2.5.1 Biological functions of methyltransferases

The proper maintenance and sustenance of life depends on methylation reactions involved in several biochemical cellular processes. One such important biochemical

processes is metabolism pathway of many drugs and xenobiotic compounds for example biosynthesis of endogenous compound epinephrine, a hormonal neurotransmitter, which is formed by a methylation reaction of the primary distal amine of noradrenaline catalyzed by phenylethanolamine N-methyltransferase (PNMT) ^[71]. PNMT belongs to the most diverse group of methyltransferases, small molecule, or natural product, methyltransferases (NPMTs). NPMTs are found to participate in the biosynthesis and modification of bioactive molecules derived from several branches of primary and secondary (specialized) metabolism, including membrane components cofactors, prosthetic groups, pigments, and signaling and defense compounds. They are usually not conserved among different species as they perform specific functions in different species. The most important example of NPMTs is the human catechol-O-methyltransferase (COMT) which is responsible for regulation of catecholamine neurotransmitters (dopamine, epinephrine, and norepinephrine). Due to its interactions with neurotransmitters, COMT is the target of several pharmaceutical drugs such as entacapone, tolcapone and nitecapone ^[72].

Apart from small molecules, methyltransferase transfer methyl groups to biological macromolecules. Methylation of DNA has been an integral part of regulation of gene transcription, gene expression, gene activation, and mutation repair in the cells. The interactions between DNA and chromatin proteins as well as specific transcription factors during gene expression are affected by methylation which may also influence development processes. For example, the inactivation of X chromosome during development is accompanied by de novo methylation ^[73] catalyzed by DNA methyltransferase mainly at the C5 position of CpG dinucleotides. Additionally, the restriction modification systems of many bacteria are regulated by methylation of adenosine or cytosine of target DNA.

Not only DNA, methylation also modulates the post translational modification of eukaryotic proteins. The target amino acids residues for protein methylation are usually arginine, lysine, histidine, glutamine, and asparagine. One of the widely investigated effects of protein methylation is the epigenetic regulation of gene expression by histones methylation ^[74]. Another prominent example of functional protein alteration is the post translational N-methylation of the calcium-binding protein calmodulin which modifies its activity and alters Ca²⁺ signaling in plants ^[75].

2.5.2 Functional diversity of methyltransferase

The methyl transferases can be broadly categorized depending upon the substrate atom they methylate, which are mainly O (54% of all MTs), N (23%), C (18%), S (3%) and other acceptors (such as halides; 2%). The most abundant MTs in all domains of life are the O-directed MTs (O-MTs). The O-MT subfamily is most common in plants and bacteria whereas only two O-MTs are found in humans [catechol O-MT (COMT) and N-acetylserotonin O-MT] and yeast [*Saccharomyces cerevisiae*; trans-aconitate methyltransferase (TMT1) ^[76] and cantharidin resistance gene (Crg1) ^[77]]. In animals, O-MTs are mainly involved in the inactivation of neurotransmitters or detoxification of mutagenic phenolics ^[78,79]. The plants O-MTs have diverse functions ranging from lignin biosynthesis, stress tolerance, to disease resistance ^[80]. The most common substrates for O-MTs are phenolic compound, such as catechol, and hexoses, along with carboxylic acids or CoA esters (Figure 2.16). One of the specific features of O-MTs is their regiospecificity, but there are certain O-MTs which are less selective for example those involved in flavonoid biosynthesis ^[81–83].

The next subclass of MTs is N-directed MTs (N-MTs), which are less diverse or numerous in comparison to O-MTs. N-MTs are mainly involved in signal transduction pathways in animals, where they regulate the function of certain signaling molecules [phenylethanolamine N-MT (PNMT), histamine N-MT (HNMT), indolethylamine N-MT (INMT)]. N-MTs are also found in plant and bacteria such as dimethylxanthine N-MT (DXNMT) involved in caffeine biosynthesis in plants and TyIM1 involved in biosynthesis of d-Mycominose, an unusual dideoxy sugar found attached to the antibiotic tylosin, a commonly used veterinarian therapeutic. The wide variety of substrates methylated by N-MTs includes non-ribosomal peptides (both peptide bonds and side chains), hexosamines, primary amines, secondary amines (i.e. indoles, imidazoles, more complex alkaloids), and tertiary amines (Figure 2.16).

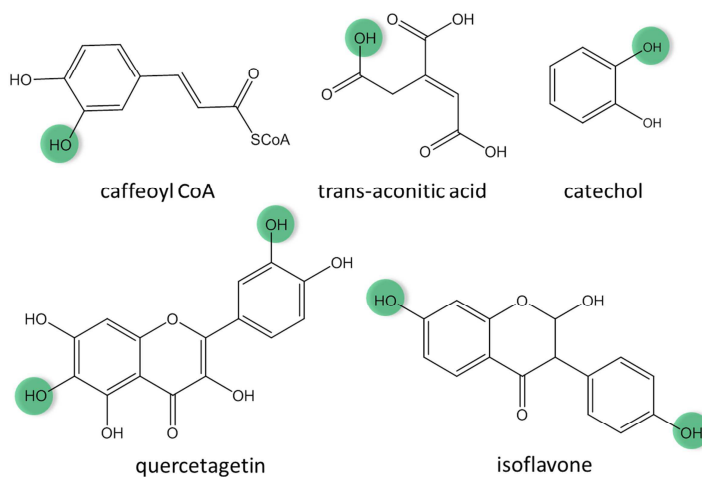
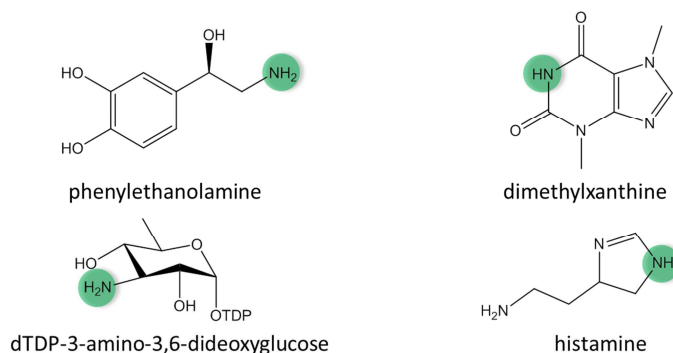
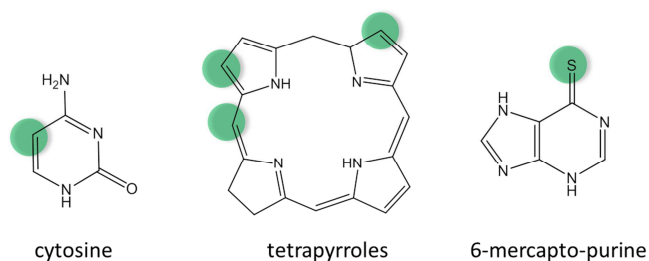
A. Substrates for O-MTs**B. Substrates for N-MTs****C. Substrates for C/S-MTs**

Figure 2.16: Chemical diversity of O-, N-, C-, and S-directed MT substrates. Methylation sites are highlighted in green. Adapted from Liscombe et al., 2012 ^[84].

C-directed methyltransferases are not so common in animals but are abundantly found in bacterial and plant systems. The most common C-MT in humans is the DNA methyltransferase which methylates primarily at the 5-carbon of the base cytosine, forming 5-methylcytosine. The known substrates for CMTs in plants and bacteria are tetrapyrroles, phenolics, aliphatics, and hexos(amin)es ^[85,86].

There are only few S-directed MTs identified or characterized so far. In plants, they participate in production of volatile halogen and sulfur compounds or biosynthetically tailor thiocyanates. [87–90] Human thiopurine S-MTs (TPMT) is involved in the detoxification of xenobiotics [91].

2.5.3 Structural diversity of methyltransferases

Methyltransferases exhibit distinct structural features even though they catalyze the same enzymatic reaction. The detail investigation about the structural features of methyltransferases is important for studying the unique mechanism involved in the methyl transfer reaction. DNA C5-cytosine methyltransferase M.HhaI is the first methyltransferase whose atomic resolution structure was solved using X-ray crystallography [92]. This has motivated many scientists whose efforts have helped solving and characterizing structures of many more methyltransferase. All the methyltransferase structures have a typical fold or characteristics which lead to the structural classification of MTs into five different classes [67].

Class I

Class I methyltransferases are involved in several physiological function such as gene regulation, protein expression, repairing mutation and DNA protection from restriction enzymes. Structurally, this class of methyltransferases is characterized by an $\alpha\beta\alpha$ sandwich structure consisting of seven stranded β -sheet flanked by two layers of alpha-helices. The β strands follow a typical architecture ($\beta 3 \downarrow \beta 2 \downarrow \beta 1 \downarrow \beta 4 \downarrow \beta 5 \downarrow \beta 7 \uparrow \beta 6 \downarrow$) where the last strands runs antiparallel in compare to other strands forming a reverse beta hairpin at the carboxyl end of the sheet. This fold bears similarity to the NAD(P)-binding Rossmann-fold domains of oxidoreductases. The C-terminal regions of the β -strands and the adjoining loops form the core of the catalytic site and mediate important interactions with the co-factor SAM and the substrate. One of the distinctive feature of class I methyltransferases is the presence of GXGXG (X - any amino acid) motif at the end of the first β strand ($\beta 1$). This motif is widely conserved and makes direct contact to the carboxypropyl group of SAM. Apart from this an acidic residue situated at the end of $\beta 2$ stand is also found to be conserved among class I MTs. This residue forms the hydrogen bond with ribose moiety of SAM. In addition to the core fold, class I MTs are also characterized by additional helices and extensions in the N-terminus which play significant roles in oligomerization and/or modulation of the substrate specificity [84,93].

Although most of them are monomers, few class I MTs could be homodimeric or even tetrameric ^[94]. All these differences suggest structural flexibility among class I MTs required for recognizing a whole range of substrates.

Class II

This class of methyltransferases is completely different to other MTs in overall architecture. They contain a long central antiparallel β strand which is flanked by groups of α helices. The cobalamin (vitamin B12)-dependent methionine synthase, MetH from *E. coli* belongs to this class of MTs. MetH transfers a methyl group from a folate to homocysteine via bound cobalamin to form methionine. MetH also consists of a reactivation domain responsible for reductive methylation of oxidized cobalamin in presence of SAM and flavodoxin. The binding site for SAM which makes hydrogen bond with conserved RxxxGY motif, is in the shallow groove along the edges of the β strands ^[95].

Class III

This structural class of methyltransferases is characterized by two $\alpha\beta\alpha$ domains which form a cleft between them. Each of these domains contains 5 β strands and 4 α helices. Similar to class I methyltransferases, a GXGXG motif is present at the C terminal end of the first β strand, but this motif is not responsible for interaction with SAM. The actual binding site of SAM is buried between two domains in the active site. CbiF, a MT responsible for cobalamin biosynthesis is a representative of class III MTs ^[96].

Class IV

This methyltransferase class consists of SPOUT family (SpoU and TrmD families) of RNA methyltransferase. They are usually present as homodimer with six stranded parallel β sheet flanked by seven α helices. The active site is located close to the subunit interface of homodimer containing residues from both the monomers. Another unique structural feature of this MTs class is the 'knot' like structure formed by back insertion of the C-terminus, typically the last ~30 residues. The presence of several catalytic residues confirms the structural importance of this substructure ^[97,98].

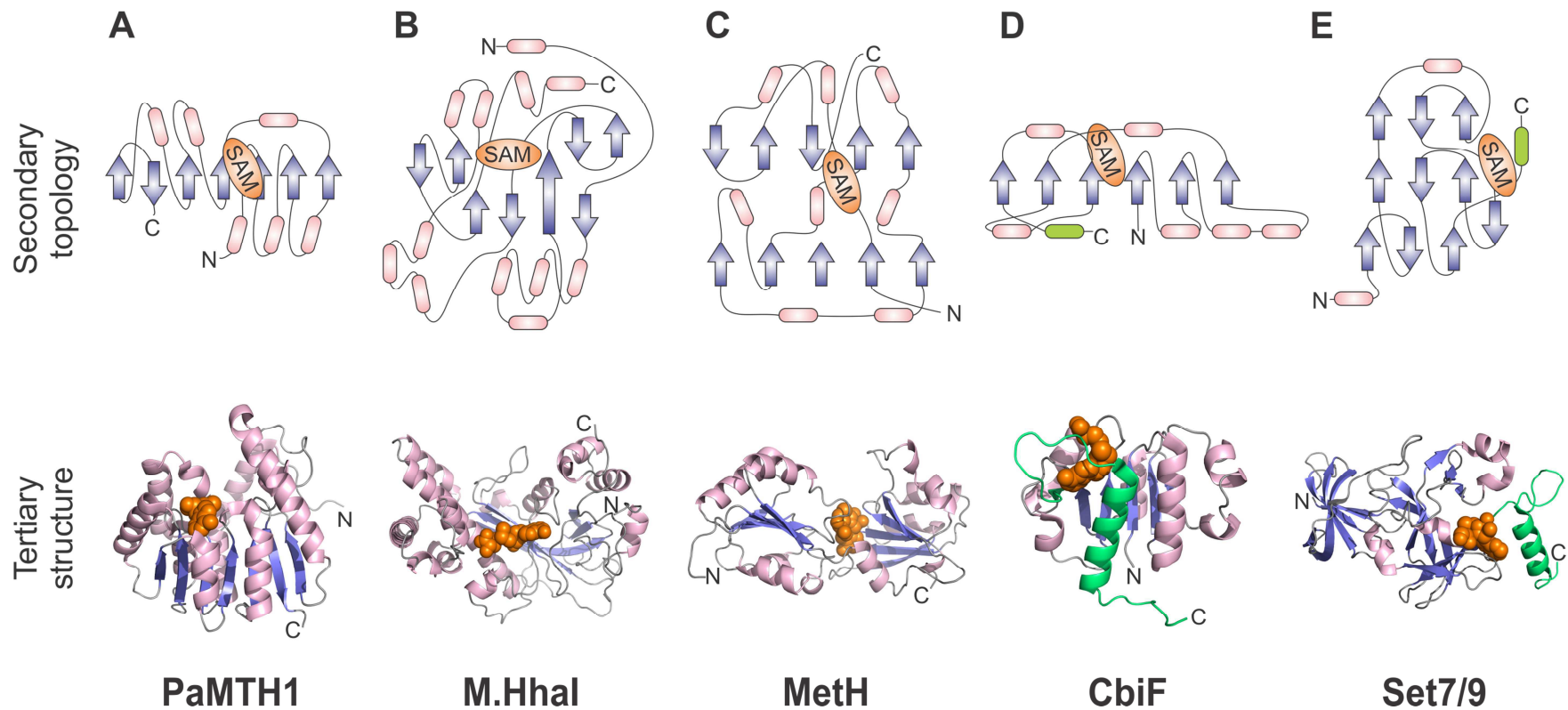


Figure 2.17: Three-dimensional structure of five classes of SAM-dependent methyltransferases. In each class a representative structure and topology diagram is given. A) Class I: enzyme M.Hhal (PDB - 6MHT), B) Class II: reactive domain of methionine synthase (PDB - 1MSK), C) Class III: the bilobal structure of CbiF (PDB - 1CBF), D) Class IV: enzyme Yibk (PDB - 1MXI), and E) Class V: histone lysine N-MT family (PDB - 1O9S). Adapted from Schubert et al., 2003^[67].

Class V

This class of methyltransferase is known as SET (Su(var)3-9, Enhancer of Zeste, Trithorax) –domain proteins. Several proteins belonging to this class have been shown to methylate lysine in flexible tails of histones or in Rubisco (Ribulose-1, 5-bisphosphate carboxylase oxygenase). Structurally, class V MTs consists of a series of 8 curved β strands forming 3 small sheets. Similar to Class IV MTs, the C terminus is also tucked to form a knot-like structure^[99–104]. The SET domain is flanked by pre- and post-SET regions consisting of diverse sequences. These regions actively participate in methyl transfer activity and are also responsible for substrate recognition and specificity.

The example and structure of each class of methyltransferases discussed above are shown in figure 2.17.

2.5.4 Clinical significance of methyltransferase

The dysfunction of methyltransferase has been linked to various diseases. Several studies suggested that polymorphisms in human methyltransferase genes are associated with increased risk for disease. One such polymorphism in human COMT, V108M variant is found to be prevalent in many patients suffering from breast cancer^[105] and neuropsychiatric diseases. Mutation in human DNMT has been associated with several genetic disorders. The altered DNMT1 activity due to mutations is the cause behind a form of hereditary sensory and autonomic neuropathy type 1 (HSAN1) with dementia and hearing loss^[106]. Moreover it has been found that DNA methylation profiles in cancer cells are unique from normal, differentiated cells^[107,108]. Hypermethylation in CpG islands located in the promoters of tumor suppressor genes, such as retinoblastoma (Rb1), von Hippel-Lindau (VHL), cyclin-dependent kinase inhibitor 2A (CDKN2A, p16), adenomatous polyposis coli (APC), has been linked to cancer development^[107–109].

The wide variety of diseases associated with methyltransferase present this protein class as a novel, chemically tractable target class for drug discovery. Several small-molecule inhibitors have been successfully designed for DNMTs and COMT. COMT inhibitors such as entacapone, tolcapone, and nitecapone are used in the treatment of Parkinson's disease^[110]. Recently two DNMT inhibitors 5-azacitidine and Decitabine have been approved by US Food and Drug Administration to treat myelodysplastic syndrome^[111]. The drug development platform for methyltransferase related disease is a growing market and its success depends on proper understanding of biochemical and structural

characteristics of newly identified methyltransferases. In this thesis, the recently discovered methyltransferase PaMTH1, the putative SAM O-MT from filamentous fungi *P. anserina* ^[112] has been studied by structural biology. PaMTH1 has been suggested to be involved in age-related methylation reactions protecting aging cultures of *P. anserina* against increasing oxidative stress ^[112,113].

2.6 Structural biology of proteins

Proteins perform a range of important functions that regulates complex cellular events. To unravel atomic details regarding those functions, a well-defined three dimensional structure of the protein is necessary. Apart from structure, biological functions are governed by both local and global conformational dynamics of the protein. Structural biology / genomic is the field of study which gives us information about both the atomic resolution structure and conformational dynamics of a protein using several biophysical techniques such as X-ray, NMR.

The history of structural biology goes back to 1954, when Max Ferdinand Perutz after a struggle of 30 years solved for the first time an atomic resolution structure of a protein, Hemoglobin using X-ray crystallography ^[114]. This was followed soon by another high-resolution crystal structure of a protein myoglobin determined by Kendrew et al. in 1958 ^[115]. For their contribution in "studies of the structures of globular proteins", both Max Ferdinand Perutz and John Cowdery Kendrew were awarded jointly the Nobel Prize in Chemistry in 1962. These initial successes open up opportunity to other crystallographers, and the rate of protein-structure determination increased rapidly in subsequent years. Soon other biophysical techniques join forces with X-ray crystallography to solve protein structures. Among those, nuclear magnetic resonance (NMR) is considered as the most prominent because of its ability to solve the structure of the protein in aqueous solution. Kurt Wüthrich and co-workers determined the first de novo protein structure of bull seminal protease inhibitor using homonuclear NMR in 1984 ^[116]. The first NMR structure having close resemblance to the crystal structure of the homologous protein PSTI (porcine pancreatic secretory trypsin inhibitor) ^[117], was criticized by the X-ray crystallographer because they speculated it to be modeled after the crystal structure. However, Wüthrich lab in 1988 ^[118] independently solved the structure of α -amylase inhibitor tendamistat using NMR. To everyone's surprise this structure turned out to be virtually identical to the one solved by Robert Huber lab in 1989 using X-ray technique ^[119]. This incident has been marked as a turning point for NMR, which became

slowly accepted as a trustworthy method to determine protein structures. In 2010, Kurt Wüthrich received Nobel Prize for his commendable effort to recognize the power of NMR in solving biomolecular structure.

Although structural biology was initially used to acquire basic knowledge about protein structure and function. But the pioneering works on proteins structures motivated scientist to open up a new frontier where systematic characterization of disease relevant proteins has been used to develop new leads for drug development platform. The last two decades have witnessed characterization of thousands of such proteins, as a result of the confluence of scientists from various disciplines. And the development of several high-throughput methods has a major impact on structural biology by solving protein structure in a faster and economic way. But solving the structures of all proteins is an impractical goal because many proteins can't be crystallized such as inherently unstructured proteins. Thus different structural genomics organizations are initiated around the world which performs collaborative and focused researches on a list of disease relevant protein targets.

2.6.1 Biophysical techniques: X-ray crystallography and NMR

Starting with the elucidation of Hemoglobin protein crystal structure ^[114] by Max Perutz in 1954, structural biology has evolved quickly into a major research arena where thousands of high-resolution structures deposited in the Protein Data Bank (PDB) every year (Figure 2.18). Statistical data provided by PDB showed that most (87%) of those structures has been solved using X-ray crystallography. But in recent years the contributions of nuclear magnetic resonance (NMR) spectroscopy and electron microscopy (EM) have increased significantly (12.5% and 0.5% of the PDB entries, respectively).

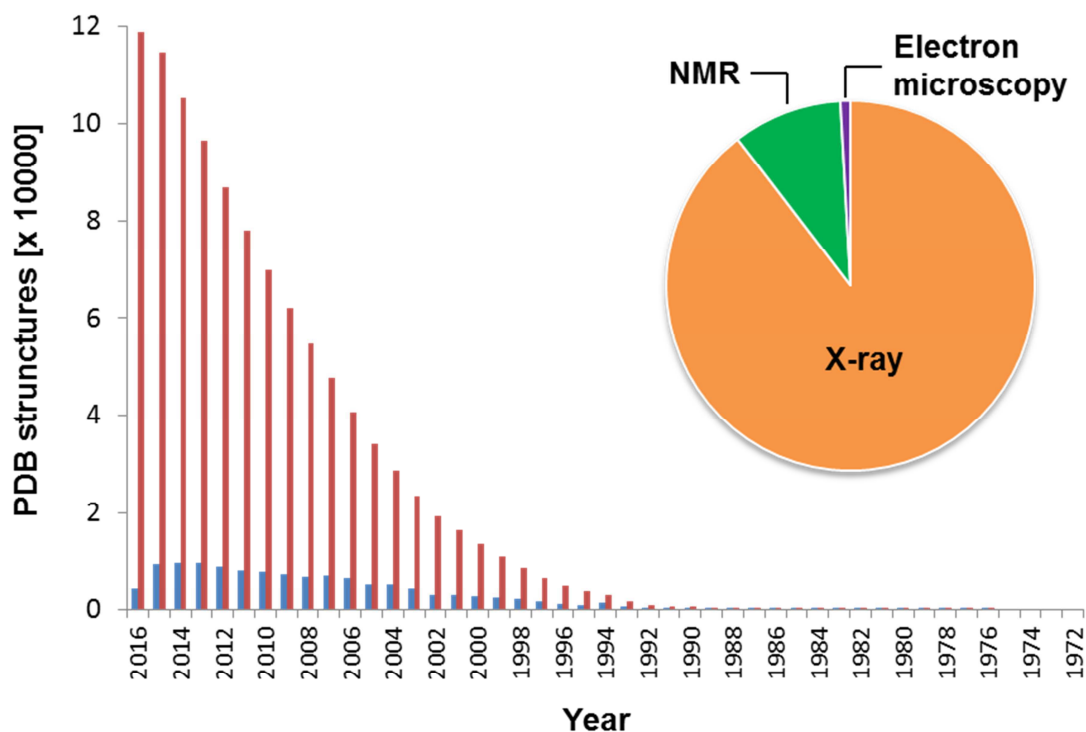


Figure 2.18: Statistics of structures deposited in PDB over the years ^[120].

Although large share of high resolution, three-dimensional protein structures deposited in PDB has been solved by X-ray crystallography as indicated in figure 2.18, NMR spectroscopy contribution to the field of structural biology is significant and has been shown to complement X-ray crystallography quite nicely ^[121]. The biological system and the question to be answered determine which among these two techniques should be utilized.

The most frequently utilized biophysical technique to solve a high-resolution, static protein structure is the X-ray crystallography. It is applied for solving structure of all kind of protein and protein complexes. Crystallography has also made major advancement in determining membrane protein structures that opens up a new frontier in drug development field. But still the main hurdle most crystallographers face is to obtain suitable crystals for the protein of interest that can diffract to a sufficient resolution. Success in getting crystal also doesn't guarantee successful determination of protein structure, since sometimes crystallization may change the conformation of proteins due to packing interactions, which can give false information regarding the structure of a protein and its interaction with other ligand or protein. Apart from that, there are some proteins which are difficult to be crystallized due to some intrinsic property like flexibility. Flexibility

in some protein prevents the formation of crystal lattice which is a prerequisite for high quality crystal. Thus intrinsically disordered proteins (IDPs) are not possible to be studied by X-ray crystallography.

The solution state NMR spectroscopy, on the other hand, can be employed for structural and dynamic studies of protein at physiological condition (e.g., in solution, ambient ionic strength, and around neutral pH). With emerging NMR structures, it is now evident that NMR spectroscopy is slowly becoming an alternative approach to obtain structural information in cases where crystallization of a target protein is not possible. Another positive aspect of NMR spectroscopy is that it can be used to investigate dynamics and protein-protein interaction which are difficult or cannot be studied by X-ray crystallography. Moreover NMR is suitable for studying real time biological processes both in vitro and in vivo at atomic resolution on a wide range of time scales. For instance in recent time, In-cell NMR have been successfully employed to reveal the dynamics and structures of protein and RNA within the physiological environment of cells.

In spite of all the positive aspects, the protein structure determination by NMR spectroscopy is far more laborious and time-consuming in comparison to X-ray crystallography. NMR spectroscopist has to overcome several hurdles which include preparation of sample, data acquisition, structure calculation and validation. To improve this condition much emphasis has been directed toward developing automated analysis method, which reduces the time to acquire NMR structure. The way of calculating a structure by NMR and X-ray crystallography is also different. In X-ray crystallography, the electron density map indicates the actual position of backbone atoms, whereas the NMR constraints used for structure calculation are mostly implicit and thus required proper assessment of the structural ensemble ^[122,123]. The main limitation of NMR spectroscopy is the molecular weight of the protein to be studied. Most of the de novo determined NMR structures have a molecular weight between 8–15 kDa. The structure determination of higher molecular weight protein using NMR is not straightforward and requires different kind of computational methods like homology modeling. Recent data on NMR structures deposited in the PDB shows that out of 8668 structures determined using NMR spectroscopy only a few structures belong to the proteins with molecular weight of 25 kDa or above. With the advancement of TROSY based NMR experiments and development of different labeling techniques, this scenario is rapidly changing leading to an increase in number of NMR structures of high molecular weight proteins.

The advantages and limitations of both NMR and X-ray crystallography techniques, in fact, make them complementary. If both methods are implemented together, there is a much higher probability of obtaining information of a particular biological system. The information gathered from crystallized protein and protein in solution offers a perspective of the effects of chaotic conditions when compared with ordered, packed structures. Thus by analyzing NMR dynamics of protein, binding information, and conformational changes in solution one can provide further insights into existing crystal structure data.

In this thesis, both X-ray crystallography and NMR techniques were employed along with other biophysical techniques to investigate PaMTH1, a novel SAM O-MT from a filamentous fungus, *P. anserina*. The crystal structure of PaMTH1 provides information about the global structure of the methyltransferase in its apo-state (Figure 2.19 A) and the binding pocket of its ligands (SAM and SAH) in its holo state (Figure 2.19 B).

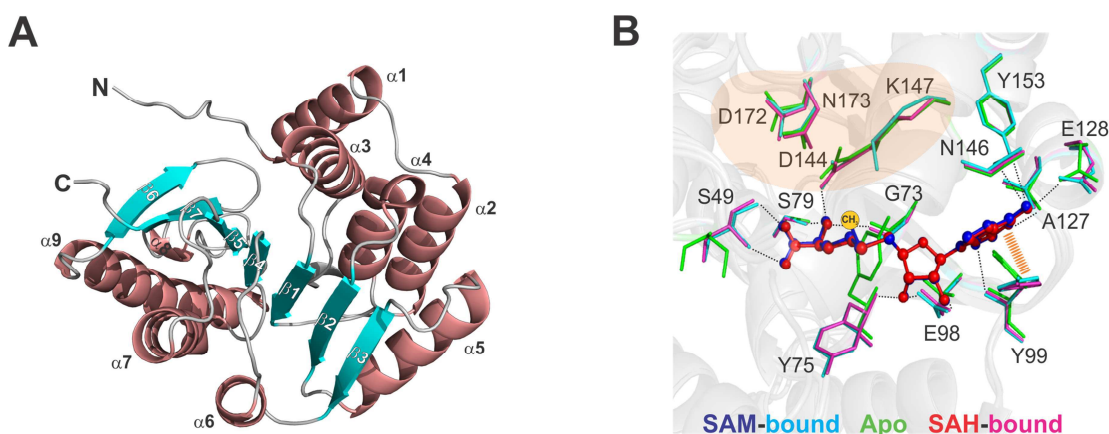


Figure 2.19: Crystal structure of PaMTH1. A. Rossmann fold architecture of PaMTH1 monomer (helices (dark salmon), β -strands (cyan), and loop (gray)). B. Close-up view of the catalytic pocket of PaMTH1, showing the ligands (SAM (blue) and SAH (red)) and the interacting amino acids (apo-state (green), SAM-bound (marine blue), and SAH-bound (magenta)). Putative substrate or metal binding residues are highlighted. Hydrogen bonds and π - π interactions are shown as black dotted lines and orange dashed lines, respectively.

But the binding affinity of these ligands was determined using NMR titration experiments by a simultaneous fit of the observed chemical shift perturbations (CSPs) to the increasing concentration of ligands (result not shown here). NMR spectroscopy was further used to investigate the enzymatic mechanism of PaMTH1, which involves the cation dependent methyl transfer reaction of PaMTH1 from the cofactor SAM to the putative substrate myricetin. A simple 1D ^1H NMR experiment shows the conversion of

the cofactor SAM to the byproduct SAH after the transfer of the methyl group (Figure 2.20 A) and the simultaneous formation of methoxy-myricetin from the substrate myricetin (Figure 2.20 B). Our study provides the best example where NMR and X-ray crystallography were successfully utilized in combination to study the different aspects of a single system and thus showing the necessity of both these techniques.

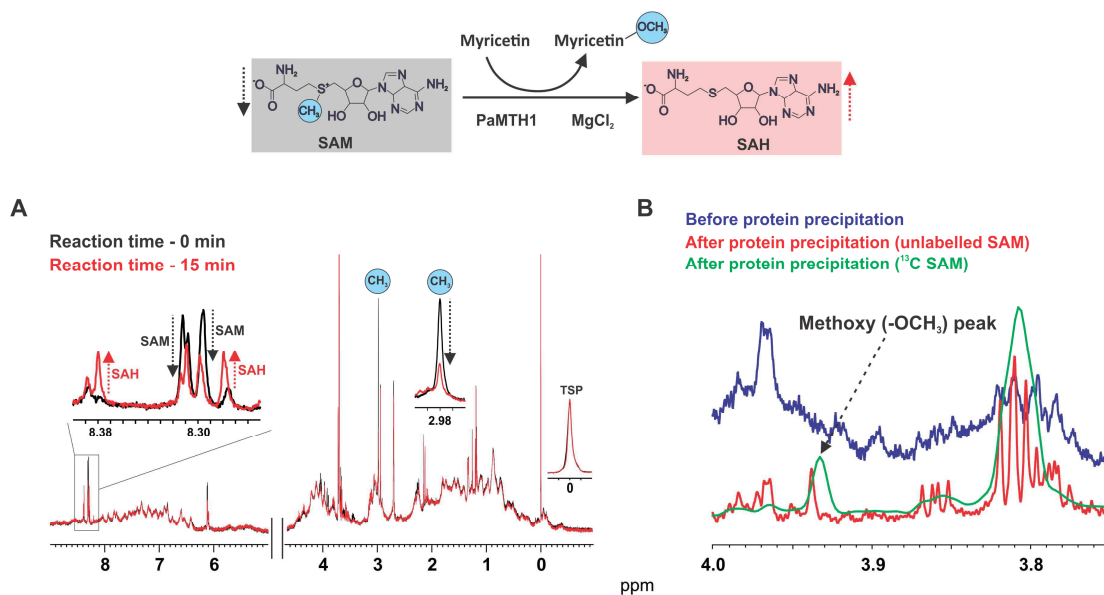


Figure 2.20: Substrate methylation monitored by NMR. A. Overlay of 1D ¹H spectra of the reaction mixture containing PaMTH1, myricetin, SAM (PaMTH1/myricetin/SAM ratio, 1:10:10), and 1 mM MgCl₂ at 0 min (black) and 15 min (red) indicates methyl group transfer from SAM and formation of SAH. B. Overlay of 1D ¹H spectra of reaction mixture before (blue) and after (unlabeled SAM (red) and ¹³C,¹⁵N-labeled SAM (green)) protein removal, indicating formation of methoxymyricetin. Schematic representation of the methyl group transfer reaction is shown above.

2.6.2 Protein dynamics studied using NMR spectroscopy

Three-dimensional protein structure can provide information about the function of the protein or its interaction with other proteins or substrates. However structural data is not enough to completely understand how a protein works. For this, a detailed insight into protein dynamics is essential [124,125]. The principle that structure of a protein regulates its function is oversimplified as it doesn't consider the profound impact of dynamics on protein behavior. Protein dynamics are defined by change of a system over time which is fundamental to a biological process. Most of these dynamical processes in proteins are governed by continuous conformational fluctuations with a wide range of time scales.

These conformational changes in protein lead to both global and local motions which can be rate limiting factors for various biological functions. Slow dynamic processes are in the range of μs to at least ms and correspond to biological processes such as protein folding/unfolding, protein-protein interactions, enzyme catalysis, domain motions, and signal transduction ^[126]. The faster dynamic processes in the range of ps to ns represent local motions such as vibrations, methyl group rotations, bond liberations, angle fluctuations, side chain rotations, and aromatic ring flips. The protein dynamics can be studied using different biophysical techniques such as Fluorescence, UV/Vis spectroscopy, Infrared spectroscopy have been developed to study these dynamical processes. But all these are lower-resolution methods which are used to investigate one or a few sites or an average over the entire system. NMR spectroscopy is the only technique which provides information about the dynamic character of protein using many different nuclei at atomic resolution in solution and near to physiological condition ^[124,125,127,128]. An overview of protein dynamics at different time scales and the biophysical method used to study these processes is shown in Figure 2.21.

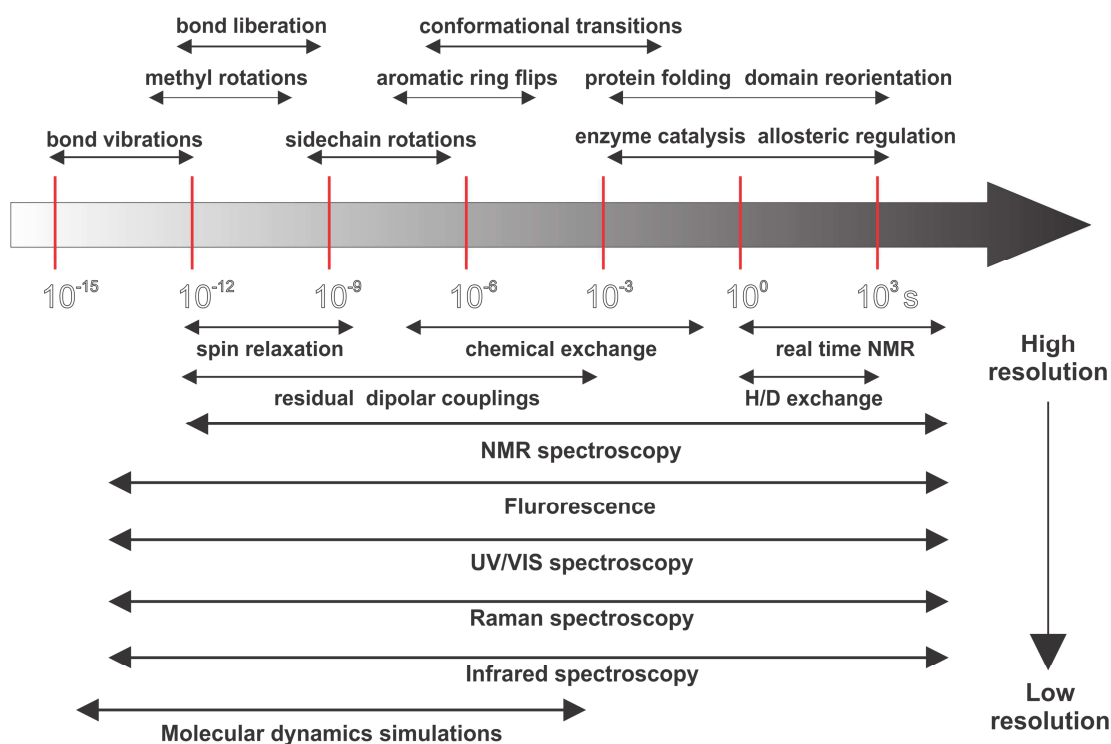


Figure 2.21: Overview of protein motions at different time scales. NMR and other biophysical techniques applied at those time scales are indicated below. Adapted from Werner et al., 2012 and Henzler-Wildman et al., 2007 ^[126,129].

The dynamic behaviors in protein can be characterized into fast, medium and slow motions based on the NMR timescale. Fast motions (faster than ns) can be effectively measured using NMR relaxation experiments. The overall rotational diffusion of the protein in solution as well as local fast motions in the protein alters the NMR properties (such as nuclear dipoles or chemical shift anisotropies) with respect to the static magnetic field and thus changes the NMR relaxation times. NMR relaxation methods are utilized to characterize picosecond-to-nano second dynamics by measuring site specific observables such as longitudinal R1 and transverse R2 relaxation rates along with heteronuclear nuclear Overhauser effect (hnNOE). These provide information regarding the amplitude (the order parameter, S2) and the timescale (τ_e , the internal correlation time) of bond fluctuations. The physical processes in this time window include bond vibration and liberation, side chain rotamer interconversion, random coil and loop motions and backbone torsion angle rotation. These motions have been implicated as important for enzyme catalysis, ligand specificity and affinity, allosteric effects ^[130,131], conformational entropy ^[132–135] and heat capacity ^[136,137].

The dynamic fluctuations on the order of milliseconds change within the duration of the NMR signal acquisition and thus affect the evolution of the NMR signals due to the interchange between the various conformers with different dynamic characters. These slow (μs – ms) motions introduce an additional contribution R_{ex} which can affect the intrinsic nuclear spin transverse relaxation. The effect of exchange on the transverse relaxation rate can be studied by relaxation dispersion NMR measurement such as rotating frame spin relaxation ($T1\rho$) or Carr–Purcell–Meiboom–Gill (CPMG) measurements ^[127,138,139]. Relaxation dispersion experiments can provide information on (i) the exchange rate, $k_{ex} = 1/\tau_{ex}$, (ii) the populations of the exchanging states and (iii) the absolute difference between the chemical shifts of the exchanging state ^[138,139]. Such information can be utilized to investigate interesting biological processes happening in the intermediated time scales, for example enzyme catalysis, ligand binding, protein folding, and allosteric regulation.

Finally the slow dynamics (ms-s) in proteins occur at a much slower timescale in comparison to NMR acquisition time which allows the independent measurement of different intermediate states. Physical processes on this timescale include protein folding, solvent hydrogen-exchange and relatively slow conformational changes such as *cis-trans* proline isomerization and domain movements that may directly affect catalytic turnover rates. These slow processes can be detected by measuring successive experiments which provide information on their kinetic parameters. In the hydrogen to deuterium

exchange experiment, the change in NMR signal intensities over time due to exchange of the labile protein backbone amide group between proton and deuterium from the solvent is measured. The hydrogen exchange rate which yields information about the solvent accessibility and local structure stability (i.e., hydrogen bonding) that can be influenced by dynamic processes. Another powerful yet simple NMR technique to measure dynamic processes on the \sim s timescale is the real time NMR, which has been discussed in details in the next section.

2.6.3 Real-time NMR

To detect the dynamic processes on the timescale of \sim s time-dependence change of NMR signal intensities are quantified using the powerful technique of real-time NMR ^[140]. This helps us to study physical processes such as protein folding, solvent -exchange and slow conformational changes, enzyme catalysis and domain rearrangements. Real-time NMR spectroscopy is ideally suited for combining high resolution data with kinetic experiments ^[140]. The first step in real-time (RT) NMR experiment is to initiate the physical process of interest using a special injection apparatus or application of laser light ^[141,142]. This is followed by a rapid acquisition of several NMR spectra which is characterized by a decrease in intensity of an initial set of NMR resonances. A new set of resonances appear at a different chemical shift resulting from alteration in the local structures and/or population of different conformers or states.

A typical real-time NMR experiment is analyzed by plotting the signal intensities from a series of spectra against time, which can be then fitted to a suitable model such as exponential function, which reveals the underlying kinetics regulating the physical process. Moreover presence of multiple signals as reporter groups can be utilized to determine whether structural changes are concerted or whether different parts of the molecule changes at different rates. A prominent example of a RT-NMR has been shown in Figure 2.22 which depicts the kinetics of five tryptophan resonances of wild type bovine rhodopsin after light illumination.

In RT-NMR, each data point corresponds to a single NMR spectrum, which means only slow process (τ = mins) can be analyzed by this experiment and that too by using 1D spectroscopy only. But recent developments in methodology have enabled the use of 2D RT-NMR with a reduced acquisition time ^[143]. One particularly noteworthy application of fast-acquisition RT-NMR involves the use of 2D SOFAST HMQC experiment.

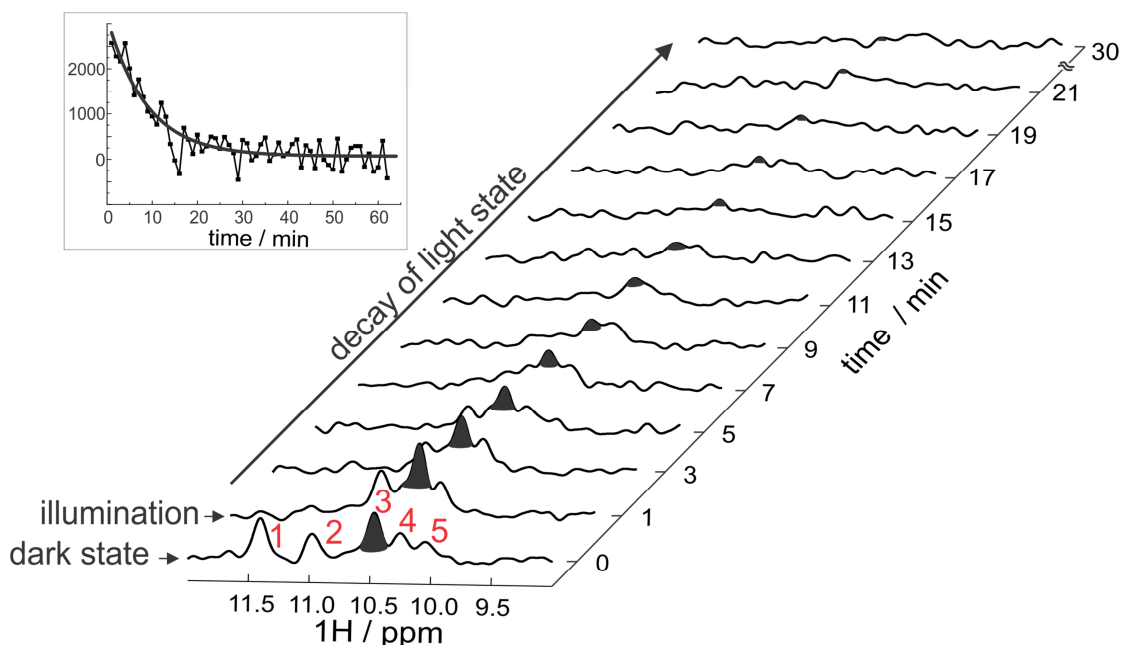


Figure 2.22: Real time NMR. A series of 1D ^1H NMR spectra of $\alpha,\epsilon\text{-}^{15}\text{N}$ -tryptophan-labeled rhodopsin recorded at different time intervals after illumination. The five resonances visible in the dark state correspond to the five tryptophan residues present in rhodopsin. After illumination, the 1D ^1H spectra were recorded with a temporal resolution of one minute (alternative measurement shown here). Inset: A mono-exponential fit was applied for extracted signal intensities of the highlighted resonance (Peak 3).

2.6.4 SOFAST-HMQC

The acquisition time for recording a high resolution 2D spectrum requires several minutes. The intrinsic low time resolution of 2D NMR spectroscopy limits its use in RT-NMR. This limitation can be overcome by implementing a SOFAST-HMQC (band-selective optimized flip-angle short transient heteronuclear multiple quantum coherence) ^[144]. SOFAST-HMQC allows the fast (within seconds) recording of a 2D ^1H - ^{15}N correlation spectra of a protein using an improved pulse sequence which allows very high repetition rates of the experiment with high quality solvent suppression. This results in a significantly increased sensitivity in relation to the recording time. The repetition rate of this pulse sequence depends on the delay between the first pulse of one scan and the first pulse of the next scan ^[145]. The shorter the inter scan delay time, the higher the repetition rate. However, if the spin system is saturated by fast rf pulses there is a significant loss in the signal to noise ratio. Thus optimization of the sensitivity can be

achieved by applying non-90° pulses known as Ernst angle pulses. The Ernst angle depends on TC and T1 and can be defined as:

$$\cos(\alpha_{Ernst}) = e^{-\frac{T_c}{T_1}}$$

α_{Ernst} is the Ernst angle; T_c is the interscan delay time; T_1 is the longitudinal relaxation time. In SOFAST-HMQC experiment, the signal loss due to B1 inhomogeneities is further reduced by using less radio frequency pulses.

The pulse sequence for SOFAST-HMQC is initiated by the variable flip angle Ernst angle pulse (α) with PC9 shape for the hydrogen nucleus (Figure 2.23). This pulse transfers the magnetization from the z-axis to the $-y$ axis with a delay time Δ corresponding to $1/(2J_{HX})$. Due to the spin evolution of PC9, an additional δ is introduced. This is followed by two 90° pulses on the nitrogen nucleus with a 180° band selective refocusing pulse applied on the hydrogen nucleus exactly in the middle of the two pulses. GARP decoupling was applied on the nitrogen nucleus during the detection. Between each scans T_{rec} is used as recycle delay. The remaining magnetization was removed by applying pulse field gradients after the detection and before the first 90° pulse and after the second 90° pulse applied to the nitrogen nucleus.

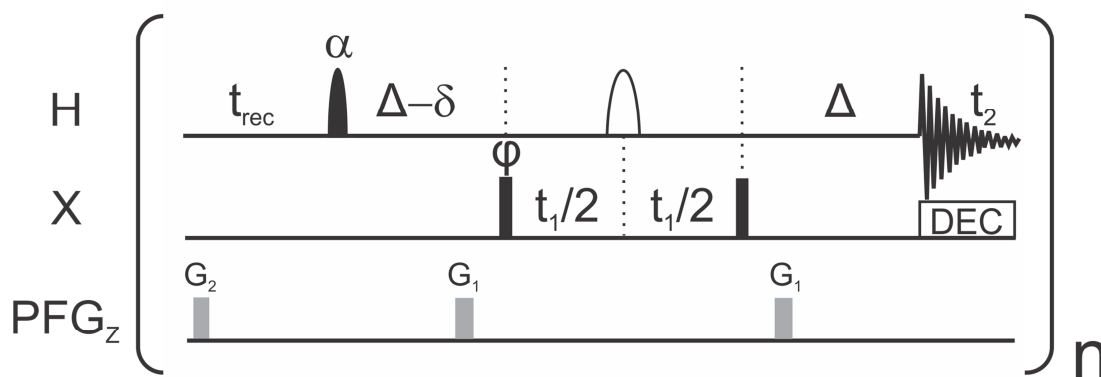


Figure 2.23: Pulse sequence of the SOFAST-HMQC experiment ^[144]. X can stand for ¹⁵N or ¹³C.

In our study we recorded a series of two dimensional ¹H, ¹⁵N SOFAST-HMQC spectra of the selectively tryptophan labeled bovine visual rhodopsin after light illumination using argon ion laser setup. The spectra recorded with a time interval of one minute were able to produce well resolved tryptophan resonances. The first eight spectra of light illuminated

rhodopsin are shown in Figure 2.24 each as an overlay of the dark state spectrum of the tryptophan indole region.

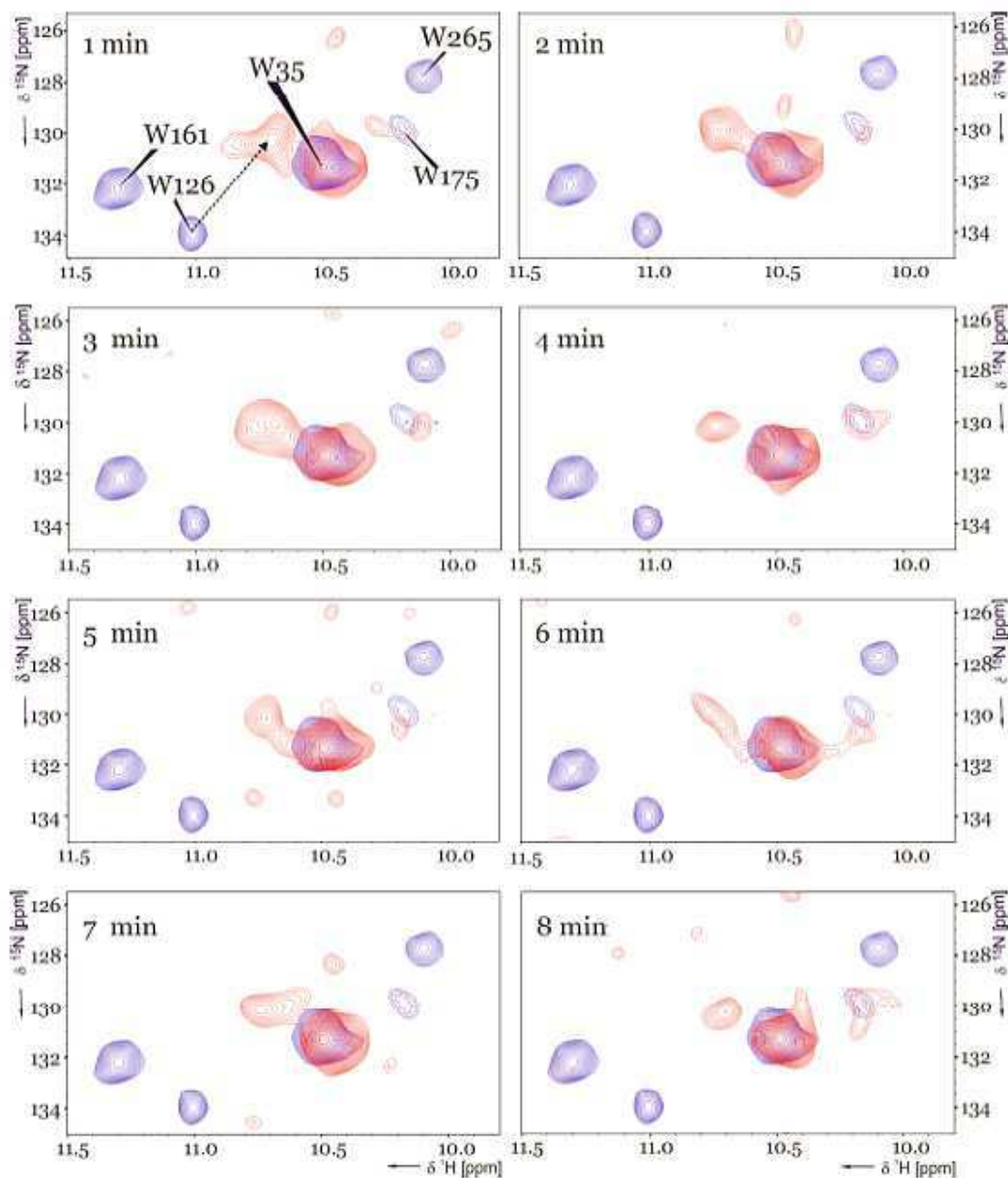


Figure 2.24: Two dimensional SOFAST-HMQC spectra of α,ϵ - ^{15}N -tryptophan labeled rhodopsin recorded in a pseudo three dimensional manner. The temporal resolution of the spectra series was one minute. The first eight spectra after the illumination are shown (red) each with the corresponding dark state spectrum (blue) as an overlay. The spectra were recorded at $T=298\text{ K}$.

2.6.5 In-situ illumination set up

In our group, 1D RT-NMR and 2D ^1H , ^{15}N -SOFAST HMQC have been utilized to study the photodynamics of bovine visual rhodopsin. To initiate the photodynamics, the NMR sample has been illuminated in situ at a wavelength of $\lambda=520$ nm using an argon ion laser (Spectra Physics) with a laser intensity of 0.3-3 W. The laser setup shown in Figure 2.25 uses optical fiber devices to directly guide the laser beam into the sample within the NMR spectrometer ^[146]. The laser beam passes through a mechanical shutter which controls the duration of the sample illumination. The mechanical shutter is connected to the console of the NMR spectrometer through an electronic device and the applied timing scheme of illumination is directly implemented into the NMR pulse sequence. An equally distributed illumination of the sample for a homogeneous sample state is ensured by using a pencil shape plunger in the NMR shigemi tube. The laser power and the applied illumination scheme are of crucial importance for the illumination efficiency of the sample.

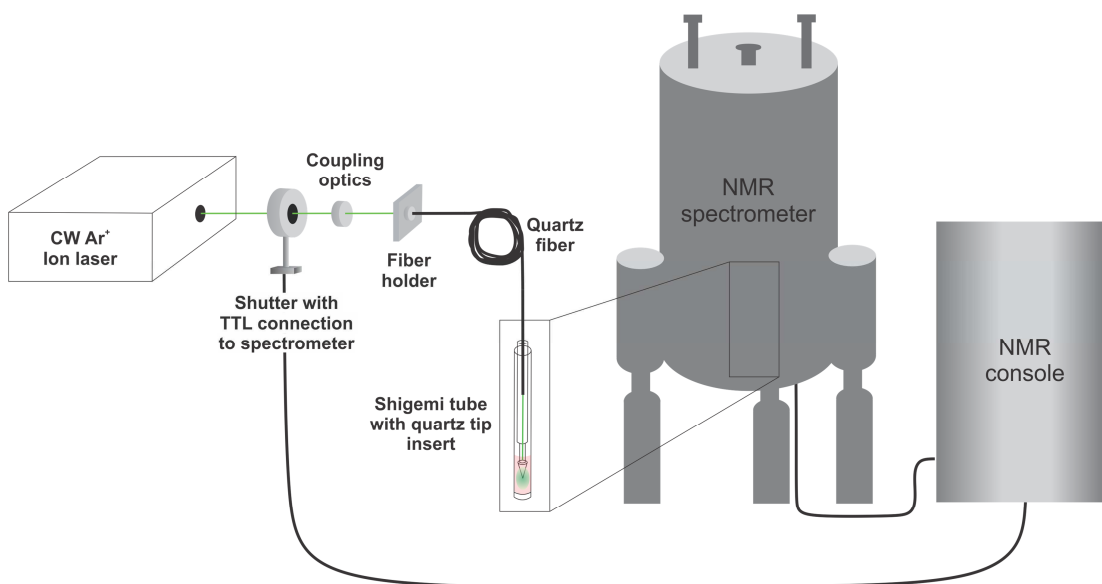


Figure 2.25: Laser set up. The argon ion laser beam is directly guided into the shigemi tube within the NMR spectrometer.

3 *NMR-spectroscopic Characterization of the Transiently Populated Photointermediates of Bovine Rhodopsin and its interaction with Arrestin*

3.1 The role of light in biology

Light is the primary source of energy essential for almost every life form on earth. Evolution of living organism to detect and respond to light is critical for the existence of life. The conversion of energy trapped in photons to chemical energy during photosynthesis is sole source of food for all living organisms. Apart from being the energy source, light has also played an important role as carrier of information. A large number of photo responsive biochemical machinery has evolved in several organisms to capture light and interpret the acquired information for environmental perception. The role of light as information carrier is the focus of discussion for this section.

Photoreceptors exist in all three domains of life: bacteriorhodopsin and bacteriophytochromes in bacteria, halorhodopsin in archaea and phytochrome and rhodopsin in eukaryote. The role of photoreceptors in all these organisms is to convert the electromagnetic energy into chemical signals, which triggers a complex system of biochemical responses. These responses differ among the biological species and can depend upon growth, movement, modulation of gene-expression pattern, differentiation, and development. One such biochemical response vertebrate vision is controlled by the most sophisticated and evolved apparatus of our nature, the animal eye. The eye provides detailed information about our surrounding through a process called visual perception in which electromagnetic information stored in photons are converted into electrochemical information. The vertebrate brain is able to translate this electrochemical information into a visual projection of our surroundings and thereby enables the phenomenon of vision. A closer look at the anatomy of the vertebrate eye is necessary for proper understanding of mechanism which regulates vision.

The visual perception is initiated by the interaction of electromagnetic energy in form of photon with certain light absorbing molecule which can convert the electromagnetic information into chemical information. These light absorbing molecules or chromophores,

are usually bound to a protein that triggers a signal cascade upon illumination of the chromophore. This chromophore-protein complex is known as photosensor or photoreceptor, which can be divided into four families: rhodopsins, phytochromes, xanthopsins and cryptochromes^[147] on the basis of the chemical structure of the attached chromophores. An overview of chromophores involved in biological signaling processes and their basic photochemistry is given in Table 1.1. Among these photoreceptors, rhodopsins which carry a retinal chromophore as a prosthetic group are the most extensively studied class.

3.2 The retina - a complex neural network

The vertebrate eye has to be organized in a way that the incoming light can reach the photosensitive cells in the retina in the back of the vitreous body. The vision is initiated when light rays are reflected off an object and enter the eyes through the cornea, the transparent outer covering of the eye. The cornea bends or refracts the rays that pass through a round hole called the pupil. The iris, or colored portion of the eye that surrounds the pupil, opens and closes (making the pupil bigger or smaller) to regulate the amount of light passing through. The light rays then pass through the lens, which actually changes shape under the control of the ciliary muscles so it can further bend the rays and focus them on the retina at the back of the eye. The retina is a thin layer of tissue at the back of the eye that contains millions of tiny light-sensing nerve cells called rods and cones, which are named for their distinct shapes. Cones are concentrated in the center of the retina, in an area called the macula. In bright light conditions, cones provide clear, sharp central vision and detect colors and fine details. Rods are located outside the macula and extend all the way to the outer edge of the retina. They provide peripheral or side vision. Rods also allow the eyes to detect motion and help us to see in dim light condition or at night. These cells in the retina convert the light into electrical impulses. The optic nerve sends these impulses to the brain where an image is produced. A cross-section of the organization of the vertebrate eye is shown in Figure 3.1.

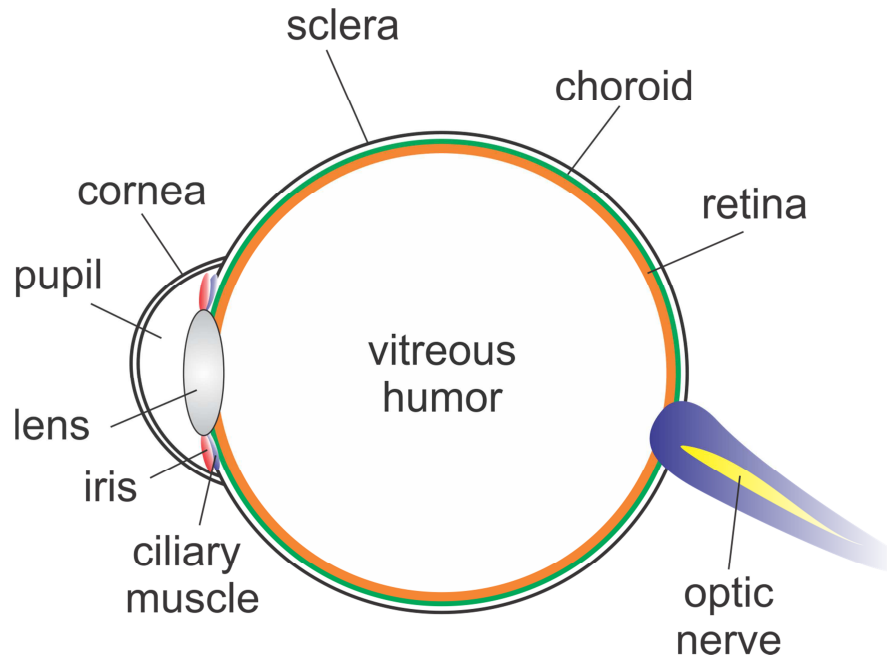


Figure 3.1: Schematic drawing of a cross section of the vertebrate eye.

3.3 Rods and cones - the photoreceptor cells

Vertebrates eyes consist of two types of photoreceptor cells – rod and cone, which are located in outmost layer of the retina, a 0.25 mm thick cell layer lining the inside of the vitreous body. The retina consists of several more layers of neuronal cells that function as neuronal signal transducers and regulators ^[148]. A cross-section of the retina is shown in Figure 3.2.

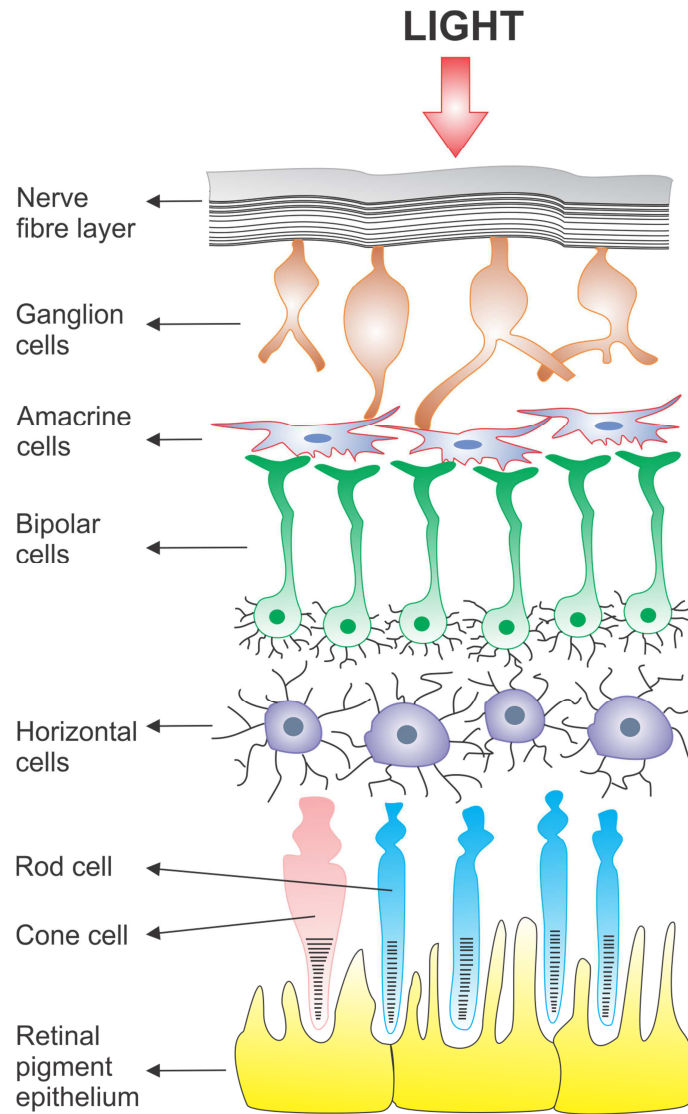


Figure 3.2: Schematic drawing of the human retina pointing out the individual layers and cell types.

A human retina contains approximately 5 million cones and 100 million rods ^[149] cells. Rods and cones cells can be differentiated on the basis of their shape, absorption properties and the associated light sensitivity. The photoreceptors in the rod cells have an absorption maximum at 500 nm and are responsible for scotopic vision, in which visual information is perceived under low light conditions. The cone cells are divided in red, green and blue cones, depending upon the presence of three different types of receptors with different absorption maxima at 570 nm, 535 nm and 440 nm. The range of wavelengths in which cone cells perform, make it ideal for photopic vision, which function

under bright light condition and helps in the perception of color. The combination of rods and cones covers a broad spectrum of environmental light conditions and thereby enhances the chances of good visual perception at bright and dim light conditions.

Rod cells are much more sensitive to light than cones. A single photon is sufficient to activate rod cells, whereas cones need at least 200 photons for producing a signal. During day light conditions when light is not a limiting factor, cones give a perfect picture of the environment. In dim light conditions, however, cones are not sensitive enough to supply a sufficient picture of the surroundings. Rods are more suitable for that purpose.

Both cell types consist of an inner and an outer segment, connected together by a cilium. The elongated rod outer segment (ROS) measures about 1 μm in diameter and 40 μm in length. It specializes in the function of the photoreception and contains the necessary compartments, the so called disc membranes. Disc membranes are formed of disc-shaped, flattened lipid bilayer in which the photoreceptor molecule rhodopsin is incorporated in the same orientation ^[150]. They are stacked in a dense manner and are enveloped by the plasma membrane of the outer segment. The narrow spaces between the disc membranes and the plasma membrane are filled with cytoplasm. The number of disc membranes in an approximately 16 nm thick rod cell varies according to species from 500 to 2000 per rod cell. The organization of rod cell is shown in Figure 3.3.

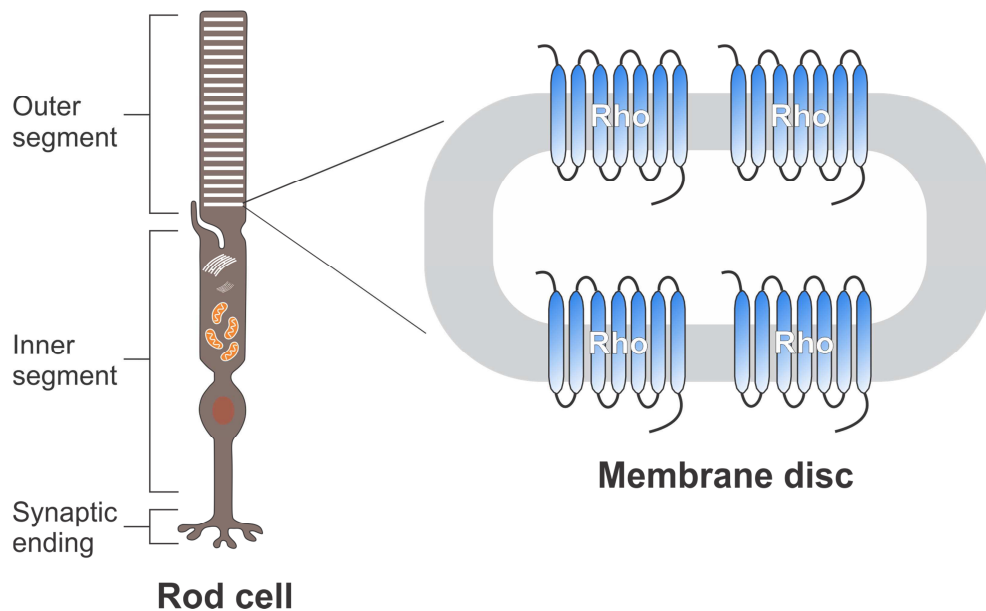


Figure 3.3: Schematic drawing of a rod with a magnified membrane disc with incorporated rhodopsin molecules. Adapted from Ernst et al., 2002 ^[151].

3.4 Signal transduction of the visual process

During the photocycle, the visual signal transduction takes place in the neural network of the eye. The signal transduction leads to a conversion of a physical signal in the form of an electromagnetic wave to an electrical signal via a biochemical pathway (Figure 3.4). The dark-adapted visual pigment rhodopsin consists of the apoprotein opsin and the chromophore 11-*cis*-retinal. By the absorption of a photon 11-*cis*-retinal isomerizes to all-*trans*-retinal and thereby induces a structural transformation of the photoreceptor. Rhodopsin thermally relaxes over several spectroscopically distinguishable intermediates bathorhodopsin, lumirhodopsin and metarhodopsin I (meta I). Meta I is in dynamic equilibrium with the enzymatically active form of rhodopsin, the metarhodopsin II (meta II). In this transition to the active form, the photoreceptor molecule undergoes the strongest structural transformation (see Section 2.3.1). Meta II binds and activates the G-protein transducin and thereby triggers the signal amplification ^[152]. In the inactive state, transducin forms a heterotrimeric complex consisting of three subunits or domains – T α (guanyl nucleotide binding domain), T β and T γ ^[153]. As a result of the light activation transducin molecule binds to the rhodopsin, which leads to signal transduction and amplification. This process is initiated by the exchange of GDP for GTP in T α domain, as a result of which the heterotrimeric complex is disintegrated to T α and T $\beta\gamma$ heterodimer. Free GTP-bound T α in turn activates the phosphodiesterase (PDE), which consists of four subunits, namely the PDE α and PDE β subunit and two small inhibitory PDE γ subunits. T α -GTP binds PDE γ subunits, activating the PDE α and PDE β subunits. The activated PDE hydrolyzes cGMP to 5'-GMP ^[154]. The decrease of cGMP concentration leads to a closure of the cGMP-gated Na⁺ ion channels, resulting in a hyperpolarization of the cell membrane. This is associated with a decreased transmitter release at the synapse of the inner segment and this is how the biochemical signal is turned into an electrical signal.

To terminate the visual signal transduction cascade, it is necessary that meta II photointermediate state is inactivated. Inactivation pathway involves two regulatory proteins, the GPCR rhodopsin kinase (GRK) and arrestin ^[155]. The arrestin competes with transducin for binding to meta II. The concentration of GRK in the rod cell is approximately one hundred times lower than that of transducins. Therefore one hundred transducin molecules are activated before a GRK molecule can interact with the catalytically active meta II. Once the GRK binds to meta II, the activation of transducin no longer takes place. The GRK phosphorylates serine residues at the C-terminus of the

activated rhodopsin ^[156]. Phosphorylated rhodopsin now has a high affinity for protein arrestin. Arrestin binds to phosphorylated rhodopsin and thus sterically blocks its interaction with transducin. This results in the termination of the enzyme cascade and the rhodopsin breaks down into its components opsin and all-*trans*-retinal. Opsin is dephosphorylated by a protein phosphatase^[157]. Finally the spontaneous association of opsin with 11-*cis* retinal regenerate new ground state rhodopsin molecule.

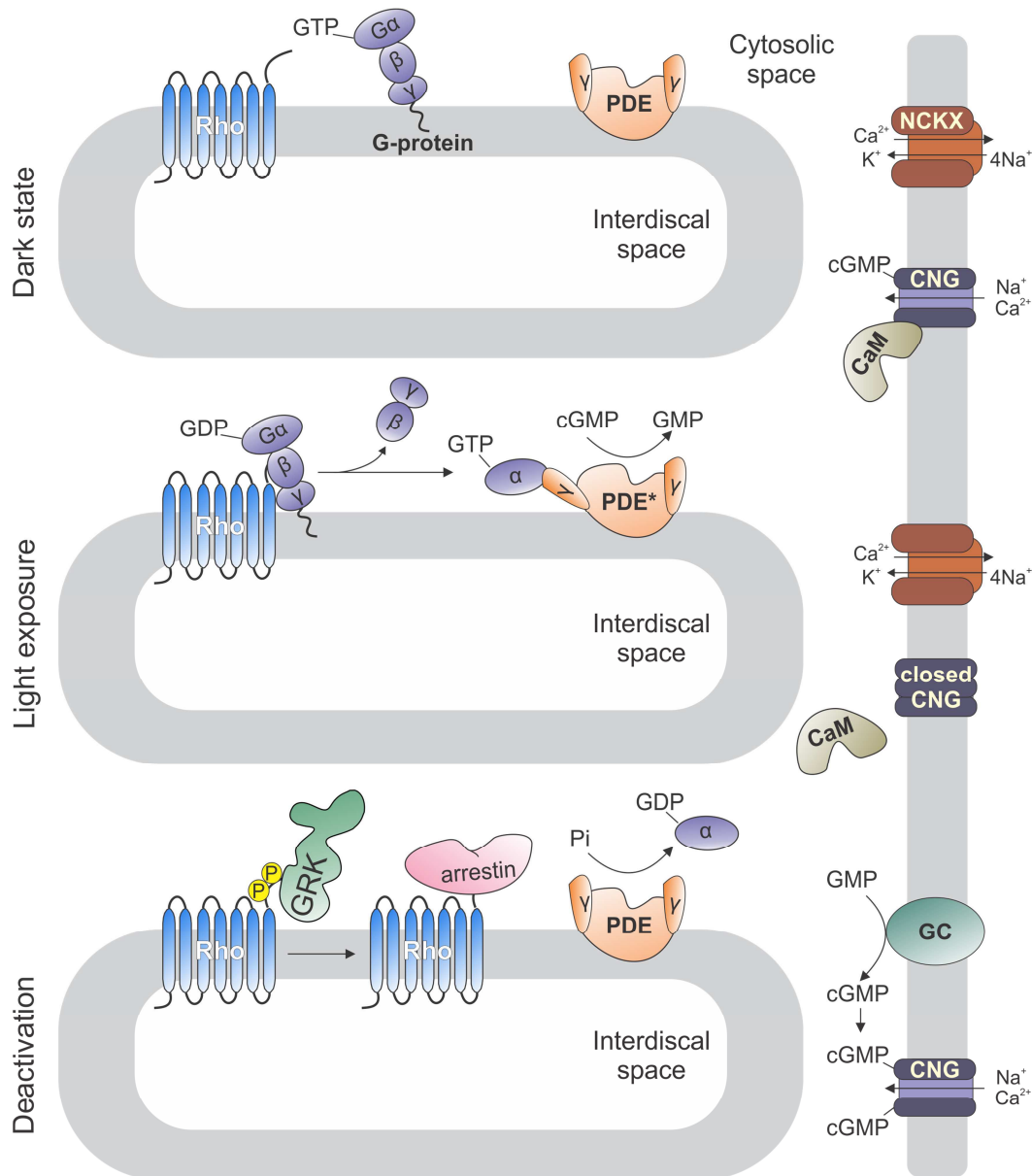


Figure 3.4: Schematic overview of the rhodopsin photo-transduction cascade. (Top) Dark state, (middle) light exposed and (bottom) inactivated rhodopsin state. Adapted from Burns et al., 2005 ^[158].

3.5 Rhodopsin - a G-protein coupled receptor

Rhodopsin belongs to the class A G-protein coupled receptor (GPCR) subfamily, which represents the largest and most diverse family of membrane receptors. These seven transmembrane (7TM) helical proteins are structurally transformed via an external signal, called agonist. In consequence of this conformational change, GPCR is activated and it binds heterotrimeric G-proteins, which ultimately leads to the signal amplification within the cell. Visual rhodopsin is the photoreceptor molecule of visual (light) signaling and is already for decades considered as a model protein to study the structure, genetics and biochemical mechanisms of GPCR. It corresponds to 90% of the protein portion of a disk membrane, which takes approximately 50% of the disk membrane surface. Visual rhodopsin is the first GPCR whose three-dimensional structure in the ground state was elucidated via X-ray crystallography ^[159]. The crystal structures of other photointermediates of rhodopsin ^[160,161] and recently the ligand-free opsin structure were also solved ^[162]. In addition to that, structures of rhodopsins from invertebrates like octopus *Todarodes pacificus* ^[163] are also now available. Moreover the structures of two isoforms of other GPCRs, the β -adrenergic receptor are also known ^[17,164].

3.5.1 Rhodopsin structure

Visual rhodopsin, the prototype GPCR, consists of a 39 kDa apoprotein opsin and a chromophore, 11-*cis*-retinal. The 348 amino acid protein contains seven membrane-spanning α -helices (helix I - VII) and a small cytoplasmic helix VIII (Figure 3.5). The chromophore 11-*cis*-retinal is located in the hydrophobic transmembrane region. In dark-adapted state it is linked to K296 amino acid side chain located in the middle of helix VII through a protonated Schiff base. The neutralization of a positive charge on the counterion of the E113 amino acid leads to the stabilization of the ground state. It has been postulated that a disruption of the salt bridge, results in a movement of helix VI ^[162]. This is initiated by a proton transfer from E181 to E113 through a H₂O molecule. As a consequence E181 now acts as a counterion, which forms a salt bridge with all-*trans*-retinal ^[165].

The post translational modifications in rhodopsin consist of an acetylation in the C-terminus and two glycosylation at the asparagine residues N2 and N15. The stability of α -helical transmembrane region is maintained by a disulfide bond between amino acids

C110 and C187, which are highly conserved among the GPCR. The residues C322 and C323 are palmitoylated and thereby anchored in the membrane. The C-terminus formed of amino acids stretch from G324 to A348 is also localized in the cytoplasm and is quite flexible in the dark-adapted state ^[166]. Within the C-terminal region are also numerous serine and threonine residues that serve as potential phosphorylation sites. These phosphorylation sites are necessary for binding arrestin, a protein that down regulates the activity of rhodopsin. The preference for the phosphorylation lies with the amino acids S334, S338 and S343. The 7TM helices are connected together by three extracellular loops and three cytoplasmic loops. The extracellular loops consist of a short loop (EI) between G101 and F105, a loop (EII) between V173 and T198, which connects helix IV and V together, and the amino acids T277 and P285 (EIII) between helix VI and VII. The EII loop along with the extracellular N-terminus, function as a "cap" of the retinal binding pocket ^[167]. The three intracellular loops correspond to amino acid sequence between Q64 and P71 (CI), E134 and H152 (CII) and R252 and Q225 (CIII). The region between helix VII and the palmitoylated C322 and C323 residues present in the short helix VIII, is often also referred to as the cytoplasmic loop CIV.

A highly conserved region in the subfamily A of GPCRs is the (D / E) R (Y / W) motif in CII loop or helix III, which for bovine and human rhodopsin corresponds to the tripeptide sequence of E134R135Y136 ^[168]. E134 is located directly on the lipid-water interface and is therefore very sensitive to small chemical changes in the immediate vicinity. A recent study has shown that protonation of E134 leads to the conversion of rhodopsin to the active state ^[169]. The E134-carboxyl group forms a salt bridge with R135 which in turn interacts with E247 and T251 of helix VI to form the so called ionic lock. This ionic lock dissociates after activation and allows helices VI and III to move away from each other. Another highly conserved GPCR motif is NPXXY motifs (NPVIY in bovine rhodopsin) between helix VII and helix VIII which plays an important role in the restructuring and is probably involved in the G-protein binding ^[170]. Several studies have shown that the cytoplasmic loops CII and CIII, as well as the cytoplasmic helix VIII are also involved in transducin binding ^[171].

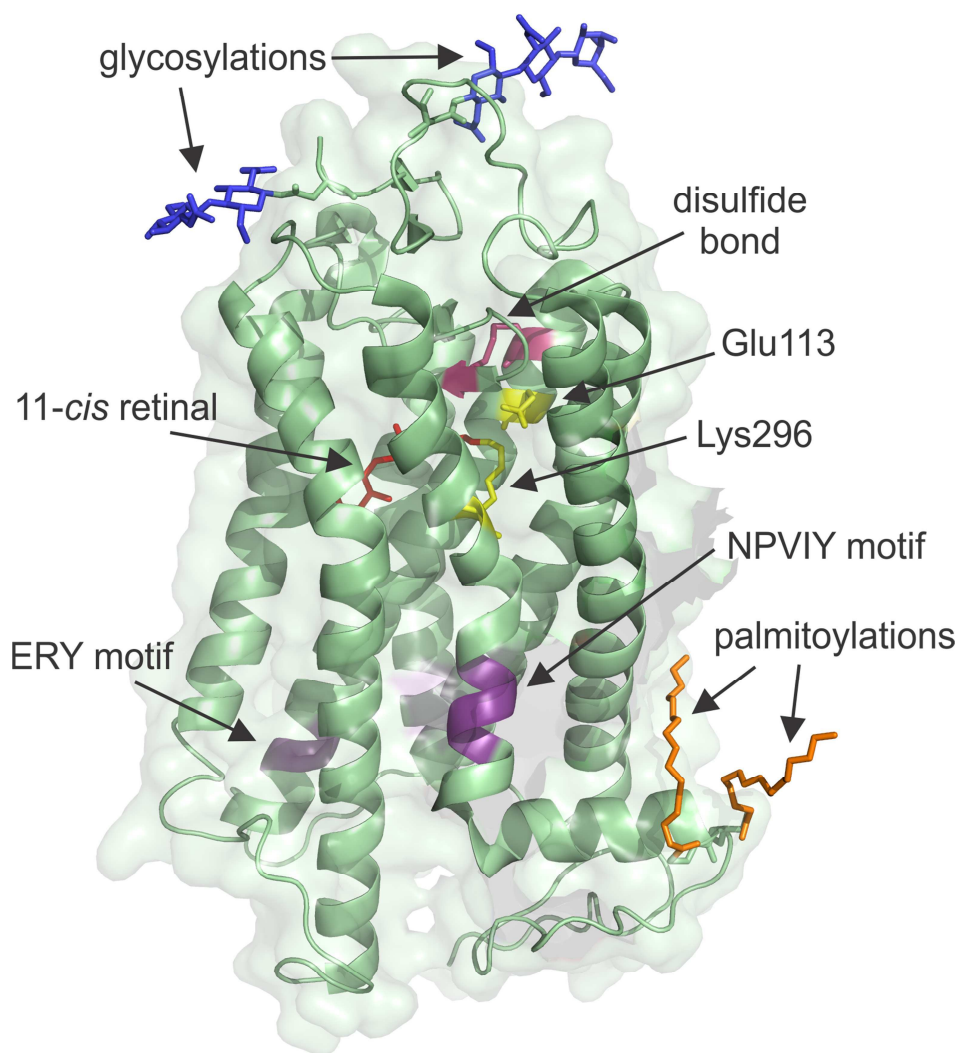


Figure 3.5: Crystal structure of bovine rhodopsin. Posttranslational modifications are indicated: palmitoylations (orange), glycosylations (blue). The conserved disulfide bond is highlighted in pink; the 11-*cis* retinal is shown in red; K296 to which retinal is linked through a protonated Schiff base is highlighted in yellow; E113 which serves as a counterion for the retinidyl Schiff base is highlighted in yellow. The highly conserved NPVIY and ERY motifs are highlighted in purple (PDB - 1U19). The figure was created using the PyMOL software package.

Rhodopsin has five tryptophan residues, which are located in helix I (W35), helix III (W126), helix IV (W161), E2 loop (W175) and helix VI (W265) (Figure 3.6A). Among these, three (W126, W161 and W265) are highly conserved among GPCRs ^[172]. The activation of rhodopsin by light illumination has been shown to affect these tryptophan residues ^[173,174], which depends on the localization of these residues and their interaction with retinal (Figure 3.6 B). For example, W265 has direct van der Waals contacts to the

bound retinal^[175,176]. The indole ring of W265 is located in close spatial proximity to the β -ionone ring of retinal and has a parallel orientation which allows π - π stacking^[30]. The C13-methyl group of retinal is also close to W265 and removal of this methyl group results in constitutive activity of rhodopsin indicating the importance of this interaction for keeping the protein in its inactive state^[177]. Light activation of rhodopsin results in the disruption of these stabilizing interactions followed by movement of helices III, VI and VII^[162]. Thus the tryptophan residues present in these helices can be potentially used as reporter groups for the activation movement. From a NMR point of view, we utilize the tryptophan residues as reporter groups since their indole resonances are shifted low field between 9.5 and 12 ppm in the proton dimension. This region is devoid of resonances from other amino acid residues resulting in well resolved, separated individual signals of tryptophan. The changes in the transmembrane helix architecture can therefore be monitored in real time though these tryptophan reporter groups via time resolved NMR spectroscopy. The spatial and temporal changes can be utilized to extract information about dynamics of rhodopsin during photocycle.

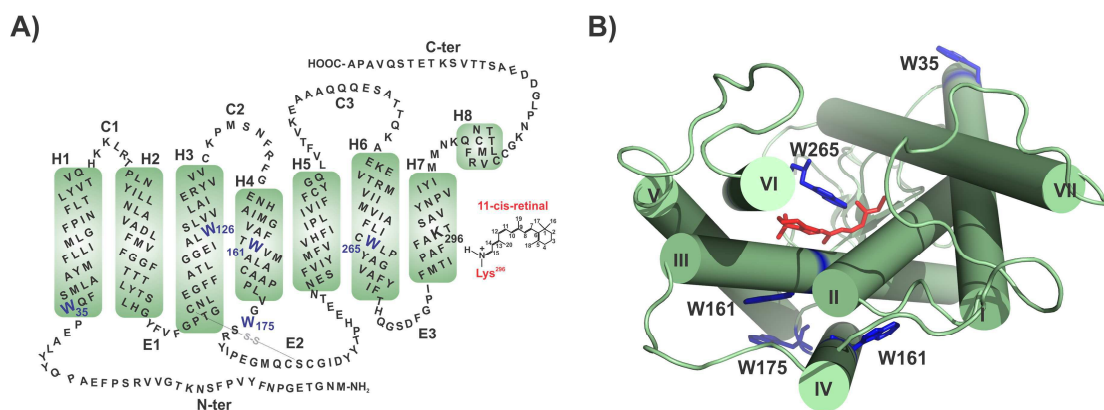


Figure 3.6: (A) Secondary structure of bovine rhodopsin. The five tryptophan residues (W35, W126, W161, W175, and W265) used as reporter groups in the NMR spectroscopic experiments are highlighted in blue. Modified after^[178]. (B) Top view of the 3D rhodopsin structure. The five tryptophans used as reporter groups in the NMR experiments are shown as stick models and highlighted in blue. The chromophore retinal is also shown as a stick model and highlighted in red. The figure was created using the PyMOL software package.

3.5.2 Rhodopsin photocycle

Photo pigments usually have a distinct absorption spectrum with two maxima, corresponding to the aromatic tryptophan residues present in the protein and the attached chromophore. In case of rhodopsin, the two maxima are at $\lambda=280$ nm (for the aromatic amino acids) and $\lambda=498$ nm (for the retinal bound to the rhodopsin). Photoinduced isomerization of the rhodopsin-bound chromophore from its 11-*cis* to all-*trans* configuration results in conformational changes in rhodopsin which lead to the formation of several transiently populated intermediate states (Figure 3.7) ^[159,161,179–183]. Each of these photointermediates has a characteristic absorption maximum and is defined by its individual photo kinetics which range from femtoseconds to minutes. Photorhodopsin, the first detectable photointermediate state has an absorption maximum of $\lambda=570$ nm and lifetime in the picosecond range. This is followed by bathorhodopsin, with an absorption maximum at $\lambda=543$ nm. This state is characterized by a distorted all-*trans* conformation which induces minor changes in the rhodopsin structure ^[161]. Bathorhodopsin decays thermally in nanoseconds to the blue shift intermediate (BSI; $\lambda=477$ nm), which can only be detected by time-resolved measurements. The next photo intermediate lumirhodopsin builds up within nanoseconds and has a characteristic absorption maximum of $\lambda=497$ nm. The retinal conformation in this state closely resembles the relaxed all-*trans* form but the overall global structure of rhodopsin shows only minor changes in helix III, close to the β -ionone ring and in helix VI close to the retinal chromophore ^[161]. The lifetime of lumirhodopsin is in the range of μ s and its decay leads to the formation of the meta I state with an absorption maximum of $\lambda=478$ nm. The meta I shows a decay kinetics of microsecond kinetics and functions as a juncture at which the photocycle bifurcates to form meta II ($\lambda=380$ nm) and meta III states ($\lambda=465$ nm) ^[184]. The conversion of meta I into meta II is accompanied by the large spectral shift from $\lambda=478$ nm to $\lambda=380$ nm, which indicates a major structural rearrangement happening during this key event of conversion of the rhodopsin from its inactive state (meta I) to its active state (meta II) ^[185]. The interaction of meta II state with the guanine nucleotide-binding protein (G protein) transducin triggers the activation signaling cascade, finally leading to hyperpolarization of photoreceptor cells. The G protein-rhodopsin interaction is interrupted by rhodopsin kinase and arrestin which results in the deactivation of phototransduction cascade ^[186]. The function of meta III state is not fully understood but several studies suggested that it may act as an energy storage state ^[187]. This storage of activated rhodopsin may play a significant role in regulating the photoreceptor regeneration as well as the light adaptation process. Both meta II and meta III states finally relax to the apoprotein opsin through

release of all-*trans*-retinal. The pathway that proceed via meta II has a decay kinetics in the range of five minutes, where the retinal is released from rhodopsin through protonation of the carboxylate counterion of Glu113. The alternative pathway that represents the meta III decay is comparatively slower and can potentially accounts for up to 30% of the meta II decay [188,189]. Several physiological conditions including temperature and pH can alter the distribution between the meta II and meta III states [190–192]. The final opsin state with common structural features of an inactive state [193–195] binds a regenerated 11-*cis*-retinal to form the ground state, which is ready for the next round of photoactivation.

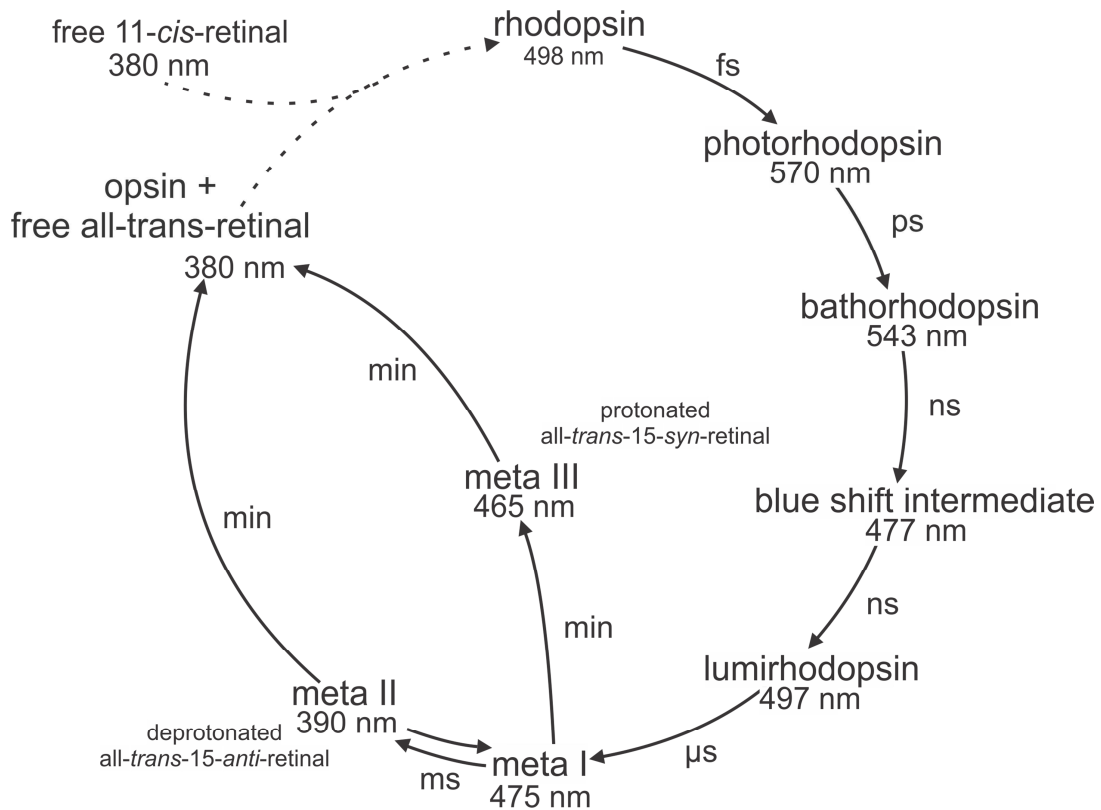


Figure 3.7: Photocycle of bovine rhodopsin. Adapted from Ernst et al., 2002 [196].

3.5.3 The meta II / meta III pathway

The meta II/meta III decay is considered as the rate limiting steps in the rhodopsin photocycle due to its slower kinetics in comparison to all previously populated intermediate states. All the intermediates prior to meta II and meta III states show not so significant structural differences from the ground state. The structural feature of ground state, meta II and meta III varies due to the different retinal conformations. In the dark state the retinal is present in its 11-*cis* 15 *anti*-configuration, the Schiff base is protonated and E113 is not protonated. Upon light illumination, a major helix rearrangement occurs during the transition from meta I to meta II. This transition is considered as the most important step in the rhodopsin photocycle which leads to the activation of rhodopsin. This change is characterized by a strong spectral shift from 478 nm to 380 nm ^[197,198] which indicates a major conformational change in the attached chromophore. The retinal in meta II state possesses an all-*trans* 15-*anti* configuration in which the Schiff base is deprotonated ^[184]. This leads to the protonation of counterion E113 which facilitates the release of all-*trans*-retinal. On the other hand, the meta III state with an absorption maxima at 465 nm, contains a re-protonated retinal Schiff base. Thermal isomerization of the C15=N of the retinal Schiff base from *anti* to *syn* configuration and parallel re-protonation of the Schiff base and deprotonation of E113 results in the meta III state. A summary of the structures in their respective configurations is shown in Figure 3.8.

The meta III state arises from the photoproduct equilibrium meta I/meta II and thermally decays to final opsin state in the time range of several minutes. The equilibrium between meta I and meta II is regulated by different physiological conditions including temperature and pH. For instance the meta I state is favored in presence of high pH (above pH~5), which is subsequently converted to the meta III state. The slow hydrolysis of meta III to all-*trans*-retinal and opsin results in buildup of meta III. A low pH value (below pH~5.1) favors the meta II state and thus the direct and fast hydrolysis of the Schiff base and its subsequent release from the protein ^[199]. Both states can be observed under physiological conditions but with different proportion. The slower and indirect pathway via the meta III state which can constitute up to 30% of the photocycle ^[200]. The meta III state is considered to be an inactive storage form of excited rhodopsin that plays a role in light adaptation and regulation. In Figure 3.9 a schematic overview of the possible pathways of meta I, meta II, and meta III intermediates are shown.

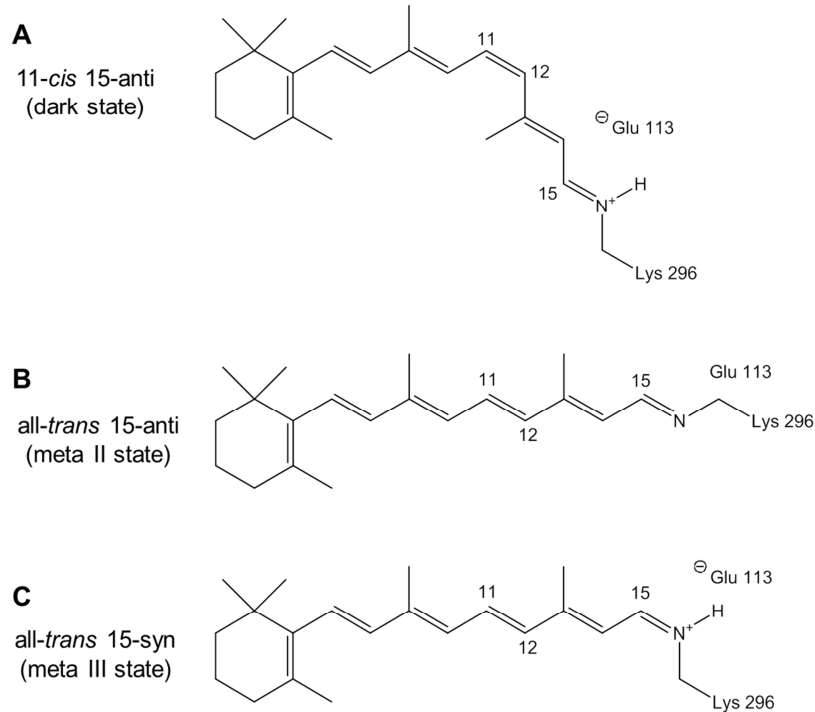


Figure 3.8: Overview of structural configurations of the retinal chromophore during the rhodopsin photocycle. (A) Retinal in the dark state with an 11-*cis* 15-*anti* configuration, a protonated Schiff base and a deprotonated E113. (B) Retinal in the meta II state with an all-*trans* 15-*anti* configuration, a deprotonated Schiff base and a protonated E113. (C) Retinal in the meta III state with an all-*trans* 15-*syn* configuration, a protonated Schiff base and a deprotonated glutamic acid 113. Adapted from Bartl et al., 2007 ^[184].

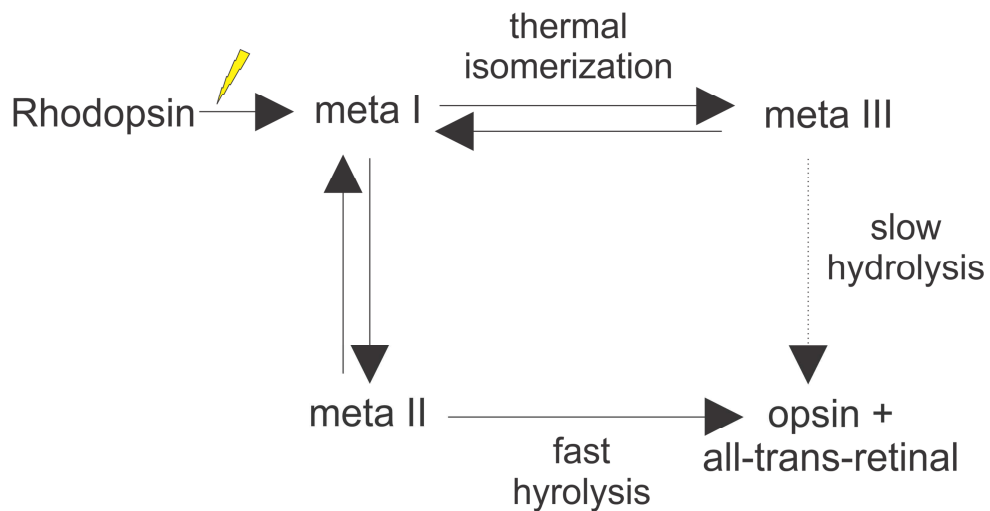


Figure 3.9: Schematic overview of alternative pathways in the rhodopsin photocycle beginning at the meta I intermediate. Prior to the meta I state only one possible pathway is observed and therefore all intermediates before meta I are ignored in this scheme. Adapted from Bartl et al., 2007 ^[184].

3.5.4 Retinal regeneration pathway: Visual cycle

The retinal regeneration pathway is a series of biochemical reactions following the phototransduction process, necessary for reproduction of the visual pigment. In mammalian vision, the phototransduction and the retinal regeneration pathway play complementary roles. As discussed before, the phototransduction is initiated by light induced isomerization of opsin bound 11-*cis*-retinal to its all-*trans* form, which is finally released in retinal outer segment. The regeneration pathway converts all-*trans*-retinal back to the 11-*cis* configuration, which facilitates the recycling of the bleached visual pigments (Figure 3.10). Although, the molecular mechanism behind the phototransduction process has been extensively studied, the biochemical understanding of the regeneration pathway is limited. Many fundamental questions regarding reactions, enzymes, and control mechanisms involved in the regeneration pathway have remain unanswered.

The thermal relaxation of photoactivated rhodopsin to the apoprotein opsin state results in the separation of the photoisomerized all-*trans*-retinal by hydrolysis of the schiff base linking all-*trans*-retinal and opsin. The free retinal is then transferred from the intradiscal to the cytosolic part of the disc membrane by adenosine triphosphate (ATP)-binding cassette transporter (ABCR) ^[201], where it is reduced to all-*trans*-retinol by an enzyme called all-*trans*-retinol dehydrogenase (RDH). RDH catalyzes the reaction in presence of reduced nicotinamide adenine dinucleotide phosphate (NADPH) ^[202]. All-*trans*-retinol then diffuses through the interphotoreceptor matrix space (the subretinal space) to enter retinal pigment epithelium (RPE) ^[203-205]. The interphotoreceptor retinoid-binding protein (IRBP) present in the subretinal space facilitates this transport. In the RPE, all-*trans*-retinol is converted to 11-*cis* retinal by a series of reaction performed by three enzymes localized in the smooth endoplasmic reticulum. At first the all-*trans*-retinol is converted to all-*trans*-retinyl ester through the activity of lecithin retinol acyl transferase (LRAT) ^[206]. The ester generated by LRAT represents the primary storage form of retinoids in the eye, which act as a driving force for subsequent reactions in the retinal regeneration pathway ^[207]. The next step involves the conversion of all-*trans*-retinyl ester to 11-*cis*-retinol and frees fatty acid by an isomerohydrolase (RPE65) ^[207-209]. 11-*cis*-retinol is then oxidized by an 11-*cis*-specific retinol dehydrogenase (11-*cis* RDH) to form the visual chromophore, 11-*cis*-retinal ^[210]. The visual chromophore, 11-*cis*-Retinal diffuses back into the photoreceptor cell where it combines with an opsin to regenerate the visual pigment and complete the cycle ^[211,212].

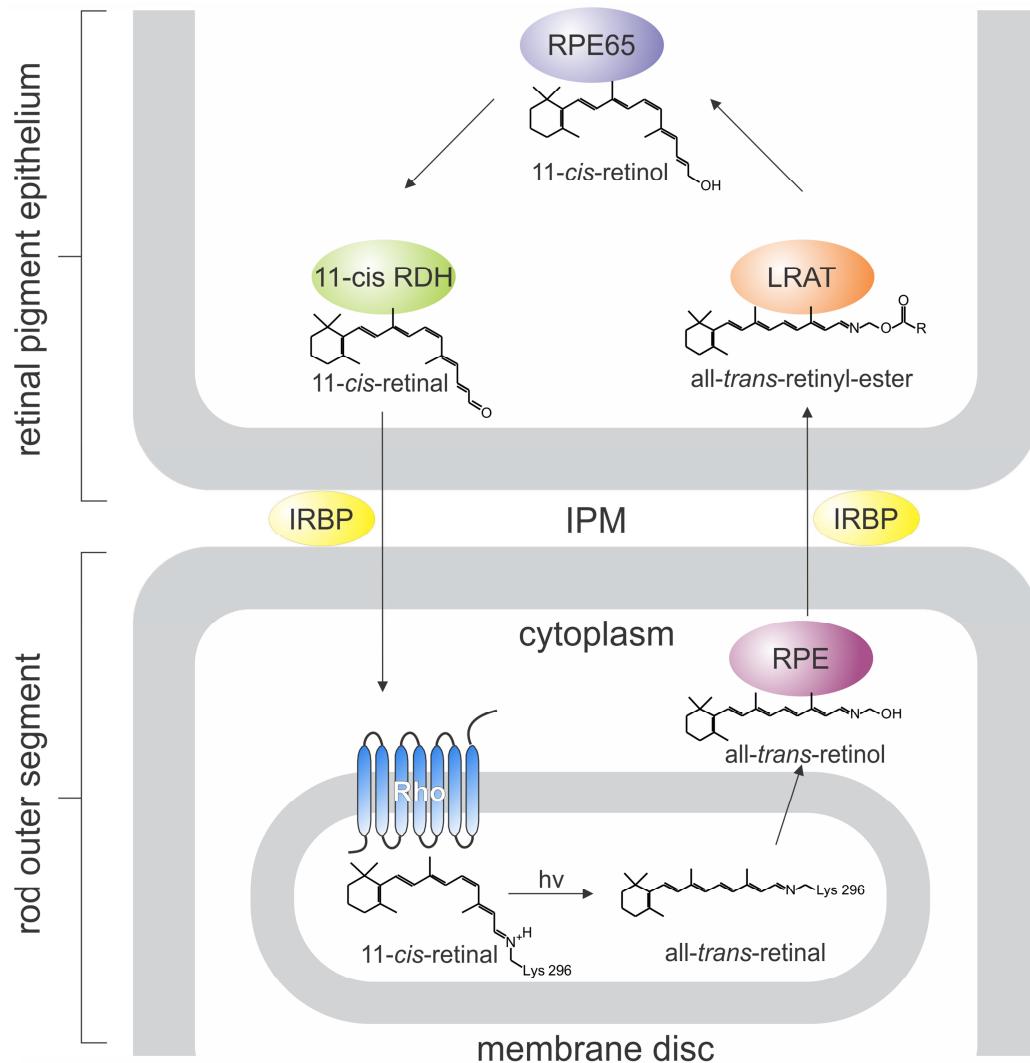


Figure 3.10: Rhodopsin visual cycle. Rhodopsin is incorporated into the disc membrane within the ROS. The starting point is the dark state of rhodopsin where retinal is present in the 11-*cis* configuration. Exposed to light, 11-*cis*-retinal undergoes an isomerization reaction resulting in free all-*trans*-retinal. The free all-*trans*-retinal then is enzymatically reduced to all-*trans*-retinol (vitamin A) by a retinol dehydrogenase (RDH). ROS and the retinal pigment epithelium are connected via the interphotoreceptor matrix (IPM). All-*trans*-retinol is transported to retinal pigment epithelium through IPM by interphotoreceptor retinoid-binding protein (IRBP). In the cytoplasm of the retinal pigment epithelium, lecithin retinol acyl transferase (LRAT) catalyzes the transfer of a fatty acyl group from phosphatidylcholine to all-*trans*-retinol resulting in an all-*trans*-retinyl ester. The RPE-specific 65-kDa protein (RPE65) catalyzes an isomerization reaction resulting in 11-*cis*-retinal. The final oxidation of 11-*cis*-retinol to 11-*cis*-retinal is catalyzed by 11-*cis*-retinal dehydrogenase (RDH). Finally, the 11-*cis*-retinal is incorporated in rhodopsin again, covalently attached via a Schiff base to Lys296.

3.5.5 Rate limiting steps in photo cycle and visual cycle

The regeneration of visual pigments is a slow process as compared to the photoisomerization of 11-*cis*-retinal in rhodopsin. The difference in the photolysis and regeneration rates would result in a rapid dissipation of the visual pigment. Moreover, prolonged exposure to light may lead to an accumulation of all-*trans*-retinal in ROS, which can be toxic to the eye due to formation of epoxides via oxidation. Harmful effects of excess retinal include visual dysfunction and retinal damage as found in several diseases like age-related macular degeneration (AMD) ^[213–215]. It has been demonstrated for human rods and cones that steady state level of bleached visual pigments is maintained at different levels of physiologic illumination. This indicates that there may be rate limiting steps which maintain the level of all-*trans*-retinal in ROS.

Retinoids extracted and analyzed from mice retinal cells before and after light illumination show accumulation of substantial amount of all-*trans*-retinal. This indicates that all processes after reduction of all-*trans*-retinal were rapid, including intercellular transport, esterification, isomerization, oxidation, and conjugation with opsin. This finding led to the conclusion that reduction of all-*trans*-retinal by NADPH determines the rate of entry of retinoid into the visual cycle and thus is considered as one rate limiting step for maintaining the retinal concentration. The rate of enzymatic turnover of RDH is slow compared to meta II decay. Therefore, the level of all-*trans*-retinal in ROS also depends on its release rate release during the photodecay of the meta II ^[216–218], and is considered as the second rate limiting steps for retinal homeostasis in ROS. The retinal accumulation in the eye initiates photocycle deactivation processes by arrestin to delay the release of retinal ^[219]. The interlinkage between photocycle and visual cycle modulating the retinal concentration in eye has been depicted schematically in Figure 3.11.

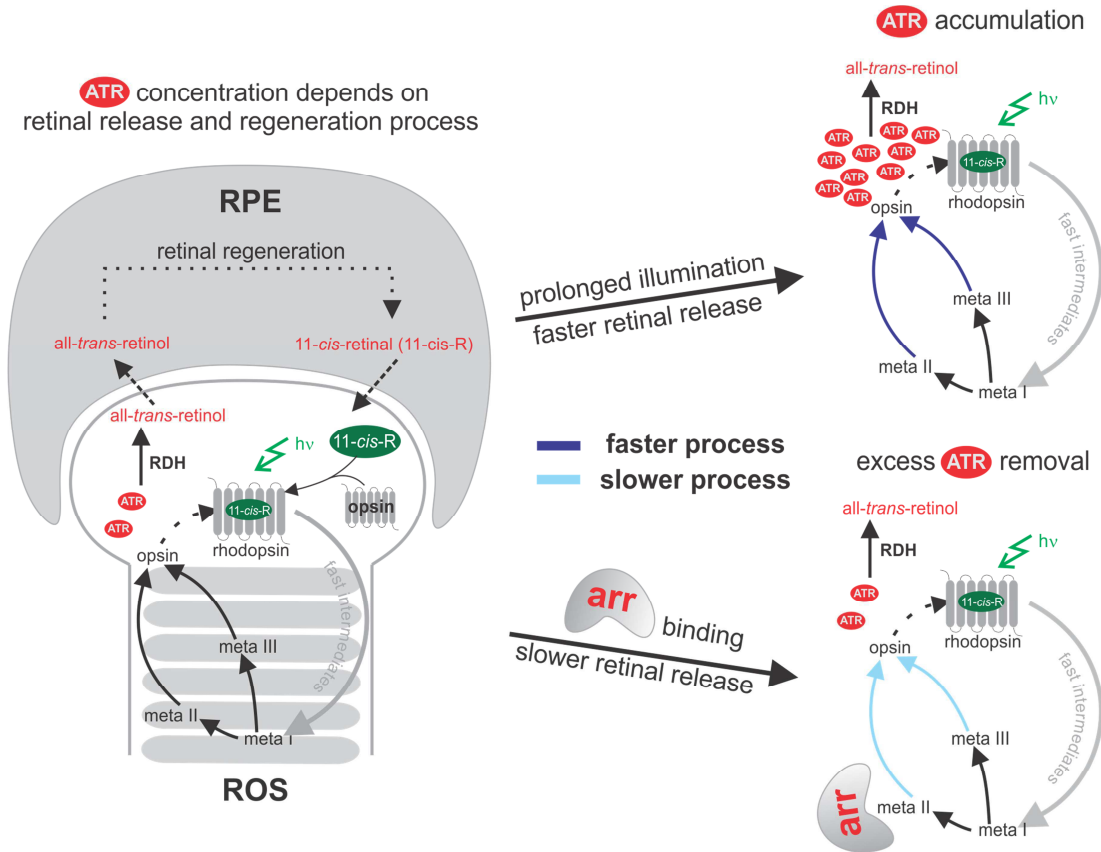


Figure 3.11: Mammalian visual cycle. The concentration of free all-*trans*-retinal (ATR) depends on two processes: 1) retinal release during the photocycle in the ROS and 2) retinal removal by a regeneration pathway in the retinal pigment epithelium (RPE) as shown on the left. Continuous exposure to light leads to the accumulation of ATR (top right), which initiates rhodopsin deactivation by arrestin (arr). Arrestin binding slows down the retinal release, which provides retinal dehydrogenase (RDH) with ample time to remove excess ATR by converting it into all-*trans*-retinol (bottom right).

3.6 Arrestin - a GPCR desensitizer

Arrestins represents a family of proteins which are involved in the regulation of GPCRs controlling several signaling cascades in our system. Mammalian cell consists of four different types of arrestin, among which two are present in photoreceptor cells: the visual arrestin (or arrestin 1) in the rod cells, and the cone-arrestin (or arrestin 4) in cone cells. Both of them are responsible for termination of the visual signal transduction, by binding to phosphorylated rhodopsin or cone opsin. This specificity towards one receptor type is not observed for the two non-visual β -arrestins (arrestin 2 and 3) as they control a vast range of GPCRs ^[220].

3.6.1 Arrestin structure

Three-dimensional crystal structures of visual arrestin ^[221,222], cone arrestin ^[223] and β -arrestin 1 ^[224,225] show similarity in their overall global fold. The arrestin structure is represented by two domains, each consisting of sandwiched β -sheets comprised of seven β -strands (Figure 3.12). A short α -helix is located on the N-terminal domain, while the C domain contains two short 3_{10} helices. These domains are connected to one another via a flexible area that is designated as a hinge region. The N-terminal domain has a depth of 24 Å and a diameter of 35 Å, whereas the C-terminal compared to that is about 10 Å smaller in diameter ^[221]. The basal state of arrestin is stabilized by interaction between its C-terminal tail and the N-domain via a three-element interaction with the N-terminal β -strand I and α -helix I ^[226]. Between the two domains, there is a structural element called the polar core, which is stabilized by several interactions between key charged amino acids residues. In the polar core, R175 (N-domain) forms a double salt bridge with D30 (N-terminal tail) and D296 (C-domain) and has hydrogen bonding to D303 (C-domain) ^[226]. Another key residue belonging to the polar core is R382 present in the C-terminal tail. Vishnivetskiy *et al.* ^[227] suggested that the polar core is necessary for the stabilization of the inactive or basal state arrestin conformation. This interaction network is disrupted upon binding of arrestin to the activated receptor conformation. Phosphorylation in the C-terminal tail of receptor disrupts the charge balance of the polar core and thus results in the release arrestin C-terminal tail. This event leads to significant rearrangement of arrestin's conformation favoring arrestin binding to the activated, phosphorylated receptor. Another structural features involved in rhodopsin binding is a loop (G68 to S78) between the β -strands V and VI, which function as a switch in receptor recognition ^[221]. This loop known as "finger loop" has been extensively studied. The finger

loop is highly flexible in basal arrestin ^[221,222,228], and its interaction with the activated receptor lead to the stabilization of the extended confirmation. This is confirmed by the immobilization of several residues in this loop upon binding to P-Rh* ^[229]. This study suggested the “finger loop as a key player in the interaction of arrestin with activated receptor.

Besides full length arrestin, p44 (Arr1–370A), a splice variant of arrestin is also present in rod cells. p44 is identical to full-length arrestin, except that its last 35 amino acids are replaced by a single alanine ^[230,231]. Although p44 is not ubiquitously present among all species (for example in mice), it has been suggested to play a role in rhodopsin deactivation ^[232–235]. The binding mechanism of p44 to rhodopsin is different from that of arrestin due to the absence of the C-terminal tail ^[232–235]. The structure of p44 arrestin is significantly different from the basal state arrestin and displays a disrupted central polar core with an exposed Arg175, the key phosphate-sensor. This explains the reason behind the high binding affinity of p44 arrestin for the phosphorylated receptor. In addition to this, p44 arrestin shows major rearrangements in key receptor-binding loops including the finger loop ^[228,229,236] in the central crest region. Apart from having higher affinity to phosphorylated rhodopsin, p44 also binds to the non-phosphorylated form ^[234,235]. Due to the later interaction, it has previously been argued that phosphorylation is not needed for p44-mediated rhodopsin deactivation ^[232,235].

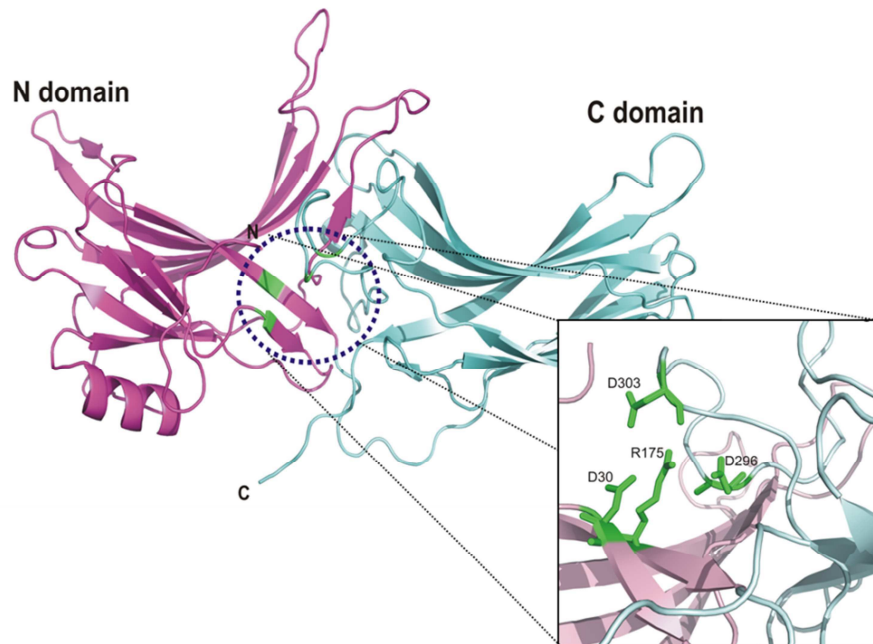


Figure 3.12: Crystal structure of arrestin (PDB: 1CF1) with polar core region marked with blue circle and close up view of the polar core region.

3.6.2 Down regulation of rhodopsin by arrestin

Deactivation of rhodopsin is necessary to timely recover the photo response which is critical for maintaining sensitivity of the receptor in steady light and for decrements of signaling intensity. The receptor deactivation begins with phosphorylation of its C-terminus by a G-protein coupled receptor kinase (GRK) which increases its affinity for arrestin (Figure 3.13) ^[237,238]. Under physiological conditions, inactive form of visual arrestin exists predominantly in the cytoplasm of the inner segment of rod cell ^[239,240]. After the light activation of the photoreceptor, translocation of arrestin takes place to the outer segment ^[239]. Arrestin, down-regulates the meta II signaling by tightly binding to rhodopsin and concomitant displacement of G protein ^[221,222]. In addition, arrestins can catalyze the removal of some GPCRs from the cell surface by interacting with the cellular internalization machinery, such as clathrin and AP-2 ^[241,242]. Once internalized in vesicles, receptors can be recycled back to the cell surface or degraded ^[21,243].

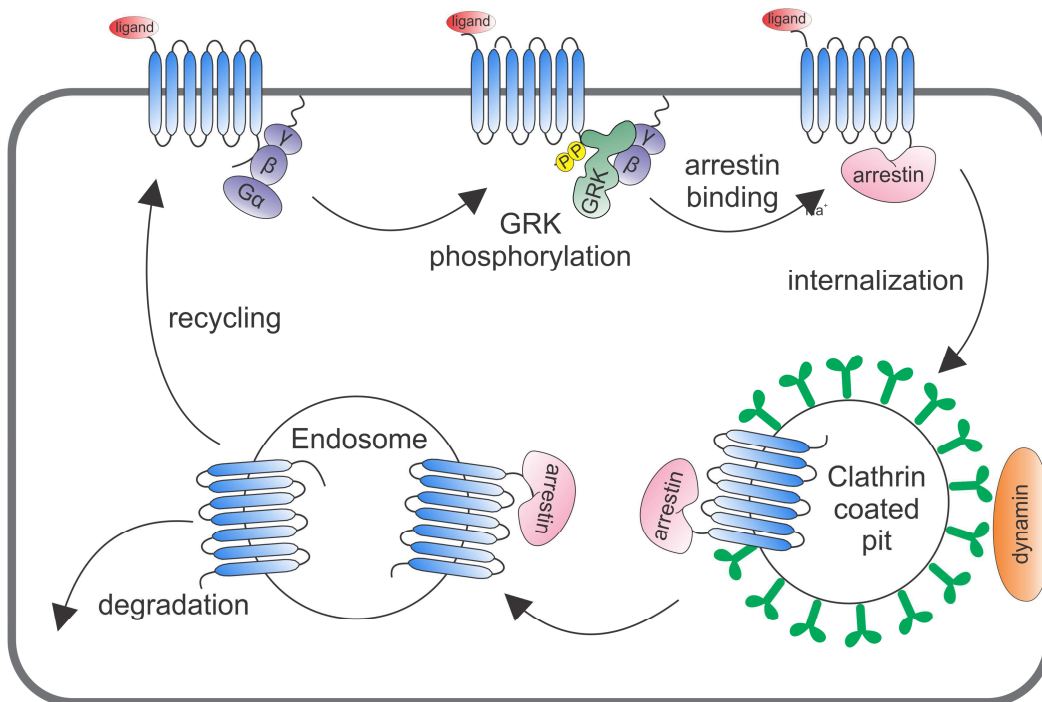


Figure 3.13: GPCR signaling attenuation by arrestin. G-protein coupled receptor kinases (GRKs) phosphorylate the C-terminal tail of the receptor. Activated, phosphorylated receptor is bound by arrestin, which blocks further G-protein activation. Arrestin also targets the receptor to clathrin-coated pits, where the receptor is internalized into acidic endosomes. Internalized receptor can either be recycled back to the cell surface or degraded. Adapted from Pierce et al., 2002 ^[244].

3.7 Motivation

One of the primary focuses of this dissertation was to understand the dynamics of the photoactivated rhodopsin. The meta II intermediate, being the active state of rhodopsin photocycle, has been extensively studied in most rhodopsin related research. But very little information is available for the alternative photodecay pathway involving meta III state, which has been considered as an energy storage state necessary for ground state receptor regeneration. Thus our initial aim was to characterize the kinetics of rhodopsin photodecay with emphasis on meta III state. In the second part of the rhodopsin project, we investigated the effect of the interaction between rhodopsin and arrestin on the release of the retinal chromophore and rhodopsin photoproduct formation. Arrestin has been previously shown to interact with meta II state of rhodopsin but its effect on rhodopsin photodecay dynamics was not completely understood. This motivated us to study the kinetics of meta II and meta III photointermediates in the presence of arrestin.

3.8 Research article 1

Characterization of the Simultaneous Decay Kinetics of Metarhodopsin States II and III in Rhodopsin by Solution-State NMR Spectroscopy.

Stehle J, Silvers R, Werner K, **Chatterjee D**, Gande S, Scholz F, Dutta A, Wachtveitl J, Klein-Seetharaman J, Schwalbe H. *Angewandte Chemie International Edition*, **2014**, 53, 2078-2084.

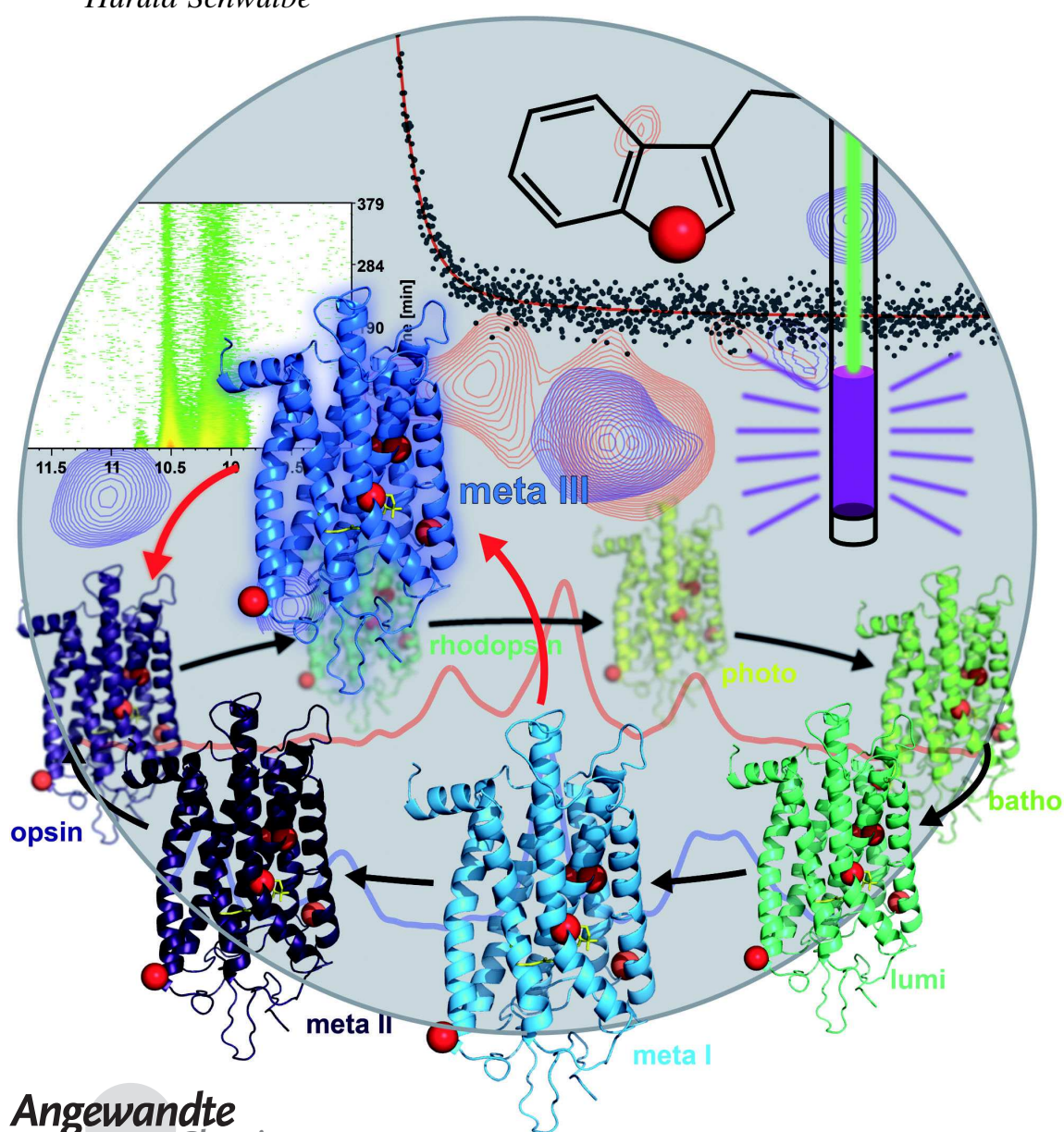
In this article, the kinetics of rhodopsin light-activation process was characterized by solution NMR spectroscopy using isotope labeled rhodopsin. The five tryptophans (W35, W126, W161, W175, W265) residues present in rhodopsin were used as reporter groups to investigate rhodopsin photodecay dynamics at atomic resolution under physiological conditions. The selectively α,ϵ - ^{15}N -tryptophan labeled rhodopsin was recombinantly expressed in stably transfected HEK293 cells. We carried out time-resolved real time 1D ^1H NMR experiments of light induced rhodopsin in DDM (n-dodecyl- β -D-maltoside) micelles to extract kinetic data of the decay of relevant photointermediate states of rhodopsin and provided information about their relative populations. Our results show kinetic partitioning in rhodopsin photodecay, revealing two parallel processes: meta II and meta III subsequent to rhodopsin activation which emerges in parallel with a relative ratio of about 3:1. The meta II state is the active state of rhodopsin which induces the visual signal transduction cascade. Although the meta III state is not active in signaling, it has been reported to function as an energy-storage state. The information gathered from spatially resolved NMR kinetic data of rhodopsin in solution could be confirmed with structural snapshots of rhodopsin photointermediates obtained by X-ray crystallography.

The NMR kinetic experiment of the wildtype rhodopsin was performed and analyzed by Dr. J. Stehle along with Dr. K. Werner. The absorption spectroscopic measurement of rhodopsin was performed by Dr. F. Scholz in the group of Prof. Dr. Josef Wachtveitl (Inst. of Physical and Theoretical Chemistry, Goethe University, Frankfurt). The expression and purification of tryptophan-to-phenylalanine mutant rhodopsins and their respective NMR spectra used for assigning the tryptophan resonances were acquired by the author of this thesis along with Dr. J. Stehle. The author has also contributed in writing the manuscript.



Characterization of the Simultaneous Decay Kinetics of Metarhodopsin States II and III in Rhodopsin by Solution-State NMR Spectroscopy**

Jochen Stehle, Robert Silvers, Karla Werner, Deep Chatterjee, Santosh Gande, Frank Scholz, Arpana Dutta, Josef Wachtveitl, Judith Klein-Seetharaman, and Harald Schwalbe*



Abstract: The mammalian visual dim-light photoreceptor rhodopsin is considered a prototype G protein-coupled receptor. Here, we characterize the kinetics of its light-activation process. Milligram quantities of α, ϵ - ^{15}N -labeled tryptophan rhodopsin were produced in stably transfected HEK293 cells. Assignment of the chemical shifts of the indole signals was achieved by generating the single-point-tryptophan to phenylalanine mutants, and the kinetics of each of the five tryptophan residues were recorded. We find kinetic partitioning in rhodopsin decay, including three half-lives, that reveal two parallel processes subsequent to rhodopsin activation that are related to the photocycle. The meta II and meta III states emerge in parallel with a relative ratio of about 3:1. Transient formation of the meta III state was confirmed by flash photolysis experiments. From analysis of the site-resolved kinetic data we propose the involvement of the E_2 -loop in the formation of the meta III state.

One of the most thoroughly studied G protein-coupled receptors (GPCRs) is the mammalian visual dim-light photoreceptor rhodopsin. The apo-protein, referred to as opsin, is covalently attached to the chromophore 11-*cis*-retinal through formation of a Schiff base. Photon absorption results in the isomerization of retinal to the *all-trans* configuration and conformational changes in the protein through a complex photocycle in which several intermediate states are transiently populated. These states differ significantly in their light absorption, structure, and dynamics and have been intensively studied.^[2] The absorption maximum of the rhodopsin-bound chromophore shifts from 380 to 570 nm during the photocycle (Figure 1).^[2a,3] Crystal structures are available for four of the kinetically identified intermediates, while some intermediates can be captured at low temperatures and in time-resolved experiments.^[1,4] The metarhodopsin I (meta I) state is the first state, where significant helix rearrangements occur.^[5] The photocycle can progress via two different intermediates, metarhodopsin II (meta II, $\lambda = 380$ nm) or metarhodopsin III

(meta III, $\lambda = 465$ nm).^[6] After reaching the meta II/meta III states, the photocycle slows down significantly to a regime on the minute timescale.^[7] The conversion of meta I into meta II is the major pathway and constitutes the key event in the photocycle. The absorption maximum (λ_{max}) is shifted by about 100 nm ($\lambda = 478$ nm to $\lambda = 380$ nm). The meta I state is inactive, and it is the meta II state^[2b] that transmits the light signal to the visual G protein. The lifetime of the interaction of the G protein with rhodopsin has been reported to last approximately 100 ms and is interrupted by rhodopsin kinase and arrestin.^[8] The active meta II state has a life-time of several minutes and decays to opsin and retinal.^[7] The formation of meta III from meta I has been reported to represent a minor pathway. Since the meta III state is not active in signaling,^[9] it is thought to represent a storage state of the light-receptor rhodopsin that is important for regeneration of the photoreceptor. This storage of activated rhodopsin could also play a significant role in the light adaptation process, since an already saturated light receptor cannot be excited further.^[6a]

The changes in the photophysics of retinal are linked to structural and dynamic changes in the protein. A number of crystal structures have been solved (see Figure 1^[2a,c-f,10,11]). We linked those crystal states by molecular morphing (see Movie S1 in the Supporting Information). From inspection of the movie, it is apparent that the most important conformational change during the photocycle is a tilt movement of helix 6 induced by disruption of the interaction network at the cytoplasmic ends of helices 3 and 6, commonly referred to as the "ionic lock" and involving the highly conserved D/ERY motif in helix 3 (see Movie S1 at times (min:s) 0:09–0:22). In a concerted process, a second set of interactions involving the cytoplasmic end of helix 7, especially F313, and helix 8, are rearranged, in particular of Y306 which is part of the conserved NPXXY motif (see Movie S1 at times 0:24–0:37).^[12]

While these crystal structures provide snapshot views of major intermediates in the photocycle, understanding the dynamics of the transitions between conformations in solution and especially of the competing decay paths from meta I to meta II or meta III requires studies under more physiologically relevant conditions. NMR spectroscopy in solution is ideally suited to address these questions.^[13,14] The kinetics of the photocycle have previously been monitored by 1D ^{19}F NMR spectroscopy, and ^{19}F chemical shifts could be differentiated between dark and meta II states as well as during the decay of meta II.^[13a]

To gain insight into the dynamic equilibrium of structures formed upon activation with light, we carried out time-resolved solution NMR experiments on α, ϵ - ^{15}N -tryptophan-labeled rhodopsin, complemented by optical data from flash photolysis experiments. We unambiguously assigned all five tryptophan resonances in dark-state rhodopsin, thus allowing us to measure the kinetics for the five tryptophan reporter signals upon activation with light. Analysis of the kinetic data reveals differences in the decay kinetics of the five signals and a significant kinetic partitioning of the decay of light-activated rhodopsin, thereby suggesting that both meta II and meta III states are populated under our experimental

[*] Dr. J. Stehle, Dr. R. Silvers, Dr. K. Werner, D. Chatterjee, Dr. S. Gande, Prof. Dr. H. Schwalbe
Institute for Organic Chemistry and Chemical Biology
Center of Biomolecular Magnetic Resonance
Johann Wolfgang Goethe-University Frankfurt
Max-von-Laue-Strasse 7, 60438 Frankfurt am Main (Germany)
E-mail: schwalbe@nmr.uni-frankfurt.de

F. Scholz, Prof. Dr. J. Wachtveitl
Institute of Physical and Theoretical Chemistry
Goethe University Frankfurt
60438 Frankfurt (Germany)

A. Dutta, Prof. Dr. J. Klein-Seetharaman
Division of Metabolic and Vascular Health, Medical School
University of Warwick, Coventry CV4 7AL (UK)

[**] The work was supported by the DFG grant SFB807. H.S. and J.W. are members of the DFG-funded cluster of excellence: macromolecular complexes. BMRZ is supported by the state of Hesse. J.K.-S. is supported by NSF grant 1144281.

Supporting information for this article (Experimental details)^[14b,16,24] is available on the WWW under <http://dx.doi.org/10.1002/anie.201309581>.

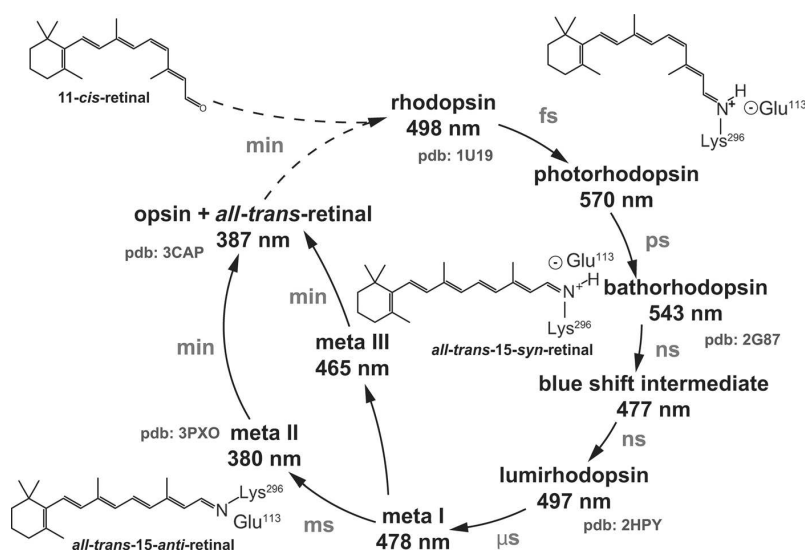


Figure 1. The photocycle of bovine rhodopsin, adapted from Ref. [1]. The photocycle involves several intermediates defined by their absorption characteristics. The first detectable intermediate after illumination is photorhodopsin, and subsequent intermediates emerge through thermal relaxation: The conversion of meta I into meta II is a key event within the rhodopsin photocycle, and constitutes the transition from the inactive state to the signal-transducing state of rhodopsin. In the meta II state, the Schiff base is deprotonated and the retinal is present in its *all-trans-15-anti* configuration. During the decay of meta II, retinal dissociates from rhodopsin, thereby resulting in free retinal and opsin. Meta III is an alternative intermediate on a second meta I decay pathway.

conditions, a proposal fully supported by the reported flash photolysis experiments. ^{15}N -Filtered NMR spectra of α,ϵ - ^{15}N -tryptophan-labeled rhodopsin show five proton resonances in the indole region which correspond to the five tryptophan moieties present in bovine rhodopsin (Figure 2, Figure S1). The ^1H NMR spectra of unlabeled rhodopsin show several additional signals stemming from backbone amide protons in this region (see Figure S2). Previous attempts to assign the NMR chemical shifts of the tryptophan indole resonances

failed because of an insufficient signal-to-noise ratio in the correlation experiments.^[14b,15] Therefore, we assigned the five tryptophan indole resonances by utilizing single-point tryptophan to phenylalanine mutants. Each of these rhodopsin mutants then shows only four of the five NMR resonances in the indole region (Figure 2B). Rhodopsin was illuminated in situ in the NMR spectrometer by using an argon ion laser as the light source that was coupled to the NMR measuring tube through fibreglass optics.^[16] By using fast NMR-acquisition schemes optimized for spectral resolution through a highly narrow spectral width in the indirect dimension it was possible to record a series of heteronuclear 2D NMR spectra of α,ϵ - ^{15}N -tryptophan-labeled rhodopsin with a temporal resolution of one minute. The first 2D $^1\text{H},^{15}\text{N}$ -SOFAST HMQC spectrum after the illumination pulse is shown in Figure 3 (see Figure S5 in the Supporting Information for the series of 2D $^1\text{H},^{15}\text{N}$ -SOFAST HMQC spectra recorded subse-

quently in one minute intervals). As a result of previous kinetic analyses revealing that the early intermediates have very short lifetimes, we can assign the first spectrum after illumination to a mixture of states mainly composed of meta II and meta III states. During the meta II/III decay, the Schiff base is cleaved and retinal is irreversibly (in vitro) released from rhodopsin. The dissociation of retinal from opsin initiates aggregation, thus resulting in a decrease in the signal intensities over several hours.

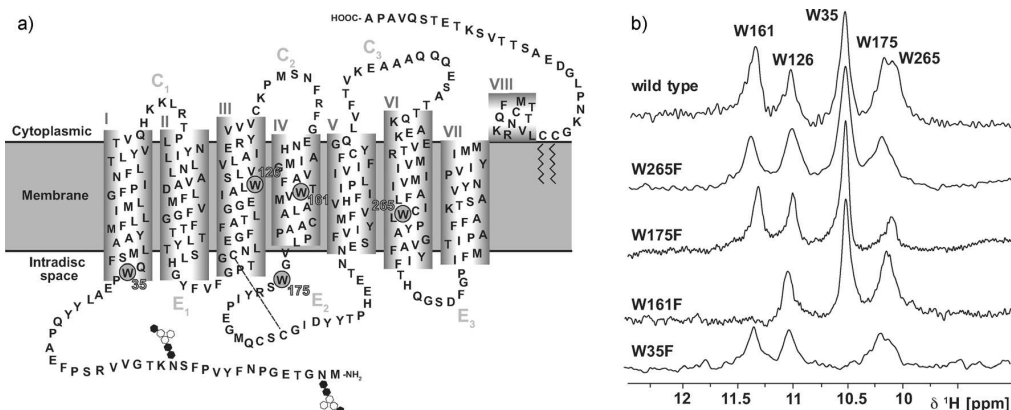


Figure 2. a) Secondary structure of bovine rhodopsin. The five tryptophan residues (W35, W126, W161, W175, and W265) used as reporter groups in the NMR experiments are indicated. b) Overlay of the indole region of 1D ^1H NMR spectra of α,ϵ - ^{15}N -tryptophan-labeled dark-state rhodopsin and the tryptophan to phenylalanine mutants: W35F, W161F, W175F, and W265F.

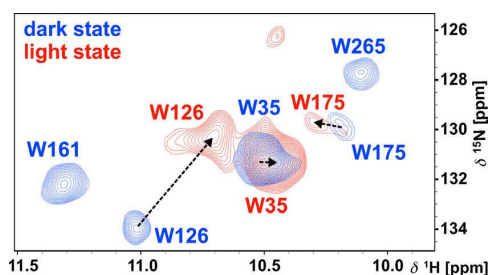


Figure 3. SOFAST HMQC spectra of the indole region of dark-state rhodopsin (blue) and light-activated-state rhodopsin (red). NMR chemical shift assignments in the dark state were transferred from 1D dimensional NMR spectra. Spectra were recorded at 800 MHz proton frequency at $T = 298$ K.

NMR chemical shifts are highly sensitive to the chemical environment, and the resonance pattern changes significantly after illumination. Only the resonances for W35 and W175 show relatively small changes in their chemical shifts upon activation with light (Figure 4a). In contrast, the resonances corresponding to W161 and W265 in the dark state are no longer observable in the light-activated state of ^{15}N -labeled rhodopsin immediately after illumination. The resonances corresponding to W265 recover and rise to a maximum after approximately 15 minutes, while the resonance corresponding to W161 can be detected only in unlabeled rhodopsin at higher concentrations (see Figure S2). The chemical shift of the resonance corresponding to W126 undergoes a large perturbation. Kinetic deconvolution of the decay data after light activation reveals three time regimes (Figure 4). The first

half-life (t_1) is in the range of four to five minutes, the second process has a half-life (t_2) in the range of 21 to 25 minutes, and the third process has a half-life (t_3) on the order of two to three hours. The half-life t_3 has large error bars and can be detected only through changes in the amplitude of signals corresponding to W175 and W265. Half-life t_3 most likely corresponds to an aggregation process initiated after the dissociation of retinal from opsin. This conclusion is also supported by the observation that the kinetics are irreversible and the end state is invisible to solution-state NMR spectroscopy. Aggregation of rhodopsin is also confirmed by precipitation in the NMR tube after several hours. We thus disregard this third process, since the half-life of 2–3 h exceeds the time range of the physiological activity of rhodopsin. Kinetic analysis could also be conducted with two mutants of sufficient concentration (see Figure S4). The process corresponding to the time constant t_1 shows an amplitude of $73 \pm 8\%$, whereas the slow process shows an amplitude of $26 \pm 7\%$.

To confirm that the meta III state indeed forms under our NMR conditions (solubilized protein in *n*-dodecyl- β -D-maltoside (DDM) micelles), we performed flash photolysis experiments under identical conditions. The meta III absorption maximum ($\lambda = 465$ nm) differs considerably from the absorption maximum of the meta II state ($\lambda = 380$ nm) and is close to the absorption maximum of the dark state ($\lambda = 500$ nm). Continuous illumination led to a depletion of the absorption maximum of the dark state and a rise of an absorption around 380 nm (Figure 5a), which corresponds to the meta II state. Time-resolved absorption changes at 500 nm and 380 nm after photoexcitation revealed an interconversion of both species

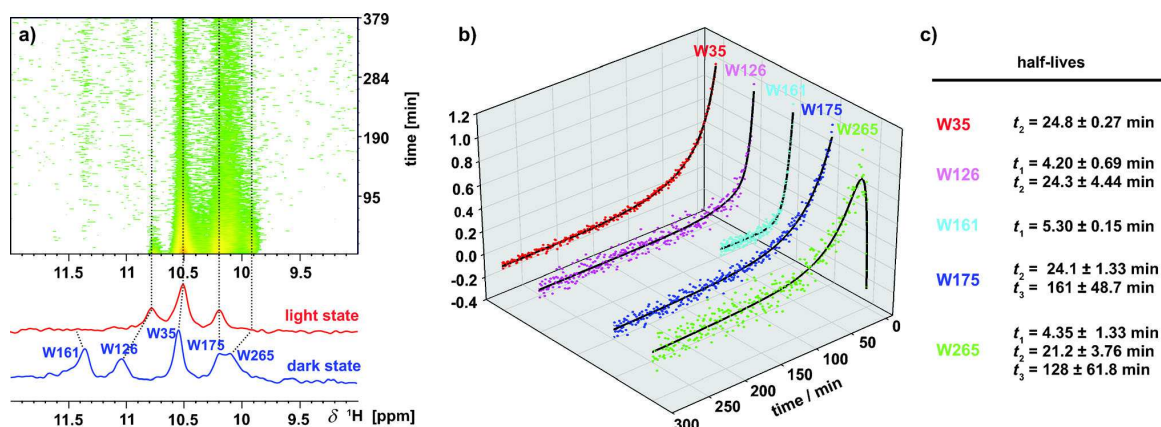


Figure 4. a) A series of 1D ^1H NMR spectra of α,ϵ - ^{15}N -tryptophan-labeled rhodopsin recorded at different time intervals after illumination. The indole region of the spectrum is shown. The five resonances visible in the dark state correspond to the five tryptophan residues present in rhodopsin. Subsequent to illumination, 1D ^1H spectra were recorded with a temporal resolution of one minute. The blue spectrum corresponds to the indole region of dark-state rhodopsin and the red spectrum corresponds to the light-activated state of rhodopsin. The dashed lines connect the corresponding resonances before and after illumination. For W161, the dashed connection was transferred from 1D ^1H NMR spectrum of the unlabeled rhodopsin sample (see Figure S2). b) Extracted signal intensities from the series of 1D ^1H NMR spectra of α,ϵ - ^{15}N -tryptophan-labeled rhodopsin. The signal intensities were normalized and plotted as a function of time. Different fitting routines have been applied to accommodate for the individual graph properties of each signal row. A mono-exponential fitting routine was applied for the signal intensities of W35 and W161, a biexponential fitting routine was applied for the signal intensities of W126 and W175, and a triexponential fitting routine was applied for the signal intensities of W265. c) Half-lives for each tryptophan indole ring were extracted by exponential fit (Figure S3).

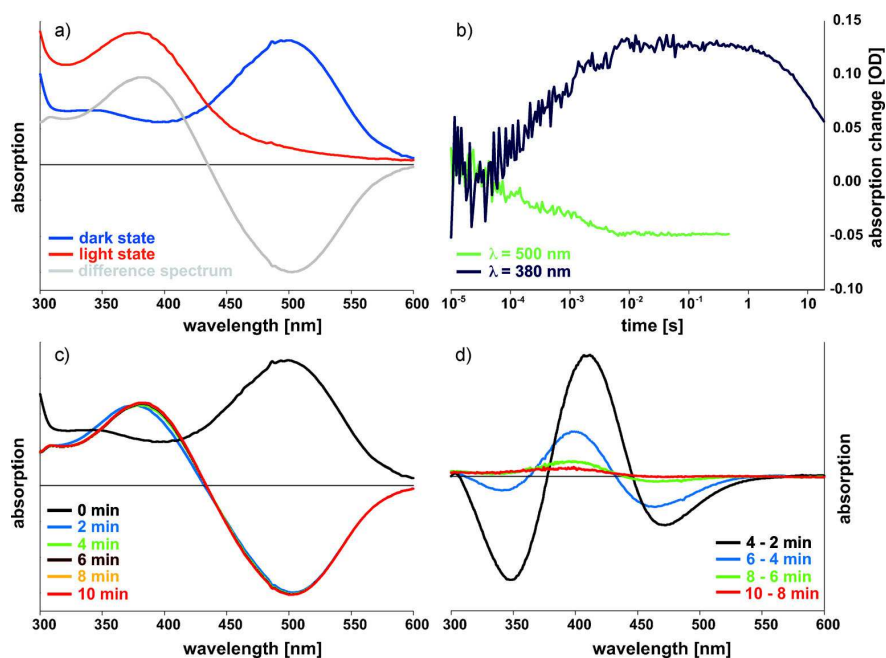


Figure 5. a) Absorption spectra of the rhodopsin dark state (blue) and after continuous illumination (red). The corresponding difference spectrum is depicted in gray. b) Time-resolved absorption changes after photoexcitation with a short laser pulse (5 ns) monitored at 380 nm (blue) and at 500 nm (green). c) Difference spectra between the absorption spectra of rhodopsin after photoexcitation at different time points and the dark state (black). d) Double difference spectra from the spectra shown in (c).

on a timescale of hundreds of microseconds (Figure 5b). The photoproduct itself decays further on a timescale of tens of seconds. Difference spectra and double difference spectra at distinct delay times after laser excitation are depicted in Figure 5c,d. The difference signal decays on a timescale of several minutes. At least three different species cause the spectral changes.^[1] The UV-absorbing species meta II rises on a millisecond timescale at 380 nm. The later photointermediate exhibits a bathochromic shift (465 nm) characteristic of meta III. After a few minutes, the meta III state converts into a species where the retinal is released from the Schiff base. The free retinal exhibits an absorption maximum around 380 nm.

The time-resolved NMR experiments reveal that the tryptophan reporter groups were affected differently in the two states, in line with the previous conclusion that motions in rhodopsin are segmental.^[18] W126, W161, and W265 show a common half-life of approximately four to five minutes, which corresponds to decay kinetics of the meta II state. The three largest chemical shift perturbations correspond to the tryptophan residues (W126, W161, W265), which show the same first half-life t_1 , whereas the two minor chemical shift perturbations correspond to the tryptophan residues (W35 and W175), which do not report on the fast kinetics associated with t_1 . Thus, the kinetic data and chemical shift perturbation data are in agreement. Furthermore, W126, W161, and W265 are highly conserved among GPCRs,^[19] thereby emphasizing the importance of these residues in the activation process of

rhodopsin and GPCRs in general. The second kinetic process observed has a half-life of approximately 24 minutes (t_2). Only W35 and W175 show this half-life.

Kinetic analysis reveals two major processes corresponding to the two time constants t_1 and t_2 . We propose that the two time constants t_1 and t_2 represent decay kinetics via the meta II or meta III photocycle alternatives, respectively. The meta II decay (t_1) shows an amplitude of $73 \pm 8\%$, while the kinetic process attributed to the meta III decay shows an amplitude of $26 \pm 7\%$. These values are highly consistent with ratios of meta II/meta III previously determined by fluorescence spectroscopic studies that support the presence of a meta III state under our conditions used for NMR spectroscopy.^[20] The NMR

data reveal that the meta II and meta III states emerge in parallel in a relative ratio of approximately 3:1, which was unambiguously confirmed by flash photolysis experiments. In the meta II state, rhodopsin is active and induces the visual signal transduction cascade, while no signal transduction is observed for the meta III state, thus indicating that the structural differences between the two states are directly related to activity.

The kinetic behavior observed for tryptophan residues can be classified into three different types: 1) meta II only, 2) meta II and meta III, and 3) meta III only. One residue, W161, shows only meta II kinetics. W161 is located in the middle of helix 4 and, even though this helix is not involved in the most intense structural rearrangements, it is directly adjacent to helix 3 and is affected by the large rearrangement process involving helix 3 (see Movie S2 at 00:07–00:19, and Figure S6). This influence is indeed observable by the change in the signal intensity of W161 as detected in the 1D ¹⁵N-filtered ¹H NMR spectra (Figure 4a). In contrast, W126 and W265 show meta II and meta III kinetics. Their involvement in both processes is in agreement with what is seen in flash photolysis experiments, where retinal kinetics can be recorded, and can be rationalized in the context of the rhodopsin structure, because both residues, W126 and W265, are tightly linked to the retinal. For W265, the interaction of its indole ring with the β ionone ring of retinal is disrupted upon rhodopsin activation, visible in the lumirhodopsin intermediate, and the retinal is free to relax and move (see

Movie S2 at times 00:20–00:32, and Figure S6). The rearrangement contributes significantly to the meta II and meta III kinetics observed for W265, since retinal is released from rhodopsin in both intermediates and leads to a significant change in the chemical environment. The structural reorientation of retinal drives the rearrangement of the hydrogen network that connects helix 3 with helix 5 in which W126 is involved (see Movie S2 at times 00:32–00:44, and Figure S6).^[21] W126 takes part in this hydrogen-bond network and is thus modulated by the same process. The changes in the signal intensity of W126 are attributed to the significant changes in the hydrogen-bond pattern between residues W126, E122, and H211 (see Movie S2 at times 00:32–00:44, and Figure S6).

Finally, W35 and W175 show exclusively meta III kinetics. The two residues are located in the extracellular domain at the N-terminal end of helix 1 and the E₂-loop, respectively (see Movie S2 at times 00:44–00:56 and at 00:56–01:09, respectively, and Figure S6). The large structural rearrangements known for the meta II state are not observed in the vicinity of W35 and W175. As a consequence of their unique position at hinge regions, both residues are not structurally perturbed during the photocycle, which is consistent with the comparatively small changes in the chemical shift seen upon activation with light (Figure 4a). Despite the spatial distance to the retinal, the decays of their NMR signals display meta III kinetics. Since both tryptophan residues are located close to the E₂-loop of rhodopsin, it is tempting to speculate that the E₂-loop plays a major role in the formation and decay of meta III. The E₂-loop contains β-sheet secondary structural elements that are part of the retinal binding pocket and, importantly, the disulfide bridge connecting the β-sheet to helix 3 that is crucial for stability and folding of rhodopsin.^[22] The E₂-loop is also involved in ligand binding in many other GPCRs.^[23]

In addition to affording functional insight into the rhodopsin activation process, the experiments presented here also constitute an important advance in method development for the study of membrane protein structure and dynamics in solution: we show that time-resolved liquid-state NMR spectroscopy can be utilized to characterize the kinetics of structural changes of membrane receptors. The technique provides, therefore, a unique opportunity to link information from structural snapshots obtained by X-ray crystallography with spatially resolved kinetic information in solution.

Received: November 4, 2013
Published online: February 6, 2014

Keywords: bovine rhodopsin · G-protein coupled receptors · membrane protein dynamics · NMR spectroscopy · photocycles

- [1] O. P. Ernst, F. J. Bartl, *ChemBioChem* **2002**, *3*, 968–974.
[2] a) H. Nakamichi, T. Okada, *Angew. Chem.* **2006**, *118*, 4376–4379; *Angew. Chem. Int. Ed.* **2006**, *45*, 4270–4273; b) S. T. Menon, M. Han, T. P. Sakmar, *Physiol. Rev.* **2001**, *81*, 1659–1688; c) K. Palczewski, T. Kumasaka, T. Hori, C. A. Behnke, H. Motoshima, B. A. Fox, I. Le Trong, D. C. Teller, T. Okada, R. E. Stenkamp, M. Yamamoto, M. Miyano, *Science* **2000**, *289*, 739–

- 745; d) H. Nakamichi, T. Okada, *Proc. Natl. Acad. Sci. USA* **2006**, *103*, 12729–12734; e) H. W. Choe, Y. J. Kim, J. H. Park, T. Morizumi, E. F. Pai, N. Krauss, K. P. Hofmann, P. Scheerer, O. P. Ernst, *Nature* **2011**, *471*, 651–655; f) J. H. Park, P. Scheerer, K. P. Hofmann, H. W. Choe, O. P. Ernst, *Nature* **2008**, *454*, 183–187; g) C. Altenbach, A. K. Kusnetzow, O. P. Ernst, K. P. Hofmann, W. L. Hubbell, *Proc. Natl. Acad. Sci. USA* **2008**, *105*, 7439–7444; h) T. D. Dunham, D. L. Farrens, *J. Biol. Chem.* **1999**, *274*, 1683–1690.
[3] S. S. Lefkowitz, D. L. Lefkowitz, J. Kethley, *Am. J. Case Rep.* **2012**, *13*, 66–68.
[4] S. J. Hug, J. W. Lewis, C. M. Einterz, T. E. Thorgeirsson, D. S. Kliger, *Biochemistry* **1990**, *29*, 1475–1485.
[5] S. Ye, E. Zaitseva, G. Caltabiano, G. F. Schertler, T. P. Sakmar, X. Deupi, R. Vogel, *Nature* **2010**, *464*, 1386–1389.
[6] a) F. J. Bartl, R. Vogel, *Phys. Chem. Chem. Phys.* **2007**, *9*, 1648–1658; b) R. Vogel, F. Siebert, X. Y. Zhang, G. Fan, M. Sheves, *Biochemistry* **2004**, *43*, 9457–9466.
[7] a) D. L. Farrens, H. G. Khorana, *J. Biol. Chem.* **1995**, *270*, 5073–5076; b) J. K. McBee, K. Palczewski, W. Baehr, D. R. Pepperberg, *Prog. Retinal Eye Res.* **2001**, *20*, 469–529.
[8] A. Mendez, M. E. Burns, A. Roca, J. Lem, L. W. Wu, M. I. Simon, D. A. Baylor, J. Chen, *Neuron* **2000**, *28*, 153–164.
[9] E. Ritter, M. Elgeti, F. J. Bartl, *Photochem. Photobiol.* **2008**, *84*, 911–920.
[10] T. Okada, M. Sugihara, A. N. Bondar, M. Elstner, P. Entel, V. Buss, *J. Mol. Biol.* **2004**, *342*, 571–583.
[11] J. Standfuss, P. C. Edwards, A. D'Antona, M. Fransen, G. Xie, D. D. Oprian, G. F. X. Schertler, *Nature* **2011**, *471*, 656–660.
[12] M. Kumauchi, T. Ebrey, *Handbook of Photosensory Receptors* (Eds: W. R. Briggs, J. L. Spudich), Wiley-VCH, Weinheim, **2005**, p. 43–76.
[13] a) J. Klein-Seetharaman, E. V. Getmanova, M. C. Loewen, P. J. Reeves, H. G. Khorana, *Proc. Natl. Acad. Sci. USA* **1999**, *96*, 13744–13749; b) M. C. Loewen, J. Klein-Seetharaman, E. V. Getmanova, P. J. Reeves, H. Schwalbe, H. G. Khorana, *Proc. Natl. Acad. Sci. USA* **2001**, *98*, 4888–4892; c) J. Klein-Seetharaman, P. J. Reeves, M. C. Loewen, E. V. Getmanova, J. Chung, H. Schwalbe, P. E. Wright, H. G. Khorana, *Proc. Natl. Acad. Sci. USA* **2002**, *99*, 3452–3457.
[14] a) E. Getmanova, A. B. Patel, J. Klein-Seetharaman, M. C. Loewen, P. J. Reeves, N. Friedman, M. Sheves, S. O. Smith, H. G. Khorana, *Biochemistry* **2004**, *43*, 1126–1133; b) K. Werner, C. Richter, J. Klein-Seetharaman, H. Schwalbe, *J. Biomol. NMR* **2008**, *40*, 49–53.
[15] K. Werner, I. Lehner, H. K. Dhiman, C. Richter, C. Glaubitz, H. Schwalbe, J. Klein-Seetharaman, H. G. Khorana, *J. Biomol. NMR* **2007**, *37*, 303–312.
[16] T. Kühn, H. Schwalbe, *J. Am. Chem. Soc.* **2000**, *122*, 6169–6174.
[17] a) S. Kaushal, K. D. Ridge, H. G. Khorana, *Proc. Natl. Acad. Sci. USA* **1994**, *91*, 4024–4028; b) S. S. Karnik, H. G. Khorana, *J. Biol. Chem.* **1990**, *265*, 17520–17524; c) B. E. Olausson, A. Grossfield, M. C. Pitman, M. F. Brown, S. E. Feller, A. Vogel, *J. Am. Chem. Soc.* **2012**, *134*, 4324–4331.
[18] T. E. Woudenberg-Vrenken, A. L. Lameris, P. Weissgerber, J. Olausson, V. Flockerzi, R. J. Bindels, M. Freichel, J. G. Hoenderop, *Am. J. Physiol.* **2012**, *303*, G879–885.
[19] A. B. Patel, E. Crocker, P. J. Reeves, E. V. Getmanova, M. Eilers, H. G. Khorana, S. O. Smith, *J. Mol. Biol.* **2005**, *347*, 803–812.
[20] M. Heck, S. A. Schadel, D. Maretzki, K. P. Hofmann, *Vision Res.* **2003**, *43*, 3003–3010.
[21] a) M. Beck, T. P. Sakmar, F. Siebert, *Biochemistry* **1998**, *37*, 7630–7639; b) E. Zaitseva, M. F. Brown, R. Vogel, *J. Am. Chem. Soc.* **2010**, *132*, 4815–4821.
[22] A. J. Rader, G. Anderson, B. Isin, H. G. Khorana, I. Bahar, J. Klein-Seetharaman, *Proc. Natl. Acad. Sci. USA* **2004**, *101*, 7246–7251.

- [23] a) A. Straßer, H.-J. Wittmann, R. Seifert, *J. Pharmacol. Exp. Ther.* **2008**, *326*, 783–791; b) M. Scarselli, B. Li, S.-K. Kim, J. Wess, *J. Biol. Chem.* **2007**, *282*, 7385–7396; c) J. M. M. Laurila, H. Xhaard, J. O. Ruuskanen, M. J. M. Rantanen, H. K. Karlsson, M. S. Johnson, M. Scheinin, *Br. J. Pharmacol.* **2007**, *151*, 1293–1304; d) H. Preuss, P. Ghorai, A. Kraus, S. Dove, A. Buschauer, R. Seifert, *Naunyn-Schmiedeberg's Arch. Pharmacol.* **2007**, *376*, 253–264.
- [24] a) A. Knowles, A. Priestley, *Vision Res.* **1978**, *18*, 115–116; b) see Ref. [13b]; c) D. D. Oprian, R. S. Molday, R. J. Kaufman, H. G. Khorana, *Proc. Natl. Acad. Sci. USA* **1987**, *84*, 8874–8878; d) P. J. Reeves, N. Callewaert, R. Contreras, H. G. Khorana, *Proc. Natl. Acad. Sci. USA* **2002**, *99*, 13419–13424; e) P. J. Reeves, J. M. Kim, H. G. Khorana, *Proc. Natl. Acad. Sci. USA* **2002**, *99*, 13413–13418; f) P. Schanda, E. Kupce, B. Brutscher, *J. Biomol. NMR* **2005**, *33*, 199–211.
-

Supporting Information

© Wiley-VCH 2014

69451 Weinheim, Germany

Characterization of the Simultaneous Decay Kinetics of Metarhodopsin States II and III in Rhodopsin by Solution-State NMR Spectroscopy**

*Jochen Stehle, Robert Silvers, Karla Werner, Deep Chatterjee, Santosh Gande, Frank Scholz, Arpana Dutta, Josef Wachtveitl, Judith Klein-Seetharaman, and Harald Schwalbe**

anie_201309581_sm_miscellaneous_information.pdf

SUPPLEMENTARY INFORMATION

Experimental Section

Construction of expression plasmids for mutant opsin genes. The wild type opsin gene was moved from pMT4 to pACMV-tetO vector to enable expression in HEK 293 cells by stable cell transfection. The W35F, W126F, W161F, W175F and W265F mutations were introduced via site directed mutagenesis. The pACMV-tetO vector was originally developed by Dr. Philip Reeves.^[1] In order to excise the opsin gene from the pMT4 vector, two unique restriction sites (NotI and KpnI) were used which were also present uniquely in the pACMV vector. The unique KpnI site in pMT4 was a few base pairs away from the starting codon of the opsin gene and thus was moved to the start of the opsin gene by site-directed mutagenesis (QuikChange kit from Stratagene, La Jolla, CA). This enabled excising the opsin gene by digesting with KpnI and NotI and then ligating into the pACMV vector.

Generation of stably transfected HEK293 cell lines containing the opsin mutant genes.

The preparation of stably transfected HEK293S cell lines containing the mutant opsin gene was carried out as described previously.^[1b, 2]

Expression and purification of selectively isotope labeled rhodopsin from HEK293S cells. Rhodopsin was expressed in tetracycline inducible HEK293S cells. For the expression of the wild type opsin gene, a 10 L fermenter was used with cell culture media composed of individual components enabling a selective isotope labeling scheme.^[1b, 3] The cells were harvested after a cell density of $\sim 2 \times 10^6$ cells/ml was achieved and resuspended in 25 ml/liter cell culture of buffer A (10 mM Na₂HPO₄, 1.8 mM KH₂PO₄, 137 mM NaCl, 2.7 mM KCl, pH 7.2). 11-*cis* retinal was added at a final concentration of 40 μ M. 11-*cis*-retinal was prepared by illuminating *all-trans*-retinal and subsequent separation of the obtained isomers as previously described.^[4] Rhodopsin was solubilized by addition of 1% DDM (n-Dodecyl β -D-maltoside) and purified via immunoaffinity chromatography. The 1D4 antibody (University of British Columbia, Vancouver, Canada) was coupled to activated Sepharose 4B as previously described.^[5] Rhodopsin was bound to the beads and washed with 20 columns of buffer B (buffer A + 0.05% DDM). Rhodopsin was subsequently eluted with buffer B containing the peptide TETSQVAPA at a concentration of 40 μ M. Fractions containing Rhodopsin were pooled and concentration by Amicon stirred cell (Millipore, Billerica, USA). The buffer of rhodopsin samples for NMR spectroscopy and flash photolysis was changed to 20 mM phosphate buffer at pH 7.4 by buffer exchange on a PD-10 column (GE Healthcare, UK).

Real time NMR spectroscopy. An argon ion laser with $\lambda=520$ nm was used for the illumination of the rhodopsin sample. The laser beam was directly guided into the sample within the NMR spectrometer via fiber optical devices.^[6] A single 3 W laser pulse was applied for 0.5s to trigger the photocycle of rhodopsin. Real time NMR experiments were conducted on a Bruker Avance I 800 MHz spectrometer at T=293 K. A series of one dimensional ¹H X-filtered spectra was recorded in a pseudo two dimensional manner. The

temporal resolution of the one dimensional experiments was ~ 1 minute. [¹⁵N, ¹H]-SOFAST-HMQC^[7] experiments were conducted in a pseudo three dimensional manner with a temporal resolution of ~1 minute. The focus was on the indole region of the spectrum where the indole side chain signals of the tryptophan residues are to be expected (with a carrier frequency of 10.6 kHz and a spectral width of 833.3 Hz). For NMR spectroscopical experiments we used a protein concentration of 1 mM in a 20 mM phosphate buffer at pH 7.4 and 298 K. Bovine rhodopsin was solubilized in the detergent DDM (n-Dodecyl β-D-maltoside) at a concentration of 1 % (w/v).

Rhodopsin kinetics were extracted from a series of one dimensional ¹H X-filtered spectra recorded in a pseudo two dimensional manner. The signal intensities were normalized and plotted as a function of time. Different exponential fitting models (1-3) were applied to accommodate for the individual graph properties of each signal row.

$$\text{mono-exponential:} \quad y = ae^{-bx} \quad (1)$$

$$\text{bi-exponential:} \quad y = ae^{-bx} + ce^{-dx} \quad (2)$$

$$\text{tri-exponential:} \quad y = ae^{-bx} + ce^{-dx} + fe^{-gx} \quad (3)$$

Variables a, c, and f are amplitudes, while variables b, d, and g are rate constants. Models leading to the lowest residuals over the entire data range were chosen as suitable fitting models.

Flash photolysis. The time-resolved absorption changes were recorded using a home-built flash-photolysis setup. A ND:YAG laser (Spotlight 600, Innolas Laser GmbH) in combination with an OPO (GWU Lasertechnik) is used to generate short laser (5 ns) pulses at a wavelength of 500 nm. Rectangular to this laser pulse a cw-beam of the appropriate

wavelength was focused into the sample. Therefore the output of a Xenon lamp (LC8, Hamamatsu) is guided to a monochromator (Photon Technologies International) for wavelength selection. After passing through the sample the light beam is guided to a second monochromator to get rid of scattering light due to laser excitation. The absorption changes were detected using a photocathode (Photosensor H6780-02, Hamamatsu). The data are recorded on a digital storage oscilloscope (Waverunner 62Xi LeCroy). The static absorption spectra were recorded on a Specord S100 (Analytik Jena). For flash photolysis we used a protein concentration of 25 μM in a 20 mM phosphate buffer at pH 7.4 and 298 K. Bovine rhodopsin was solubilized in the detergent DDM (n-Dodecyl β -D-maltoside) at a concentration of 1 % (w/v).

SUPPLEMENTARY FIGURES

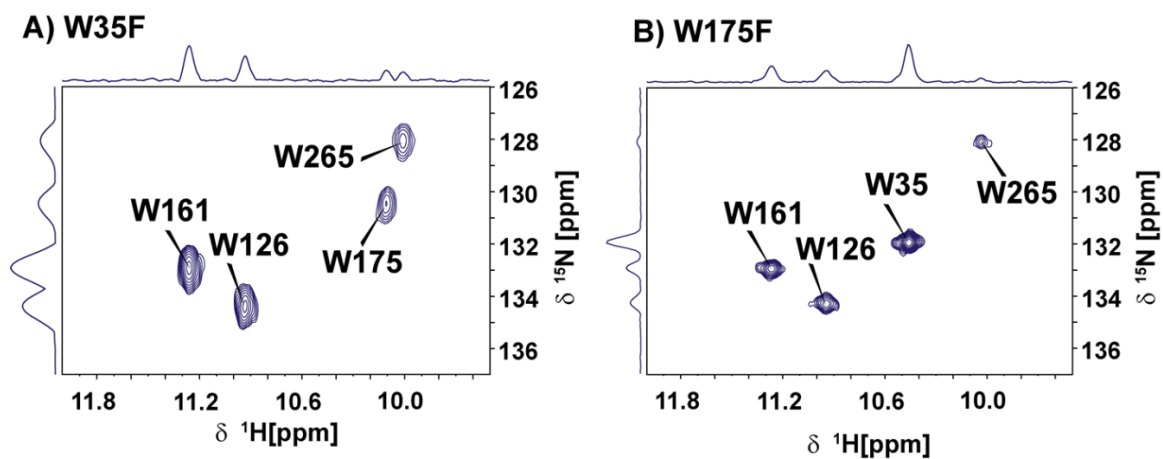


Figure S1: 2D HSQC spectrum of α,ϵ - ^{15}N -tryptophan labeled rhodopsin mutants (A) W35F and (B) W175F showing the indole region. Four of the five tryptophan signals are observed in each spectrum as expected for a tryptophan to phenylalanine mutant. For W35F and W175F rhodopsin mutants, beside 1D NMR spectra, also 2D NMR spectra could be recorded with sufficient signal-to-noise. Spectra were recorded at 800 MHz proton frequency at $T=298$ K.

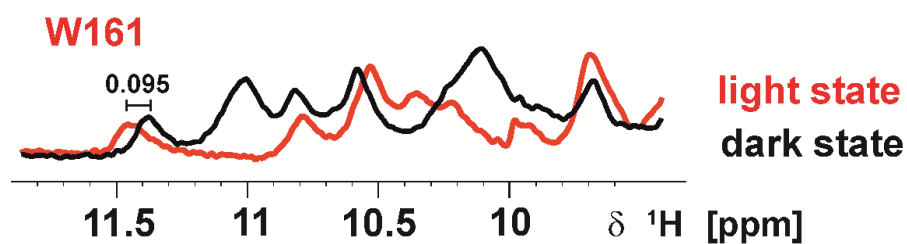


Figure S2: 1D ^1H NMR spectra of unlabeled wild type bovine rhodopsin. The black spectrum corresponds to the indole region of dark state rhodopsin whereas the red spectrum corresponds to the light state of rhodopsin. The chemical shift perturbation (CSP) is indicated for W161 as the CSP cannot be determined for this tryptophan residue in the of $\alpha,\epsilon\text{-}^{15}\text{N}$ -tryptophan labeled rhodopsin 1D ^1H NMR spectra.

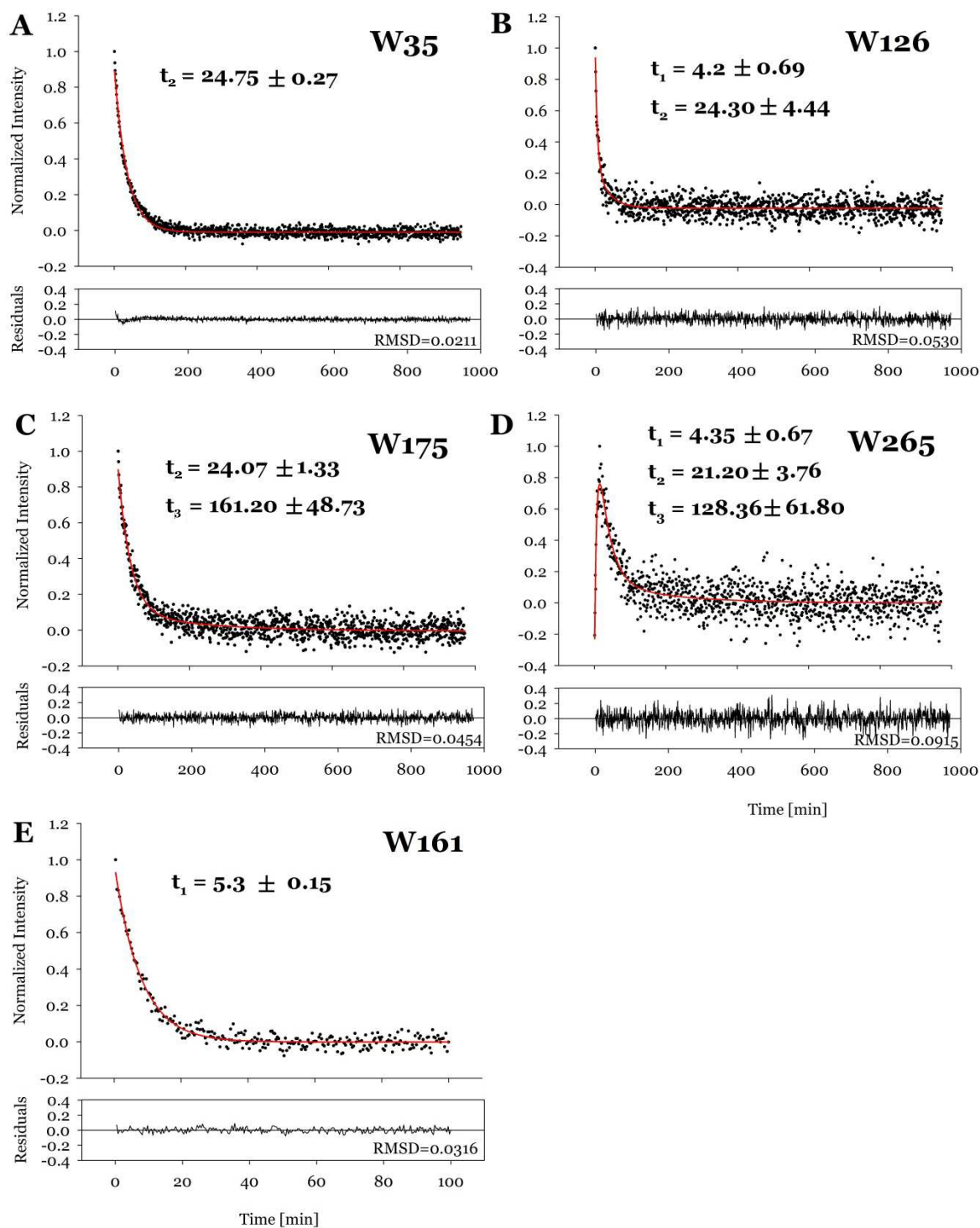
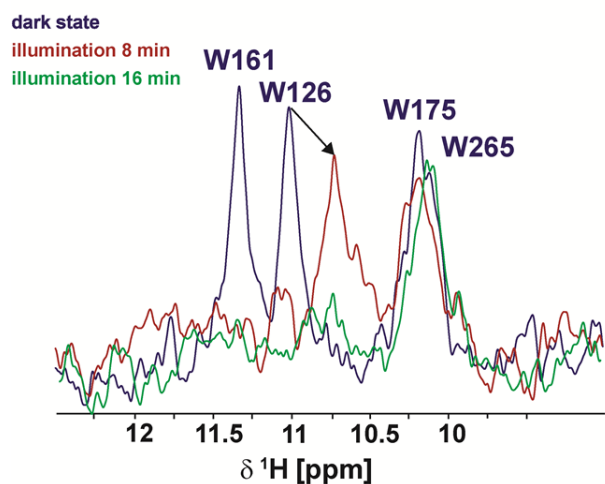


Figure S3: (A-D) Extracted signal intensities from the series of 1D ^1H NMR spectra of $\alpha,\epsilon\text{-}^{15}\text{N}$ tryptophan labeled rhodopsin. (E) Extracted signal intensities from the series of 1D ^1H NMR spectra of unlabeled rhodopsin recorded previously (5). The signal intensities were normalized and plotted as a function of time. Different fitting routines have been applied to accommodate for the individual graph properties of each signal row. (A, E) For the signal intensities of tryptophan 35 and tryptophan 161 a mono exponential fitting routine has been applied, (B,C) for the signal intensities of tryptophan 126 and tryptophan 175 a bi exponential fitting routine has been applied and (D) for the signal intensities of tryptophan 265 a tri exponential fitting routine has been applied. The residuals are shown for the fitting routine of each tryptophan.

A) W35F



B) W175F

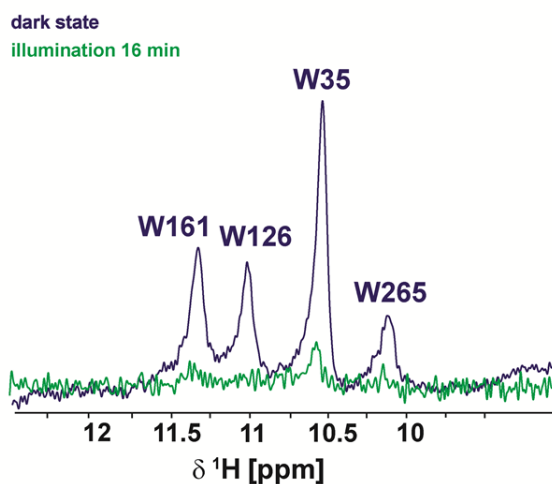


Figure S4: A series of 1D ^1H NMR spectra of α,ϵ - ^{15}N -tryptophan labeled W35F (A) and W175F (B) rhodopsin mutant recorded eight and sixteen minutes (W35F) as well as sixteen minutes (W175F) after light pulse. The focus is on the indole region of the spectrum. The dark state spectrum is shown in blue, the spectrum eight minutes after light pulse is shown in red and the spectrum 16 minutes after illumination is shown in green. The spectra were recorded at 800 MHz proton frequency ($T=298$ K) with 512 (W35F) and 1024 (W175F) scans. The sample concentrations were 100 μM (W35F) and 50 μM (W175F).

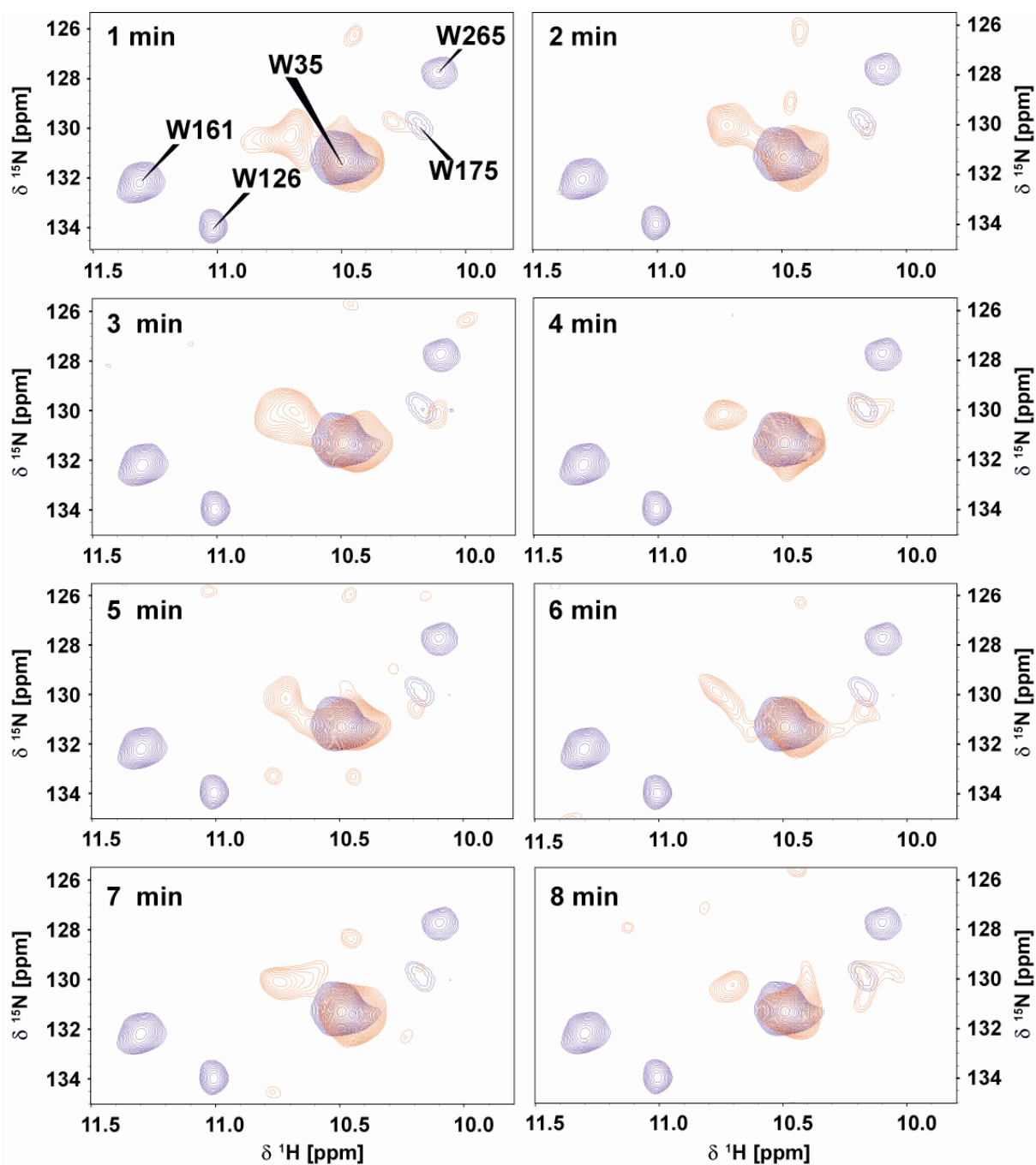


Figure S5: Two dimensional SOFAST-HMQC spectra of α, ϵ - ^{15}N -tryptophan labeled rhodopsin recorded in a pseudo three dimensional manner. The temporal resolution of the spectra series was one minute. The first eight spectra after the illumination are shown (red) each with the corresponding dark state spectrum (blue) as an overlay. The spectra were recorded at a Bruker Avance I 800 MHz spectrometer at $T=298$ K.

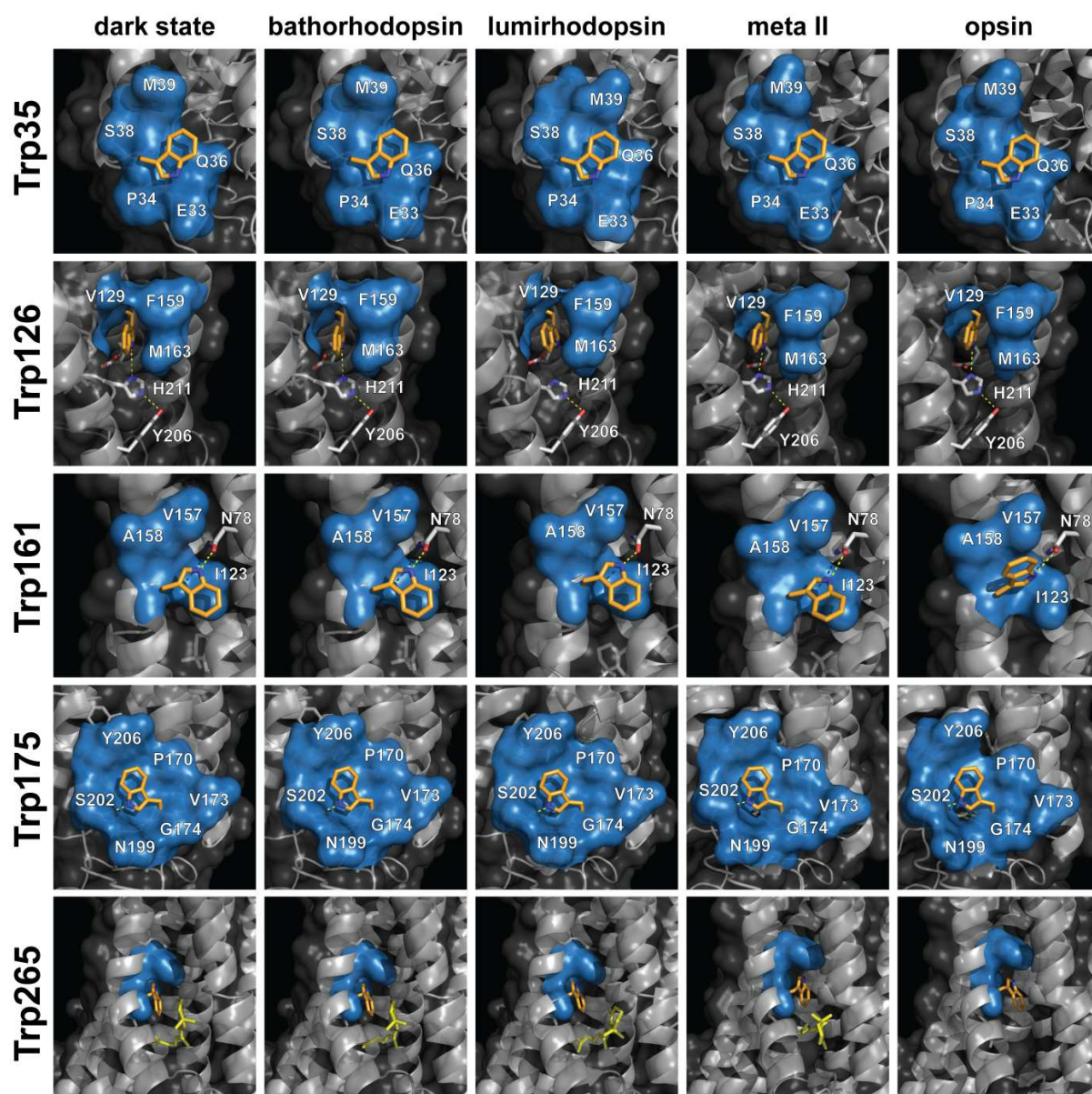


Figure S6: Snapshot gallery of photocycle intermediates focusing on one of the five tryptophan moieties respectively. For five intermediate states a crystal structure is available. The corresponding PDB codes are: 1U19 (dark state), 2G87 (bathorhodopsin), 2HYP (lumirhodopsin), 3PXO (meta II), and 3CAP (opsin). The backbone structures are shown in grey, the tryptophan residues are depicted in orange except for the indole nitrogen that is shown in blue. Residues depicted as blue surfaces are part of the tryptophan binding pocket. Residues that take part in hydrogen bonding to the corresponding tryptophans are shown as sticks. The retinal is shown in yellow.

SUPPLEMENTARY VIDEOS

Video S1: A simulated conversion from the inactive dark state rhodopsin (PDB code: 1U19) to the active meta II state (PDB code: 3PXO) and opsin (PDB code: 3CAP) plus the short lived intermediates bathorhodopsin (PDB code: 2G87) and lumirhodopsin (PDB code: 2HYP) is shown. The meta III state is not included in the simulation since there is no structural information available. The seven transmembrane alpha helices of rhodopsin are shown in blue. In yellow the retinal is shown in its dark state 11-cis configuration. In red the residues involved in the hydrogen bond network connecting helix 6 and helix 3 are shown in a stick model. This is the so called “ionic lock”. In helix 3 the highly conserved sequential motif ERY is present that is involved in the hydrogen bond network. Upon activation of rhodopsin helix 6 moves away from helix 3 thereby disrupting the hydrogen bond network. In helix 7 the second highly conserved sequential motif is present, the NPVIY motif, and in a concerted process helix 7 moves into the gap between helix 3 and helix 6. Here especially the tyrosine 306 which makes the rhodopsin activation an essentially irreversible process. The simulation has been created using the PyMol software package.

Video S2: A simulated conversion from the inactive dark state rhodopsin (PDB code: 1U19) to the active meta II state (PDB code: 3PXO) and opsin (PDB code: 3CAP) via the short lived intermediates bathorhodopsin (PDB code: 2G87) and lumirhodopsin (PDB code: 2HYP) is shown focusing on the five tryptophan residues present in rhodopsin. The structure morphing was done using the PyMOL software package and the structures of each morphing step (60 frames) were subsequently aligned using Python including the Biopython module yielding one combined structure array containing 295 frames. The backbone residues of rhodopsin are shown in grey depicted as cartoon and all residues including side chains are also shown as gray, transparent surface. Residues forming most of the tryptophan binding pocket are shown as a blue surface. Tryptophan moieties themselves are shown as sticks (C:orange, N:blue). Other important residues are shown as sticks (C:gray, N:blue, O: red). Hydrogen bonds are shown as yellow dashed lines. Throughout the video, the morphing from the dark state (dark) to opsin (opsin) via bathorhodopsin (batho), lumirhodopsin (lumi), and metarhodopsin II (meta II) can be followed. All frames were rendered using the PyMOL software package.

(Intro - 00:00-00:07) As introduction, a 360° rotation along the axis parallel to the average helical orientation is shown.

(W161 – 00:07-00:19) The binding pocket of Trp161 is formed mainly by residues Ile123, Val157, Ala158, and Thr160 (blue surface). Asn78 forms a hydrogen bond with Trp161 (yellow, dashed line). During the photocycle, Trp161 undergoes a side chain flip in the meta II state as compared to the dark state structure. Due to that side chain rotation, the length and orientation of the hydrogen bond is changed during the photocycle. In the NMR data a significant change of the indole signal is observed as well.

(W265 – 00:20-00:32) The binding pocket of Trp265 is formed mainly by residues Phe261, Cys264, Ala295, and Ser298 (blue surface). Retinal is shown as sticks and is colored yellow. The indole ring of Trp265 is located parallel to the beta ionone ring of retinal and interacts with the retinal via van-der-Waals interactions. Due to the retinal flip and removal, the chemical environment of Trp265 is modulated significantly during the photocycle, a process that is also visible by our kinetic analysis.

(W126 – 00:32-00:44) The binding pocket of Trp126 is formed mainly by residues Leu125, Val129, Pro215, Phe159, Thr160, and Met163 (blue surface). Glu122, Tyr206, and His211 form a hydrogen bond network with Trp126 (yellow, dashed line). This hydrogen bond network is altered throughout the photocycle. Therefore a change in the indole signal upon light activation is in line with the kinetic data of meta II.

(W35 – 00:44-00:56) The binding pocket of Trp35 is formed mainly by residues Ala32, Glu33, Pro34, Gln36, Phe37, Ser38, and Met39 (blue surface). For Trp35 no significant changes can be observed comparing the dark state and the meta II state which is in line with the observed kinetic data obtained by real time NMR spectroscopy.

(W175 – 00:56-01:09) The binding pocket of Trp175 is formed mainly by residues Pro170, Val173, Gly174, Thr198, Asn199, Ser202, Phe203, and Tyr206 (blue surface). A hydrogen bond between Trp175 and Ser202 is shown (yellow, dashed line) Tryptophan 175 is located in the E2 loop and no significant structural changes are observed. In the kinetic experiments this residue does also not report on the meta II decay.

References

- [1] aP. J. Reeves, N. Callewaert, R. Contreras, H. G. Khorana, *Proceedings of the National Academy of Sciences of the United States of America* **2002**, *99*, 13419-13424; bP. J. Reeves, J. M. Kim, H. G. Khorana, *Proceedings of the National Academy of Sciences of the United States of America* **2002**, *99*, 13413-13418.
- [2] M. C. Loewen, J. Klein-Seetharaman, E. V. Getmanova, P. J. Reeves, H. Schwalbe, H. G. Khorana, *Proceedings of the National Academy of Sciences of the United States of America* **2001**, *98*, 4888-4892.
- [3] K. Werner, C. Richter, J. Klein-Seetharaman, H. Schwalbe, *Journal of biomolecular NMR* **2008**, *40*, 49-53.
- [4] A. Knowles, A. Priestley, *Vision Res* **1978**, *18*, 115-116.
- [5] D. D. Oprian, R. S. Molday, R. J. Kaufman, H. G. Khorana, *Proceedings of the National Academy of Sciences of the United States of America* **1987**, *84*, 8874-8878.
- [6] T. Kühn, H. Schwalbe, *Journal of the American Chemical Society* **2000**, *122*, 6169-6174.
- [7] P. Schanda, E. Kupce, B. Brutscher, *Journal of biomolecular NMR* **2005**, *33*, 199-211.

3.9 Research article 2

Influence of Arrestin on the Photodecay of Bovine Rhodopsin.

Chatterjee D*, Eckert CE*, Slavov C, Saxena K, Fürtig B, Sanders CR, Gurevich VV, Wachtveitl J, Schwalbe H. *Angewandte Chemie International Edition*, **2015**, 54, 13555-13560. * Equal contribution

In this article, the interaction of arrestin with rhodopsin in DHPC (1,2-diheptanoyl-*sn*-glycero-3-phosphocholine) micelles was investigated by solution NMR techniques and flash photolysis experiment. Our results show that formation of the rhodopsin-arrestin complex markedly influences partitioning in the decay kinetics of rhodopsin, which involves the simultaneous formation of a meta II and a meta III state from the meta I state. Binding of arrestin leads to an increase in the population of the meta III state and consequently to an approximately two fold slower release of all-*trans*-retinal from rhodopsin. Our findings suggest that the meta III decay can be considered as a rate-limiting factor for the homeostasis of the free all-*trans*-retinal concentration in ROS essential for the functionality of the eye at varying light intensities.

The author of this thesis has performed all molecular biology work (mammalian cells expression and purification) and NMR experiments (real time NMR experiments and kinetic analysis of the rhodopsin and rhodopsin-arrestin complex). The flash photolysis experiments were performed by author, in part together with C.E. Eckert in the group of Prof. Dr. Josef Wachtveitl (Inst. of Physical and Theoretical Chemistry, Goethe University, Frankfurt). The author of this thesis also contributed in all the aspects of writing the manuscript.

Influence of Arrestin on the Photodecay of Bovine Rhodopsin

Deep Chatterjee, Carl Elias Eckert, Chavdar Slavov, Krishna Saxena, Boris Fürtig, Charles R. Sanders, Vsevolod V. Gurevich, Josef Wachtveitl,* and Harald Schwalbe*

Abstract: Continued activation of the photocycle of the dim-light receptor rhodopsin leads to the accumulation of all-trans-retinal in the rod outer segments (ROS). This accumulation can damage the photoreceptor cell. For retinal homeostasis, deactivation processes are initiated in which the release of retinal is delayed. One of these processes involves the binding of arrestin to rhodopsin. Here, the interaction of pre-activated truncated bovine visual arrestin (Arr^{Tr}) with rhodopsin in 1,2-diheptanoyl-sn-glycero-3-phosphocholine (DHPC) micelles is investigated by solution NMR techniques and flash photolysis spectroscopy. Our results show that formation of the rhodopsin–arrestin complex markedly influences partitioning in the decay kinetics of rhodopsin, which involves the simultaneous formation of a meta II and a meta III state from the meta I state. Binding of Arr^{Tr} leads to an increase in the population of the meta III state and consequently to an approximately twofold slower release of all-trans-retinal from rhodopsin.

The mammalian visual cycle is a complex process involving activation, deactivation, and regeneration pathways.^[1–6] The prototype G-protein-coupled receptor (GPCR) rhodopsin plays a pivotal role in this system. The extensive study of this system has provided much information that is believed to generally apply to the signaling pathways of other GPCRs.^[7–9] One of the breakthroughs in rhodopsin and GPCR research was the elucidation of the crystal structure of bovine rhodopsin,^[10] which provided a platform for future structural and functional studies on GPCRs.^[7–9]

Rhodopsin adopts a seven transmembrane α -helical structure and carries the covalently attached retinal chromophore. Photoinduced isomerization of the chromophore from its 11-*cis* to all-*trans* configuration results in conformational changes in rhodopsin that lead to the formation of several transiently populated intermediate states (Figure 1).^[10–16] Early photointermediates are short-lived and convert into a meta I state on a sub-millisecond time scale. This meta I state functions as a juncture at which the photocycle bifurcates to form meta II and meta III states.^[17] The meta II state interacts with the guanine nucleotide binding protein (G protein) transducin and triggers the activation signaling cascade, finally leading to hyperpolarization of photoreceptor cells. The meta III state has been reported to function as an energy-storage state.^[18] The distribution between states populated along the photodecay can be shifted by changing the conditions, including temperature and pH.^[19–21] Both the meta II and meta III states finally relax to the apoprotein opsin through release of all-*trans*-retinal.

Prolonged exposure to light can lead to an accumulation of free all-*trans*-retinal in the rod outer segment (ROS), which can be toxic to the eye owing to the formation of epoxides by oxidation. Harmful effects of excess retinal include visual dysfunction and retinal damage as found in several diseases, such as age-related macular degeneration (AMD).^[22–24] Previously published data^[25,26] suggest that there are two rate-limiting steps that maintain the level of all-*trans*-retinal in the ROS: 1) the release of free all-*trans*-retinal that depends on the photodecay kinetics and 2) the conversion of retinal into retinol by the enzyme retinal dehydrogenase (RDH; Figure 1). As the rate of enzymatic turnover of RDH is slow compared to meta II decay, retinal can accumulate in the ROS.^[25,27,28] When retinal accumulates, the eye initiates photocycle deactivation processes to delay the release of retinal.^[29]

Visual arrestin, a protein that belongs to the arrestin subfamily, acts as the major facilitator that down-regulates rhodopsin signaling by tightly binding to rhodopsin and concomitant displacement of G protein.^[30,31] A recently published crystal structure of the rhodopsin–arrestin complex has provided insights into the static nature of this interaction.^[32] Arrestin binding has been shown to slow down retinal release by stabilization of the meta II state.^[33] However, the effect of arrestin on the meta III photodynamics has not been studied in detail.

Aside from full-length arrestin, p44 (Arr1–370A), a splice variant of arrestin,^[34] is also present in rod cells. Although p44 is not ubiquitously present among all species (for example, in mice), it has been suggested to play a role in rhodopsin deactivation.^[34–37] The binding mechanism of p44 to rhodopsin is different from that of arrestin owing to the absence of the C-terminal tail.^[34–37] p44 not only binds more tightly to

[*] D. Chatterjee,^[†] Dr. K. Saxena, Dr. B. Fürtig, Prof. Dr. H. Schwalbe
 Institute of Organic Chemistry and Chemical Biology
 Center of Biomolecular Magnetic Resonance (BMRZ)
 Goethe University Frankfurt/Main
 Max-von-Laue-Strasse 7, 60438 Frankfurt am Main (Germany)
 E-mail: schwalbe@nmr.uni-frankfurt.de

C. E. Eckert,^[†] Dr. C. Slavov, Prof. Dr. J. Wachtveitl
 Institute of Physical and Theoretical Chemistry
 Goethe University Frankfurt/Main
 Max-von-Laue-Strasse 7, 60438 Frankfurt am Main (Germany)
 E-mail: wweitl@theochem.uni-frankfurt.de

Prof. Dr. C. R. Sanders
 Department of Biochemistry, Center for Structural Biology, Institute
 of Chemical Biology, Vanderbilt University School of Medicine
 Nashville, TN 37232 (USA)

Prof. Dr. V. V. Gurevich
 Department of Pharmacology
 Vanderbilt University School of Medicine
 Nashville, TN 37232 (USA)

[†] These authors contributed equally to this work.

Supporting information for this article is available on the WWW
 under <http://dx.doi.org/10.1002/anie.201505798>.

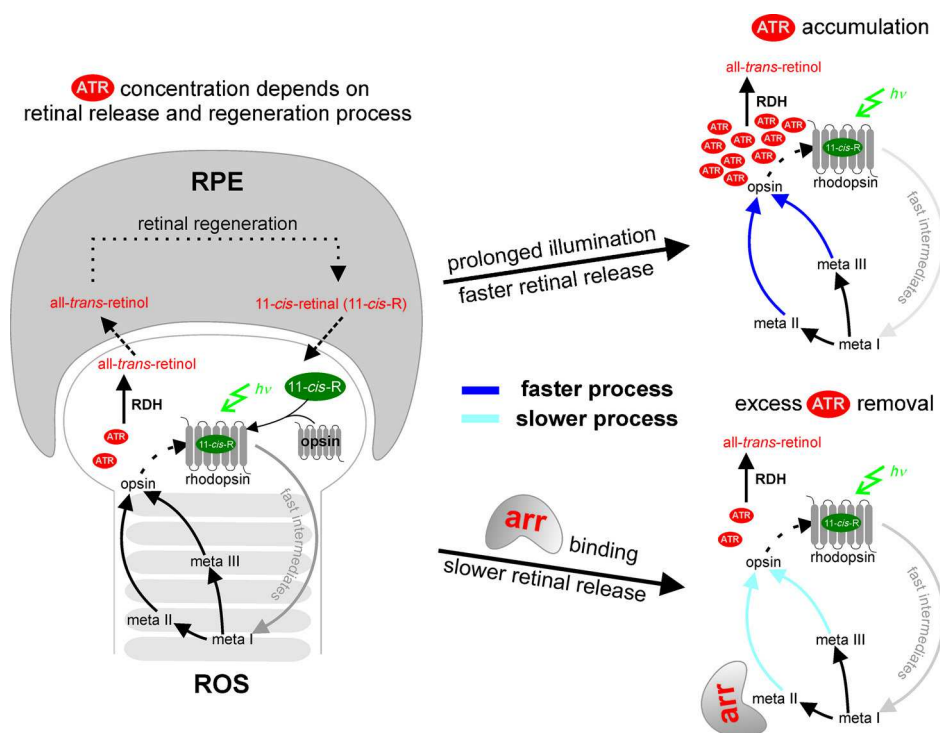


Figure 1. Mammalian visual cycle. The concentration of free all-*trans*-retinal (ATR) depends on two processes: 1) retinal release during the photocycle in the rod outer segment (ROS) and 2) retinal removal by a regeneration pathway in the retinal pigment epithelium (RPE) as shown on the left. Continuous exposure to light leads to the accumulation of ATR (top right), which initiates rhodopsin deactivation by arrestin (arr). Arrestin binding slows down the retinal release, which provides retinal dehydrogenase (RDH) with ample time to remove excess ATR by converting it into all-*trans*-retinol (bottom right).

phosphorylated rhodopsin, but also binds to the non-phosphorylated form.^[36,37] Owing to the latter interaction, it has previously been argued that phosphorylation is not needed for p44-mediated rhodopsin deactivation.^[34,37] However, it is not known how p44 manipulates the rhodopsin decay kinetics, especially the meta III dynamics.

Herein, we investigated the effect of p44 on the photodecay kinetics of rhodopsin. We employed a truncated mutant (Arr1–378) of visual arrestin (Arr^{Tr}),^[38] which is devoid of the C-terminal tail. Arr^{Tr} closely resembles p44, including phosphorylation-independent deactivation of rhodopsin.^[38] We utilized Arr^{Tr} instead of p44 as it is less prone to aggregation. To analyze the interaction, we employed a strategy combining two biophysical techniques, NMR spectroscopy and flash photolysis.

Our NMR analysis of the dynamics of photoactivated rhodopsin was based on the kinetic behavior of five tryptophan residues present in rhodopsin, which were used as reporter groups (Figure 2a). All five tryptophan indole resonances were previously assigned in *n*-dodecyl- β -D-maltoside (DDM) micelles by utilizing single-point tryptophan to phenylalanine mutants.^[17] As previous studies had shown that arrestin is destabilized in the presence of DDM,^[39] we utilized 1,2-diheptanoyl-*sn*-glycero-3-phosphocholine (DHPC) for the interaction studies of rhodopsin and Arr^{Tr}.^[34,37] Rhodopsin is expressed in HEK293 cells;^[40,41] this expression yields the non-phosphorylated form of the protein.

Initially, the differences in the ground-state structures of DDM- and DHPC-solubilized rhodopsin were characterized using 2D NMR spectroscopy, followed by an investigation of the effect of different detergents on the photodecay of rhodopsin. The chemical shift perturbations (CSPs) for the tryptophan indole resonances in DHPC micelles remain almost identical to those in DDM (Figure 2b). Hence the assignments for each of these tryptophan resonances could be easily transferred from the previous assignment in DDM. The similarity of the CSPs also indicates that the overall fold of rhodopsin is not significantly altered upon replacing the DDM with DHPC micelles.

To investigate the influence of Arr^{Tr} on the dark state of rhodopsin, we performed 2D ¹H, ¹⁵N correlation experiments. The interaction with Arr^{Tr} induces both CSPs and the disappearance of a subset of NMR signals in the amide region of the spectra arising from residues in the flexible C-terminal part of rhodopsin

(Figure 2c).^[42–47] The five NMR resonances of the tryptophan indole sidechains (Figure 2d), however, are not altered, indicating that low-affinity transient binding of Arr^{Tr} to rhodopsin in the dark does not lead to a major structural rearrangement in the transmembrane helical part.^[37,39]

Our previous results on the kinetic analysis of rhodopsin in DDM micelles showed complex photodecay kinetics with two different rate constants detected for different tryptophan reporter groups and a third, substantially slower decay constant owing to protein aggregation.^[17] In DDM, W126, W161, and W265 formed a first group of residues with a common lifetime of 8 min (t_1). The second process, which could be observed for W35 and W175, had a lifetime of 34 min (t_2). We previously proposed that these two lifetimes represent decay by a direct route involving meta II and by a branched route populating an alternative-pathway meta III state, respectively.^[17]

Time-resolved NMR experiments of the rhodopsin kinetics in a DHPC micelle (Figure 3a) revealed faster decay of the five tryptophan resonances than in a DDM micelle. A lower signal-to-noise ratio and the significantly faster decay in DHPC made the analysis of the NMR-derived kinetic data more difficult. Therefore, we focused on the kinetic analysis of the two most intense indole signals, W126 and W35 (Figure 3b). W126 showed a decay time of 5 min, whereas W35 showed a decay time of 7 min (Table 1). Similar to our previous kinetic analysis in DDM, the presence of two

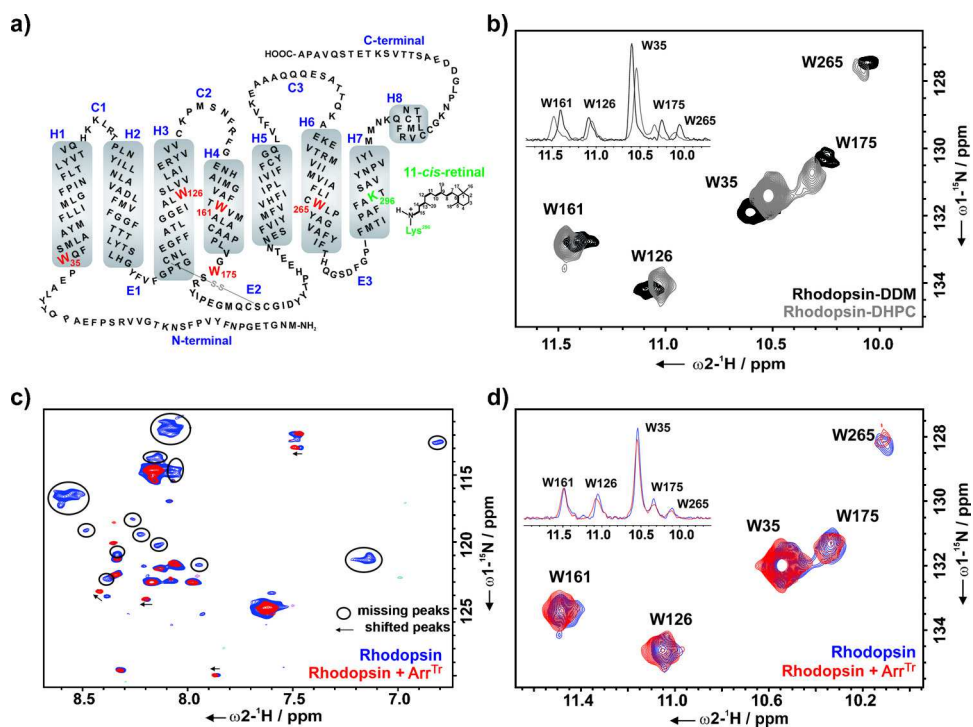


Figure 2. a) Secondary structure of bovine rhodopsin with the five tryptophan residues (W35, W126, W161, W175, and W265) used as reporter groups in the NMR experiments. b) Overlay of the indole region of 2D ^1H , ^{15}N SOFAST-HMQC spectra of α,ϵ - ^{15}N -tryptophan-labeled rhodopsin in DDM (black) and DHPc (gray) micelles. c, d) Overlays of the 2D ^1H , ^{15}N SOFAST-HMQC spectra of α,ϵ - ^{15}N -tryptophan-labeled rhodopsin without (blue) and with Arr^{Tr} (red; rhodopsin/Arr^{Tr} = 1:2) showing the backbone (c) and indole (d) regions of the spectra. Overlays of the 1D projections of the corresponding cross peaks of the indole region of the 2D spectra are shown in the insets (b and d). All spectra were recorded at 800 MHz ($T=298\text{ K}$) in the following buffer solutions: DDM spectrum: 20 mM sodium phosphate buffer, pH 7.4; DHPc spectra: 25 mM Tris, pH 7.5, 100 mM NaCl, 0.1 μM EDTA, 10% D_2O , and 1 mM 3-(trimethylsilyl)-2,2',3,3'-tetra-deuteriopropionic acid ($[\text{D}_4]$ -TSP).

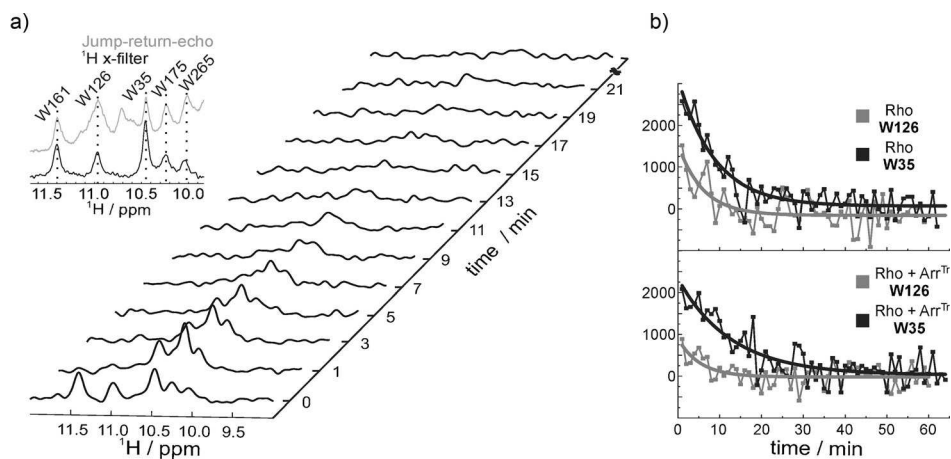


Figure 3. NMR kinetics. a) A series of 1D ^1H NMR spectra of α,ϵ - ^{15}N -tryptophan-labeled rhodopsin recorded at different time intervals after illumination. The indole region of the spectrum is shown. The five resonances visible in the dark state correspond to the five tryptophan residues present in rhodopsin. After illumination, the 1D ^1H spectra were recorded with a temporal resolution of one minute. Inset: Overlay of the spectra of the jump–return–echo (gray) and ^1H x-filter (black) NMR experiments with rhodopsin samples. The dashed lines connect the corresponding resonances of the five tryptophan residues. b) Extracted signal intensities from a series of 1D ^1H NMR spectra of α,ϵ - ^{15}N -tryptophan-labeled rhodopsin in the presence and absence of Arr^{Tr}. A mono-exponential fit was applied for the signal intensities of W35 (black curve) and W126 (gray curve).

lifetimes in our current data suggest that the kinetic partitioning of the photodecay, seen in DDM^[17] and even in native disk,^[21] was preserved in DHPc.

Upon addition of Arr^{Tr}, all five tryptophan indole resonances broadened, indicating the formation of a Arr^{Tr}–rhodopsin complex. After illumination, Arr^{Tr} binding did not change the lifetime of the W126 resonance, but it increased the lifetime of the W35 resonance by a factor of 1.6 from 7 min to 9.6 min. This result indicates that Arr^{Tr} induces a change in the decay kinetics of rhodopsin photo-intermediates.

To investigate these complex photodynamics in more detail, we performed broadband flash photolysis. We employed a multichannel detection system to obtain spectrally resolved transient absorption data (see the Supporting Information). We used the reported absorption maxima of the relevant intermediates of rhodopsin determined for hypotonically extracted ROS disk membranes from retina^[48] as references for the assignment of the spectral signatures in our transient absorption data. The transient spectra of DHPc-solubilized rhodopsin in the absence (Figure 4a) or presence of Arr^{Tr} (Figure 4b) were mainly determined by ground state bleaching (GSB) at about 500 nm and the formation of free all-*trans*-retinal at approximately 380 nm. Double difference spectra (Figure 4c, d) were calculated by subtracting the absorption change recorded at the maximum delay time from the transient absorption data. They depicted a positive signature at 400 nm, reporting on meta II decay, and a spectrally broad positive change in the absorption at 460–560 nm, representing met-

Table 1: Lifetimes of the tryptophan resonances of rhodopsin (150 μM) in the absence (–) and presence (+) of Arr^{Tr}.

	Lifetime [min]	
	–Arr ^{Tr} (0 μM)	+Arr ^{Tr} (300 μM)
W35	6.92 \pm 0.38	9.58 \pm 1.94
W126	5.03 \pm 0.40	5.23 \pm 2.05

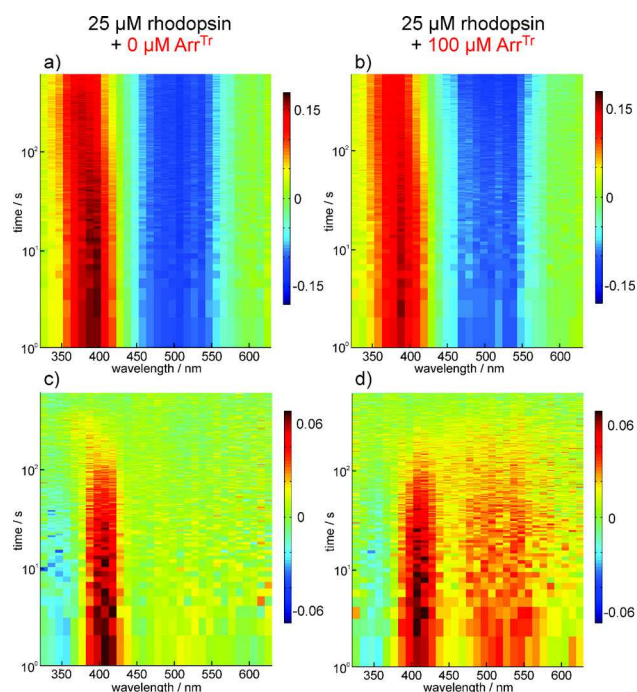


Figure 4. a, b) Transient absorption spectra of rhodopsin without (a) and with (b) Arr^{Tr}. Red and blue denote positive and negative changes in absorption, respectively. c, d) Double difference spectra of the spectra shown in (a) and (b), respectively, calculated by subtracting the absorption change recorded at the maximum delay time from the transient absorption data.

a III and potentially meta I. With Arr^{Tr}, the meta III signature was clearly more pronounced.

To visualize and quantify differences in the kinetics of these intermediates with and without Arr^{Tr}, a global lifetime analysis (GLA)^[49,50] was performed on the transient absorption data $I(\lambda, t)$ (see the Supporting Information). The GLA provided the lifetimes of meta II (1–2 min) and meta III (6–7 min) decay (Figure S3) and also suggested increased meta III formation in the presence of Arr^{Tr}. The GLA lifetimes are comparable to the two lifetimes observed in the NMR kinetic analysis (Table 1).

To corroborate the GLA results, we additionally performed a lifetime density analysis (LDA).^[50] With this method, the pre-exponential amplitudes of the sum of a large number (typically ca. 100) of exponential functions with fixed lifetimes (τ) are determined,

$$I(\lambda, t) = \int_0^\infty \Phi(\lambda, \tau) e^{-t/\tau} d\tau \quad (1)$$

where τ is the time, $I(\lambda, t)$ is the normalized decay function, and $\Phi(\lambda, \tau)$ is the spectral density function. The kinetic information contained in the time-resolved data is then presented in the form of a 2D lifetime distribution map. In contrast to GLA, the LDA is model-independent and thereby also extracts non-exponential or stretched exponential kinetics.

The lifetime density maps (LDMs; Figure 5) consist of four prominent distributions, as indicated by the letters C–F, describing the photodecay dynamics (Table 2, see also the Supporting Information, Table S1). The spectral signatures A (free retinal absorption) and B (ground-state bleach) in the LDMs (Figure 5) are long-lived non-decaying components that do not describe any photodecay dynamics. Similar to the GLA results, we observed a distribution for a short lifetime describing meta II decay (C) and meta III formation (D). The distribution for the longer lifetime corresponds to meta III decay (E). We assigned signature F to the formation of free retinal. The temporal position of F indicated that retinal release proceeds through both meta II and meta III decay in the absence of Arr^{Tr}. In the presence of Arr^{Tr}, the formation of free retinal (F) was significantly delayed, which is shown by the strong shift in the lifetime of signature F from 2.5 min to

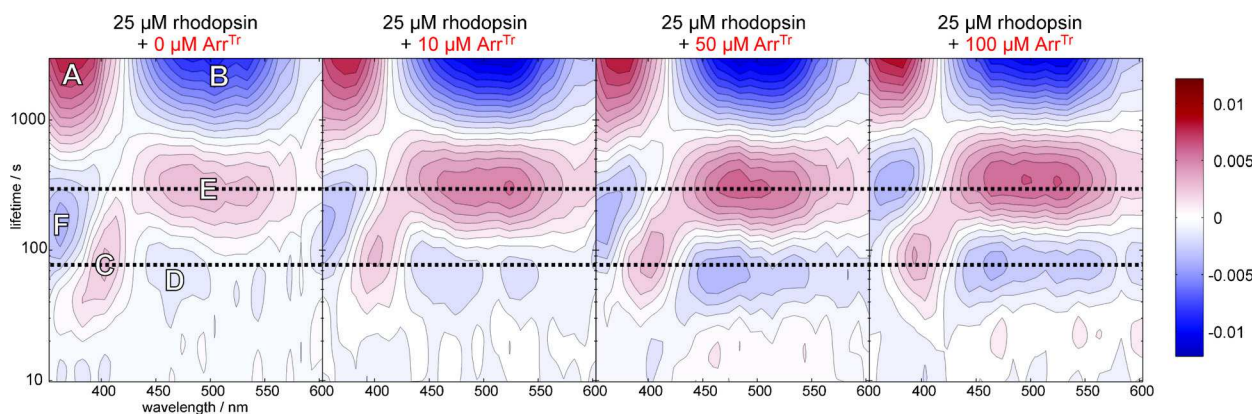


Figure 5. Lifetime density analysis of the transient absorption data. LDMs of rhodopsin samples with increasing Arr^{Tr} concentration. The reading of the LDMs is as for decay associated spectra (DAS) in GLA, with positive (red) amplitudes accounting for a decay of absorption and negative (blue) amplitudes accounting for an increase in absorption. The lifetimes and the distribution maxima of the signatures C–F are shown in Table 1.

Table 2: Lifetimes, distribution maxima, and amplitudes of the signatures C–F of the LDMs of rhodopsin (25 μM) in the absence (–) and presence (+) of Arr^{Tr}.

	Lifetime [min]		Wavelength [nm]		Amplitude	
	–Arr ^{Tr} [e]	+Arr ^{Tr} [f]	–Arr ^{Tr}	+Arr ^{Tr}	–Arr ^{Tr}	+Arr ^{Tr}
C ^[a]	1.3	1.5	400	390	0.003	0.004
D ^[b]	1.2	1.3	465	465	–0.001	–0.003
E ^[c]	5.0	5.3	460–540	460–540	0.003	0.007
F ^[d]	2.5	5.3	365	375	–0.004	–0.004

[a] Meta II decay. [b] Meta III formation. [c] Meta III decay. [d] Free retinal formation. [e] Arr^{Tr} concentration: 0 μM . [f] Arr^{Tr} concentration: 100 μM .

5.3 min. Moreover, the amplitudes signifying the formation (D) and decay (E) of meta III were more pronounced. From these observations, we conclude that the Arr^{Tr}–rhodopsin interaction slowed down the photodecay and thereby inhibited retinal release via meta II. As a consequence, the meta II–meta I equilibrium shifted towards meta I, which led to the accumulation of meta III. Subsequently, retinal release is delayed by a factor of two as meta III has a longer decay lifetime than meta II. A similar effect was observed in the NMR kinetic data as the decay lifetime of the W35 resonance was prolonged upon addition of Arr^{Tr} (Table 1). This effect can be attributed to a change in the protein dynamics influenced by the retinal release process.

Our findings indicate that meta III decay may have a physiological relevance on the regulation of the free all-*trans*-retinal concentration in ROS. We suggest that aside from the previously discussed rate-limiting factor for retinal regeneration within the photocycle of rhodopsin, namely the release of retinal from meta II, meta III decay can also be considered as an additional important factor for the homeostasis of the free all-*trans*-retinal concentration in ROS essential for the functionality of the eye at varying light intensities. The role of meta III, which was envisioned as an energy-storage state, as previously proposed by Bartl and Vogel^[51] who stated that under “bright light and thus high bleaching conditions, a delayed release of all-*trans*-retinal during meta II decay by formation of a meta III storage might be physiologically advantageous”, is fully consistent with our analysis. Here, we thus provide evidence for the function of meta III as a physiologically relevant energy-storage state.

In conclusion, this study has not only provided detailed insight into rhodopsin deactivation and the retinal regeneration process, but also pushed our time-resolved NMR and flash photolysis techniques to new limits. The data analysis was based on single-shot experiments because of the non-cyclic photodynamics of bovine rhodopsin. It required high NMR fields and advanced data analysis techniques (GLA and LDA). By using two different spectroscopic techniques, the role of arrestin in stabilizing meta III storage in the bifurcated photodecay of visual rhodopsin was unraveled at high temporal and amino acid resolution.

Acknowledgements

The work was supported by the DFG (SFB807). H.S. and J.W. are members of the DFG-funded cluster of excellence “Macromolecular Complexes”. B.M.R.Z. is supported by the state of Hesse. C.R.S. and V.V.G. are supported by NIH grants (U54 GM094608 and EY011500, respectively).

Keywords: arrestin · NMR spectroscopy · retinal regeneration · rhodopsin · UV/Vis spectroscopy

How to cite: *Angew. Chem. Int. Ed.* **2015**, *54*, 13555–13560
Angew. Chem. **2015**, *127*, 13759–13764

- [1] K. D. Ridge, K. Palczewski, *J. Biol. Chem.* **2007**, *282*, 9297–9301.
- [2] R. O. Parker, R. K. Crouch, *Exp. Eye Res.* **2010**, *91*, 788–792.
- [3] P. H. Tang, M. Kono, Y. Koutalos, Z. Ablonczy, R. K. Crouch, *Prog. Retinal Eye Res.* **2013**, *32*, 48–63.
- [4] D. A. Baylor, M. E. Burns, *Eye (Lond)*. **1998**, *12*, 521–525.
- [5] X. E. Zhou, K. Melcher, H. E. Xu, *Acta Pharmacol. Sin.* **2012**, *33*, 291–299.
- [6] V. Y. Arshavsky, T. D. Lamb, E. N. Pugh, *Annu. Rev. Physiol.* **2002**, *64*, 153–187.
- [7] X. Deupi, *Biochim. Biophys. Acta Bioenerg.* **2014**, *1837*, 674–682.
- [8] O. P. Ernst, D. T. Lodowski, M. Elstner, P. Hegemann, L. S. Brown, H. Kandori, *Chem. Rev.* **2014**, *114*, 126–163.
- [9] S. Wolf, S. Grünwald, *PLoS One* **2015**, *10*, e0123533.
- [10] K. Palczewski et al., *Science* **2000**, *289*, 739–745.
- [11] H. Nakamichi, T. Okada, *Angew. Chem. Int. Ed.* **2006**, *45*, 4270–4273; *Angew. Chem.* **2006**, *118*, 4376–4379.
- [12] H.-W. Choe, Y. J. Kim, J. H. Park, T. Morizumi, E. F. Pai, N. Krauss, K. P. Hofmann, P. Scheerer, O. P. Ernst, *Nature* **2011**, *471*, 651–655.
- [13] P. Scheerer, J. H. Park, P. W. Hildebrand, Y. J. Kim, N. Krauss, H.-W. Choe, K. P. Hofmann, O. P. Ernst, *Nature* **2008**, *455*, 497–502.
- [14] C. Altenbach, A. K. Kusnetzow, O. P. Ernst, K. P. Hofmann, W. L. Hubbell, *Proc. Natl. Acad. Sci. USA* **2008**, *105*, 7439–7444.
- [15] T. D. Dunham, D. L. Farrens, *J. Biol. Chem.* **1999**, *274*, 1683–1690.
- [16] H. Nakamichi, T. Okada, *Proc. Natl. Acad. Sci. USA* **2006**, *103*, 12729–12734.
- [17] J. Stehle, R. Silvers, K. Werner, D. Chatterjee, S. Gande, F. Scholz, A. Dutta, J. Wachtveitl, J. Klein-Seetharaman, H. Schwalbe, *Angew. Chem. Int. Ed.* **2014**, *53*, 2078–2084; *Angew. Chem.* **2014**, *126*, 2110–2116.
- [18] E. Ritter, M. Elgeti, F. J. Bartl, *Photochem. Photobiol.* **2008**, *84*, 911–920.
- [19] R. G. Matthews, R. Hubbard, P. K. Brown, G. Wald, *J. Gen. Physiol.* **1963**, *47*, 215–240.
- [20] K. Zimmermann, E. Ritter, F. J. Bartl, K. P. Hofmann, M. Heck, *J. Biol. Chem.* **2004**, *279*, 48112–48119.
- [21] R. Vogel, F. Siebert, X. Y. Zhang, G. Fan, M. Sheves, *Biochemistry* **2004**, *43*, 9457–9466.
- [22] R. A. Radu, N. L. Mata, A. Bagla, G. H. Travis, *Proc. Natl. Acad. Sci. USA* **2004**, *101*, 5928–5933.
- [23] J. R. Sparrow, N. Fishkin, J. Zhou, B. Cai, Y. P. Jang, S. Krane, Y. Itagaki, K. Nakanishi, *Vision Res.* **2003**, *43*, 2983–2990.
- [24] A. Wenzel, C. Grimm, M. Samardzija, C. E. Remé, *Prog. Retinal Eye Res.* **2005**, *24*, 275–306.
- [25] C. Chen, E. Tsina, M. C. Cornwall, R. K. Crouch, S. Vijayaraghavan, Y. Koutalos, *Biophys. J.* **2005**, *88*, 2278–2287.
- [26] M. E. Sommer, W. C. Smith, D. L. Farrens, *J. Biol. Chem.* **2005**, *280*, 6861–6871.

- [27] K. Palczewski, J. P. Van Hooser, G. G. Garwin, J. Chen, G. I. Liou, J. C. Saari, *Biochemistry* **1999**, *38*, 12012–12019.
- [28] K. P. Hofmann, A. Pulvermüller, J. Buczyko, P. Van Hooser, K. Palczewski, *J. Biol. Chem.* **1992**, *267*, 15701–15706.
- [29] M. E. Sommer, K. P. Hofmann, M. Heck, *Nat. Commun.* **2012**, *3*, 1–10.
- [30] J. A. Hirsch, C. Schubert, V. V. Gurevich, P. B. Sigler, *Cell* **1999**, *97*, 257–269.
- [31] J. Granzin, U. Wilden, H. W. Choe, J. Labahn, B. Krafft, G. Büldt, *Nature* **1998**, *391*, 918–921.
- [32] Y. Kang et al., *Nature* **2015**, *523*, 561–567.
- [33] M. E. Sommer, D. L. Farrens, *Vision Res.* **2006**, *46*, 4532–4546.
- [34] W. C. Smith, A. H. Milam, D. Dugger, A. Arendt, P. A. Hargrave, K. Palczewski, *J. Biol. Chem.* **1994**, *269*, 15407–15410.
- [35] J. Granzin, A. Cousin, M. Weirauch, R. Schlesinger, G. Büldt, R. Batra-Safferling, *J. Mol. Biol.* **2012**, *416*, 611–618.
- [36] Y. J. Kim, K. P. Hofmann, O. P. Ernst, P. Scheerer, H.-W. Choe, M. E. Sommer, *Nature* **2013**, *497*, 142–146.
- [37] K. Schröder, A. Pulvermüller, K. P. Hofmann, *J. Biol. Chem.* **2002**, *277*, 43987–43996.
- [38] V. V. Gurevich, *J. Biol. Chem.* **1998**, *273*, 15501–15506.
- [39] T. Zhuang, Q. Chen, M.-K. Cho, S. A. Vishnivetskiy, T. M. Iverson, V. V. Gurevich, C. R. Sanders, *Proc. Natl. Acad. Sci. USA* **2013**, *110*, 942–947.
- [40] P. J. Reeves, J.-M. Kim, H. G. Khorana, *Proc. Natl. Acad. Sci. USA* **2002**, *99*, 13413–13418.
- [41] P. J. Reeves, N. Callewaert, R. Contreras, H. G. Khorana, *Proc. Natl. Acad. Sci. USA* **2002**, *99*, 13419–13424.
- [42] R. Langen, K. Cai, C. Altenbach, H. Gobind Khorana, W. L. Hubbell, *Biochemistry* **1999**, *38*, 7918–7924.
- [43] K. Werner, I. Lehner, H. K. Dhiman, C. Richter, C. Glaubitz, H. Schwalbe, J. Klein-Seetharaman, H. G. Khorana, *J. Biomol. NMR* **2007**, *37*, 303–312.
- [44] K. Werner, C. Richter, J. Klein-Seetharaman, H. Schwalbe, *J. Biomol. NMR* **2008**, *40*, 49–53.
- [45] E. Getmanova, A. B. Patel, J. Klein-Seetharaman, M. C. Loewen, P. J. Reeves, N. Friedman, M. Sheves, S. O. Smith, H. G. Khorana, *Biochemistry* **2004**, *43*, 1126–1133.
- [46] J. Klein-Seetharaman, P. J. Reeves, M. C. Loewen, E. V. Getmanova, J. Chung, H. Schwalbe, P. E. Wright, H. G. Khorana, *Proc. Natl. Acad. Sci. USA* **2002**, *99*, 3452–3457.
- [47] J. Klein-Seetharaman, N. V. K. Yanamala, F. Javed, P. J. Reeves, E. V. Getmanova, M. C. Loewen, H. Schwalbe, H. G. Khorana, *Proc. Natl. Acad. Sci. USA*, **2004**, *101*, 3409–3413.
- [48] O. P. Ernst, F. J. Bartl, *ChemBioChem* **2002**, *3*, 968–974.
- [49] I. H. M. Van Stokkum, D. S. Larsen, R. Van Grondelle, *Biochim. Biophys. Acta Bioenerg.* **2004**, *1657*, 82–104.
- [50] C. Slavov, H. Hartmann, J. Wachtveitl, *Anal. Chem.* **2015**, *87*, 2328–2336.
- [51] F. J. Bartl, R. Vogel, *Phys. Chem. Chem. Phys.* **2007**, *9*, 1648–1658.

Received: June 24, 2015

Revised: August 11, 2015

Published online: September 18, 2015

Supporting Information

Influence of Arrestin on the Photodecay of Bovine Rhodopsin

*Deep Chatterjee, Carl Elias Eckert, Chavdar Slavov, Krishna Saxena, Boris Fürtig,
Charles R. Sanders, Vsevolod V. Gurevich, Josef Wachtveitl,* and Harald Schwalbe**

anie_201505798_sm_miscellaneous_information.pdf

Supporting Information

Table of contents

Experimental Section.....	2
Generation of stably transfected HEK293 cell lines containing the opsin genes	2
Expression and purification of selectively ¹⁵N tryptophan, labeled rhodopsin from HEK293S cells	2
Expression and purification of Arr^{Tr}	3
Real-time NMR spectroscopy	3
Arr ^{Tr} -rhodopsin interaction.....	3
Flash photolysis	4
Arr ^{Tr} -rhodopsin interaction.....	4
Global Lifetime Analysis (GLA) and Lifetime Density Analysis (LDA)	5
References	7
Supplementary figures.....	8
Figure S1: Schematic diagram for the laser setup of NMR and flash photolysis experiment.	8
Figure S2: NMR kinetic data.	9
Figure S3: Global lifetime analysis.....	10
Table S1: The lifetimes, the distribution maxima and the amplitudes of the signatures C-F of the LDMs of rhodopsin.....	11

Experimental Section

Generation of stably transfected HEK293 cell lines containing the opsin genes

Previously in our group the wild type opsin gene was cloned to pACMV-tetO vector to enable expression in stably transfected HEK293 cells.^[1,2] The pACMV-tetO vector was originally developed by Reeves et al.^[3,4] The preparation of stably transfected HEK293 cell lines containing the opsin gene was carried out as described previously.^[4,5]

Expression and purification of selectively ¹⁵N tryptophan, labeled rhodopsin from HEK293S cells

Rhodopsin was expressed in tetracycline inducible HEK293 cells. For the expression of the wild type opsin gene, the cells were grown in 143 cm² cell culture petri dishes. The cells were induced using cell culture media consisting of individual components enabling a selective isotope labeling scheme.^[4,6] Cells were harvested 2 - 3 days after induction. For sample preparation, cells harvested from 150 - 200 (for NMR experiments) or 50 - 70 (for flash photolysis experiments) petri dishes were resuspended in phosphate buffered saline (PBS) at pH 7.4. 11-cis-retinal was added to the cell suspension at a final concentration of 40 μM. 11-cis-retinal was prepared by illuminating all-trans-retinal and subsequent separation of the obtained isomers as previously described.^[7] Rhodopsin was solubilized by addition of 1% DDM (n-Dodecyl-β-D-maltoside) and purified via immunoaffinity chromatography. The 1D4 antibody (obtained from University of British Columbia, Vancouver, Canada) was coupled to activated Sepharose 4B as previously described.^[8] Rhodopsin was bound to the beads and washed with 10 column volumes of buffer A (25 mM Tris buffer at pH 7.5 + 0.05 % DDM). The detergent exchange was performed on the column by applying 10 column volumes of buffer B (buffer A + 0.2 % DHPC (1,2-diheptanoyl-*sn*-

glycero-3-phosphocholine)). Rhodopsin was subsequently eluted with buffer B containing the peptide TETSQVAPA at a concentration of 100 μM . Fractions containing rhodopsin were pooled and concentrated by amicon centrifuge concentrator (Millipore, Billerica, USA).

Expression and purification of Arr^{Tr}

The procedure for expression and purification of Arr^{Tr} was published previously.^[9]

Real-time NMR spectroscopy

Arr^{Tr}-rhodopsin interaction. NMR experiments of bovine rhodopsin were performed with a protein concentration of 150 μM in 25 mM Tris buffer at pH 7.5. Rhodopsin was solubilized in the detergent DHPC (1.5 - 2 % (w/v)). For interaction studies, rhodopsins in DHPC micelles were mixed with two fold higher concentration of Arr^{Tr} (300 μM) in the same buffer.

¹H, ¹⁵N SOFAST-HMQC^[10,11] (Heteronuclear Multiple Quantum Correlation) experiments were performed to determine chemical shift perturbations in tryptophan residues of rhodopsin to map the structural differences in rhodopsin upon solubilization in DDM and DHPC micelles. ¹H, ¹⁵N SOFAST-HMQC spectra were also recorded to structurally map the interaction between Arr^{Tr} and rhodopsin in the dark state.

Real-time NMR experiments were conducted on a Bruker Avance I 800 MHz spectrometer at T = 298 K. An argon ion laser with emission wavelength $\lambda = 514$ nm was used for the illumination of the rhodopsin sample. The laser beam was directly guided into the NMR sample via an optical fiber (Figure S1 a).^[12] A cw-beam of 300 mW was applied for 0.5 s to trigger the photocycle of rhodopsin.

Photodynamics of rhodopsin in absence or presence of Arr^{Tr} were studied by recording a series of one dimensional ¹H X-filtered^[13] spectra in a pseudo two dimensional manner. X-filter experiments were performed to avoid resonance ambiguities and simplify the NMR spectrum. The temporal resolution of the one dimensional experiments was ~ 1 minute. The focus was on the indole region of the spectrum where the indole side chain signals of the tryptophan residues are to be expected (with a carrier frequency of 10.6 kHz and a spectral width of 833.3 Hz).

Rhodopsin kinetics was extracted from these 1D ¹H X-filtered spectra. The kinetic behavior of individual amino acids was determined by applying an exponential decay fitting model on the corresponding signal row as follows:

$$I(t) = a + b * e^{-t/\tau}$$

Variable a is the offset, b is the amplitude and variable τ is the lifetime.

Flash photolysis

Arr^{Tr}-rhodopsin interaction. Transient absorption measurements were performed with a home-built flash photolysis setup (Figure S1 b). The samples were photoexcited using a single ns-pulse with the central wavelength of $\lambda_{\max}=500$ nm using a Nd:YAG laser (Spitlight 600, Innolas Laser GmbH) and an optical parametric oscillator (OPO, preciScan, GWU-Lasertechnik). For probing the absorption change, the transmitted intensity from a xenon flash lamp that provides spectrally broad μ s-pulses, was detected. The transmitted intensity $I_{sig}(\lambda, t)$ was measured with an ICCD camera (PI-MAX 3, Princeton Instruments). To increase the signal-to-noise ratio the intensity spectrum of the detection light $I_{ref}(\lambda, t)$ was measured separately. In the same manner, the transmission of the sample and the reference were measured

before the photoexcitation event, $I_{sig}^0(\lambda)$ and $I_{ref}^0(\lambda)$. Based on this, the change in absorption was calculated as follows:

$$\Delta A(\lambda, t) = -\log\left(\frac{I_{sig} * I_{ref}^0}{I_{ref} * I_{sig}^0}\right)$$

Since the rhodopsin photodynamics is not cyclic, only a single non-repetitive measurement could be conducted. Hence, the measurements had a relatively low signal-to-noise ratio. The spectral range of detection is 316 – 649 nm and the spectral resolution was ~0.5 nm. The raw data set was binned into wavelength resulting in a resolution of ~10 nm. The analysis of the data was performed entirely based on the binned data. The temporal resolution of the measurements was 1 sec within a range from 0 to 10 min. The sample for these experiments consist of DHPC solubilized rhodopsin (25 μ M) in a 20 mM Tris buffer at pH 7.4 and Arr^{Tr} with increasing concentration from 0 μ M to 100 μ M. All the experiments were performed at room temperature.

Global Lifetime Analysis (GLA) and Lifetime Density Analysis (LDA)

Typically, transient absorption data were analyzed by global lifetime analysis (GLA) using sums of a small number ($\sim < 10$) of exponentials:

$$I(\lambda, t) = \sum_{i=1}^n A_i(\lambda) e^{-\frac{t}{\tau}}$$

with t for time, τ for the lifetime, and λ for the wavelength.

In GLA, the number of exponential functions determines the complexity of the kinetic process. Thus, the data analysis is model-dependent that determines decay associated spectra $A_i(\lambda)$ (DAS) for each fitted lifetime. In DAS, the positive pre-exponential amplitudes (red) describe either decay of absorption or the rise of

bleaching, while negative pre-exponential amplitudes (blue) reflect either decay of bleaching or the rise of absorption.

However, the spectral signature of the photodecay kinetics of rhodopsin consists of spectrally and temporally interfering signals. In addition, the decay cycle involving linear and branched intermediates may result in non-exponential processes. Both aspects make the interpretation of the resulting decay-associated spectra (DAS) ambiguous. Therefore, we additionally performed a lifetime density analysis (LDA). With this method the pre-exponential amplitudes $\Phi(\lambda, \tau)$ of the sum of a large number (typically ~ 100) of exponential functions were determined. For each exponential function, the lifetime was fixed. Time-resolved data are quantitatively modelled by a spectrum of lifetimes, τ :

$$I(\lambda, t) = \int_0^{\infty} \Phi(\lambda, \tau) e^{-t/\tau} d\tau$$

where $I(\lambda, t)$ is the normalized decay function and $\Phi(\lambda, \tau)$ is the spectral density function. An inverse Laplace transform of $I(\lambda, t)$ was performed to determine $\Phi(\lambda, \tau)$. Hence, LDA covers a spectrally resolved distribution for each lifetime. The results can be presented in the form of a contour map, which is designated as lifetime density map (LDM). The maps can be read in the similar manner as described for DAS. In contrast to GLA, LDA is model-independent. Moreover, it can also reveal non-exponential or stretched exponential kinetics which cannot be determined in GLA.

References

- [1] J. Stehle, R. Silvers, K. Werner, D. Chatterjee, S. Gande, F. Scholz, A. Dutta, J. Wachtveitl, J. Klein-Seetharaman, H. Schwalbe, *Angew. Chem. Int. Ed. Engl.* **2014**, *53*, 2078–2084.
- [2] J. Stehle, R. Silvers, K. Werner, D. Chatterjee, S. Gande, F. Scholz, A. Dutta, J. Wachtveitl, J. Klein-Seetharaman, H. Schwalbe, *Angew. Chemie* **2014**, *126*, 2110–2116.
- [3] P. J. Reeves, J.-M. Kim, H. G. Khorana, *Proc. Natl. Acad. Sci. U. S. A.* **2002**, *99*, 13413–13418.
- [4] P. J. Reeves, N. Callewaert, R. Contreras, H. G. Khorana, *Proc. Natl. Acad. Sci. U. S. A.* **2002**, *99*, 13419–13424.
- [5] M. C. Loewen, J. Klein-Seetharaman, E. V Getmanova, P. J. Reeves, H. Schwalbe, H. G. Khorana, *Proc. Natl. Acad. Sci. U. S. A.* **2001**, *98*, 4888–4892.
- [6] K. Werner, C. Richter, J. Klein-Seetharaman, H. Schwalbe, *J. Biomol. NMR* **2008**, *40*, 49–53.
- [7] A. Knowles, A. Priestley, *Vision Res.* **1978**, *18*, 115–116.
- [8] D. D. Oprian, R. S. Molday, R. J. Kaufman, H. G. Khorana, *Proc. Natl. Acad. Sci. U. S. A.* **1987**, *84*, 8874–8878.
- [9] V. V. Gurevich, *J. Biol. Chem.* **1998**, *273*, 15501–15506.
- [10] P. Schanda, E. Kupce, B. Brutscher, *J. Biomol. NMR* **2005**, *33*, 199–211.
- [11] P. Schanda, B. Brutscher, *J. Am. Chem. Soc.* **2005**, *127*, 8014–8015.
- [12] T. Kühn, H. Schwalbe, *J. Am. Chem. Soc.* **2000**, *122*, 6169–6174.
- [13] E. Woergoetter, G. Wagner, K. Wuethrich, *J. Am. Chem. Soc.* **1986**, *108*, 6162–6167.
- [14] A. Bax, D. G. Davis, *J. Magn. Reson.* **1985**, *65*, 355–360.
- [15] M. Piotto, V. Saudek, V. Sklenář, *J. Biomol. NMR* **1992**, *2*, 661–665.
- [16] V. Sklenar, M. Piotto, R. Leppik, V. Saudek, *J. Magn. Reson. Ser. A* **1993**, *102*, 241–245.
- [17] T. L. Hwang, A. J. Shaka, *J. Magn. Reson. Ser. A* **1995**, *112*, 275–279.
- [18] J. Granzin, U. Wilden, H. W. Choe, J. Labahn, B. Krafft, G. Büldt, *Nature* **1998**, *391*, 918–921.

Supplementary figures

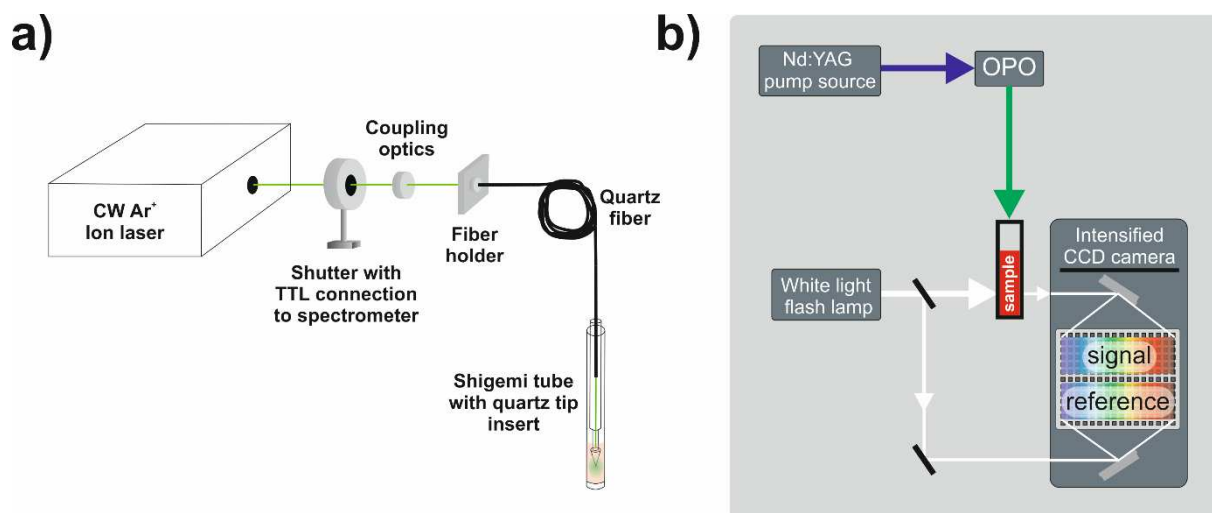


Figure S1: Schematic diagram for the laser setup of NMR and flash photolysis experiment. a) NMR. The laser beam emitted at $\lambda = 514$ nm and guided directly into a quartz fiber by coupling optics. The end of the quartz fiber was attached to a shigemi tube with the sample. b) Flash photolysis. The pump pulse was generated by an optical parametric oscillator (preciScan, GWU-Lasertechnik) and an Nd:YAG laser system (Spitlight 600, Innolas Laser GmbH). The excitation wavelength was adjusted to 500 nm (absorption maximum of dark-state bovine rhodopsin). For detection a xenon white light flash lamp was used. The transmission of these pulses (indicated as *signal* in the scheme) was measured via an ICCD detector (PI-MAX3, Princeton Instruments). Simultaneously the spectrum of the detection light was measured (indicated as *reference* in the scheme) in order to increase the signal-to-noise ratio.

a)

rhodopsin	lifetime (min)	amplitude ratio
W35 (meta III)	6.9 ± 0.4	1.6 ± 0.3
W126 (meta II)	5.0 ± 0.4	

rhodopsin + Arr ^{Tr}	lifetime (min)	amplitude ratio
W35 (meta III)	9.6 ± 1.9	2.4 ± 0.6
W126 (meta II)	5.2 ± 2.1	

b)

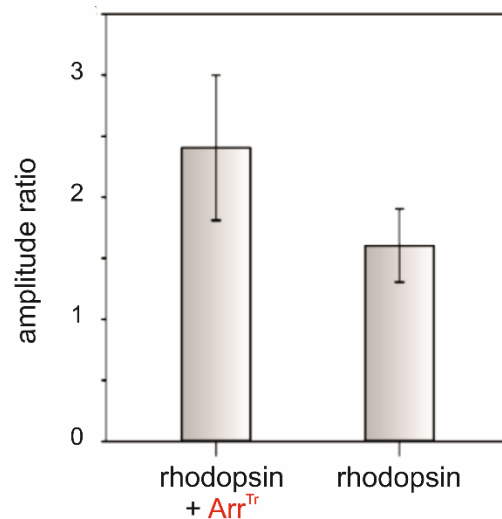


Figure S2: NMR kinetic data. a) Lifetime and initial amplitude ratio of W35 and W126 indole resonances (above – rhodopsin, below – rhodopsin + Arr^{Tr}) as extracted from the exponential fit (Figure 3b). b) Graphical representation of the amplitude ratios of W35 and W126 with error bars.

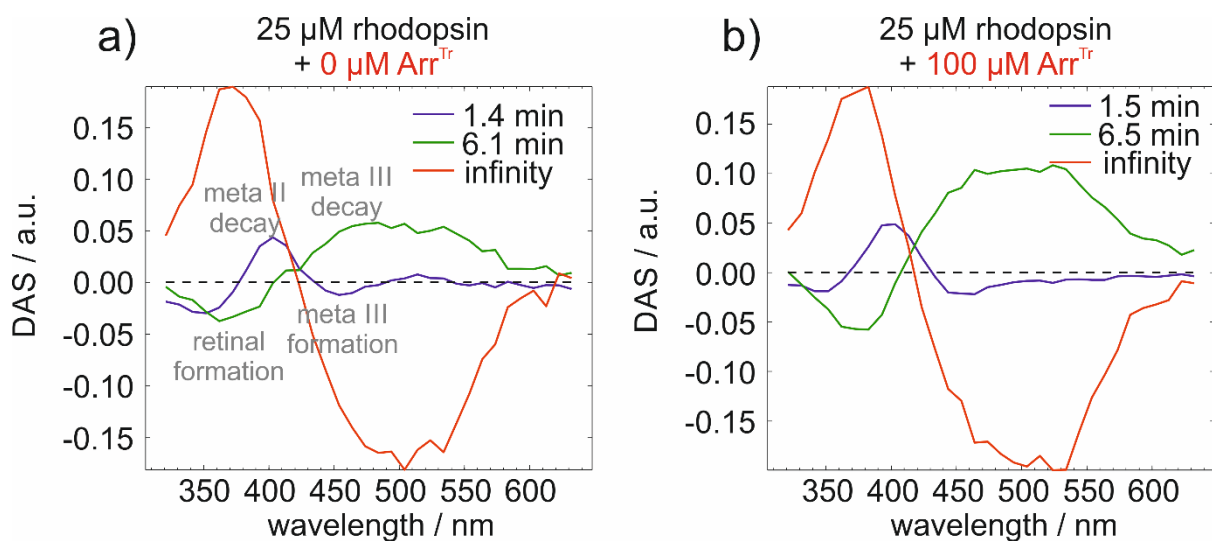


Figure S3: Global lifetime analysis. Decay associated spectra (DAS) from the global lifetime analysis (GLA) of the transient absorption data in the absence (a) and presence (b) of Arr^{Tr}. The GLA provides **one fast lifetime (blue curve; 1-2 min)** corresponding to meta II decay (~400 nm), the free retinal release (~350 nm) and the formation of meta III (~460 nm), **one slower lifetime (green curve; 6-7 min)** corresponding to the decay of meta III (above 450 nm) and the formation of free retinal (370 nm) and **one infinity lifetime (red curve)** corresponding to the change in absorption at the end of the photodynamics. In the presence of Arr^{Tr} the DAS signatures for the formation and decay of meta III (~460 nm) were more pronounced.

Table S1: The lifetimes, the distribution maxima and the amplitudes of the signatures C-F of the LDMs of rhodopsin (25 μM) in absence (-) and presence (10 μM / 50 μM / 100 μM) of Arr^{Tr}.

	lifetime / min				wavelength / nm				amplitude / a.u.			
	0 μM Arr ^{Tr}	10 μM Arr ^{Tr}	50 μM Arr ^{Tr}	100 μM Arr ^{Tr}	0 μM Arr ^{Tr}	10 μM Arr ^{Tr}	50 μM Arr ^{Tr}	100 μM Arr ^{Tr}	0 μM Arr ^{Tr}	10 μM Arr ^{Tr}	50 μM Arr ^{Tr}	100 μM Arr ^{Tr}
C ^[1]	1.3	1.6	1.5	1.5	400	400	400	390	0.003	0.003	0.004	0.004
D ^[2]	1.2	1.0	1.1	1.3	465	465	465	465	-0.001	-0.002	-0.003	-0.004
E ^[3]	5.0	5.0	5.5	5.3	460- 540	460- 540	460- 540	460- 540	0.003	0.006	0.007	0.007
F ^[4]	2.5	2.7	2.7	5.3	365	355	365	375	-0.004	-0.003	-0.004	-0.004

[1] meta II decay [2] meta III formation [3] meta III decay [4] free retinal formation

4 *Structural and Biophysical Characterization of PaMTH1, a putative SAM dependent O-Methyltransferase from filamentous fungi Podospora anserina*

4.1 Aging and Molecular Aging Research

Biological aging is a progressive irreversible process. With aging our body encounters a continuous decline of physiological functions and an increase in disease incidence (morbidity) and mortality of the aging organism ^[245]. The process of aging is unregulated causing accidental damage to the cells for example by reactive oxygen species (ROS) ^[246]. To gain insight into negative effects of aging, study of aging at the molecular level started at a very early stage. Demographic developments have shown a rise in the number of older people in proportion to the number of younger people in the industrialized and developed countries, which in turn facilitated the increased interest in aging research in those countries. One of the primary goals of aging research is to find out the conditions necessary for a healthy aging. Much improvement has been achieved in the context of healthy aging in comparison to earlier times, but there is still more to be optimized. This has been possible only through the reduction of health problems which is also associated with the improvement in the quality of life in old age. A condition for the achievement of these goals is to understand the mechanisms of aging on a molecular level. For the most part due to ethical reasons, the required experimental studies are conducted on model organisms. In many of those model systems, it has been shown that both gene expression and the formation of specific proteins change during aging and the effects of these changes were investigated further. One of the first theories of aging, called the "rate of living" theory ^[247], was proposed by the American researcher, Raymond Pearl in 1928. In this theory, it was assumed that the lifespan of an organism is dependent on the rate of its metabolism and the turnover must be kept as small as possible in order to extend the lifetime. There have been findings which suggest that by biological modulation of certain genes expression, delay in the process of aging can be achieved. This has been successfully shown in the filamentous ascomycete *P. anserina* ^[248,249] and in the nematode *Caenorhabditis elegans* ^[250], both of which have long been used as a model system in aging research. Only in recent years, protein formation and the composition of

the proteins present in an organism at a particular time are investigated by differential proteomics. With the help of this versatile method, senescence specific differences are identified and these results provide new aspects to the study of the process of aging in the respective investigated model system.

4.2 Formation and effects of reactive oxygen species

Reactive oxygen species (ROS) are the critical factors that play an important role in the process of ageing. This is the basis of Free Radical Theory of Aging proposed by Denham Harman in the 1950s ^[246]. Several forms of ROS are constantly generated in organisms growing under aerobic conditions (hyperoxia). The process of ROS generation could be either endogenous during metabolic processes or exogenous due to environmental exposure ^[251]. Several studies have shown that low concentrations of ROS (nitric oxide (NO), superoxide anion ($O_2^{\bullet-}$), hydrogen peroxide (H_2O_2)) facilitate important signaling and biological functions. But an increase in the concentration of the certain ROS (H_2O_2 , hydroxyl radicals (OH^{\bullet}) and $O_2^{\bullet-}$) have been proven detrimental for the cells since it can potentially damage proteins, lipids, carbohydrates and DNA. The cellular damage by ROS results in several pathological occurrences like aging and age-associated diseases including cancer ^[252,253] and constitutes the basis for the free radical (oxidative stress) theory of aging ^[246,251]. The most common ways by which ROS interferes cellular functions include oxidative inactivation of enzymes with sulfhydryl groups, increase in membrane permeability via lipid peroxidation, depolymerization of polysaccharides, or degradation of DNA ^[254,255]. Cells have antioxidant networks which function as scavengers to lower the excessively produced ROS within the system. Thus the oxidative stress experienced by cell depends on the activity of both ROS generating reactions and ROS scavenging system (Figure 4.1) which includes endogenous antioxidant enzymes such as superoxide dismutase (SOD), catalase, glutathione peroxidase (GPx), glutathione (GSH), proteins, and low-molecular-weight scavengers, like uric acid, coenzyme Q, and lipoic acid.

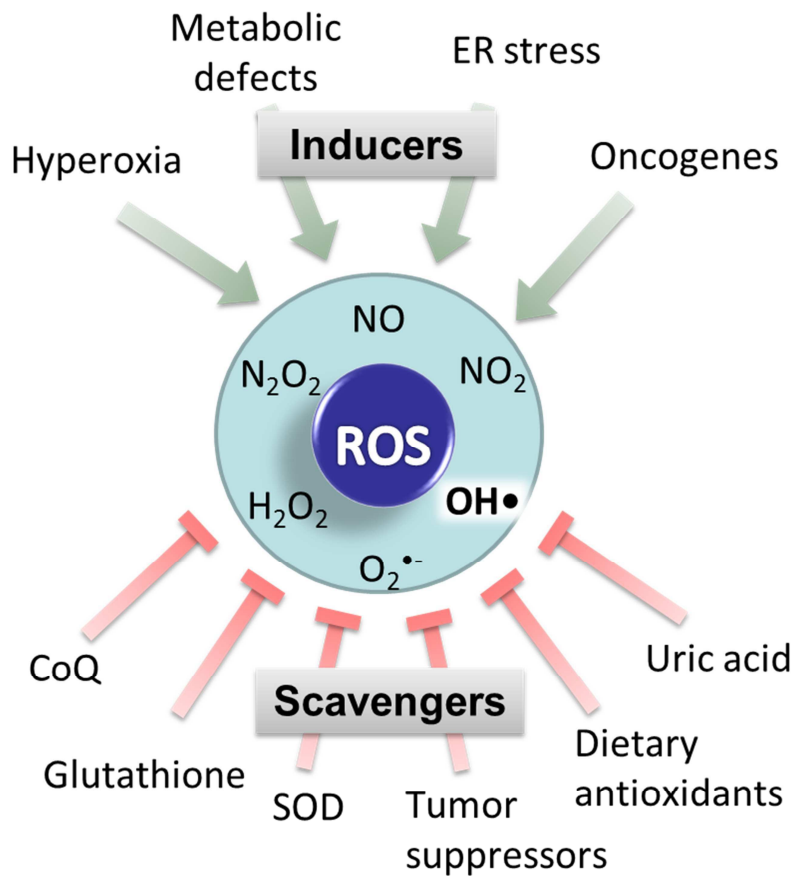


Figure 4.1: The oxidative stress inducers and ROS scavenging system found in cell.

The reactive oxygen species (ROS), include the superoxide anion $O_2^{\bullet-}$ and also the slightly more stable hydrogen peroxide H_2O_2 . Some transition metals, in particular iron and copper catalyze the formation of hydroxyl radical ($\bullet OH$) from superoxide radical or hydrogen peroxide (Haber-Weiss and Fenton's reaction). Among all three ROS, $\bullet OH$ is the most reactive and toxic ^[256]. In next section, the formation of reactive oxygen species and also the interception of these harmful compounds by catechol-containing substances are described.

4.3 ROS formation in the mitochondrial respiratory chain

Approximately 0.4-4% of the consumed oxygen in the cellular mitochondria is converted to ROS ^[257]. These occur mainly at the respiratory chain complexes I and III. The electron transport chain (Figure 4.2) comprises of multiple redox centers in complexes that facilitate transfer of electrons to their final acceptor, molecular oxygen, which is reduced by electrons to water at complex IV. But premature leak of electrons from the redox centers leads to reduction of molecular oxygen to form the superoxide radical ($O_2^{\bullet-}$). Superoxide dismutase-2 in the matrix converts superoxide to H_2O_2 , which can then escape in the surrounding medium. The sites that are involved in mitochondrial superoxide formation include respiratory complexes I and III [5] and [6]. In complex I there are two sites: the flavin in the NADH-oxidizing site (site IF) and the ubiquinone-reducing site (site IQ) [8]. In complex III, the superoxide is thought to arise from the quinol oxidizing site (site IIIQo) [9], [10] and [11]. For example in complex I, during the conversion of ubiquinone to ubiquinol, spontaneous electron leaks from the intermediate semiquinone to oxygen results in the formation of superoxide ($O_2^{\bullet-}$). This superoxide anion is released both in the mitochondrial matrix as well as in the intermembrane space ^[258]. It has been shown that these faulty electron transfer increases during aging ^[259]. This relationship between mitochondrial function and the biological aging was shown in the "mitochondrial theory of aging" (Harman, 1956). The first targets that are damaged by ROS are the membrane-bound complexes of respiratory chain, for example, the iron sulfur center in complex ^[260] by release of an iron atom from the complex. A free iron (II) ion further generates ROS via Fenton reaction ^[254,261]. Besides the described mitochondrial ROS formation other ways of ROS formation also exist in the cell. The formation of ROS under certain conditions can be initiated by catechol-containing compounds.

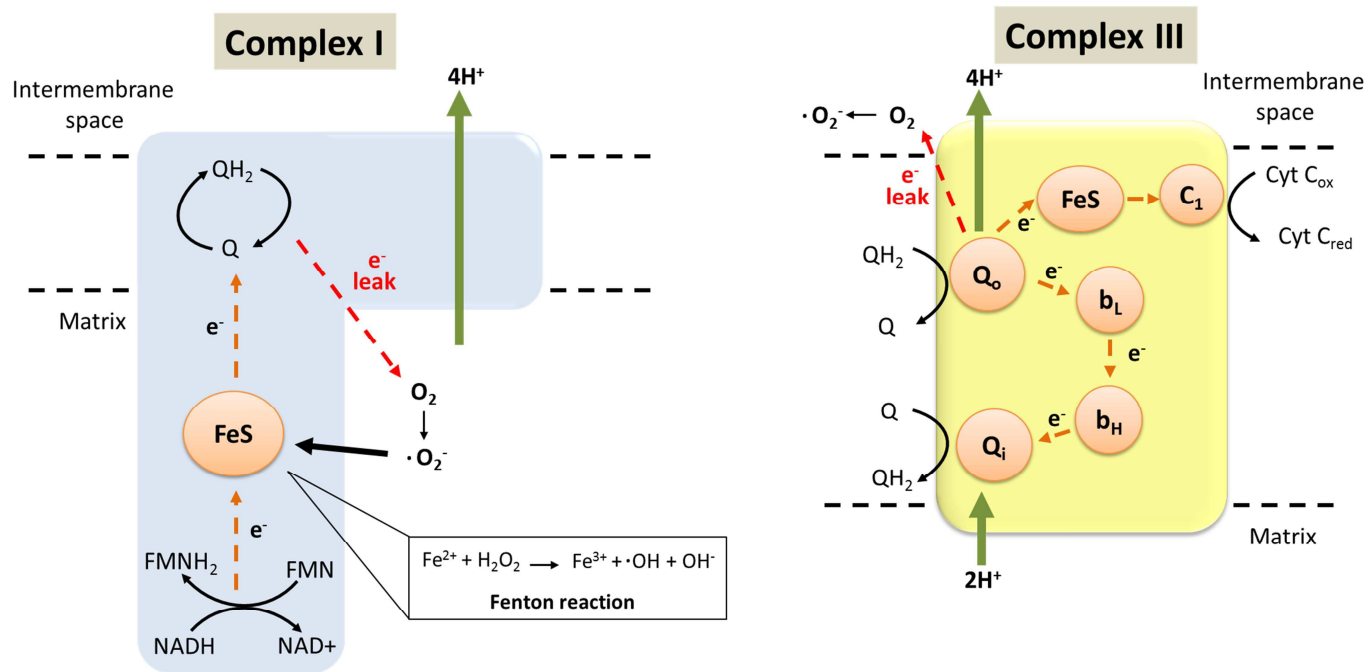


Figure 4.2: Formation of ROS in the respiratory chain complexes I (left) and III (right). The electron flow in the complex is represented by dashed orange arrows. Dashed red arrows indicate the leaky flow of electron leading to the formation of ROS. The membrane potential formed at both complexes by pumping of the protons is shown by green arrows. Superoxide radicals ($\cdot O_2^-$) formed in two complexes by the faulty transmission of single electrons to oxygen molecules are released in the mitochondrial matrix (complex I) and the intermembrane space (complex III). Abbreviations: Ubiquinol (QH₂), ubiquinone (Q), nicotinamide adenine dinucleotide (NAD), flavin (FMN), iron-sulfur center (FeS); external (Q_o) and internal (Q_i) quinone binding site, b types hemes (b_L, b_H), c type heme (C₁), cytochrome (C Cyt C), low and high potential (H). The superoxide formed damages the iron-sulfur centers of complexes (Complex I) is shown here) through Fenton reaction shown in the box. The stoichiometries of the electron are not shown. Adapted from Dröse et al., 2008 ^[258].

4.4 ROS formation by catechol-containing compounds

The catechol derived metabolites are called so, since they contain catechol group, i.e., a benzene ring with two adjacent dihydroxyl moieties (vicinal OH-groups). In biological systems they are formed from certain polyaromatic hydrocarbons substances for example flavonoids.

Flavonoids are natural substances present in our daily diet such as vegetables. In general, they exhibit their beneficial antioxidant properties by inhibiting several enzymes including oxidases, lipases and protein kinases ^[262–266]. One such flavonoid, quercetin functions as a cell-protecting additive by scavenging free radicals such as the superoxide anion radical (see Figure 4.3 A). In addition, quercetin has been shown to chelate metal ions, such as copper and iron and thus inhibiting metal-ion catalyzed radical formation ^[267,268].

However, apart from these beneficial effects, some flavonoids in vitro are known to be mutagenic, due to their prooxidant behavior ^[269]. The same quercetin which shows antioxidant behavior, acts as prooxidative agent ^[270,271], especially in the presence of high concentrations of transition metals such as iron or copper and large superoxide radical masses. Under these conditions, quercetin interacts with superoxide radical (see Figure 4.3 B) and is oxidized to semiquinone or the aroxyl radical. The semiquinone in turn reacts with molecular oxygen ^[270,272] and generates by electron transfer to this oxygen more superoxide radicals (see Figure 4.3 C). The superoxide radicals are further converted by superoxide dismutases to hydrogen peroxide and via Fenton reaction with reduced transition metals to very harmful hydroxyl radicals (see Figure 4.3 D). This leads to enhanced sulfhydryl group oxidation of the enzyme glyceraldehyde 3-phosphate dehydrogenase and its subsequent inactivation. In the absence of metal ions, quercetin becomes protective in function and prevents sulfhydryl oxidation ^[273,274]. Therefore, the presence/absence of metal ions modulates the biological or pharmacological behavior of flavonoids to act as an antioxidant or prooxidant ^[275]. Several studies in model organisms have established substantial correlation between age-related accumulation of metal ions and enhanced formation of ROS ^[276,277].

Several defense mechanisms (enzymes, vitamins, metabolites) in the cells are involved in either preventing the formation of ROS or inactivating them ^[278]. Particularly, in flavonoids, methylation of the vicinal hydroxyl groups and their subsequent conversion to methyl ester prevents their interaction with metals thereby abolishing their prooxidant activity ^[79].

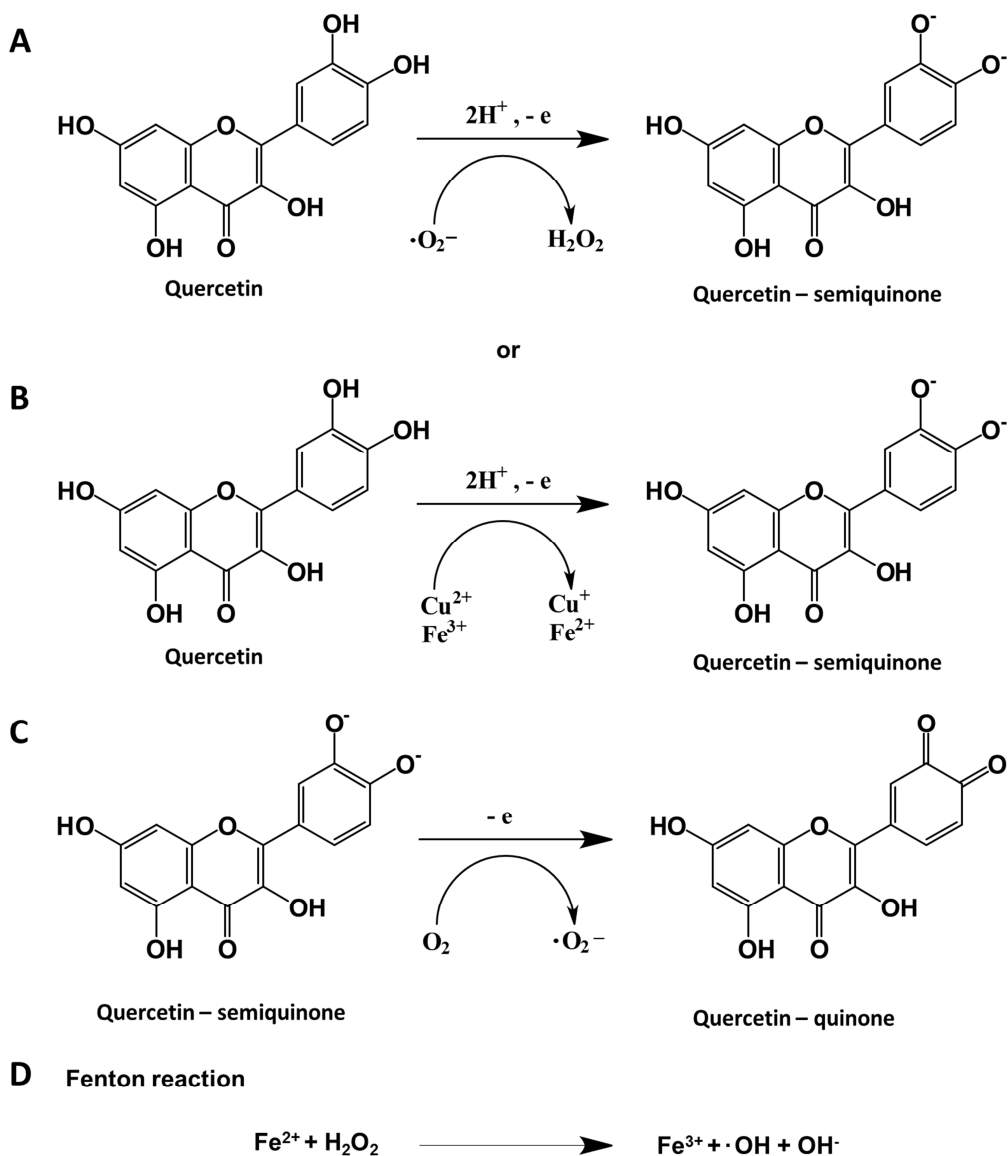


Figure 4.3: Anti- and Pro-oxidant effect of quercetin. (A) Quercetin has two adjacent OH groups that can be easily oxidized to semiquinone by super oxide radical ($\cdot\text{O}_2^-$) in presence of two hydrogens and one electron. (D) Hydrogen peroxide formed in the above reaction in turn produces reactive hydroxyl radical in presence of high concentrations of reduced metal ions by Fenton reaction. (C) The quercetin-semiquinone radical reacts with molecular oxygen in the presence of high concentrations of metal ions to form quinone and superoxide radical. (B) In addition the quercetin is converted to semiquinone in presence of metal ions (Cu^+ and Fe^{2+}). The semiquinones then generate superoxide radical which is further converted to hydrogen peroxide and hydroxyl radicals later. Adapted from Cao et al., 1997 ^[275].

4.5 The filamentous ascomycete *Podospora anserina*

Podospora anserina is a filamentous ascomycetes (sac fungi) belonging to the order Sordariales, within the class Sordariomycetes. It lives as saprovore (substrate-utilizing) on herbivore dung. *P. anserina* cultures consist of a dense network of "tube-like" branched filaments (hyphae), which as a whole is called mycelium. In contrast to other ascomycetes such as the *Neurospora crassa* or the pathogenic fungus *Aspergillus fumigatus*, mycelia of *P. anserina* are characterized by a definite life span^[113]. The wild type 's' strain show senescence phenotype after about 25 days growth in standard medium, with morphological changes such as hyperpigmentation, a reduced formation of aerial mycelium and a growth arrest. This has established this fungus as a model for the study of the mechanisms of aging for decades. The benefits of using *P. anserina* as aging model include ease of cultivation, short generation times, and the possibility of studying each life stage (juvenile, aged and senescence) phenotypically.

The age related research in *P. anserina* focused on the mitochondria and mitochondrial chromosome (note that animals, closely related to fungi, contain similar organelles like mitochondria), since the reactive oxygen species produced during the life span has a deleterious effect on mitochondrial DNA. It has been shown in many studies that aging process in *P. anserina* influences many changes in mitochondrial morphology which includes mitochondrial DNA reorganizations^[279] and mitochondria fragmentation^[280]. It was also shown that there is a change in protein composition in *P. anserina* during senescence. One such senescence specific protein found in *P. anserina* was identified as O-methyltransferases (s. 1. 3. 4).

4.5.1 Proteome analysis in *P. anserina* during aging

In 2000, Osiewicz group in Frankfurt performed proteome analysis of total and mitochondrial extracts from the senescent wild strain of *P. anserina*, which shows a very prominent protein band. Upon sequencing this protein band was identified as a methyltransferase, PaMTH1^[112]. Based on conserved amino acid sequence and motifs, PaMTH1, a 27 kDa protein, is classified as an enzyme belonging to the cation-dependent subclass (class I) of SAM-MTs. PaMTH1 shows a striking sequence similarity with catechol-O-methyltransferase (COMT), an enzyme belonging to the same super family and is involved in the methylation of catechols in both plants and humans. Constitutive overexpression of PaMth1 in *P. anserina* resulted in increased resistance against

exogenous oxidative stress and marked reduction in ROS-induced damage of proteins, thereby prolonging the life span ^[281]. Deletion of PaMth1 resulted in increased sensitization for several stress factors including metals (copper) and hydrogen peroxide ^[282]. All these results suggested that PaMTH1 may play a key role during aging ^[112] and thus our work focus on the biophysical characterization of PaMTH1 for better understanding of their molecular mechanism. But before that the general features in structure and function of the SAM-dependent O-methyltransferases has been extensively discussed in the following section.

4.6 PaMTH1- SAM dependent O-methyltransferases

Methylation of biological compounds in cells is an important mechanism for regulation of various physiological processes such as protein trafficking, signal transduction, biosynthesis, metabolism and gene expression ^[67]. And this methylation reaction is performed by proteins called methyltransferases (MTs), which catalyze transfer of a methyl group from a donor to an acceptor molecule, resulting in the formation of methylated products and a by-product. They utilize a SN2-like nucleophilic substitution reaction for the methylation process. The most common methyl donor in cell is S-adenosyl-L-methionine (SAM), an essential metabolic intermediate. SAM was first discovered in 1951 ^[283]. It is formed by the transfer of methionine on adenosine triphosphate, which is catalyzed by the enzyme methionine-adenosylsynthetase. SAM can be used as a methyl donor, since the methyl group at the sulfur atom of methionine moiety is chemically active. S-adenosyl homocysteine (SAH) is the by-product of methylation and is a potent feedback inhibitor of many SAM dependent methyltransferases (SAM-MTs).

SAM-MTs are ubiquitously present in prokaryotic and eukaryotic organisms and are involved in the methylation of a number of different substrates, which includes RNA, DNA, proteins or secondary metabolites ^[84,93]. As described earlier, depending upon the target SAM-MTs can be grouped into protein MTs, DNA MTs and natural product MTs. Among these natural product MTs are the most diverse group which can be categorized as O, N, C, or S depending upon the methyl accepting atom on the substrates. SAM-dependent O-methyltransferases which is the largest class among natural product methyltransferases mainly perform hydroxyl group methylation (O-methylation) of its substrate. For many of these hydroxyl-modifying SAM-MTs, the catalytic activity is dependent on the presence of divalent metal ions like Mg²⁺ or Ca²⁺. These divalent cations play a key role in structural

stabilization and typically participate directly in substrate binding to certain metal-dependent O-MTs^[84].

4.6.1 Sequence homology of PaMTH1 with other SAM O-MTs

Most of the natural product MTs belong to class I methyl transferase which contain a typical Rossmann fold necessary for SAM binding. The Rossmann-like fold is characterized by an $\alpha\beta\alpha$ sandwich structure consisting of seven β -strands flanked by two layers of α -helices. The C-terminal regions of the β -strands and the adjoining loops form the core of the catalytic site and mediate important interactions with the co-factor SAM and the substrate. The GxGxG motif present at the end of β 3-strand in Rossmann-fold containing SAM-MTs is widely conserved and makes direct contact to the carboxypropyl group of SAM. Another typical feature of the class I methyltransferases is cation dependency for the methyl transfer reaction. Moreover, the class I methyltransferases are rather small in size with molecular weight in the range of 25-30 kDa^[284].

Comparison of the PaMTH1 protein sequence from *P. anserina* with that of other known methyltransferases (Figure 4.4) from plant (caffeoyl-CoA-methyltransferase from *Vitis vinifera* (*V.vinifera* CCoAOMT)), animal (catechol O-methyltransferase from rat and human (*Rattus norvegicus* COMT; *Homo sapiens* COMT)) and bacteria (O-methyl transferase from *Leptospira interrogans* (*L. interrogans* LiOMT)) show significant sequence identity^[112]. The sequence homology indicates the presence of clear methyltransferases specific motifs I-III^[285] in the PaMTH1 sequence. The motif I in O-MTs^[285] is necessary for its interaction with the methyl donor S- Adenosyl-methionine (SAM). The presence of this motif in PaMTH1 clearly shows that it is kind of SAM-dependent methyltransferases enzyme. Sequence comparison also shows that several residues (D144, K147, D172 and N173) which are important for divalent cation binding are highly conserved in PaMTH1. Based on these observations, PaMTH1 can be classified as an enzyme belonging to the cation-dependent subclass (class I) of SAM-MTs.

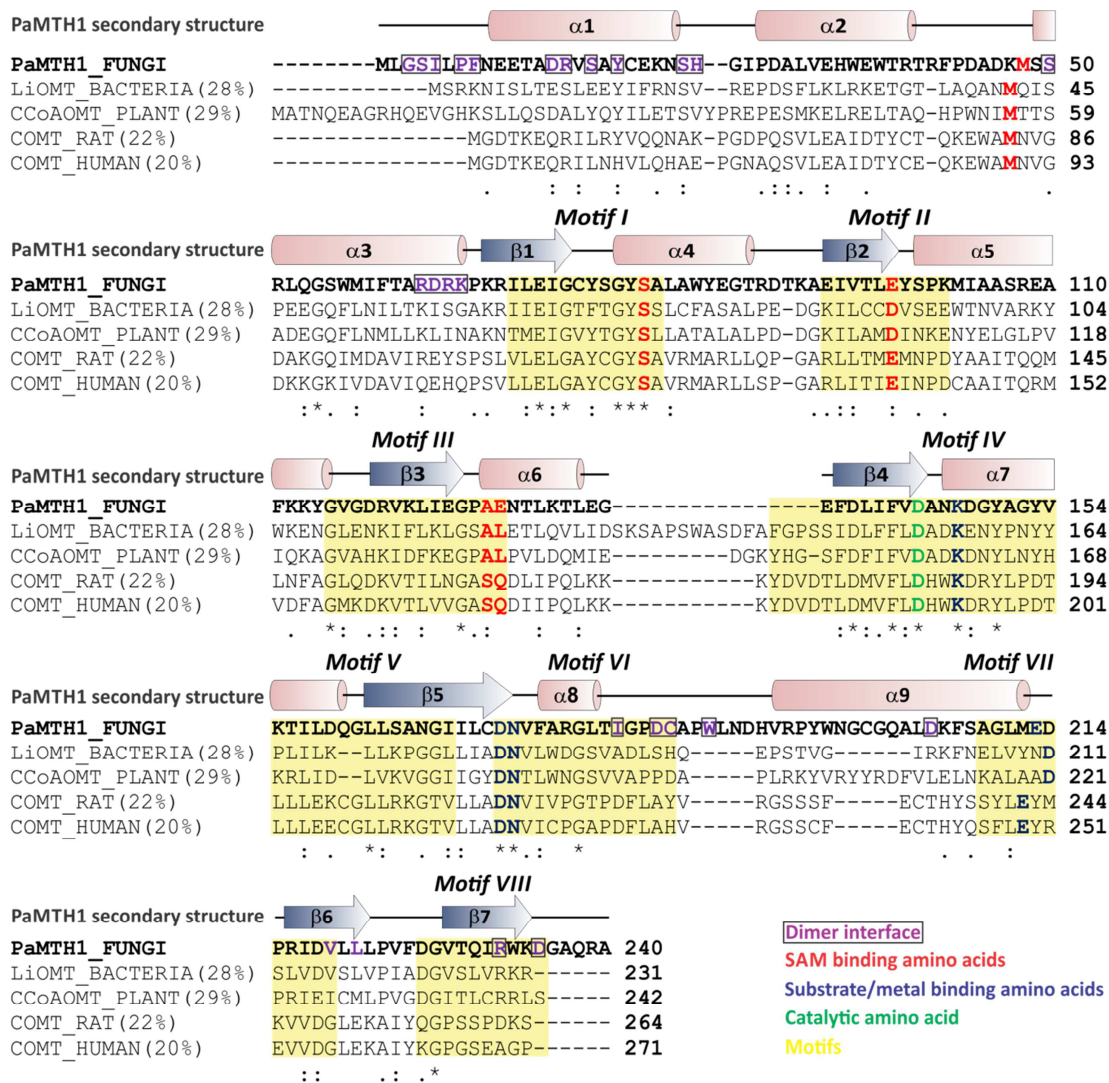


Figure 4.4: Multiple sequence alignment. Sequence alignment of the amino acid sequences of PaMTH1 from *P. anserina*, LiOMT from *L. interrogans*, caffeoyl-CoA-3-O-methyltransferase, CCoAOMT from *V. vinifera*, catechol O-methyltransferase, COMT from *R. norvegicus* and *H. sapiens*. The secondary structure of PaMTH1 is indicated above the sequences and the percent sequence identity of PaMTH1 to other O-MTs is mentioned in parenthesis. The α -helices and β -strands are indicated by cylinders (pink) and arrows (blue), respectively. The analysis was performed by multiple alignment program CLUSTALW. Strictly conserved residues among the 4 proteins are marked by (*), and highly conserved residues are indicated by (:), and (.). The highly conserved motifs (I-VIII) are highlighted in yellow boxes. Amino acids involved in the dimer interface are indicated by violet box, and the ones involved in SAM binding, substrate/metal binding and catalysis are indicated by red, blue and green color respectively.

4.6.2 Structural diversity in SAM O-MTs

The sequence homology comparison between PaMTH1 and other SAM-MTs only provides some basic information about some plausible structural features of PaMTH1, but has given no indication of other properties, such as, dimer formation or substrate specificity which varies significantly within the methyltransferase protein family.

In addition to the core SAM binding fold, additional helices and extensions in the N-terminus of SAM-MTs play a significant role in oligomerization and/or modulate the substrate specificity^[93]. The explicit substrate selectivity in SAM-MTs is achieved through the movement of the loops decorating the conserved SAM-binding site together with the side chain variation in the substrate binding region leading to reconfiguration of the active site surface. In certain bacteria and plants the O-MT subfamily has undergone significant functional and genetic expansion to accommodate a wide variety of substrates. Certain plant MTs, such as caffeic acid O-MT and CCoAOMT show promiscuity in substrate selection, while most other plant O-MTs act on unique substrates. However, in humans only two O-MTs (catechol O-MT and N-acetyl-serotonin O-MT) are found which are involved in neurotransmitter metabolism and melatonin biosynthesis, respectively.

In addition, many SAM-MTs contain an additional N-terminal extension or dimerization domain also important for substrate binding and specificity^[84,93]. Interestingly, in the dimeric structures of two bacterial O-MTs (LiOMT from *L. interrogans*^[286] and SynOMT from cyanobacterium *Synechocystis sp.*^[287]) the amino-terminal loop (first 10-13 residues) plays an important role either in dimerization or catalysis (Figure 4.5). The amino-terminal loop in LiOMT is domain-swapped and involved in dimerization, although the functional significance is not known. However, in case of SynOMT, although the loop is not involved in dimerization it inserts into the monomer catalytic pocket and plays a critical role in catalysis. All these observations indicate that although the overall fold of the protein is conserved, the divergence between bacterial, plant and animal MTs results in altered oligomerization states, different substrate recognition modes or even leading to altered catalytic mechanism of methyl transfer.

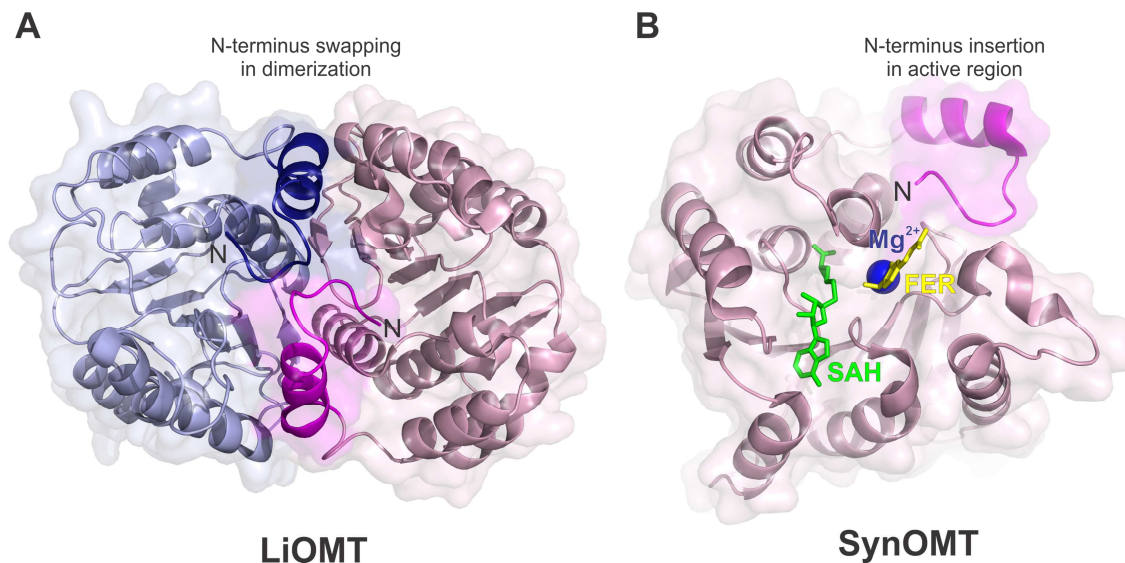


Figure 4.5: Role of amino-terminal region in O-MTs. A. N-terminus of LiOMT from *Leptosira interrogans* stabilized dimer through domain swapping. B. N-terminus of SynOMT from cyanobacterium *Synechocystis* sp. involved in catalytic activity by inserting into the active region.

4.7 Motivation

The unavailability of structural insights for apo PaMTH1 and holo PaMTH1 bound to co-factor (SAM) and the substrate hinders a complete description of the binding pocket involved in its catalysis. Thus the primary focus of this work is to gather information about the molecular architecture of apo and holo state of PaMTH1. Moreover, activity and biochemical analysis revealed specificity of this protein for flavonoids containing vicinal hydroxyl groups in general and myricetin in particular. In spite of having knowledge about the putative substrate of PaMTH1, the biophysical basis it's methyl transfer reaction still remains unknown. The structures (apo- and holoenzyme) of PaMTH1 and biophysical characterization of its interaction with putative substrates will facilitate future studies involving the identification of endogenous polyphenolic compounds directly involved in metal-induced oxidative stress.

4.8 Research article 3

Structure and Biophysical Characterization of the S-Adenosylmethionine-dependent O-Methyltransferase PaMTH1, a Putative Enzyme Accumulating during Senescence of *Podospora anserina*.

Chatterjee D, Kudlinzki D, Linhard V, Saxena K, Schieborr U, Gande SL, Wurm JP, Wöhnert J, Abele R, Rogov VV, Dötsch V, Osiewacz HD, Sreeramulu S, Schwalbe H. *The Journal of Biological Chemistry*, **2015**, 290, 16415-16430.

In this article, we elucidated the crystal structures of apo and holo states (SAM and SAH bound) of PaMTH1. Our result shows that PaMTH1 adopts the Rossmann fold typical for many SAM-binding methyltransferases and forms a tight dimer through N-terminal swapping. Structural comparisons of PaMTH1 with other O-methyltransferases, reveals similarity in SAM or SAH binding pocket but differences in the substrate binding region. This indicates specific structural features required for substrate selection. Moreover, we investigated the catalytic mechanism of PaMTH1 which transfer a methyl group from SAM to one hydroxyl group of the myricetin by different biophysical and biochemical method such as NMR, mass spectrometry, and site-directed active site mutagenesis.

The SEC-MALS experiment was performed by PD Dr. R. Abele (Goethe University, Frankfurt). The crystal structure was determined by Dr. D. Kudlinzki and analyzed by author of this thesis along with Dr. S. Sreeramulu. The author has performed all molecular biology work and NMR analysis. The isothermal titration calorimetry experiments were also performed by the author under the supervision of Dr. V.V. Rogov in the group of Prof. Doetsch (Goethe University, Frankfurt). The author has also contributed in all the aspects of writing the manuscript.

Structure and Biophysical Characterization of the S-Adenosylmethionine-dependent O-Methyltransferase PaMTH1, a Putative Enzyme Accumulating during Senescence of *Podospira anserina**

Received for publication, April 22, 2015, and in revised form, May 14, 2015. Published, JBC Papers in Press, May 15, 2015, DOI 10.1074/jbc.M115.660829

Deep Chatterjee^{‡§§}, Denis Kudlinzki^{‡§§}, Verena Linhard^{‡§§}, Krishna Saxena^{‡§§}, Ulrich Schieborr^{‡§§}, Santosh L. Gande^{‡§§}, Jan Philip Wurm^{||§§}, Jens Wöhnert^{||§§}, Rupert Abele^{**}, Vladimir V. Rogov^{††}, Volker Dötsch^{††1}, Heinz D. Osiewacz^{||1}, Sridhar Sreeramulu^{+§§2}, and Harald Schwalbe^{+§§1,3}

From the [‡]Institute for Organic Chemistry and Chemical Biology, ^{§§}Center for Biomolecular Magnetic Resonance (BMRZ), Johann Wolfgang Goethe University, Max-von-Laue-Strasse 7, D-60438 Frankfurt am Main, Germany, the ^{||}Institute for Molecular Biosciences, ^{**}Institute of Biochemistry, Biocenter, and ^{††}Institute of Biophysical Chemistry and Center for Biomolecular Magnetic Resonance (BMRZ), Johann Wolfgang Goethe University, Max-von-Laue-Strasse 9, D-60438 Frankfurt am Main, Germany, the [§]German Cancer Consortium (DKTK), Heidelberg D-69210, Germany, and the [†]German Cancer Research Center (DKFZ), Heidelberg D-69210, Germany

Background: PaMTH1, a putative O-methyltransferase protects *Podospira anserina* from oxidative stress during senescence and acts as a longevity assurance factor.

Results: Crystal structures of PaMTH1/PaMTH1-SAM/SAH co-complexes and NMR-based characterization of enzymatic methylation of its substrate were obtained.

Conclusion: PaMTH1 catalyzes methyl group transfer from the co-factor to the substrate in a cation-dependent manner.

Significance: This work facilitates the identification of endogenous polyphenolic compounds directly involved in metal-induced oxidative stress.

Low levels of reactive oxygen species (ROS) act as important signaling molecules, but in excess they can damage biomolecules. ROS regulation is therefore of key importance. Several polyphenols in general and flavonoids in particular have the potential to generate hydroxyl radicals, the most hazardous among all ROS. However, the generation of a hydroxyl radical and subsequent ROS formation can be prevented by methylation of the hydroxyl group of the flavonoids. O-Methylation is performed by O-methyltransferases, members of the S-adenosyl-L-methionine (SAM)-dependent O-methyltransferase superfamily involved in the secondary metabolism of many species across all kingdoms. In the filamentous fungus *Podospira anserina*, a well established aging model, the O-methyltransferase (PaMTH1) was reported to accumulate in total and mitochondrial protein extracts during aging. *In vitro* functional studies revealed fla-

vonoids and in particular myricetin as its potential substrate. The molecular architecture of PaMTH1 and the mechanism of the methyl transfer reaction remain unknown. Here, we report the crystal structures of PaMTH1 apoenzyme, PaMTH1-SAM (co-factor), and PaMTH1-S-adenosyl homocysteine (by-product) co-complexes refined to 2.0, 1.9, and 1.9 Å, respectively. PaMTH1 forms a tight dimer through swapping of the N-termini. Each monomer adopts the Rossmann fold typical for many SAM-binding methyltransferases. Structural comparisons between different O-methyltransferases reveal a strikingly similar co-factor binding pocket but differences in the substrate binding pocket, indicating specific molecular determinants required for substrate selection. Furthermore, using NMR, mass spectrometry, and site-directed active site mutagenesis, we show that PaMTH1 catalyzes the transfer of the methyl group from SAM to one hydroxyl group of the myricetin in a cation-dependent manner.

Organisms growing under aerobic conditions are constantly exposed to several forms of reactive oxygen species (ROS)⁴ gen-

* This work was supported by the Deutsche Forschungsgemeinschaft (DFG) in Collaborative Research Center 807 and by the Cluster of Excellence: Macromolecular Complexes (Deutsche Forschungsgemeinschaft). The center for Biomolecular magnetic resonance (BMRZ) is supported by the state of Hesse. The authors declare that they have no conflicts of interest with the contents of this article.

The atomic coordinates and structure factors (codes 4QVK, 4YMG, and 4YMH) have been deposited in the Protein Data Bank (<http://www.pdb.org/>).

¹ Member of the DFG-funded Cluster of Excellence: Macromolecular Complexes.

² To whom correspondence may be addressed: Johann Wolfgang Goethe University, Frankfurt am Main, Institute for Organic Chemistry and Chemical Biology, Centre for Biomolecular Magnetic Resonance (BMRZ), Max-von-Laue-Strasse 7, D-60438 Frankfurt am Main, Germany. Tel.: 49-69-79829933; E-mail: sridhar@nmr.uni-frankfurt.de.

³ To whom correspondence may be addressed: Johann Wolfgang Goethe University, Frankfurt am Main, Institute for Organic Chemistry and Chemical Biology, Centre for Biomolecular Magnetic Resonance (BMRZ), Max-von-Laue-Strasse 7, D-60438 Frankfurt am Main, Germany. Tel.: 49-69-79829737; Fax: 49-69-79829515; E-mail: schwalbe@nmr.uni-frankfurt.de.

⁴ The abbreviations used are: ROS, reactive oxygen species; SAM, S-adenosyl-L-methionine; SAH, S-adenosyl homocysteine; PaMTH1, *P. anserina* O-methyltransferase; MT, methyltransferase; SAM-MT, SAM-dependent methyltransferase; COMT, catechol-O-methyltransferase; CCoAOMT, coffeoyl-CoA-O-methyltransferase; LiOMT, *L. interrogans* O-methyltransferase; SEC, size exclusion chromatography; MALS, multiangle laser light scattering; TSP-*d*₃, 3-(trimethylsilyl)-2,2',3,3'-tetra-deuteriopropionic acid; HSQC, heteronuclear spin quantum correlation; CSP, chemical shift perturbation; RMSD, root mean square deviation; TCEP, tris(2-carboxyethyl)phosphine; BisTris, 2-[bis(2-hydroxyethyl)amino]-2-(hydroxymethyl)propane-1,3-diol; MAD, multiple-wavelength anomalous dispersion.

Structure and Biophysical Characterization of PaMTH1

erated either endogenously during metabolic processes or exogenously due to environmental exposure (1). Accumulation of ROS can potentially damage proteins, lipids, carbohydrates, and DNA, resulting in several pathological occurrences like aging and age-associated diseases, including cancer (2, 3). ROS interfere with cellular functions by either inactivating enzymes with sulfhydryl groups via oxidation, lipid peroxidation, and subsequent increase in membrane permeability; depolymerization of polysaccharides; or degradation of DNA (4, 5). Although low concentrations of ROS (nitric oxide (NO), superoxide anion (O_2^-), and hydrogen peroxide (H_2O_2)) facilitate important signaling and biological functions, high concentrations of H_2O_2 , hydroxyl radicals (OH^\cdot), and O_2^- can be damaging to biologically significant targets and constitute the basis for the free radical (oxidative stress) theory of aging (1, 6). Among all three ROS, the hydroxyl radical is the most reactive and toxic, and no detoxification system exists for it (7).

Some transition metals, in particular iron and copper, catalyze the formation of hydroxyl radicals from superoxide radicals or hydrogen peroxide (Haber-Weiss and Fenton's reaction) (4). Apart from generating ROS via the above reaction, metals like iron and copper are also known to interact with naturally occurring antioxidants like polyphenolic compounds (flavonoids) or vitamin C, thereby transforming an antioxidant into a prooxidant (8). Flavonoids, a frequent component of the human diet, in general exhibit their beneficial antioxidant properties by inhibiting several enzymes, including oxidases, lipases, and protein kinases (9–13). However, apart from these beneficial effects, some flavonoids *in vitro* are known to be mutagenic, due to their prooxidant behavior (14). For example, quercetin, a plant flavonoid, in the presence of ferrous ions generates hydroxyl radicals and leads to enhanced sulfhydryl group oxidation of the enzyme glyceraldehyde 3-phosphate dehydrogenase and its subsequent inactivation. In the absence of metal ions, quercetin becomes protective in function and prevents sulfhydryl oxidation (15, 16). Therefore, the presence/absence of metal ions modulates the biological or pharmacological behavior of flavonoids to act as an antioxidant or prooxidant (17). Several studies in model organisms have established substantial correlation between age-related accumulation of metal ions and enhanced formation of ROS (18, 19). Most of the polyphenols, including flavonoids, react with metals via their vicinal dihydroxyl system and lead to generation of ROS (20).

Several defense mechanisms (enzymes, vitamins, and metabolites) in the cells are involved in either preventing the formation of ROS or inactivating them (21). Particularly, in flavonoids, methylation of the vicinal hydroxyl groups and their subsequent conversion to methyl ethers prevent their interaction with metals, thereby abolishing their prooxidant activity (22). Methylation of biological compounds is also an integral part of various cellular processes, such as protein trafficking, signal transduction, biosynthesis, metabolism, and gene expression (23). Methyltransferases (MTs), via an S_N2 -like nucleophilic substitution reaction mechanism, catalyze the transfer of a methyl group from a donor to an acceptor molecule, resulting in the formation of methylated products and a by-product. Most often, methylation is catalyzed by *S*-adenosyl-*L*-methio-

nine (SAM)-dependent methyltransferases. SAM-dependent methyltransferases (SAM-MTs) are ubiquitously present throughout prokaryotic and eukaryotic organisms and are responsible for methylation of structurally distinct biological and natural product substrates (24, 25). SAM, an essential metabolic intermediate in several organisms, functions classically as the electron-deficient methyl donor. *S*-Adenosyl homocysteine (SAH) is the by-product of methylation and is a potent feedback inhibitor of many SAM-MTs. Depending on the methyl-accepting atom on the substrates, MTs are categorized as *O*, *N*, *C*, or *S*. Hydroxyl group methylation (*O*-methylation) is performed by SAM-dependent *O*-methyltransferases.

Structurally, many SAM-MTs adopt a Rossmann-like fold with an α/β domain, a characteristic requirement for binding of nucleotide-containing co-factors. The Rossmann-like fold is characterized by an $\alpha\beta\alpha$ sandwich structure consisting of seven β -strands flanked by two layers of α -helices. The C-terminal regions of the β -strands and the adjoining loops form the core of the catalytic site and mediate important interactions with the co-factor SAM and the substrate. The GXGXG motif present at the end of the β_1 -strand in Rossmann fold-containing SAM-MTs is widely conserved and makes direct contact with the carboxypropyl group of SAM. In addition to the core fold, additional helices and extensions in the N terminus play a significant role in oligomerization and/or modulate the substrate specificity (25). For many hydroxyl-modifying SAM-MTs, the catalytic activity is dependent on the presence of divalent metal ions like Mg^{2+} or Ca^{2+} . These divalent cations play a key role in structural stabilization and typically participate directly in substrate binding to certain metal-dependent *O*-MTs (24).

For more than 5 decades, *Podospora anserina*, a filamentous ascomycete, has been a well studied and well established aging model (26). Interestingly, during senescence, an *O*-MT, PaMTH1, was reported to accumulate in total and mitochondrial extracts. This result suggested that PaMTH1 plays a key role during aging (27). Subsequent sequence analysis of PaMTH1 revealed significant homology to SAM-MTs. It was hypothesized that PaMTH1 has a protective function against oxidative stress. Activity and biochemical analysis revealed specificity of this protein for flavonoids containing vicinal hydroxyl groups in general and myricetin in particular (28), which in the presence of metals can generate ROS. Constitutive overexpression of *PaMth1* in *P. anserina* resulted in increased resistance against exogenous oxidative stress and marked reduction in ROS-induced damage of proteins, thereby prolonging the life span (28). Deletion of *PaMth1* resulted in increased sensitization for several stress factors, including metals (copper) and hydrogen peroxide (29).

PaMTH1, a 27-kDa protein, based on conserved amino acid sequence motifs, is classified as an enzyme belonging to the cation-dependent subclass (class I) of SAM-MTs. PaMTH1 shows a striking sequence similarity with catechol-*O*-methyltransferase (COMT), an enzyme belonging to the same superfamily, and is involved in the methylation of catechols in both plants and humans. However, the molecular architecture of PaMTH1 and the biophysical basis for the methyl transfer reaction remain unknown.

Structure and Biophysical Characterization of PaMTH1

Here, we present crystal structures of the PaMTH1 apo-enzyme, a PaMTH1-SAM (co-factor) co-complex, and a PaMTH1-SAH (by-product) co-complex refined to 2.0, 1.9, and 1.9 Å, respectively. The enzyme is a highly stable dimer both in solution and in the crystal due to swapping of the N termini. Structural analysis of the apo- and holoenzyme reveals an overall architecture similar to SAM-MTs but shows significant differences in the substrate binding region. The α 2- α 3 loop, involved in substrate binding, adopts a “closed” conformation in the presence of SAM/SAH, as observed in other SAM/SAH-bound structures, and an “open” conformation in the apo-enzyme. In addition, using sequence and structural homology, residues important for substrate binding were predicted and probed using site-directed mutagenesis. Based on NMR chemical shift perturbations, we show that SAM and the substrate (myricetin) bind to PaMTH1 and catalyze the methyl group transfer from SAM to one hydroxyl group of myricetin in a cation-dependent manner. Furthermore, by using mass spectrometry, we confirmed the conversion of myricetin to monomethylated myricetin.

Experimental Procedures

Protein Expression and Purification—The *PaMth1* gene was cloned into the expression vector pETTEV-16b and transformed in *Escherichia coli* BL21 (DE3) cells (Invitrogen) for overexpression of the fusion protein with an N-terminal His₇ tag. Transformed *E. coli* cells were grown at 37 °C in autoinduction medium ZYM-5052 (30) containing 100 μ g/ml ampicillin to an A_{600} of \sim 0.6, and then the temperature was reduced to 20 °C to support soluble protein expression. After 48–60 h of cell growth (due to the long induction time, hydrolysis of the antibiotic can occur, so ampicillin was replenished every 24 h), bacteria were harvested by centrifugation (20 min, 4000 rpm) and resuspended in lysis buffer (20 mM Tris-HCl, pH 8.0, 200 mM NaCl, 10 mM β -mercaptoethanol) with the addition of complete protease inhibitor (1 tablet/100 ml of EDTA-free; Roche Applied Science). Selenomethionine-derivatized protein was expressed according to standard EMBL protocols (see the EMBL Web site). The cells were lysed using microfluidizer (15,000 p.s.i., 2 cycles), and the cell debris was separated by centrifugation (30 min, 16,000 rpm). The supernatant was filtered and passed through a 5-ml nickel-nitrilotriacetic acid column (GE Healthcare), washed with 10 bed volumes of wash buffer (same as lysis buffer), and the His-tagged protein was eluted using an isocratic gradient (0–100%) of wash buffer and elution buffer (20 mM Tris-HCl, pH 8.0, 200 mM NaCl, 500 mM imidazole, 15 mM β -mercaptoethanol) for 8 column volumes. The eluted fractions were analyzed by SDS-PAGE, and the ones containing PaMTH1 were pooled, incubated with tobacco etch virus protease to remove the N-terminal His tag (1 mg of tobacco etch virus protease (in-house produced) per 10 mg of PaMTH1) and dialyzed for 24 h at 4 °C against 25 mM Tris, pH 8.0, 100 mM NaCl, 15 mM β -mercaptoethanol, and 5% glycerol. The cleaved protein was reloaded onto a nickel-nitrilotriacetic acid column for removal of the tag and the tobacco etch virus protease. Further purification of protein was achieved by gel filtration chromatography on a Superdex-200 column (GE Healthcare) equilibrated with 25 mM HEPES, pH 7.5, 100 mM

NaCl, and 1 mM DTT. Fractions containing the target protein were pooled and concentrated up to \sim 5 mg/ml and stored at -80 °C or immediately used for experiments. ¹⁵N-Labeled protein was expressed in M9 minimal medium containing ¹⁵NH₄Cl (1 g/liter) as the sole nitrogen source.

Mutagenesis—Site-directed mutagenesis was used to introduce the catalytic mutations (K147A, D144A/K147A, D172A/N173A) and N-terminal swapping region mutation (S4A/P7A) into the wild-type PaMTH1 plasmids following the protocol mentioned in QuikChange kit (Stratagene). Mutations were confirmed by sequencing (Eurofins Genomics). N-terminal swapping region deletion was achieved through PCR amplification of wild-type plasmid using 5'-gtgtgcatatggagacggcggacc-3' (forward) and 5'-gtgtgtagatcttcaagccgctgag-3' (reverse) primers and cloning of the restriction-digested PCR products in pETTEV-16b vector. All of the mutant proteins were purified following the same protocol as the wild-type PaMTH1. Circular dichroism and ¹H,¹⁵N HSQC (heteronuclear spin quantum correlation) spectra for the wild type and the mutants are mostly similar, indicating that there are no significant changes in the secondary structure due to mutation. Further, size exclusion chromatography (SEC) analysis of the mutants showed no change in their respective oligomeric state due to mutation (data not shown).

SEC Coupled with Multiangle Laser Light Scattering (SEC-MALS)—SEC-MALS was performed using a TSK-GEL G3000SWXL column (15 ml; Tosoh Bioscience, Stuttgart, Germany); a light scattering detector (TREOS) and refractometer (Optilab rEX) from Wyatt Technology (Dernbach, Germany); and a UV detector, HPLC pump, and degasser from Jasco (Gross-Umstadt, Germany). The system was equilibrated with 2 column volumes of SEC buffer (50 mM Tris, 150 mM NaCl, pH 6.9, filtered through 0.1- μ m pore size VVLP filters (Merck Millipore, Darmstadt, Germany)) following a recirculation through the system for at least 1 day at 0.5 ml/min to improve the baseline drastically by removing air bubbles and particles by the degasser and preinjection filter (0.1 μ m). Per measurement, 200–300 μ g of protein in 200 μ l of SEC buffer were injected and analyzed at a flow rate of 0.5 ml/min at 4 °C. The light scattering detector was calibrated every day by using monomeric BSA and carboanhydrase. The obtained signals were processed with the ASTRA software package version 5.3.4.13 (Wyatt Technology) to calculate the molecular mass using the UV signal for concentration determination. A refractive index increment dn/dc of 0.185 ml/g and an extinction coefficient ϵ_{280} of 51,910 liters/(cm mol) was assumed.

Isothermal Titration Calorimetry—All titration experiments were performed at 25 °C using a VP-ITC microcalorimeter (MicroCal Inc.). All titrations were performed using buffer containing 25 mM Tris, pH 7.5, 100 mM NaCl, 0.5 mM TCEP. SAM at a concentration of 940 μ M was titrated into 36 μ M PaMTH1 protein solution in 26 steps; SAH (930 μ M) was titrated into 34 μ M PaMTH1 protein in 21 steps. In the presence of 10 mM MgCl₂, the concentrations of compounds and protein were reduced in order to avoid regularly present aggregation of the protein/complex (300 μ M SAM into 19 μ M PaMTH1 in 26 steps; 220 μ M SAH into 22 μ M PaMTH1 in 31 steps).

Structure and Biophysical Characterization of PaMTH1

The protein concentrations were calculated from the UV absorption at 280 nm with a Nanodrop spectrophotometer (Thermo Fisher Scientific) using the extinction coefficient obtained from the amino acid sequence (51,910 liters/(cm mol)). Concentrations of compounds were obtained similarly using the known extinction coefficient (ϵ_{260} of 15,400 liters/(cm mol) for both SAM and SAH). The raw ITC data were analyzed with the ITC-Origin version 7.0 software with a “one-site” binding model after correction for the dilution heat of the compounds.

Protein Crystallization and Structure Determination—The purified native and selenomethionine PaMTH1 protein was concentrated up to 5 mg/ml in a buffer containing 20 mM Tris (pH 8.0), 200 mM NaCl, 10 mM DTT and crystallized at 277 K by hanging drop vapor diffusion against a reservoir containing 100 mM BisTris (pH 7.0), 200 mM NaCl, 20% (w/v) PEG 3350, and 20 mM spermine tetrahydrochloride. Crystals were transferred to mother liquor with 30% PEG 400 for flash freezing. For co-crystallization experiments, the following conditions were used: PaMTH1-SAM (6 mg/ml PaMTH1 + 1.1 mM MgCl₂ + 0.22 mM SAM in 0.2 M lithium sulfate, 100 mM BisTris, pH 6.0, 25% (w/v) PEG 3350; 4 °C; sitting drop; reservoir, 300 μ l; drop size, 1 μ l + 1 μ l; cryoprotectant: 30% PEG 400 + 70% mother liquor + 10 mM SAM) and PaMTH1-SAH (3 mg/ml PaMTH1 + 0.55 mM MgCl₂ + 0.11 mM SAH in 0.1 M lithium sulfate, 100 mM BisTris, pH 5.5, 25% (w/v) PEG 3350; 4 °C; sitting drop; reservoir, 300 μ l; drop size, 1 μ l + 1 μ l; cryoprotectant: 30% PEG 400 + 70% mother liquor + 10 mM SAH). Diffraction data were collected on BL14.2 operated by the Joint Berlin MX-Laboratory at the BESSY II electron storage ring (Berlin-Adlershof, Germany) (31). All data were processed using XDSAPP (32) or autoPROC (33). Structure determination by molecular replacement failed, so the data were phased using experimental selenium multiple-wavelength anomalous dispersion (Se-MAD) (34). An x-ray fluorescence scan of selenium-labeled PaMTH1 crystals was performed to determine optimal wavelengths for anomalous scattering (f' , f''). Consecutively, 2.5 Å data of four different wavelengths (peak, 0.97989 Å; inflection point, 0.98004 Å; high remote, 0.97626 Å; low remote, 0.98401 Å) of an identical rotation range of each selenomethionine crystal were measured. Nine of 10 expected selenium atom positions were determined using PHENIX AutoSol (35, 36). PHENIX AutoBuild (37) was used for initial model building, structure refinement, and density modification. The space group is P212121 with $a = 73.38$ Å, $b = 79.72$ Å, $c = 84.39$ Å and two molecules in the asymmetric unit. The initial model was replaced against non-anomalous data of 1.97 Å resolution. The structures of the PaMTH1-SAM/SAH co-complexes were solved by molecular replacement, and their crystallographic data and refinement statistics are listed in Table 1. Further model building was performed using Coot (38), and iterative refinement was done with PHENIX Refine (39). Stereochemical analysis of the refined models using PROCHECK of the CCP4 package (40) revealed main-chain and side-chain parameters better than or within the typical range of values for protein structures determined at corresponding resolutions. The models were deposited in the RCSB Protein Data Bank (41) under

codes 4QVK (PaMTH1), 4YMG (PaMTH1-SAM), and 4YMH (PaMTH1-SAH).

NMR Spectroscopy—NMR experiments were performed at $T = 298$ K on Bruker 600-, and 800-MHz spectrometers equipped with room temperature TXI-HCN probes. NMR samples were prepared with 10% D₂O to lock the spectrometers, and 3-(trimethylsilyl)-2,2',3,3'-tetradeuteropropionic acid (TSP- d_4 ; 1 mM) was used as an internal standard for spectral referencing. The processing and analysis of NMR spectra were done in Topspin version 2.1 (Bruker Biospin).

All ligands, including co-factor (SAM), by-product (SAH), and putative substrates (apigenin, kaempferol, pyrocatechol, and myricetin) were purchased from Sigma-Aldrich and used without further purifications. The solubility of ligands (in H₂O and buffer 25 mM Tris, pH 7.5, 100 mM NaCl, 5 mM TCEP) were determined by a one-dimensional ¹H NMR experiment (Bruker, 600 MHz) using peak integrals of ¹H peaks of the ligands, which were normalized against the calibrated peak of 1 mM TSP at 0 ppm. The assignments of one-dimensional ¹H peaks corresponding to SAM (BMRB ID: bmse000059), SAH (BMRB ID: bmse000289), and pyrocatechol (BMRB ID: bmse000385) were obtained from the Biological Magnetic Resonance Bank (BMRB) metabolomics database, and the assignment for myricetin (HMDB ID: HMDB02755) was obtained from the Human Metabolomics Data Base (HMDB).

PaMTH1-ligand interactions were studied by recording two-dimensional ¹H,¹⁵N HSQC (42) (Bruker, 800 MHz) of PaMTH1 (500 μ M ¹⁵N-labeled PaMTH1 in 25 mM Tris, pH 6.5, 100 mM NaCl, 5 mM TCEP) in the presence or absence of the ligands. The ligands were added to the protein in 2-fold excess (2:1).

NMR titration experiments were performed by adding increasing amounts of ligand (0.125, 0.25, 0.375, 0.5, 1, and 2 mM SAM, 0.0625, 0.125, 0.25, 0.5, and 1 mM SAH) to 480 μ M ¹⁵N-PaMTH1 at pH 6.5 and acquiring a series of two-dimensional ¹H,¹⁵N HSQC spectra at 298 K. Chemical shift perturbations (CSPs) from NMR titrations were quantified using the following equation (43).

$$\Delta = \sqrt{(\delta H)^2 + 0.17 \times (\delta N)^2} \quad (\text{Eq. 1})$$

The affinity for each titration was determined by a simultaneous fit of the titration parameters to the observed CSPs. The affinity of the titrated ligand and the chemical shifts in the complex structure were used as fitting parameters. A single step binding mechanism in the fast or intermediate exchange regime was presumed. The differential equations were solved numerically to determine the equilibrium concentrations, presuming a given affinity. No statistical evidence for more complicated binding mechanisms could be found.

The enzymatic reaction of PaMTH1 (wild type and mutants) was monitored by recording a series of one-dimensional ¹H NMR experiments (Bruker 600 MHz) of the reaction mixture containing 100 μ M PaMTH1, 1 mM SAM (unlabeled), and 1 mM myricetin (1:10:10) in deuterated Tris buffer containing MgCl₂ (25 mM *d*-Tris, pH 7.5, 100 mM NaCl, 1 mM MgCl₂, 5 mM TCEP). The methoxy peak of the product was identified by measuring one-dimensional ¹H NMR spectra of the reaction mixture after removal of the protein (denaturation by heat at

TABLE 1
Crystallographic data and refinement statistics for PaMTH1

	PaMTH1 apo	PaMTH1 SAM	PaMTH1 SAH
Protein Data Bank code	4QVK	4YMG	4YMH
Space group	P 21 21 21	P 21 21 21	P 21 21 2
Resolution (Å)	26.27-1.97 (2.02-1.97) ^a	41.36-1.90 (1.95-1.90)	48.77-1.88 (1.92-1.88)
Unit cell dimensions <i>a</i> , <i>b</i> , <i>c</i> (Å)	73.38 79.72 84.39	75.04 78.79 82.72	84.23 239.30 50.56
α , β , γ (degrees)	90.0 90.0 90.0	90.00 90.00 90.00	90.00 90.00 90.00
Unique reflections	35,407	39,322	84,455
Completeness (%)	99.3 (99.7)	99.8 (98.7)	99.5 (97.3)
Average redundancy	5.1	6.6	6.6
R_{meas} (%) ^b	6.7 (93.9)	13.7 (95.1)	11.7 (89.3)
I/σ	17.0 (1.8)	12.75 (2.08)	13.00 (2.30)
Wilson <i>B</i> -factor (Å ²)	37.7	22.2	30
Average <i>B</i> (Å ²)	38.0	22.7	33.2
Mosaicity (degrees)	0.155	0.232	0.117
R_{working} (%) ^c	17.4 (26.8)	15.9 (24.9)	16.4 (24.1)
R_{free} (%) ^d	20.6 (30.4)	20.2 (26.2)	20.4 (30.6)
RMSD bonds (Å)	0.012	0.008	0.008
RMSD angles (degrees)	1.264	0.999	1.062
RMSD dihedral angles (degrees)	13.693	14.839	14.424
RMSD chirality (degrees)	0.058	0.041	0.043
Ramachandran favored (%)	97.4	97.4	98.1
Ramachandran allowed (%)	2.6	2.6	1.9
Ramachandran outliers (%)	0	0	0

^a Values in parentheses are for the highest resolution shells.^b $R_{\text{merge}} = \sum |I_h - \langle I_h \rangle| / \sum I_h$, where $\langle I_h \rangle$ is the average intensity over symmetry-equivalent reflections.^c $R_{\text{working}} = \sum |F_o| - |F_c| / \sum |F_o|$, where F_o and F_c are the observed and calculated structure-factor amplitudes, respectively.^d R_{free} was calculated using 5% of data excluded from refinement.

70 °C for 5 min, followed by centrifugation at 13,000 rpm for 10 min). Two-dimensional ¹H,¹³C HSQC (44) and multiplicity-edited ¹H,¹³C HSQC (45) (Bruker 800 MHz) experiments were employed to confirm the methylation status of myricetin. The reaction mixture for the two-dimensional NMR experiments was prepared using ¹³C,¹⁵N-labeled SAM (synthesized enzymatically from ¹³C,¹⁵N-labeled ATP and ¹³C,¹⁵N-labeled methionine as described previously (46)). To further corroborate the formation and methylation status of the product (methoxymyricetin), electron spray ionization-mass spectrometry of the reaction mixture was also performed.

Results

Overall Structure of PaMTH1—Recombinant PaMTH1 was overexpressed in *E. coli* and purified both in native and selenomethionine-substituted forms. The crystal structure refined to 2.0 Å was solved using experimental Se-MAD (Table 1). The protein crystallizes as a homodimer (Fig. 1A). On SEC, PaMTH1, a 27-kDa protein, eluted as a single peak and with an elution volume corresponding to a 44-kDa protein. To independently ascertain the exact molecular weight in solution, we performed in-line SEC-MALS. The measured molecular weight confirms that PaMTH1 exists as a dimer in solution (Fig. 1A, inset).

Most of the structurally characterized plant O-MTs are dimers (47), including the coffeoyl-CoA O-methyltransferase (CCoAOMT), which displays significant sequence homology to PaMTH1 (Fig. 2). Previous structures of O-MTs have shown that the SAM-binding site is located in the vicinity of the dimer interface. In addition, many MTs contain an additional N-terminal extension or dimerization domain also important for substrate binding and specificity (24, 25). PaMTH1 lacks such an additional dimerization domain, and the interaction between the monomers in the dimer appears to be unique. The dimerization interface buries 6270 Å² of surface area and

accounts for 32% of the total available surface area of the dimer, consistent with previously reported small molecule O-MTs. Importantly, the first 10 N-terminal loop residues are swapped between the two monomers (Fig. 1, A and B). Additionally, the interface includes interactions involving helices $\alpha 1$, $\alpha 3$, and $\alpha 9$ and β -strands $\beta 6$ and $\beta 7$. The N-terminal loop directly inserts into the catalytic pocket of the neighboring molecule and fixes the positions of helix $\alpha 3$ and the $\alpha 8$ - $\alpha 9$ loop in the substrate binding region via a hydrogen bond network, suggesting a critical role in substrate binding (Fig. 1B). The hydroxyl group of Ser⁴ (chain A) in the loop hydrogen bonds with the hydroxyl group of Ser⁵⁰ (chain B) of helix $\alpha 3$, and the carbonyl oxygen of the Pro⁷ (chain A) hydrogen bonds with the Ne1 hydrogen of Trp¹⁸⁸ (chain B) in the $\alpha 8$ - $\alpha 9$ loop (Fig. 1B). An analysis of the PaMTH1 dimer using PISA (48) shows that the dimer interface is predominantly composed of 34 hydrogen bonds, 17 salt bridges, and several non-bonded interactions. The regions involved in hydrogen bonding include N-terminal loop (residues Gly³, Ser⁴, Ile⁵, Pro⁷, and Phe⁸), $\alpha 1$ (Asp¹⁴, Arg¹⁵, Ser¹⁷, and Tyr¹⁹), $\alpha 1$ - $\alpha 2$ loop (Ser²⁴ and His²⁵), $\alpha 3$ (Ser⁵⁰, and Arg⁶²-Lys⁶⁵), $\alpha 8$ - $\alpha 9$ loop (Ile¹⁸¹, Asp¹⁸⁴, Cys¹⁸⁵, and Trp¹⁸⁸), $\alpha 9$ (Asp²⁰⁵), $\beta 6$ (Val²¹⁹ and Leu²²¹), and $\beta 7$ (Arg²³² and Asp²³⁵). CCoAOMT (*Medicago sativa*) (Protein Data Bank entry 1SUI) is one of the closest structural homologues of PaMTH1 and also crystallizes as a dimer. The dimerization interface buries 25% of the total available surface area of the dimer. In the context of catalysis, dimerization of CCoAOMT is not critical for its activity (49). However, similar to other plant O-MTs, dimerization of PaMTH1 might be required either for catalysis or to impart substrate specificity, because its N-terminal loop contributes to the active site of the dyad-related monomer. Interestingly, in the dimeric structures of two bacterial O-MTs (LiOMT from *Leptospira interrogans* (50) and SynOMT from cyanobacterium *Synechocystis* sp. (51)), the N-terminal loop (first 10–13 residues) plays an important

Structure and Biophysical Characterization of PaMTH1

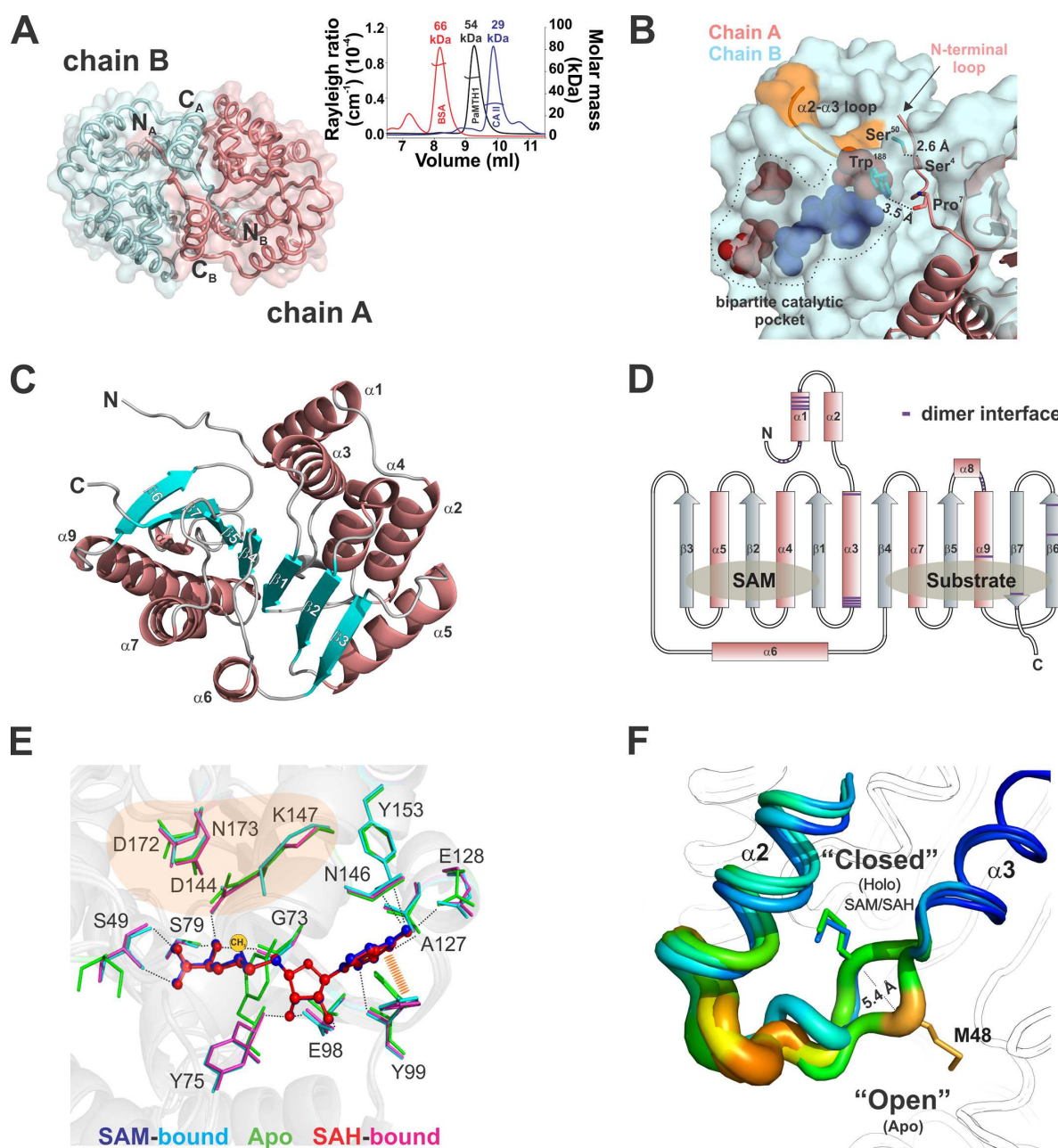


FIGURE 1. Crystal structure of PaMTH1. *A*, schematic surface representation of PaMTH1 dimer (chain B (cyan) and chain A (salmon)). The inset shows an SEC-MALS analysis of PaMTH1. *B*, close-up view of the PaMTH1 dimer interface, showing the N-terminal loop of chain A (schematic representation, salmon) inserted into a groove of the dyad-related molecule (chain B, surface representation; cyan). Hydrogen bonds between representative amino acids of chain A (Ser⁴ and Pro⁷) and chain B (Ser⁵⁰ and Trp¹⁸⁵) are indicated with their respective bond lengths. *C*, Rossmann fold architecture of PaMTH1 monomer (helices (dark salmon), β -strands (cyan), and loop (gray)). *D*, schematic representation of the topology and structural motifs of PaMTH1 (helices (salmon) and β -strands (light cyan)), indicating a putative SAM-binding site, substrate-binding site, and dimer interface (violet). *E*, close-up view of the catalytic pocket of PaMTH1, showing the ligands (SAM (blue) and SAH (red)) and the interacting amino acids (apo-state (green), SAM-bound (marine blue), and SAH-bound (magenta)). Putative substrate or metal binding residues are highlighted. Hydrogen bonds and π - π interactions are shown as black dotted lines and orange dashed lines, respectively. *F*, superposition of apo- and holo (SAM/SAH)-PaMTH1 (*B*-factor mapping) with *sausage* representation indicating conformational flexibility in the α 2- α 3 loop.

role either in dimerization or catalysis. The N-terminal loop in LiOMT is domain-swapped and involved in dimerization, although the functional significance is not known. However,

in the case of SynOMT, although the loop is not involved in dimerization, it inserts into the monomer catalytic pocket and plays a critical role in catalysis.

Structure and Biophysical Characterization of PaMTH1

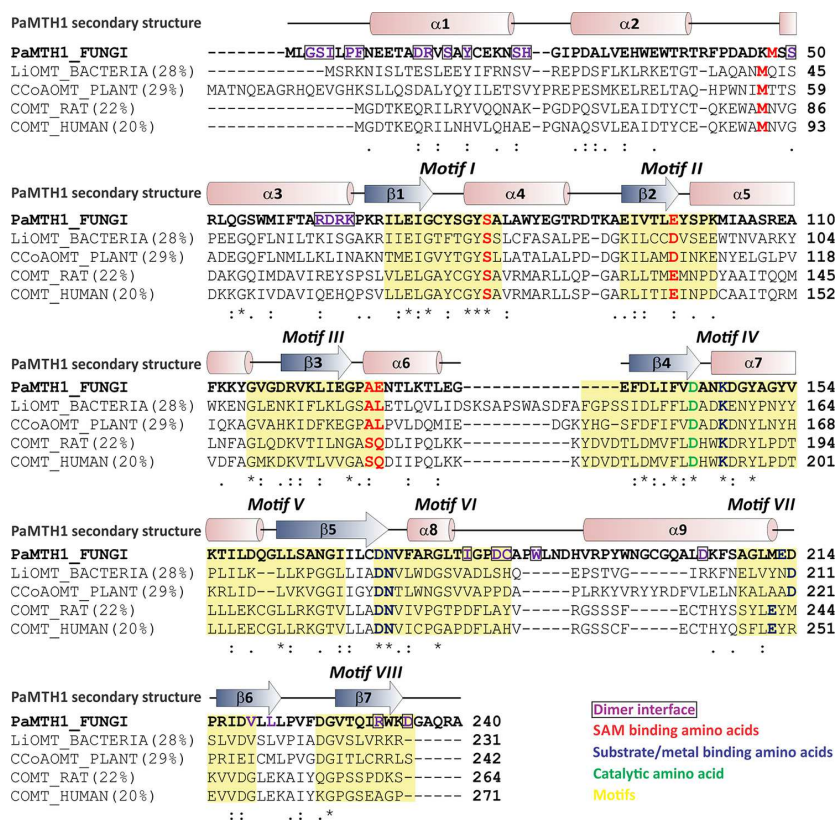


FIGURE 2. **Multiple sequence alignment.** Sequence alignment of the amino acid sequences of PaMTH1 from *P. anserina*, LiOMT from *Leptospira interrogans*, CCoAOMT from *V. vinifera*, and COMT from *R. norvegicus* and *H. sapiens*. The secondary structure of PaMTH1 is indicated above the sequences, and the percentage sequence identity of PaMTH1 to other O-MTs is shown in parenthesis. The α -helices and β -strands are indicated by cylinders (pink) and arrows (blue), respectively. The analysis was performed by multiple-alignment program ClustalW. Strictly conserved residues among the four proteins are marked by an asterisk, and highly conserved residues are indicated by a colon and dot. The highly conserved motifs (I–VIII) are highlighted in yellow boxes. Amino acids involved in the dimer interface are indicated by violet boxes, and the ones involved in SAM binding, substrate/metal binding, and catalysis are indicated by red, blue, and green, respectively.

Each monomer subunit of PaMTH1 consists of nine α -helices and seven β -strands, and folds into a globular tertiary structure consisting of a core α/β Rossmann fold (Fig. 1C), typical for many SAM-binding MTs. The seven-stranded β -sheet core is sandwiched between two helical regions. As in all Rossmann fold SAM-dependent MTs, the β -sheet adopts a strand topology $\beta_3, \beta_2, \beta_1, \beta_4, \beta_5, \beta_7, \beta_6$, with all strands oriented parallel to each other except for β_7 , which is antiparallel (Fig. 1D).

PaMTH1 Binding to Co-factor (SAM), By-product (SAH), and Substrate—We used NMR spectroscopy to investigate the PaMTH1-SAM/SAH interaction in solution. $^1\text{H}, ^{15}\text{N}$ HSQC experiments can detect ligand binding to a target through CSPs and serve as a qualitative tool for identifying binders. In addition to the CSPs, the complete disappearance of signals can also occur upon complexation, which is also indicative of binding. An overlay of $^1\text{H}, ^{15}\text{N}$ HSQC spectra of PaMTH1 in the presence and absence of SAM/SAH shows that the addition of the ligand induces both CSPs and disappearance of a subset of NMR signals, indicating specific binding (Fig. 3, A and B). Previous studies have shown that both SAM and SAH occupy

the same binding pocket in most methyltransferases. A comparison between SAM- and SAH-induced NMR-spectra changes reveals that there is a significant overlap, suggesting an identical or at least overlapping binding pocket for SAM and SAH in PaMTH1.

Subsequently, we co-crystallized SAM/SAH with PaMTH1 and solved the three-dimensional structures of the co-complexes refined to 1.9 Å (Table 1). The structures of PaMTH1 in complex with SAM and SAH clearly reveal a conserved SAM/SAH binding motif (Fig. 1E). Positional conservation of the amino acids involved in the co-factor/by-product binding is directly evident from the crystal structures of SAM/SAH bound to PaMTH1 as well as sequence alignments of the closely related MTs (Fig. 2). Analogous to other SAM-MTs, the binding pocket is located on the C-terminal end of the β -strands. SAM/SAH binding within the active site pocket of PaMTH1 is mediated through hydrogen bond networks and van der Waals and π - π stacking interactions (Fig. 1E). The GXGXG motif is highly conserved in Rossmann fold SAM-dependent MTs and is considered to be a hallmark of the SAM-binding site (25). In PaMTH1, this region (GCYSG) is well conserved except that

Structure and Biophysical Characterization of PaMTH1

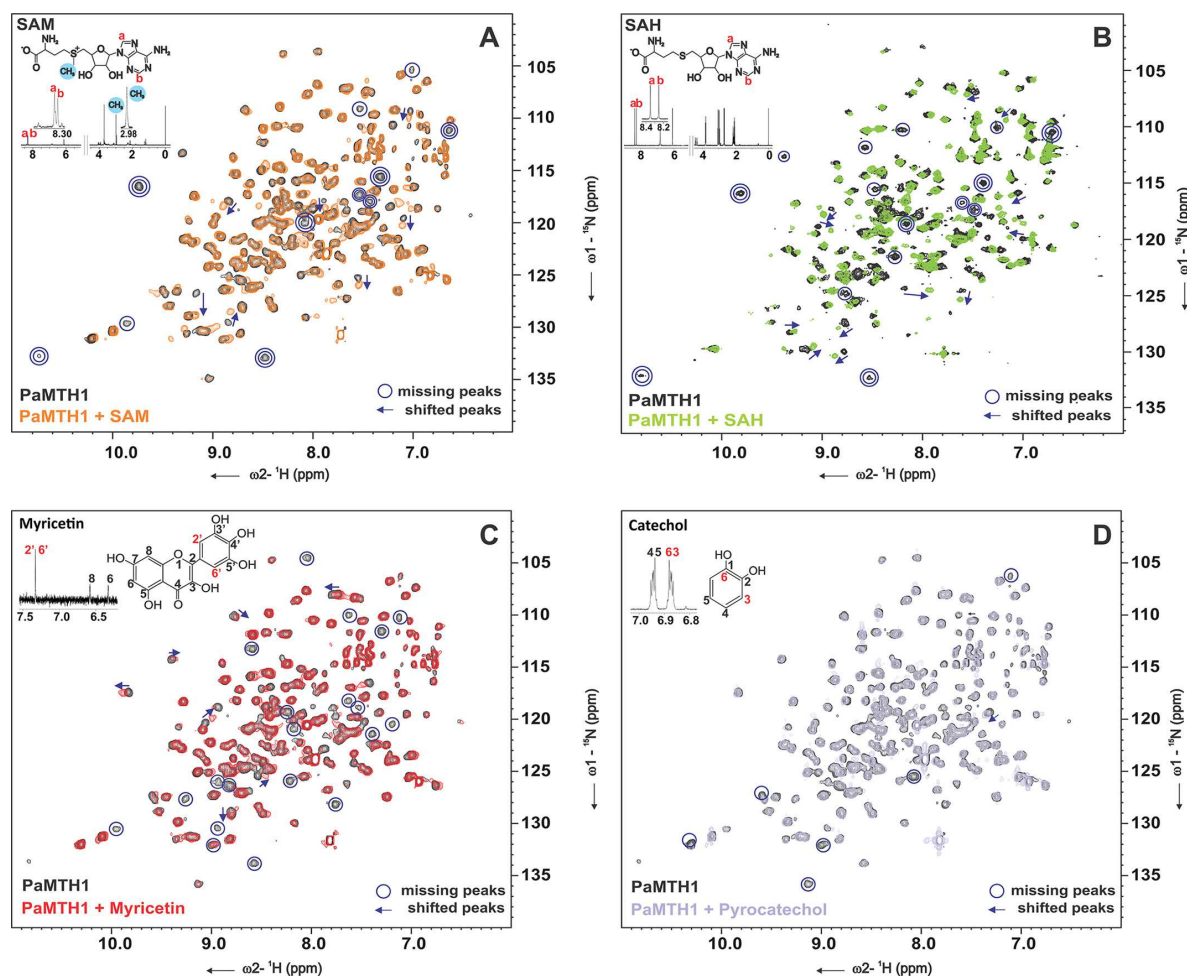


FIGURE 3. PaMTH1 binding to co-factor and product. Overlay of two-dimensional $^1\text{H},^{15}\text{N}$ HSQC spectra of PaMTH1 without (black) and with ligands (protein/ligand ratio 1:2). A, SAM (orange); B, SAH (green); C, myricetin (red); and D, pyrocatechol (gray). The inset shows one-dimensional ^1H spectra of A, SAM with protons from the adenosine moiety (a and b) and the methyl group (d) B, SAH with protons from the adenosine moiety (a and b). C, myricetin. D, pyrocatechol is shown with protons from the catechol moiety highlighted. All spectra were acquired at 800 MHz ($T = 298$ K) in the following buffer: 25 mM Tris, pH 6.5, 100 mM NaCl, 5 mM TCEP, 10% D_2O , and 1 mM TSP- d_4 .

the central glycine of the GXGXG motif is substituted by a tyrosine (Tyr⁷⁵). In the apoenzyme, Tyr⁷⁵ points into the SAM/SAH binding pocket, and upon SAM/SAH binding, it flips and reorients to establish direct hydrogen bonding with Asp⁴⁴, thereby stabilizing the $\alpha 2$ - $\alpha 3$ loop (Fig. 1E). This reorientation of the Tyr⁷⁵ and the subsequent stabilization of the $\alpha 2$ - $\alpha 3$ loop in a closed conformation might possibly function to allow substrate specificity and binding.

Flavonoids are potential substrates of PaMTH1. Previous biochemical functional assays tested several phenolic putative PaMTH1 substrates and showed that the flavonoid myricetin was the best recognized substrate (28). However, the biophysical and structural evidence for methylation by PaMTH1 remains unknown. Three putative flavonoids (apigenin, kaempferol, and myricetin) and pyrocatechol were chosen for characterization of their interaction with PaMTH1 by NMR. Solubility of a compound is one of the essential factors for inter-

action studies. One-dimensional NMR-based solubility analysis of the chosen compounds in the interaction buffer revealed that two compounds (apigenin and kaempferol) were insoluble under the conditions of the experiment, whereas myricetin and pyrocatechol were soluble (data not shown). $^1\text{H},^{15}\text{N}$ HSQC spectra of PaMTH1 in the presence and absence of myricetin or pyrocatechol show that the addition of the ligand induces both CSPs and disappearance of a subset of NMR signals, indicating specific binding (Fig. 3, C and D) even in the absence of co-factor.

Cation-dependent Methylation of Substrate by PaMTH1—Previously, based on the sequence and the size of PaMTH1 (27 kDa), it had been suggested that the protein belongs to the small cation-dependent class I and not to the cation-independent class II with a molecular mass of about 40 kDa (28). Sequence comparison shows that the residues Asp¹⁴⁴, Lys¹⁴⁷, Asp¹⁷², and Asn¹⁷³, which are important for divalent cation binding, are

highly conserved in PaMTH1. Cation binding is important for substrate binding and orientation for the transmethylation reaction. We investigated the cation dependence of the myricetin *O*-methylation catalyzed by PaMTH1 using NMR spectroscopy. The protons of the methyl group bound to the oxygen of an aromatic ring (methoxy) resonate around at ~ 4 ppm, whereas protons of aliphatic methyl groups typically are found at ~ 1 ppm. SAM acts as a methyl group donor required for methylation of the substrate. In a proton one-dimensional NMR spectrum of SAM, the thiomethyl group appears as a singlet peak at 2.98 ppm (Fig. 3A, *inset*). We then took advantage of the typical chemical shifts of methyl/methoxy groups and based our analysis on the fact that the catalytic transfer of a methyl group from SAM to the aromatic hydroxyl oxygen of the substrate will result in a decrease in the intensity of the thiomethyl signal of SAM and the appearance of the methoxy methyl signal of the product at distinct chemical shifts.

To determine the metal requirements of the myricetin methylation reaction, we investigated the effect of the presence and absence of Mg^{2+} and Ca^{2+} ion on the catalytic activity of PaMTH1. The one-dimensional 1H NMR spectrum of a reaction mixture of SAM, substrate (myricetin), and PaMTH1 shows that in the absence of cations, the intensity of the methyl group signal of SAM remains constant even after 8 h, indicating no catalysis (Fig. 4A). In the presence of Mg^{2+} , we observe a fast decrease in the intensity of the methyl group signal, indicating catalysis of the methyl transfer reaction (Fig. 4B). In the presence of Ca^{2+} , the enzymatic activity is significantly slowed down (Fig. 4C). This strongly suggests that PaMTH1 is a divalent cation (Mg^{2+})-dependent methyltransferase. The influence of the Mg^{2+} ion on the catalytic activity of PaMTH1 may be directly associated with the enhanced ability of the enzyme to form a more stable complex with myricetin (see also below). Although pyrocatechol binds to PaMTH1 (Fig. 3D), even in the absence of Mg^{2+} , the enzyme does not catalyze its methylation even in the presence of Mg^{2+} (Fig. 4D), suggesting that flavonoids are the preferred substrates.

During enzymatic methyl group transfer to myricetin, SAM donates the methyl group and is converted to SAH. Comparison of the aromatic region of the one-dimensional 1H NMR spectrum reveals a decrease in the signal intensity of the adenosine protons of SAM and a simultaneous increase in the signal intensity for SAH adenosine protons, confirming the formation of SAH (Fig. 5A). It should also be possible to directly detect the formation of methoxymyricetin by inspecting the spectral region at ~ 4 ppm typical for the methoxy signal. However, due to significant overlap with protein signals in this region, a methoxy signal could not be resolved. Upon removal of the protein by heat denaturation, however, a clear signal for the methoxy protons could be resolved at 3.93 ppm (Fig. 5B, *inset*), confirming the formation of methoxymyricetin. Further, using ^{13}C , ^{15}N -labeled SAM, we were able to detect and confirm the formation of methoxymyricetin by measuring multiplicity-edited two-dimensional 1H , ^{13}C HSQC spectra in which the methyl group signals are inverted in comparison with CH and CH_2 signals. Only one clear cross-peak ($^1H = 3.93$ and $^{13}C = 58.9$ ppm) for the methoxy group was detected, indicating the specific methylation of a single hydroxyl group of myricetin

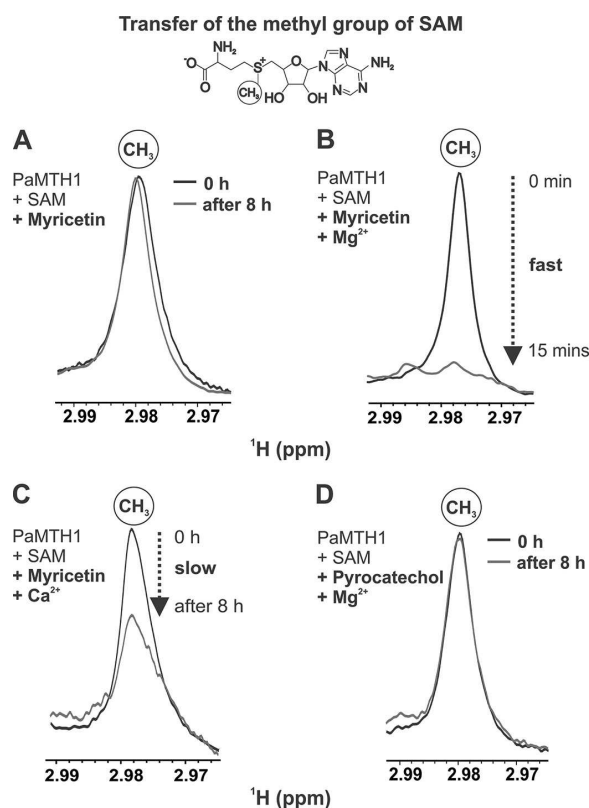


FIGURE 4. Cation-dependent methyl transfer by PaMTH1. Time-resolved one-dimensional 1H NMR spectra of SAM (methyl group) in the presence of PaMTH1 + myricetin (A), PaMTH1 + myricetin + Mg^{2+} (B), PaMTH1 + myricetin + Ca^{2+} (C), and PaMTH1 + pyrocatechol + Mg^{2+} (D). All spectra were acquired at 600 MHz ($T = 298$ K) in the following buffer: 25 mM *d*-Tris, pH 7.5, 100 mM NaCl, 5 mM TCEP, 10% D_2O , and 1 mM TSP- d_4 .

(Fig. 5B). Further, mass spectrometry analysis of the reaction mixture confirmed that myricetin is monomethylated (Fig. 5C). However, several attempts to isolate methoxymyricetin by HPLC and characterize the position of methylation were unsuccessful, presumably due to its low stability.

Feedback Inhibition of PaMTH1 by SAH—SAH, the by-product of methionine transmethylation, acts as feedback inhibitor of many SAM-dependent MTs and plays a role in the control of the overall methyl transfer rates (52). The time-dependent one-dimensional 1H NMR spectra recorded for a reaction mixture of SAM, substrate (myricetin), and PaMTH1-SAH (PaMTH1 saturated with SAH, 1:20 ratio) shows a significant decrease in the reaction rate as monitored by the decrease in intensity of the thiomethyl group NMR signal of SAM. This result demonstrates that SAH saturation of PaMTH1 (Fig. 6A) significantly reduced the catalytic efficiency compared with free PaMTH1 (Fig. 5B). Further, the 1H , ^{15}N HSQC spectrum of PaMTH1 bound to SAH shows no changes upon the addition of SAM, indicating that SAH has a higher binding affinity to PaMTH1 compared with SAM (Fig. 6B). We then used isothermal titration calorimetry to determine the binding affinities of SAM and SAH to PaMTH1, respectively. In line with the NMR results, ITC data show that SAH binds ($K_D = 3.2 \mu M$) to PaMTH1

Structure and Biophysical Characterization of PaMTH1

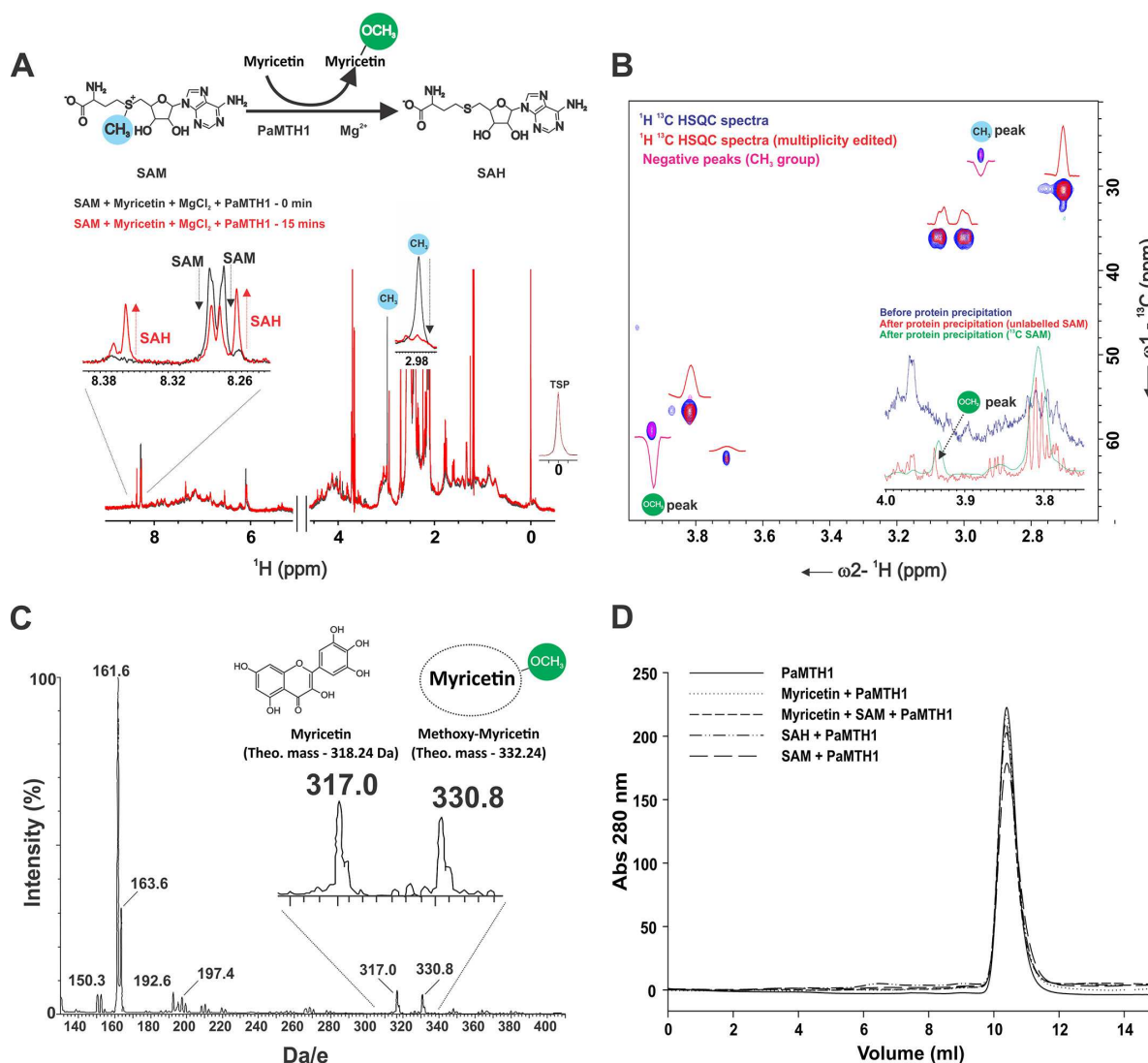


FIGURE 5. Substrate methylation monitored by NMR. *A*, overlay of one-dimensional ^1H spectra of the reaction mixture containing PaMTH1, myricetin, SAM (PaMTH1/myricetin/SAM ratio, 1:10:10), and 1 mM MgCl_2 at 0 min (black) and 15 min (red) indicates methyl group transfer from SAM and formation of SAH. Schematic representation of the methyl group transfer reaction is shown above. *B*, overlay of two-dimensional ^1H , ^{13}C HSQC (blue) and multiplicity-edited (red) spectra of reaction mixture after protein precipitation. The negative peaks of multiplicity-edited spectra are shown in magenta. The one-dimensional projections (magenta) of two-dimensional cross-peaks of multiplicity-edited spectra are shown above corresponding peaks. Inset, overlay of one-dimensional ^1H spectra of reaction mixture before (blue) and after (unlabeled SAM (red) and ^{13}C , ^{15}N -labeled SAM (green)) protein removal, indicating formation of methoxy-myricetin. *C*, electron spray ionization-MS annotated with experimental and theoretical molecular mass of myricetin and methoxymyricetin. *D*, SEC analysis of PaMTH1 in the presence of different ligands. The spectra were acquired at 600 MHz (A) and 800 MHz (B) ($T = 298\text{ K}$) in the following buffer: 25 mM *d*-Tris, pH 7.5, 100 mM NaCl, 5 mM TCEP, 10% D_2O , and 1 mM TSP- d_4 .

>30-fold tighter than SAM ($K_D = 113\ \mu\text{M}$). Additionally, the presence of Mg^{2+} enhances the binding affinity ~ 10 -fold for both SAM ($K_D = 21\ \mu\text{M}$) and SAH ($K_D = 0.35\ \mu\text{M}$). The K_D values obtained from ^1H , ^{15}N HSQC-based NMR titration experiments are in good agreement with the ITC measurements (Fig. 7 and Table 2).

Structural Comparisons with Other O-MTs—The unavailability of structural information for the ternary complex of PaMTH1 bound to co-factor (SAM) and the substrate hinders a complete description of the binding pocket involved in cataly-

sis. Instead, we used sequence homology and the Dali server to compare PaMTH1 with the structures of other O-MTs with known function.

PaMTH1 presents significant homology to various MTs. A DALI (53) search for three-dimensional structure similarity resulted in 40 structures with Z scores greater than 15. The first five structures with the highest Z scores are from bacterial O-MTs with Z scores ranging from 26.2 to 25.7, followed by CCoAOMT (25.6) from the plant *M. sativa* and human COMT with 24.3 (Table 3). It is interesting to note that most of the

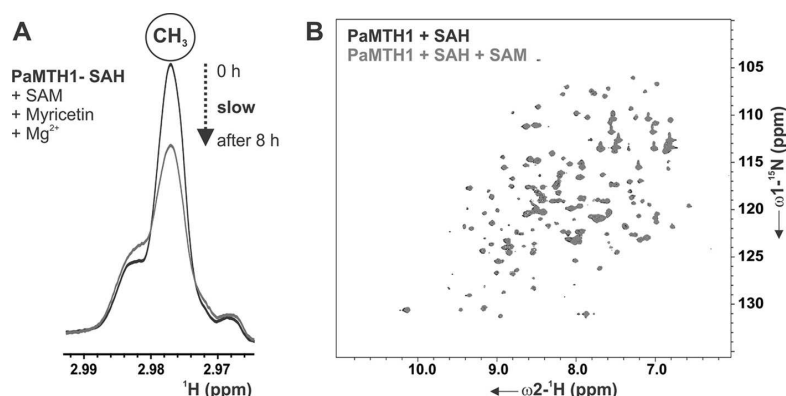


FIGURE 6. **SAH is a feedback inhibitor of PaMTH1.** *A*, time-resolved one-dimensional ^1H NMR spectra of SAM (methyl group) in the presence of PaMTH1-SAH (PaMTH1 saturated with SAH) + myricetin + Mg^{2+} . The spectrum was acquired at 600 MHz ($T = 298$ K) in the following buffer: 25 mM *d*-Tris, pH 7.5, 100 mM NaCl, 5 mM TCEP, 10% D_2O , and 1 mM TSP- d_4 . *B*, overlay of two-dimensional ^1H , ^{15}N HSQC spectra of PaMTH1 with SAH (1:2 ratio) (black) and after the addition of an equivalent concentration of SAM (gray). The spectrum was acquired at 800 MHz ($T = 298$ K) in the following buffer: 25 mM Tris, pH 6.5, 100 mM NaCl, 5 mM TCEP, 10% D_2O , and 1 mM TSP- d_4 .

closest bacterial structural homologues are involved in antibiotic synthesis pathways, whereas the plant CCoAOMT and human-COMT are involved in lignin biosynthesis and the metabolism of catecholamine neurotransmitters, respectively. A superposition of each of the closest homologue structures with a monomer of PaMTH1 revealed an overlap with root mean square deviations (RMSDs) ranging from 1.3 to 1.8 Å for C α atoms (RMSDs generated using PyMOL (54)). ClustalW-based multiple-sequence alignment of the amino acid sequence shows that PaMTH1 contains eight motifs (motifs I–VIII) with a high degree of identity to the corresponding stretches of plant CCoAOMT, bacterial LiOMT, rat COMT, and human COMT (Fig. 2). The individual motifs in a tertiary fold together form the defining feature of the bipartite active site to accommodate SAM and in addition Mg^{2+} that can bind catechol substrates. Motifs I–V are mainly involved in SAM binding. Asp¹⁴⁴, Lys¹⁴⁷, Asp¹⁷², and Asn¹⁷³ are important for divalent cation binding, which in turn is required for substrate binding and hydroxyl orientation before the transmethylation reaction of some *O*-MTs. All four residues are highly conserved in PaMTH1 and structurally adopt a conformation similar to that of CCoAOMT and human COMT, suggesting that PaMTH1 might share a similar metal-dependent catalytic mechanism (Fig. 1E). Mutation of these residues (K147A and double mutants D144A/K147A and D172A/N173A) either abrogates or slows down the transmethylation reaction, suggesting a crucial role in catalysis (Fig. 8).

In the substrate binding region, conformational differences in the $\alpha 2$ - $\alpha 3$, $\beta 5$ - $\alpha 9$, and $\beta 6$ - $\beta 7$ loops play an important role in mediating divalent cation and substrate binding at least in rat and mouse COMT (55). Further, conformational changes in the $\alpha 2$ - $\alpha 3$ loop upon ligand binding reposition the hydrophobic side chain of a conserved methionine (within the loop) onto the aromatic ring of the catechol and shield the Mg^{2+} binding site, displaying a critical role during catalysis, at least in COMT. In PaMTH1, both apo- and holoenzyme superpose well with each other with an RMSD of 0.42 Å calculated over all C α atoms excluding the $\alpha 2$ - $\alpha 3$ loop region, which shows an RMSD of 1.7

(PaMTH1-SAM) and 2.3 Å (PaMTH1-SAH), respectively. The conformation of the $\alpha 2$ - $\alpha 3$ loop is not dominated by crystal contacts. Additionally, the side chain of the Met⁴⁸ in SAM/SAH-bound PaMTH1 is swung 5.4 Å into the active site (“closed”), whereas it is solvent-exposed in the apoenzyme (“open”) (Fig. 1F). The two conformational states observed for Met⁴⁸ indicate that the $\alpha 2$ - $\alpha 3$ loop in PaMTH1 could play a similar role as observed in rat and mouse COMT and could mediate substrate binding or specificity.

Discussion

Small molecule natural product MTs play an important role in modulating diverse biological processes, such as cell signaling and biosynthesis. Most of the natural product MTs belong to two (Class I and Class III) of 15 currently known protein fold superfamilies of SAM-binding proteins (25, 56). Depending on the substrate atom accepting the methyl group, *O*-directed MTs (*O*-MTs) are the most abundant natural product MTs found across all kingdoms of life. Many of these *O*-MTs belong to the Class I or Rossmann-like fold family. Subtle modifications of this conserved fold are responsible for the wide variety in substrate selectivity and specificity. The explicit selectivity is achieved through the movement of the loops decorating the conserved core together with the side chain variation in the substrate binding region, leading to reconfiguration of the active site surface. Additionally, structural elaborations in the N-terminal region modulate the dimerization interface, thereby introducing diversity in the active site topology. In certain bacteria and plants, the *O*-MT subfamily has undergone significant functional and genetic expansion to accommodate a wide variety of substrates. Certain plant MTs, such as caffeic acid *O*-MT and CCoAOMT, show promiscuity in substrate selection, whereas most other plant *O*-MTs act on unique substrates. However, in humans, only two *O*-MTs (catechol *O*-MT and *N*-acetyl-serotonin *O*-MT) are found, which are involved in neurotransmitter metabolism and melatonin biosynthesis, respectively.

Structure and Biophysical Characterization of PaMTH1

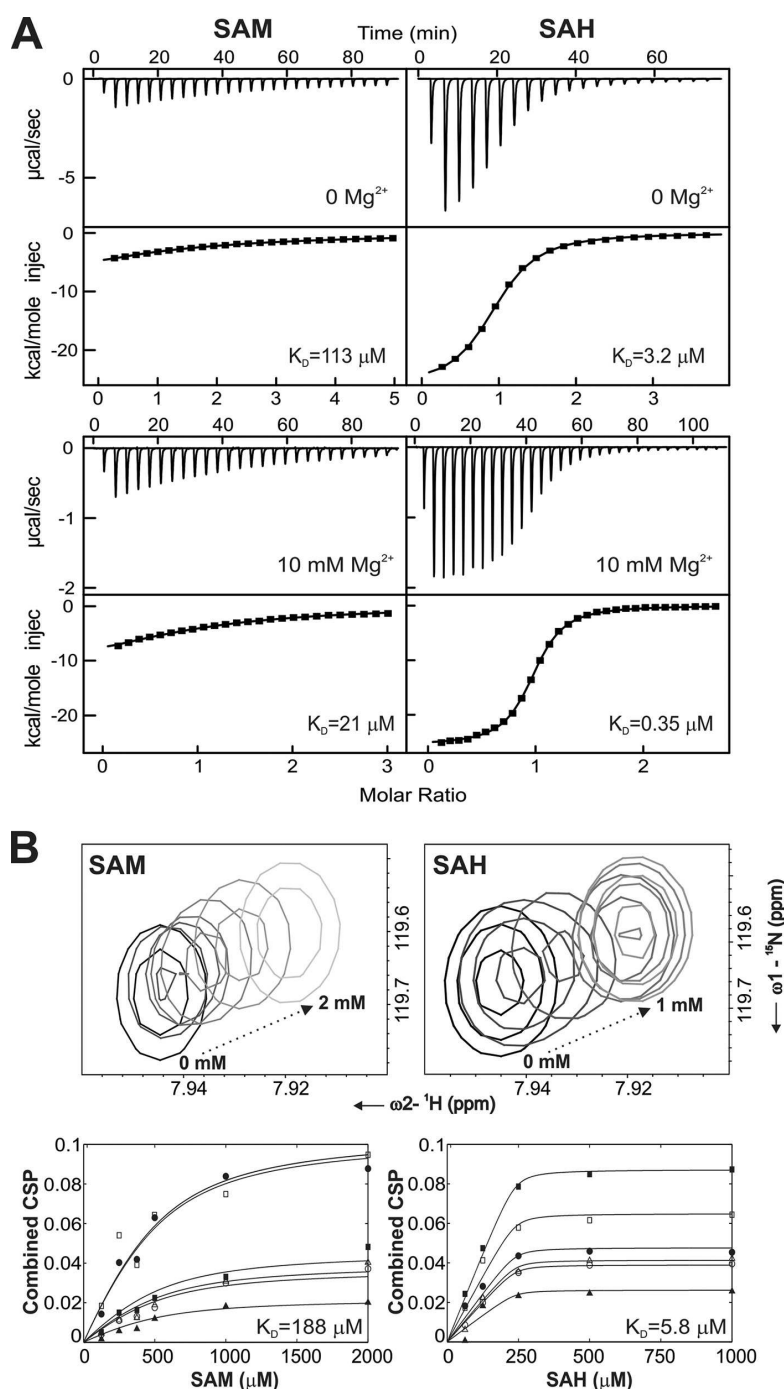


FIGURE 7. Binding of SAM/SAH to PaMTH1. *A*, isothermal titration calorimetry. The *top panel* of each graph shows the raw heat changes with each injection as a function of time. The *bottom panel* shows the recalculated enthalpies per injection versus the molar ratio of ligand (*squares*). The data were fitted (*lines*) to a single-site binding model using the MicroCal Origin software package. The K_D value of each interaction is indicated. *Left panels*, PaMTH1 + SAM without Mg^{2+} (*top*) and PaMTH1 + SAM with 10 mM Mg^{2+} (*bottom*). *Right panels*, PaMTH1 + SAH without Mg^{2+} (*top*) and PaMTH1 + SAH with 10 mM Mg^{2+} (*bottom*). *B*, two-dimensional NMR-based titration. Binding curve fits for titrations using SAM (*left*) and SAH (*right*), in which combined chemical shift perturbations are plotted against increasing ligand (SAM and SAH) concentration. Representative peak spectra for one of the binding curves (\blacksquare) are shown above (*B*). All spectra were acquired at 800 MHz ($T = 298 \text{ K}$) in the following buffer: 25 mM Tris, pH 6.5, 100 mM NaCl, 5 mM TCEP, 10% D_2O , and 1 mM TSP- d_4 .

TABLE 2

Thermodynamic parameters for the association of PaMTH1 with SAM/SAH derived from ITC measurements

Uncertainty in measurement is given in parentheses. K_a , association constant; K_D , dissociation constant; ΔG , Gibbs free energy change; ΔH , enthalpy change; $-T\Delta S$, entropy contribution term; ΔS , entropy change; n , number of binding sites upon interaction (stoichiometry number).

PaMTH1	K_a	K_D	ΔG	ΔH	$-T\Delta S$	ΔS	n
	$\times 10^3 \text{ mol}^{-1}$	μM	<i>kcal/mol</i>	<i>kcal/mol</i>	<i>kcal/mol</i>	<i>kcal/mol/K</i>	
With SAM	8.82 (0.42)	113	-5.40	-19.70 (2.27)	+14.3	-48.0	0.984 (0.100)
With SAH	308.0 (10)	3.2	-7.94	-26.46 (0.21)	+19.0	-63.6	0.939 (0.005)
With SAM/Mg ²⁺	48.6 (1.54)	21	-6.48	-15.08 (0.20)	+8.6	-29.1	1 ^a
With SAH/Mg ²⁺	2740 (67)	0.36	-8.79	-25.56 (0.07)	+16.8	-56.3	0.959 (0.002)

^a The n value was fixed to 1.0 upon fitting.

TABLE 3

Structural homologues of PaMTH1 using DALI server

Pos ^a	Protein Data Bank code	Z ^b	RMSD ^c	LALI ^d	LSEQ ^e	%IDE ^f	Description
1	2HNK	26.2	2.1	213	233	27	O-methyltransferase, LiOMT (<i>L. interrogans</i>) (50)
2	3CBG	26.1	2.0	205	219	31	Hydroxycinnamic acids O-methyltransferase, SynOMT (Cyanobacterium <i>Synechocystis</i> sp. strain PCC 6803) (51)
3	3TR6	25.9	2.3	214	223	27	O-Methyltransferase (<i>C. burnetii</i>) ^g
4	3DUW	25.8	2.1	208	221	27	Flavonoid O-methyltransferase, BcOMT2 (<i>B. cereus</i>) (63)
5	3TFW	25.7	2.3	211	221	28	Putative O-methyltransferase (<i>Klebsiella pneumoniae</i>) ^g
6	1SUI	25.6	2.3	213	227	29	Alfalfa caffeoyl-CoA O-methyltransferase, CCoAOMT (<i>M. sativa</i>) (49)
7	3C3Y	25.4	2.3	213	226	26	Flavonoid O-methyltransferase, PFOMT (<i>Mesembryanthemum crystallinum</i>) (64)
8	4PCA	25.0	3.1	214	222	19	O-Methyltransferase (<i>Anaplasma phagocytophilum</i>) ^g
9	2AVD	24.3	2.6	209	219	28	Human catechol-O-methyltransferase, COMT (<i>Homo sapiens</i>) ^g
10	3R3H	24.2	2.2	207	217	28	O-Methyltransferase (<i>Legionella pneumophila</i>) ^g

^a Position in the numerical listing of structural homologues.

^b Z-score; strength of structural similarity in S.D. above expected.

^c Positional root mean square deviation of superimposed C α atoms in Å.

^d Total number of equivalent residues.

^e Length of the entire chain of the equivalent structure.

^f Percentage of sequence identity over equivalent positions

^g Structures obtained from the Protein Data Bank.

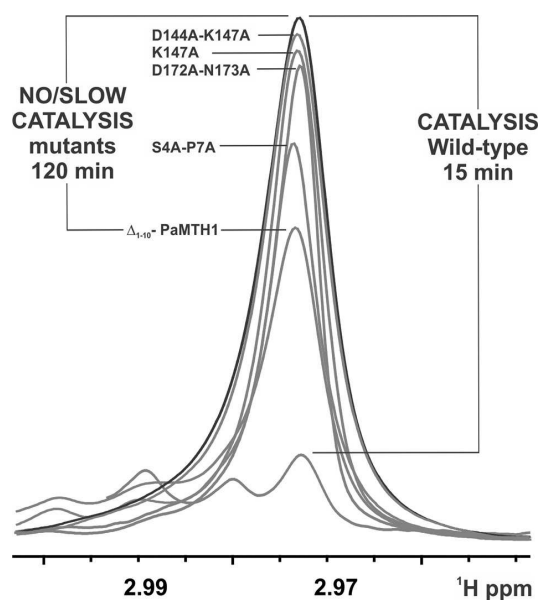


FIGURE 8. Catalytic activity of wild-type and mutant PaMTH1. One-dimensional ¹H NMR spectra of SAM (methyl group) were used to monitor the enzyme activity of PaMTH1 (wild type and mutants). Wild-type PaMTH1 catalyzes the transmethylation reaction within 15 min, whereas the mutants showed either slow or no catalysis even after 120 min. All spectra were acquired at 800 MHz ($T = 298 \text{ K}$) in the following buffer: 25 mM *d*-Tris, pH 7.5, 100 mM NaCl, 5 mM TCEP, 10% D₂O, and 1 mM TSP-*d*₄.

PaMTH1 shows significant sequence identity to other known O-MTs (bacterial LiOMT, alfalfa CCoAOMT, rat COMT, and human COMT). The highest degree of sequence identity is found for the stretches involved in the co-factor SAM-binding amino acids and shows subtle differences in the substrate binding regions. Further, a Dali search for structural homology identified 10 structures with a Z-score greater than 24. All 10 structures belonged to cation-dependent O-MTs and can be superimposed to PaMTH1 with an RMSD of less than 3 Å. Sequence and structural comparison demonstrates that a high degree of structural similarity is observed for the SAM-binding region in many species across all kingdoms of life, despite differences in the substrate specificity. Although the overall fold of the protein is conserved, the divergence between bacterial, plant, and animal MTs results in altered oligomerization states, different substrate recognition modes, or even altered catalytic mechanism of methyl transfer. PaMTH1 exists as a dimer both in solution and crystals. An SEC analysis shows that in the presence of putative substrate (myricetin) and co-factor (SAM), the oligomeric state of PaMTH1 is not altered (Fig. 5D), suggesting that dimerization might be a functional requirement. Within the crystal structure of the PaMTH1 homodimer, two features distinguish PaMTH1 from its homologues: the first 10 residues of the N-terminal region and an unusual insertion between $\beta 5$ and $\alpha 9$ (Ala¹⁸⁶-His¹⁹², "capping loop"; Fig. 9). Strikingly, the N-terminal loop swaps onto the dyad-related monomer and makes direct contacts with the capping loop before entering into the catalytic region, thereby

Structure and Biophysical Characterization of PaMTH1

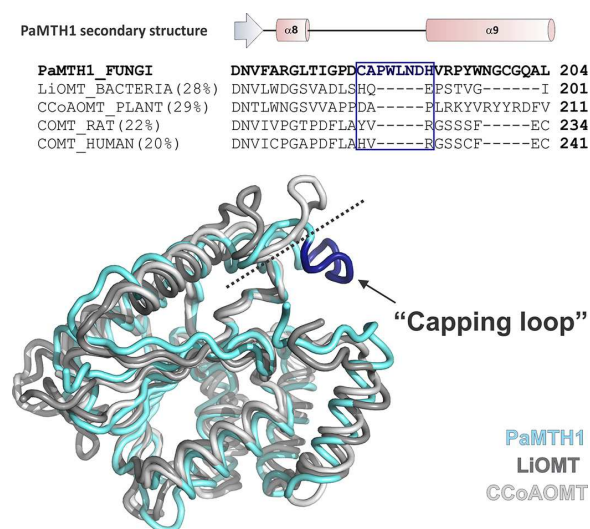


FIGURE 9. Comparison of PaMTH1 and structural homologues. Shown is a schematic representation of structural superposition of PaMTH1 (cyan), LIOMT (dark gray), and CCoAOMT (light gray) with the capping loop from PaMTH1 shown in dark blue. Top, sequence alignment of the amino acid sequences of PaMTH1, LIOMT, CCoAOMT, COMT_RAT, and COMT_HUMAN with the amino acids forming the capping loop highlighted with a blue box.

forming a unique dimerization interface. The side-chain Ne of Trp¹⁸⁸ (chain B) in the capping loop hydrogen-bonds with the carbonyl oxygen of the Pro⁷ (chain A) on the N terminus of the dyad-related molecule and stabilizes the interaction interface. Both mutation of key N-terminal residues (S4A/P7A double mutant) and the N-terminal deletion mutant (Δ_{1-10} PaMTH1) considerably slow down the catalysis, suggesting a definitive role in substrate binding (Fig. 8). These observations suggest that the capping loop and the residues therein might play a critical role in substrate selection and binding. Insertions to the common core Rossmann fold in the structures of MTs seem to be an evolutionary way of imparting unique features necessary for substrate selectivity (57, 58). Furthermore, the conformational flexibility within the residues of the $\alpha 2$ - $\alpha 3$ loop and in particular a well conserved methionine whose side chain sequesters aromatic moieties of the substrates at least in other MTs (55) could also play a similar role in PaMTH1.

The natural *in vivo* substrate of PaMTH1 is unknown. However, previous studies suggested that PaMTH1 specifically methylates flavonoids and not *l*-3,4-dihydroxyphenylalanine, a substrate of mammalian COMT (28). In this study, we have given direct biophysical evidence and show by NMR and mass spectrometry that PaMTH1 binds to the co-factor (SAM) and methylates the flavonoid myricetin in a cation-dependent manner. Taking into account the three-dimensional structure of PaMTH1, we suggest a catalytic mechanism; the side chains of conserved residues Asp¹⁴⁴, Asp¹⁷², and Asn¹⁷³ and the hydroxyl groups of the flavonoid coordinate the Mg²⁺. Mg²⁺ probably acts as weak Lewis acid, and during catalysis, the conserved Lys¹⁴⁷ can act as a Brønsted base. Further, the positive charge of Mg²⁺ may also result in a decrease of the pK_a for the Lys¹⁴⁷ side chain, followed by positioning of the side chain amino group of Lys¹⁴⁷ against the hydroxyl group to be methylated resulting in

an abstraction of a proton and generation of a reactive phenolic oxyanion near the reactive methyl group of SAM. Such a metal-dependent catalytic mechanism of methyl transfer persists in several related MTs (24, 55).

Understanding the aging process and improving the life span of organisms has become a specific aim of many research activities, resulting in significant fundamental advances (59). Aging and several age-related diseases, including cancer, are fuelled by damage to the macromolecules in cells and tissues (60, 61). Studies involving genetically tractable model organisms like the ascomycete *Podospora anserina*, yeast, *Caenorhabditis elegans*, *Drosophila melanogaster*, and mice have shown that specific genes are involved in the regulation of aging (62). PaMTH1 protects *P. anserina* from oxidative stress during senescence and acts as a longevity assurance factor. Identification of its natural substrates and thus elucidation of the underlying principle mechanisms contributing to life span increase still remains a challenge. To this end, the structures (apo- and holoenzyme) of PaMTH1 and biophysical characterization of its interaction with putative substrates will facilitate future studies involving the identification of endogenous polyphenolic compounds directly involved in metal-induced oxidative stress.

Acknowledgments—We thank Helmholtz-Zentrum Berlin and the Swiss Light Source for the allocation of synchrotron radiation beam time.

References

1. Thanickal, V. J., and Fanburg, B. L. (2000) Reactive oxygen species in cell signaling. *Am. J. Physiol. Lung Cell. Mol. Physiol.* **279**, L1005–L1028
2. Stadtman, E. R. (2004) Role of oxidant species in aging. *Curr. Med. Chem.* **11**, 1105–1112
3. Trachootham, D., Alexandre, J., and Huang, P. (2009) Targeting cancer cells by ROS-mediated mechanisms: a radical therapeutic approach? *Nat. Rev. Drug Discov.* **8**, 579–591
4. Halliwell, B., and Gutteridge, J. M. (1984) Oxygen toxicity, oxygen radicals, transition metals and disease. *Biochem. J.* **219**, 1–14
5. Slater, T. F. (1984) Free-radical mechanisms in tissue injury. *Biochem. J.* **222**, 1–15
6. Harman, D. (1956) Aging: a theory based on free radical and radiation chemistry. *J. Gerontol.* **11**, 298–300
7. McCord, J. M. (1985) Oxygen-derived free radicals in postischemic tissue injury. *N. Engl. J. Med.* **312**, 159–163
8. Orhan, H., Gurer-Orhan, H., Vriese, E., Vermeulen, N. P., and Meerman, J. H. (2006) Application of lipid peroxidation and protein oxidation biomarkers for oxidative damage in mammalian cells: a comparison with two fluorescent probes. *Toxicol. In Vitro* **20**, 1005–1013
9. Agullo, G., Gamet-Payrastré, L., Manenti, S., Viala, C., Rémésy, C., Chap, H., and Payrastré, B. (1997) Relationship between flavonoid structure and inhibition of phosphatidylinositol 3-kinase: a comparison with tyrosine kinase and protein kinase C inhibition. *Biochem. Pharmacol.* **53**, 1649–1657
10. Hoult, J. R., Moroney, M. A., and Payá, M. (1994) Actions of flavonoids and coumarins on lipoxygenase and cyclooxygenase. *Methods Enzymol.* **234**, 443–454
11. Laughton, M. J., Evans, P. J., Moroney, M. A., Hoult, J. R., and Halliwell, B. (1991) Inhibition of mammalian 5-lipoxygenase and cyclo-oxygenase by flavonoids and phenolic dietary additives. Relationship to antioxidant activity and to iron ion-reducing ability. *Biochem. Pharmacol.* **42**, 1673–1681
12. Lolli, G., Cozza, G., Mazzorana, M., Tibaldi, E., Cesaro, L., Donella-Deana, A., Meggio, F., Venerando, A., Franchin, C., Sarno, S., Battistutta, R., and

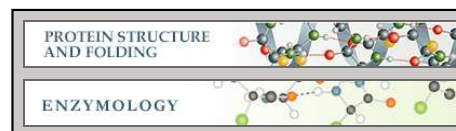
- Pinna, L. A. (2012) Inhibition of protein kinase CK2 by flavonoids and tyrphostins: a structural insight. *Biochemistry* **51**, 6097–6107
13. Moroney, M. A., Alcaraz, M. J., Forder, R. A., Carey, F., and Hoult, J. R. (1988) Selectivity of neutrophil 5-lipoxygenase and cyclo-oxygenase inhibition by an anti-inflammatory flavonoid glycoside and related aglycone flavonoids. *J. Pharm. Pharmacol.* **40**, 787–792
 14. Rietjens, I. M., Boersma, M. G., van der Woude, H., Jeurissen, S. M., Schutte, M. E., and Alink, G. M. (2005) Flavonoids and alkenylbenzenes: mechanisms of mutagenic action and carcinogenic risk. *Mutat. Res.* **574**, 124–138
 15. Bakir, T., Sönmezöglü, I., Imer, F., and Apak, R. (2014) Antioxidant/prooxidant effects of α -tocopherol, quercetin and isorhamnetin on linoleic acid peroxidation induced by Cu(II) and H₂O₂. *Int. J. Food Sci. Nutr.* **65**, 226–234
 16. Schmalhausen, E. V., Zhlobek, E. B., Shalova, I. N., Firuzi, O., Saso, L., and Muronetz, V. I. (2007) Antioxidant and prooxidant effects of quercetin on glyceraldehyde-3-phosphate dehydrogenase. *Food Chem. Toxicol.* **45**, 1988–1993
 17. Cao, G., Sofic, E., and Prior, R. L. (1997) Antioxidant and prooxidant behavior of flavonoids: structure-activity relationships. *Free Radic. Biol. Med.* **22**, 749–760
 18. Cook, C. L., and Yu, B. P. (1998) Iron accumulation in aging: modulation by dietary restriction. *Mech. Ageing Dev.* **102**, 1–13
 19. Zatta, P., Drago, D., Zambenedetti, P., Bolognin, S., Nogara, E., Peruffo, A., and Cozzi, B. (2008) Accumulation of copper and other metal ions, and metallothionein I/II expression in the bovine brain as a function of aging. *J. Chem. Neuroanat.* **36**, 1–5
 20. Jungbluth, G., Ruhling, I., and Ternes, W. (2000) Oxidation of flavonols with Cu(II), Fe(II) and Fe(III) in aqueous media. *J. Chem. Soc. Perkin Trans. 2*, 1946–1952
 21. Decker, H., and van Holde, K. E. (2011) Coping with Oxygen. in *Oxygen and the Evolution of Life* (Decker, H., and van Holde, K. E., eds) pp. 43–59, Springer, New York
 22. Zhu, B. T., Ezell, E. L., and Liehr, J. G. (1994) Catechol-O-methyltransferase-catalyzed rapid O-methylation of mutagenic flavonoids. Metabolic inactivation as a possible reason for their lack of carcinogenicity *in vivo*. *J. Biol. Chem.* **269**, 292–299
 23. Schubert, H. L., Blumenthal, R. M., and Cheng, X. (2003) Many paths to methyltransfer: a chronicle of convergence. *Trends Biochem. Sci.* **28**, 329–335
 24. Liscombe, D. K., Louie, G. V., and Noel, J. P. (2012) Architectures, mechanisms and molecular evolution of natural product methyltransferases. *Nat. Prod. Rep.* **29**, 1238–1250
 25. Kozbial, P. Z., and Mushegian, A. R. (2005) Natural history of S-adenosylmethionine-binding proteins. *BMC Struct. Biol.* **5**, 19
 26. Scheckhuber, C. Q., and Osiewacz, H. D. (2008) *Podospora anserina*: a model organism to study mechanisms of healthy ageing. *Mol. Genet. Genomics* **280**, 365–374
 27. Averbek, N. B., Jensen, O. N., Mann, M., Schägger, H., and Osiewacz, H. D. (2000) Identification and characterization of PaMTH1, a putative O-methyltransferase accumulating during senescence of *Podospora anserina* cultures. *Curr. Genet.* **37**, 200–208
 28. Kunstmann, B., and Osiewacz, H. D. (2008) Over-expression of an S-adenosylmethionine-dependent methyltransferase leads to an extended lifespan of *Podospora anserina* without impairments in vital functions. *Ageing Cell* **7**, 651–662
 29. Kunstmann, B., and Osiewacz, H. D. (2009) The S-adenosylmethionine dependent O-methyltransferase PaMTH1: a longevity assurance factor protecting *Podospora anserina* against oxidative stress. *Ageing* **1**, 328–334
 30. Studier, F. W. (2005) Protein production by auto-induction in high density shaking cultures. *Protein Expr. Purif.* **41**, 207–234
 31. Mueller, U., Darowski, N., Fuchs, M. R., Förster, R., Hellmig, M., Paithankar, K. S., Pühlinger, S., Steffien, M., Zocher, G., and Weiss, M. S. (2012) Facilities for macromolecular crystallography at the Helmholtz-Zentrum Berlin. *J. Synchrotron Radiat.* **19**, 442–449
 32. Krug, M., Weiss, M. S., Heinemann, U., and Mueller, U. (2012) XDSAPP: a graphical user interface for the convenient processing of diffraction data using XDS. *J. Appl. Crystallogr.* **45**, 568–572
 33. Vonrhein, C., Flensburg, C., Keller, P., Sharff, A., Smart, O., Paciorek, W., Womack, T., and Bricogne, G. (2011) Data processing and analysis with the autoPROC toolbox. *Acta Crystallogr. D Biol. Crystallogr.* **67**, 293–302
 34. Hendrickson, W. A. (1991) Determination of macromolecular structures from anomalous diffraction of synchrotron radiation. *Science* **254**, 51–58
 35. Adams, P. D., Afonine, P. V., Bunkóczi, G., Chen, V. B., Davis, I. W., Echols, N., Headd, J. J., Hung, L. W., Kapral, G. J., Grosse-Kunstleve, R. W., McCoy, A. J., Moriarty, N. W., Oeffner, R., Read, R. J., Richardson, D. C., Richardson, J. S., Terwilliger, T. C., and Zwart, P. H. (2010) PHENIX: a comprehensive Python-based system for macromolecular structure solution. *Acta Crystallogr. D Biol. Crystallogr.* **66**, 213–221
 36. Terwilliger, T. C., Adams, P. D., Read, R. J., McCoy, A. J., Moriarty, N. W., Grosse-Kunstleve, R. W., Afonine, P. V., Zwart, P. H., and Hung, L. W. (2009) Decision-making in structure solution using Bayesian estimates of map quality: the PHENIX AutoSol wizard. *Acta Crystallogr. D Biol. Crystallogr.* **65**, 582–601
 37. Terwilliger, T. C., Grosse-Kunstleve, R. W., Afonine, P. V., Moriarty, N. W., Zwart, P. H., Hung, L. W., Read, R. J., and Adams, P. D. (2008) Iterative model building, structure refinement and density modification with the PHENIX AutoBuild wizard. *Acta Crystallogr. D Biol. Crystallogr.* **64**, 61–69
 38. Emsley, P., and Cowtan, K. (2004) Coot: model-building tools for molecular graphics. *Acta Crystallogr. D Biol. Crystallogr.* **60**, 2126–2132
 39. Afonine, P. V., Grosse-Kunstleve, R. W., Echols, N., Headd, J. J., Moriarty, N. W., Mustyakimov, M., Terwilliger, T. C., Urzhumtsev, A., Zwart, P. H., and Adams, P. D. (2012) Towards automated crystallographic structure refinement with phenix.refine. *Acta Crystallogr. D Biol. Crystallogr.* **68**, 352–367
 40. Winn, M. D., Ballard, C. C., Cowtan, K. D., Dodson, E. J., Emsley, P., Evans, P. R., Keegan, R. M., Krissinel, E. B., Leslie, A. G. W., McCoy, A., McNicholas, S. J., Murshudov, G. N., Pannu, N. S., Potterton, E. A., Powell, H. R., Read, R. J., Vagin, A., and Wilson, K. S. (2011) Overview of the CCP4 suite and current developments. *Acta Crystallogr. D Biol. Crystallogr.* **67**, 235–242
 41. Berman, H. M., Westbrook, J., Feng, Z., Gilliland, G., Bhat, T. N., Weissig, H., Shindyalov, I. N., and Bourne, P. E. (2000) The Protein Data Bank. *Nucleic Acids Res.* **28**, 235–242
 42. Mori, S., Abeygunawardana, C., Johnson, M. O., and van Zijl, P. C. (1995) Improved sensitivity of HSQC spectra of exchanging protons at short interscan delays using a new fast HSQC (FHSQC) detection scheme that avoids water saturation. *J. Magn. Reson. B* **108**, 94–98
 43. Williamson, M. P. (2013) Using chemical shift perturbation to characterise ligand binding. *Prog. Nucl. Magn. Reson. Spectrosc.* **73**, 1–16
 44. Palmer, A. G., Cavanagh, J., Wright, P. E., and Rance, M. (1991) Sensitivity improvement in proton-detected 2-dimensional heteronuclear correlation NMR-spectroscopy. *J. Magn. Reson.* **93**, 151–170
 45. Willker, W., Leibfritz, D., Kerssebaum, R., and Bermel, W. (1993) Gradient selection in inverse heteronuclear correlation spectroscopy. *Magn. Reson. Chem.* **31**, 287–292
 46. Ottink, O. M., Nelissen, F. H., Derks, Y., Wijmenga, S. S., and Heus, H. A. (2010) Enzymatic stereospecific preparation of fluorescent S-adenosyl-L-methionine analogs. *Anal. Biochem.* **396**, 280–283
 47. Zubieta, C., He, X. Z., Dixon, R. A., and Noel, J. P. (2001) Structures of two natural product methyltransferases reveal the basis for substrate specificity in plant O-methyltransferases. *Nat. Struct. Biol.* **8**, 271–279
 48. Krissinel, E., and Henrick, K. (2007) Inference of macromolecular assemblies from crystalline state. *J. Mol. Biol.* **372**, 774–797
 49. Ferrer, J. L., Zubieta, C., Dixon, R. A., and Noel, J. P. (2005) Crystal structures of alfalfa caffeoyl coenzyme A 3-O-methyltransferase. *Plant Physiol.* **137**, 1009–1017
 50. Hou, X., Wang, Y., Zhou, Z., Bao, S., Lin, Y., and Gong, W. (2007) Crystal structure of SAM-dependent O-methyltransferase from pathogenic bacterium *Leptospira interrogans*. *J. Struct. Biol.* **159**, 523–528
 51. Kopycki, J. G., Stubbs, M. T., Brandt, W., Hagemann, M., Porzel, A., Schmidt, J., Schliemann, W., Zenk, M. H., and Vogt, T. (2008) Functional and structural characterization of a cation-dependent O-methyltransferase from the cyanobacterium *Synechocystis* sp. strain PCC 6803. *J. Biol. Chem.* **283**, 20888–20896

Structure and Biophysical Characterization of PaMTH1

52. Garibotto, G., Valli, A., Anderstam, B., Eriksson, M., Suliman, M. E., Balbi, M., Rollando, D., Vigo, E., and Lindholm, B. (2009) The kidney is the major site of *S*-adenosylhomocysteine disposal in humans. *Kidney Int.* **76**, 293–296
53. Holm, L., and Rosenström, P. (2010) Dali server: conservation mapping in 3D. *Nucleic Acids Res.* **38**, W545–W549
54. DeLano, W. L. (2010) *The PyMOL Molecular Graphics System*, version 1.3r1, Schroedinger, LLC, New York
55. Ehler, A., Benz, J., Schlatter, D., and Rudolph, M. G. (2014) Mapping the conformational space accessible to catechol-*O*-methyltransferase. *Acta Crystallogr. D Biol. Crystallogr.* **70**, 2163–2174
56. Martin, J. L., and McMillan, F. M. (2002) SAM (dependent) I AM: the *S*-adenosylmethionine-dependent methyltransferase fold. *Curr. Opin. Struct. Biol.* **12**, 783–793
57. Lee, J. H., Bae, B., Kuemin, M., Circello, B. T., Metcalf, W. W., Nair, S. K., and van der Donk, W. A. (2010) Characterization and structure of Dhpl, a phosphonate *O*-methyltransferase involved in dehydrophos biosynthesis. *Proc. Natl. Acad. Sci. U.S.A.* **107**, 17557–17562
58. Singh, S., McCoy, J. G., Zhang, C., Bingman, C. A., Phillips, G. N., Jr., and Thorson, J. S. (2008) Structure and mechanism of the rebeccamycin sugar 4'-*O*-methyltransferase RebM. *J. Biol. Chem.* **283**, 22628–22636
59. Knab, B., and Osiewacz, H. D. (2010) Methylation of polyphenols with vicinal hydroxyl groups: a protection pathway increasing organismal lifespan. *Cell Cycle* **9**, 3387–3388
60. Serrano, M., and Blasco, M. A. (2007) Cancer and ageing: convergent and divergent mechanisms. *Nat. Rev. Mol. Cell Biol.* **8**, 715–722
61. de Magalhães, J. P. (2013) How ageing processes influence cancer. *Nat. Rev. Cancer* **13**, 357–365
62. Guarente, L., and Kenyon, C. (2000) Genetic pathways that regulate ageing in model organisms. *Nature* **408**, 255–262
63. Cho, J. H., Park, Y., Ahn, J. H., Lim, Y., and Rhee, S. (2008) Structural and functional insights into *O*-methyltransferase from *Bacillus cereus*. *J. Mol. Biol.* **382**, 987–997
64. Kopycki, J. G., Rauh, D., Chumanevich, A. A., Neumann, P., Vogt, T., and Stubbs, M. T. (2008) Biochemical and structural analysis of substrate promiscuity in plant Mg²⁺-dependent *O*-methyltransferases. *J. Mol. Biol.* **378**, 154–164



Protein Structure and Folding:
Structure and Biophysical Characterization
of the *S*-Adenosylmethionine-dependent *O*
-Methyltransferase PaMTH1, a Putative
Enzyme Accumulating during Senescence
of *Podospira anserina*



Deep Chatterjee, Denis Kudlinzki, Verena Linhard, Krishna Saxena, Ulrich Schieborr, Santosh L. Gande, Jan Philip Wurm, Jens Wöhnert, Rupert Abele, Vladimir V. Rogov, Volker Dötsch, Heinz D. Osiewacz, Sridhar Sreeramulu and Harald Schwalbe
J. Biol. Chem. 2015, 290:16415-16430.
doi: 10.1074/jbc.M115.660829 originally published online May 15, 2015

Access the most updated version of this article at doi: [10.1074/jbc.M115.660829](https://doi.org/10.1074/jbc.M115.660829)

Find articles, minireviews, Reflections and Classics on similar topics on the [JBC Affinity Sites](#).

Alerts:

- [When this article is cited](#)
- [When a correction for this article is posted](#)

[Click here](#) to choose from all of JBC's e-mail alerts

This article cites 62 references, 12 of which can be accessed free at <http://www.jbc.org/content/290/26/16415.full.html#ref-list-1>

German summary

Biologische Zellen können zahlreiche unterschiedliche Funktionen wie Signaltransduktion (Informationsübertragung), Transport, Immunabwehr und Metabolismus ausführen und steuern. Das Wissen um die Wirkweise der Prozesse dieser molekularen Mechanismen ist die Grundlage für zielorientiertes und rationales Wirkstoffdesign. Hierfür ist es hilfreich, die strukturellen und funktionellen Aspekte aller beteiligten Makromoleküle zu analysieren. Die vorliegende Dissertation beschreibt die biophysikalische Charakterisierung von Proteinstrukturen und evaluiert die biologische Signifikanz von Informationen zur Proteindynamik. Membranrezeptoren und Enzyme regulieren diese Vielschichtigkeit von Funktionen in biologischen Systemen und sind daher hervorragend für Struktur- und Funktionsuntersuchungen geeignet. Aus pharmazeutischem Blickwinkel stellen Rezeptoren und Enzyme eminent wichtige Wirkstoff-Zielproteine (Drug targets) dar, da der Großteil der aktuellen Medikamente an diese zwei Proteinklassen (30% an Rezeptoren und 47% an Enzymen) bindet. Wissenschaftliche Untersuchungen an diesen Proteinklassen ermöglichen daher nicht nur detaillierte neue Erkenntnisse über das einzelne Proteinmolekül, sondern bilden zumeist das Fundament für neue pharmazeutische Applikationen. Daher stammt das Gros der Informationen über Rezeptoren und deren Aktivierung oder über Enzymaktivitäten aus solchen Struktur-/Funktionsuntersuchungen.

Kapitel 1 (Allgemeine Einleitung) der vorliegenden Arbeit umfasst die Einführung in die Welt der Proteine. Dieses Kapitel beschreibt detailliert G-Protein gekoppelten Rezeptoren (GPCRs) und Methyltransferasen (MT). Der erste Teil des Kapitels ist GPCRs gewidmet und fasst deren Klassifizierung, strukturelle Merkmale und Funktionen zusammen. GPCRs sind mit einem Anteil von fast 15% aller Membranproteine die häufigsten Membranrezeptoren in Säugetierzellen. Die Superfamilie der GPCRs besteht aus ca. 800 Vertretern und wird in sechs Klassen (A-F) unterteilt. Klasse A umfasst die Rhodopsine, Peptidhormone und olfaktorischen GPCRs und ist somit die weit verbreitetste Klasse mit 85% aller GPCRs. Der strukturelle Aufbau mit 7-transmembranen α -Helices mit verschiedenen Liganden-Bindungsstellen ist hochkonserviert. Obwohl GPCRs sehr verschiedene Liganden von subatomaren Partikeln (Photon) bis hin zu Proteinen binden können, ist der generelle Aktivierungsmechanismus nach Ligandenbindung und der anschließende Signaltransduktionsprozess hochkonserviert. Es werden zwei Haupt-Signaltransduktionswege bei GPCRs unterschieden: der cAMP-abhängige Signalweg und der Phosphatidylinositol-Signalweg. Die GPCR-Proteinklasse

besitzt eine große therapeutische Relevanz, so dass ein großer Anteil (30%) der zugelassenen Arzneimittel GPCRs als Wirkort haben. Der zweite Teil des Kapitels beschäftigt sich mit der detaillierten strukturellen und funktionellen Charakterisierung von Methyltransferasen. Unterschiedliche relevante Zellprozesse wie zum Beispiel der Wirkstoff-Metabolismus, die Transkription von Genen oder epigenetische Regulationen werden durch Methylierung moduliert, wobei die modifizierten Zielmoleküle von kleinen Biomolekülen bis hin zu großen Proteinen variieren. Die Proteinklasse der Methyltransferasen (MTs) katalysieren diese Methylierungsreaktionen, indem sie den Methylgruppentransfer auf ein Akzeptor-Molekül durch eine SN₂-ähnliche nukleophile Substitution verwirklichen. MTs können aufgrund ihrer Zielatomspezifität klassifiziert werden, wobei der Transfer auf ein O (54% aller MTs), N (23%), C (18%), S (3%) und andere Akzeptoren (wie Halide; 2%) erfolgen kann. Eine andere Kategorisierung in fünf verschiedene Klassen (Klasse I-V) ergibt sich aus unterschiedlichen strukturellen Eigenschaften, die Substrat-Erkennung und katalytischen Aktivität bestimmen. Zwei charakteristische Strukturmodule von MTs sind Rossmann- und SET-Domänen (*Drosophila* Su(var)3-9 und 'Enhancer of zeste' Proteine). Eine Fehlfunktion von MTs konnte - ähnlich wie bei GPCR-Fehlfunktionen - bei verschiedenen Krankheiten (zum Beispiel bei neuropsychiatrischen Erkrankungen und Krebs) diagnostiziert werden. Daher sind auch MTs vielversprechende Zielmoleküle für die Wirkstoffentwicklung. Der letzte Teil dieses Kapitels diskutiert die biologische Bedeutung der Strukturbiologie, die Informationen zu räumlichen Struktur und zur konformationellen Dynamik von Proteinen generiert. Zahlreiche strukturbiologische Untersuchungen fokussieren sich hauptsächlich auf zwei biophysikalische Techniken, Röntgenstrukturanalyse und NMR, wobei die Vor- und Nachteile dieser Methoden im Kapitel diskutiert werden. Anschließend wird das dynamische Verhalten von Proteinen mit Beispielen für die verschiedenen Zeitbereiche aufgezeigt. Bei der Erforschung dieser dynamischen Prozesse auf atomarer Ebene unter physiologischen Bedingungen spielt die NMR Spektroskopie eine entscheidende Rolle. Exemplarisch für eine besonders leistungsfähige NMR-Technik zur Charakterisierung von Proteindynamiken wird die Echtzeit-NMR-Spektroskopie (real time NMR) beschrieben, die extensiv zur Erforschung von physikalischen Prozessen wie Proteinfaltung, Enzymkatalyse, Proteindomänen-Neuanordnung im Detail erklärt wird.

Der zweite (kumulative) Teil der vorliegenden Arbeit enthält die innerhalb der Doktorarbeit veröffentlichten Originalpublikationen, welche in zwei Kapiteln gemäß ihrer Themen gegliedert sind:

- *NMR-spectroscopic characterization of the transiently populated photointermediates of bovine rhodopsin and its interaction with arrestin (Kapitel 3)*

- *Structural and biophysical characterization of PaMTH1, a putative SAM dependent O-methyltransferase from filamentous fungi Podospora anserina (Kapitel 4)*
Jedes Kapitel beginnt mit einer kurzen Einleitung, die den Hintergrund und die Grundstruktur der bearbeiteten wissenschaftlichen Fragestellung erläutert.

Kapitel 2 behandelt das bovine visuelle Rhodopsin, das Modellsystem aller GPCRs, welches eine bedeutende Rolle bei der visuellen Signaltransduktion in Stäbchenzellen von Säugetieren spielt. Die Struktur, die Aktivierung und die Inaktivierungswege des Rhodopsins werden hier ausführlich und im Hinblick auf dessen Fotozyklus diskutiert. Die lichtabhängige Isomerisierung des Rhodopsinretinal-Chromophors von 11-cis zur all-trans Konfiguration führt zu erheblichen Konformationsänderungen mit anschließender Bildung verschiedener transient-populierter Intermediatzuständen. Unter diesen Zwischenzuständen erscheinen die meta II und meta III Zustände als wissenschaftlich besonders interessant, weil sie durch ihre langsamere Zerfallskinetik als die geschwindigkeitsbestimmenden Schritte erachtet werden. Im **Kapitel 3.8** sind die Ergebnisse der Publikation über die Echtzeit-NMR Charakterisierung der lichtinduzierten meta II und meta III Zwischenzustände (Abbildung 5.1) beschrieben. Hierzu wurden die fünf Tryptophane (W35, W126, W161, W175 und W265) im Rhodopsin selektiv ^{15}N -isotopenmarkiert und fungierten als Reportergruppen für die kinetischen Prozesse nach Lichtaktivierung. Die hierbei gewonnenen Informationen über dynamische Prozesse des Rhodopsins (Aktivierung, Signalweitergabe und Inaktivierung) sind fundamental für das Verständnis der GPCR-Regulationsprozesse innerhalb der GPCR Proteinfamilie.

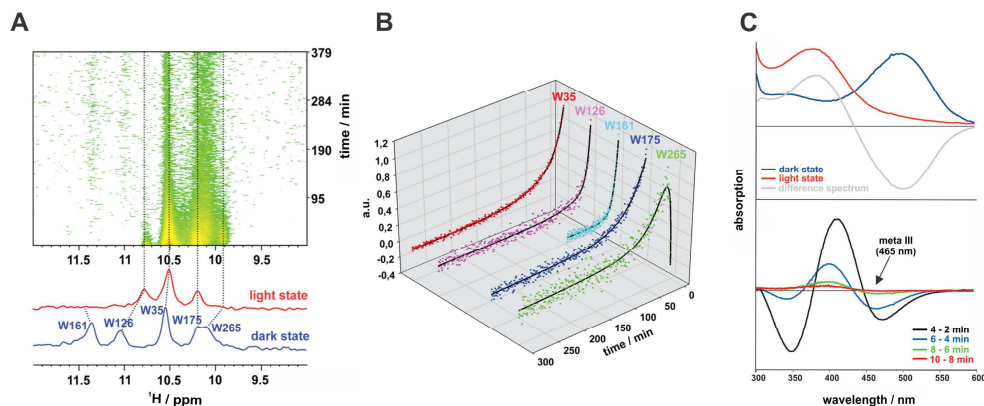


Abbildung 5.1: Photodynamische Untersuchungen am bovinen Rhodopsin. A) 1D ^1H NMR Spektren des α,ϵ - ^{15}N -Tryptophan-markierten Rhodopsins nach Belichtung. B) Extrahierte Signalintensitäten der NMR Spektren wurden normalisiert und in Abhängigkeit von der Zeit dargestellt. Jeder Plot wurde als Exponentialfunktion ausgewertet. C) oben: Absorptionsspektren des unbelichteten (blau) und belichteten (rot) Rhodopsins. Das entsprechende Differenzspektrum ist in grau dargestellt. unten: Doppeldifferenzspektren des Rhodopsins nach Belichtung zu unterschiedlichen Zeitpunkten.

Ergebnisse

- Etablierung eines rekombinanten humanen Expressionssystem (stabile Rhodopsin Expression in HEK293 Zellen) im Großmaßstab für posttranslational modifizierte und isotopenmarkierte Gewinnung von Rhodopsin für NMR Studien.
- Die kinetische Analyse des meta II und meta III Aktivierungs- und Zerfallsprozesses wurde unter physiologischen Bedingungen durchgeführt.
- Die Auswertung der kinetischen Daten der räumlich unterschiedlichen Tryptophan-Reportergruppen bestätigt und erweitert die mittels Proteinkristallographie erhaltenen Strukturinformationen über die Rhodopsin-Photointermediatzustände.

Kapitel 3 beschäftigt sich mit der Interaktion des bovinen Rhodopsins mit visuellem Arrestin, das zu einer Proteinfamilie gehört, welche die Deaktivierungsprozesse von GPCRs steuert. Die Proteinstruktur und die Funktion des visuellen Arrestins bei der Deaktivierung des Rhodopsins werden in **Kapitel 3.6** beschrieben. Der veröffentlichte Artikel in **Kapitel 3.9** zeigt die Effekte des bovinen visuellen Arrestins (verkürzte Form Arr^{Tr}) auf die photodynamischen Prozesse des meta II und meta III Rhodopsinzwischenzustände (Abbildung 5.2).

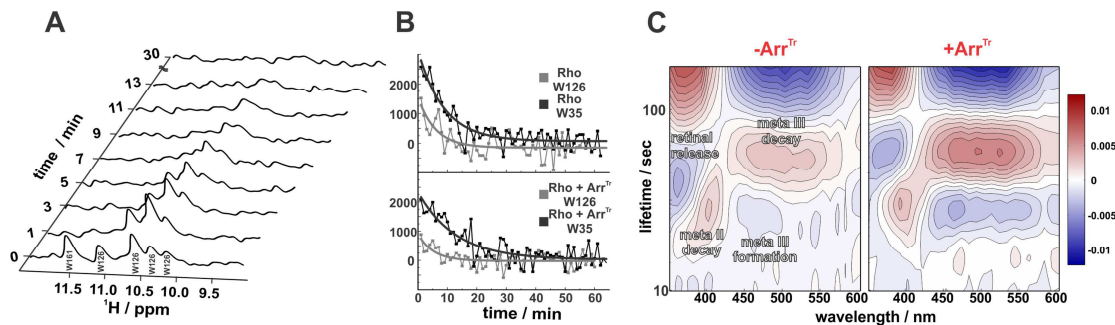


Abbildung 5.2: Interaktion des bovinen visuellen Rhodopsins mit Arrestin. A) 1D ¹H NMR Spektren des α,ϵ -¹⁵N-Tryptophan-markierten Rhodopsins nach Beleuchtung in verschiedenen Zeitintervallen mit und ohne Arrestin (Arr^{Tr}). B) Extrahierte Signalintensitäten der NMR Spektren von Rhodopsin mit und ohne Arrestin (Arr^{Tr}). Ein monoexponentieller Plot ergab sich für die Signalintensitäten des W35 (schwarze Kurve) und für W126 (graue Kurve). C) "Lebenszeit-Dichte"-Analyse (Lifetime density analysis, (LDM)) der transienten Absorptionsdaten des Rhodopsins (25 μ M) mit und ohne Arr^{Tr} (100 μ M).

Ergebnisse

- Mit Hilfe zweier biophysikalischen Techniken (NMR und Blitz-Photolyse-Absorptionsspektroskopie) erhielt man Einblicke in die Rolle von Arrestin bei der Deaktivierung des Rhodopsins und des Regenerationsprozesses von Retinal.

- Ein stabilisierender Einfluss von Arrestin auf den meta III Zustand im Rhodopsin-Fotozyklus konnte beobachtet werden, der für die Regulation der freien *all-trans* Retinalkonzentration im Stäbchen-Außensegment (rod outer segment) benötigt wird.

Kapitel 4 behandelt PaMTH1, eine putative SAM-abhängige O-Methyltransferase (MT) des filamentösen Pilzes *Podospora anserina*. Es wird angenommen, dass diese MT in Alterungsprozesse involviert ist, da sie eine Rolle bei altersbedingten Methylierungsreaktionen spielt und alternde *P. anserina* Kulturen gegen oxidativen Stress schützt. Der veröffentlichte Artikel diskutiert die Proteinstruktur und die biophysikalische Charakterisierung von PaMTH1. Der enzymatische Mechanismus wird in **Kapitel 4.8** beschrieben (Abbildung 5.3).

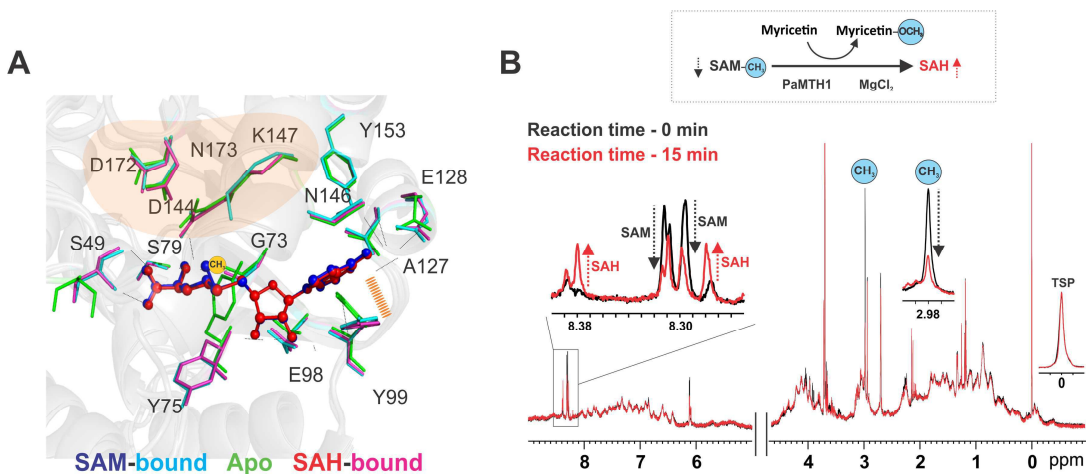


Abbildung 5.3: Biophysikalische Charakterisierung von PaMTH1. A. PaMTH1 Kristallstrukturen: apo (grün) und mit gebundenen Substraten SAM (blau) / SAH (rot) mit Blick auf die katalytische Tasche. B. Nachweis des PaMTH1-katalysierten Methylgruppentransfers mittels 1D ¹H NMR.

Ergebnisse

- Aufklärung verschiedener PaMTH1 Kristallstrukturen mit (SAM, SAH) und ohne gebundene Substrate.
- Nachweis der enzymatisch katalysierten Methylierung des Substrats Myricetin durch PaMTH1 mit Hilfe von NMR-Experimenten und anderen biophysikalischen Techniken.

References

- [1] J. C. Venter, *Science*. **2001**, *291*, 1304–1351.
- [2] J. Drews, *Nat. Biotechnol.* **1996**, *14*, 1516–1518.
- [3] J. Drews, S. Ryser, *Nat. Biotechnol.* **1997**, *15*, 1318–1319.
- [4] D. Bailey, E. Zanders, P. Dean, *Nat. Biotechnol.* **2001**, *19*, 207–209.
- [5] A. L. Hopkins, C. R. Groom, *Nat. Rev. Drug Discov.* **2002**, *1*, 727–730.
- [6] E. Worgotter, G. Wagner, K. Wiithrich, **1986**, *108*, 6162–6167.
- [7] G. von Heijne, *J. Intern. Med.* **2007**, *261*, 543–557.
- [8] R. Fredriksson, M. C. Lagerström, L.-G. Lundin, H. B. Schiöth, *Mol. Pharmacol.* **2003**, *63*, 1256–1272.
- [9] W. B. Vanti, S. Swaminathan, R. Blevins, J. A. Bonini, B. F. O'Dowd, S. R. George, R. L. Weinshank, K. E. Smith, W. J. Bailey, *Expert Opin. Ther. Pat.* **2001**, *11*, 1861–1887.
- [10] O. Civelli, R. K. Reinscheid, Y. Zhang, Z. Wang, R. Fredriksson, H. B. Schiöth, *Annu. Rev. Pharmacol. Toxicol.* **2013**, *53*, 127–146.
- [11] T. K. Bjarnadóttir, D. E. Gloriam, S. H. Hellstrand, H. Kristiansson, R. Fredriksson, H. B. Schiöth, *Genomics* **2006**, *88*, 263–273.
- [12] T. K. Attwood, J. B. Findlay, *Protein Eng.* **1994**, *7*, 195–203.
- [13] L. F. Kolakowski, *Receptors Channels* **1994**, *2*, 1–7.
- [14] S. M. Foord, T. I. Bonner, R. R. Neubig, E. M. Rosser, J.-P. Pin, A. P. Davenport, M. Spedding, A. J. Harmar, *Pharmacol. Rev.* **2005**, *57*, 279–288.
- [15] P. Joost, A. Methner, *Genome Biol.* **2002**, *3*, 1-16.
- [16] S. M. Migglin, O. A. Lawler, B. T. Kinsella, *J. Biol. Chem.* **2003**, *278*, 6947–6958.
- [17] V. Cherezov, D. M. Rosenbaum, M. A. Hanson, S. G. F. Rasmussen, F. S. Thian, T. S. Kobilka, H.-J. Choi, P. Kuhn, W. I. Weis, B. K. Kobilka, et al., *Science*. **2007**, *318*, 1258–1265.
- [18] P. G. Charest, M. Bouvier, *J. Biol. Chem.* **2003**, *278*, 41541–41551.
- [19] E. Ponimaskin, A. Dumuis, F. Gaven, G. Barthet, M. Heine, K. Glebov, D. W. Richter, M. Oppermann, *Mol. Pharmacol.* **2005**, *67*, 1434–1443.
- [20] M. J. Lohse, J. L. Benovic, J. Codina, M. G. Caron, R. J. Lefkowitz, *Science* **1990**, *248*, 1547–1550.
- [21] L. M. Luttrell, R. J. Lefkowitz, *J. Cell Sci.* **2002**, *115*, 455–465.
- [22] A. J. Harmar, *Genome Biol.* **2001**, *2*, 1-10.
- [23] H. Ohashi, T. Maruyama, H. Higashi-Matsumoto, T. Nomoto, S. Nishimura, Y. Takeuchi, *Zeitschrift für Naturforschung. C, J. Biosci.* **2002**, *57*, 348–355.
- [24] N. Nakayama, A. Miyajima, K. Arai, *EMBO J.* **1985**, *4*, 2643–2648.
- [25] A. C. Burkholder, L. H. Hartwell, *Nucleic Acids Res.* **1985**, *13*, 8463–8475.
- [26] L. Marsh, I. Herskowitz, *Proc. Natl. Acad. Sci. U. S. A.* **1988**, *85*, 3855–3859.
- [27] J. Taipale, J. K. Chen, M. K. Cooper, B. Wang, R. K. Mann, L. Milenkovic, M. P. Scott, P. A. Beachy, *Nature* **2000**, *406*, 1005–1009.
- [28] C. C. Malbon, *Front. Biosci.* **2004**, *9*, 1048–1058.
- [29] “GPCR network. in <http://gpcr.scripps.edu/>,” **2013**.
- [30] K. Palczewski, T. Kumasaka, T. Hori, C. A. Behnke, H. Motoshima, B. A. Fox, I. Le Trong, D. C. Teller, T. Okada, R. E. Stenkamp, et al., *Science* **2000**, *289*, 739–745.
- [31] P. Scheerer, J. H. Park, P. W. Hildebrand, Y. J. Kim, N. Krauss, H.-W. Choe, K. P. Hofmann, O. P. Ernst, *Nature* **2008**, *455*, 497–502.
- [32] D. Zhang, Q. Zhao, B. Wu, *Mol. Cells* **2015**, *38*, 836–842.
- [33] A. J. Venkatakrisnan, X. Deupi, G. Lebon, C. G. Tate, G. F. Schertler, M. M. Babu, *Nature* **2013**, *494*, 185–194.
- [34] B. K. Kobilka, *Biochim. Biophys. Acta* **2007**, *1768*, 794–807.
- [35] D. M. Rosenbaum, S. G. F. Rasmussen, B. K. Kobilka, *Nature* **2009**, *459*, 356–63.
- [36] B. Kobilka, G. F. X. Schertler, *Trends Pharmacol. Sci.* **2008**, *29*, 79–83.

- [37] T. H. Ji, M. Grossmann, I. Ji, *J. Biol. Chem.* **1998**, *273*, 17299–17302.
- [38] J.-P. Pin, T. Galvez, L. Prézéau, *Pharmacol. Ther.* **2003**, *98*, 325–354.
- [39] H. E. Hamm, *J. Biol. Chem.* **1998**, *273*, 669–72.
- [40] N. Tuteja, *Plant Signal. Behav.* **2009**, *4*, 942–947.
- [41] A. G. Gilman, *Annu. Rev. Biochem.* **1987**, *56*, 615–49.
- [42] D. Horton, A. R., Moran, A. L., Scrimgeour, G., Perry, M., Rawn, *Principles of Biochemistry*, Pearson Prentice Hall Inc., **2006**.
- [43] C. W. Voet, D., Voet, J. G., Pratt, *Fundamentals of Biochemistry*, Wiley, **2002**.
- [44] D. E. Logothetis, Y. Kurachi, J. Galper, E. J. Neer, D. E. Clapham, *Nature* **1987**, *325*, 321–6.
- [45] C. E. Ford, N. P. Skiba, H. Bae, Y. Daaka, E. Reuveny, L. R. Shekter, R. Rosal, G. Weng, C. S. Yang, R. Iyengar, et al., *Science* **1998**, *280*, 1271–1274.
- [46] P. Rondard, T. Iiri, S. Srinivasan, E. Meng, T. Fujita, H. R. Bourne, *Proc. Natl. Acad. Sci. U. S. A.* **2001**, *98*, 6150–6155.
- [47] M. T. Drake, S. K. Shenoy, R. J. Lefkowitz, *Circ. Res.* **2006**, *99*, 570–582.
- [48] N. Kawakami, K. Miyoshi, S. Horio, H. Fukui, *J. Pharmacol. Sci.* **2004**, *94*, 449–458.
- [49] J.-F. Chen, P. K. Sonsalla, F. Pedata, A. Melani, M. R. Domenici, P. Popoli, J. Geiger, L. V. Lopes, A. de Mendonça, *Prog. Neurobiol.* **2007**, *83*, 310–331.
- [50] W. Duan, L. Gui, Z. Zhou, Y. Liu, H. Tian, J.-F. Chen, J. Zheng, *J. Neurol. Sci.* **2009**, *285*, 39–45.
- [51] P. A. Insel, C.-M. Tang, I. Hahntow, M. C. Michel, *Biochim. Biophys. Acta* **2007**, *1768*, 994–1005.
- [52] S. Li, S. Huang, S.-B. Peng, *Int. J. Oncol.* **2005**, *27*, 1329–1339.
- [53] H. F. Vischer, J. W. Hulshof, I. J. P. de Esch, M. J. Smit, R. Leurs, *Ernst Schering Found. Symp. Proc.* **2006**, 187–209.
- [54] J. R. Kirshner, K. Staskus, A. Haase, M. Lagunoff, D. Ganem, *J. Virol.* **1999**, *73*, 6006–6014.
- [55] S. Montaner, A. Sodhi, A. K. Ramsdell, D. Martin, J. Hu, E. T. Sawai, J. S. Gutkind, *Cancer Res.* **2006**, *66*, 168–174.
- [56] J. Drews, *Science* **2000**, *287*, 1960–1964.
- [57] P. Ma, R. Zimmel, *Nat. Rev. Drug Discov.* **2002**, *1*, 571–572.
- [58] D. K. Vassilatis, J. G. Hohmann, H. Zeng, F. Li, J. E. Ranchalis, M. T. Mortrud, A. Brown, S. S. Rodriguez, J. R. Weller, A. C. Wright, et al., *Proc. Natl. Acad. Sci. U. S. A.* **2003**, *100*, 4903–4908.
- [59] J. P. Overington, B. Al-Lazikani, A. L. Hopkins, *Nat. Rev. Drug Discov.* **2006**, *5*, 993–996.
- [60] J. B. Sumner, *J. Biol. Chem.* **1926**, *69*, 435–441.
- [61] C. C. Blake, D. F. Koenig, G. A. Mair, A. C. North, D. C. Phillips, V. R. Sarma, *Nature* **1965**, *206*, 757–761.
- [62] EMBL-EBI, “<http://www.ebi.ac.uk/thornton-srv/databases/enzymes/>,” **2004**.
- [63] NC-IUBMB, **1955**.
- [64] K. Tipton, S. Boyce, *Bioinformatics* **2000**, *16*, 34–40.
- [65] P. Siedlecki, P. Zielenkiewicz, *Acta Biochim. Pol.* **2006**, *53*, 245–256.
- [66] G. L. Cantoni, *Annu. Rev. Biochem.* **1975**, *44*, 435–451.
- [67] H. L. Schubert, R. M. Blumenthal, X. Cheng, *Trends Biochem. Sci.* **2003**, *28*, 329–335.
- [68] S. C. Lu, *Int. J. Biochem. Cell Biol.* **2000**, *32*, 391–395.
- [69] R. W. Woodard, M. D. Tsai, H. G. Floss, P. A. Crooks, J. K. Coward, *J. Biol. Chem.* **1980**, *255*, 9124–9127.
- [70] J. C. Wu, D. V. Santi, *J. Biol. Chem.* **1987**, *262*, 4778–4786.
- [71] M. Goodall, N. Kirshner, *Circulation* **1958**, *17*, 366–371.
- [72] P. T. Männistö, I. Ulmanen, K. Lundström, J. Taskinen, J. Tenhunen, C. Tilgmann, S. Kaakkola, *Prog. drug Res. Fortschritte der Arzneimittelforschung. Progrès des*

- Rech. Pharm.* **1992**, *39*, 291–350.
- [73] A. Razin, H. Cedar, *Microbiol. Rev.* **1991**, *55*, 451–458.
- [74] S. I. S. Grewal, J. C. Rice, *Curr. Opin. Cell Biol.* **2004**, *16*, 230–238.
- [75] J. A. Cobb, D. M. Roberts, *J. Biol. Chem.* **2000**, *275*, 18969–18975.
- [76] T. Wlodarski, J. Kutner, J. Towpik, L. Knizewski, L. Rychlewski, A. Kudlicki, M. Rowicka, A. Dziembowski, K. Ginalski, *PLoS One* **2011**, *6*, e23168.
- [77] E. Lissina, B. Young, M. L. Urbanus, X. L. Guan, J. Lowenson, S. Hoon, A. Baryshnikova, I. Riezman, M. Michaut, H. Riezman, et al., *PLoS Genet.* **2011**, *7*, e1002332.
- [78] J. Vidgren, L. A. Svensson, A. Liljas, *Nature* **1994**, *368*, 354–358.
- [79] B. T. Zhu, E. L. Ezell, J. G. Liehr, *J. Biol. Chem.* **1994**, *269*, 292–299.
- [80] T. Bureau, K. C. Lam, R. K. Ibrahim, B. Behdad, S. Dayanandan, *Genome* **2007**, *50*, 1001–1013.
- [81] G. V Louie, M. E. Bowman, Y. Tu, A. Mouradov, G. Spangenberg, J. P. Noel, *Plant Cell* **2010**, *22*, 4114–4127.
- [82] J. G. Kopycki, M. T. Stubbs, W. Brandt, M. Hagemann, A. Porzel, J. Schmidt, W. Schliemann, M. H. Zenk, T. Vogt, *J. Biol. Chem.* **2008**, *283*, 20888–20896.
- [83] J. G. Kopycki, D. Rauh, A. A. Chumanevich, P. Neumann, T. Vogt, M. T. Stubbs, *J. Mol. Biol.* **2008**, *378*, 154–164.
- [84] D. K. Liscombe, G. V Louie, J. P. Noel, *Nat. Prod. Rep.* **2012**, *29*, 1238–1250.
- [85] K. Wada, J. Harada, Y. Yaeda, H. Tamiaki, H. Oh-Oka, K. Fukuyama, *FEBS J.* **2007**, *274*, 563–573.
- [86] J. Vévodová, R. M. Graham, E. Raux, H. L. Schubert, D. I. Roper, A. A. Brindley, A. Ian Scott, C. A. Roessner, N. P. J. Stamford, M. Elizabeth Stroupe, et al., *J. Mol. Biol.* **2004**, *344*, 419–433.
- [87] J. W. Schmidberger, A. B. James, R. Edwards, J. H. Naismith, D. O'Hagan, *Angew. Chem. Int. Ed. Engl.* **2010**, *49*, 3646–3648.
- [88] Y. Nagatoshi, T. Nakamura, *J. Biol. Chem.* **2009**, *284*, 19301–19309.
- [89] H. Toda, N. Itoh, *Phytochemistry* **2011**, *72*, 337–343.
- [90] J. M. Attieh, A. D. Hanson, H. S. Saini, *J. Biol. Chem.* **1995**, *270*, 9250–9257.
- [91] Y. Peng, Q. Feng, D. Wilk, A. A. Adjei, O. E. Salavaggione, R. M. Weinshilboum, V. C. Yee, *Biochemistry* **2008**, *47*, 6216–6225.
- [92] X. Cheng, S. Kumar, S. Klimasauskas, R. J. Roberts, *Cold Spring Harb. Symp. Quant. Biol.* **1993**, *58*, 331–338.
- [93] P. Z. Kozbial, A. R. Mushegian, *BMC Struct. Biol.* **2005**, *5*, 19.
- [94] Y. Huang, J. Komoto, K. Konishi, Y. Takata, H. Ogawa, T. Gomi, M. Fujioka, F. Takusagawa, *J. Mol. Biol.* **2000**, *298*, 149–162.
- [95] M. M. Dixon, S. Huang, R. G. Matthews, M. Ludwig, *Structure* **1996**, *4*, 1263–1275.
- [96] H. L. Schubert, K. S. Wilson, E. Raux, S. C. Woodcock, M. J. Warren, *Nat. Struct. Biol.* **1998**, *5*, 585–592.
- [97] G. Michel, V. Sauvé, R. Larocque, Y. Li, A. Matte, M. Cygler, *Structure* **2002**, *10*, 1303–1315.
- [98] O. Nureki, M. Shirouzu, K. Hashimoto, R. Ishitani, T. Terada, M. Tamakoshi, T. Oshima, M. Chijimatsu, K. Takio, D. G. Vassilyev, et al., *Acta Crystallogr. D. Biol. Crystallogr.* **2002**, *58*, 1129–1137.
- [99] X. Zhang, H. Tamaru, S. I. Khan, J. R. Horton, L. J. Keefe, E. U. Selker, X. Cheng, *Cell* **2002**, *111*, 117–127.
- [100] R. C. Trievel, B. M. Beach, L. M. A. Dirk, R. L. Houtz, J. H. Hurley, *Cell* **2002**, *111*, 91–103.
- [101] J. R. Wilson, C. Jing, P. A. Walker, S. R. Martin, S. A. Howell, G. M. Blackburn, S. J. Gamblin, B. Xiao, *Cell* **2002**, *111*, 105–115.
- [102] J. Min, X. Zhang, X. Cheng, S. I. S. Grewal, R.-M. Xu, *Nat. Struct. Biol.* **2002**, *9*, 828–832.

- [103] S. A. Jacobs, J. M. Harp, S. Devarakonda, Y. Kim, F. Rastinejad, S. Khorasanizadeh, *Nat. Struct. Biol.* **2002**, *9*, 833–838.
- [104] T. Kwon, J. H. Chang, E. Kwak, C. W. Lee, A. Joachimiak, Y. C. Kim, J. Lee, Y. Cho, *EMBO J.* **2003**, *22*, 292–303.
- [105] S. Wedrén, T. R. Rudqvist, F. Granath, E. Weiderpass, M. Ingelman-Sundberg, I. Persson, C. Magnusson, *Carcinogenesis* **2003**, *24*, 681–687.
- [106] C. J. Klein, M.-V. Botuyan, Y. Wu, C. J. Ward, G. A. Nicholson, S. Hammans, K. Hojo, H. Yamanishi, A. R. Karpf, D. C. Wallace, et al., *Nat. Genet.* **2011**, *43*, 595–600.
- [107] A. P. Feinberg, B. Vogelstein, *Nature* **1983**, *301*, 89–92.
- [108] A. D. Riggs, P. A. Jones, *Adv. Cancer Res.* **1983**, *40*, 1–30.
- [109] P. C. Taberlay, P. A. Jones, *Prog. drug Res. Fortschritte der Arzneimittelforschung. Progrès des Rech. Pharm.* **2011**, *67*, 1–23.
- [110] M. J. Bonifácio, P. N. Palma, L. Almeida, P. Soares-da-Silva, *CNS Drug Rev.* **2007**, *13*, 352–379.
- [111] E. J. B. Derissen, J. H. Beijnen, J. H. M. Schellens, *Oncologist* **2013**, *18*, 619–624.
- [112] N. B. Averbeck, O. N. Jensen, M. Mann, H. Schägger, H. D. Osiewacz, *Curr. Genet.* **2000**, *37*, 200–208.
- [113] H. D. Osiewacz, *Mech. Ageing Dev.* **2002**, *123*, 755–764.
- [114] D. W. Green, V. M. Ingram, M. F. Perutz, *Proc. R. Soc. A Math. Phys. Eng. Sci.* **1954**, *225*, 287–307.
- [115] J. C. Kendrew, G. Bodo, H. M. Dintzis, R. G. Parrish, H. Wyckoff, D. C. Phillips, *Nature* **1958**, *181*, 662–666.
- [116] M. P. Williamson, T. F. Havel, K. Wüthrich, *J. Mol. Biol.* **1985**, *182*, 295–315.
- [117] M. Bolognesi, G. Gatti, E. Menegatti, M. Guarneri, M. Marquart, E. Papamokos, R. Huber, *J. Mol. Biol.* **1982**, *162*, 839–868.
- [118] A. D. Kline, W. Braun, K. Wüthrich, *J. Mol. Biol.* **1988**, *204*, 675–724.
- [119] M. Billeter, A. D. Kline, W. Braun, R. Huber, K. Wüthrich, *J. Mol. Biol.* **1989**, *206*, 677–687.
- [120] H. M. Berman, *Nucleic Acids Res.* **2000**, *28*, 235–242.
- [121] K. Wüthrich, *Acta Crystallogr. D. Biol. Crystallogr.* **1995**, *51*, 249–70.
- [122] J. F. Doreleijers, G. Vriend, M. L. Raves, R. Kaptein, *Proteins* **1999**, *37*, 404–16.
- [123] S. B. Nabuurs, E. Krieger, C. A. E. M. Spronk, A. J. Nederveen, G. Vriend, G. W. Vuister, *J. Biomol. NMR* **2005**, *33*, 123–134.
- [124] L. E. Kay, *Nat. Struct. Biol.* **1998**, *5 Suppl*, 513–517.
- [125] R. Ishima, D. A. Torchia, *Nat. Struct. Biol.* **2000**, *7*, 740–743.
- [126] T. Werner, M. B. Morris, S. Dastmalchi, W. B. Church, *Adv. Drug Deliv. Rev.* **2012**, *64*, 323–343.
- [127] A. G. Palmer, F. Massi, *Chem. Rev.* **2006**, *106*, 1700–1719.
- [128] A. Mittermaier, L. E. Kay, *Science* **2006**, *312*, 224–228.
- [129] K. Henzler-Wildman, D. Kern, *Nature* **2007**, *450*, 964–972.
- [130] S.-R. Tzeng, C. G. Kalodimos, *Nature* **2009**, *462*, 368–372.
- [131] N. Popovych, S. Sun, R. H. Ebright, C. G. Kalodimos, *Nat. Struct. Mol. Biol.* **2006**, *13*, 831–838.
- [132] C. Bracken, P. A. Carr, J. Cavanagh, A. G. Palmer, *J. Mol. Biol.* **1999**, *285*, 2133–2146.
- [133] N. Trbovic, J.-H. Cho, R. Abel, R. A. Friesner, M. Rance, A. G. Palmer, *J. Am. Chem. Soc.* **2009**, *131*, 615–622.
- [134] M. S. Marlow, J. Dogan, K. K. Frederick, K. G. Valentine, A. J. Wand, *Nat. Chem. Biol.* **2010**, *6*, 352–358.
- [135] D. Yang, L. E. Kay, *J. Mol. Biol.* **1996**, *263*, 369–382.
- [136] A. L. Lee, A. J. Wand, *Nature* **2001**, *411*, 501–504.
- [137] E. L. Kovrigin, R. Cole, J. P. Loria, *Biochemistry* **2003**, *42*, 5279–5291.
- [138] A. G. Palmer, M. J. Grey, C. Wang, *Methods Enzymol.* **2005**, *394*, 430–465.

- [139] A. G. Palmer, C. D. Kroenke, J. P. Loria, *Methods Enzymol.* **2001**, 339, 204–238.
- [140] M. Zeeb, J. Balbach, *Methods* **2004**, 34, 65–74.
- [141] S. M. Harper, L. C. Neil, I. J. Day, P. J. Hore, K. H. Gardner, *J. Am. Chem. Soc.* **2004**, 126, 3390–3391.
- [142] A. Corazza, E. Rennella, P. Schanda, M. C. Mimmi, T. Cutuil, S. Raimondi, S. Giorgetti, F. Fogolari, P. Viglino, L. Frydman, et al., *J. Biol. Chem.* **2010**, 285, 5827–5835.
- [143] I. C. Felli, B. Brutscher, *Chemphyschem* **2009**, 10, 1356–1368.
- [144] P. Schanda, E. Kupce, B. Brutscher, *J. Biomol. NMR* **2005**, 33, 199–211.
- [145] M. Salzmann, K. Pervushin, G. Wider, H. Senn, K. Wüthrich, *J. Biomol. NMR* **1999**, 14, 85–88.
- [146] T. Kühn, H. Schwalbe, *J. Am. Chem. Soc.* **2000**, 122, 6169–6174.
- [147] Y. Furutani, H. Shimizu, Y. Asai, T. Fukuda, S. Oiki, H. Kandori, *J. Phys. Chem. Lett.* **2012**, 3, 3806–3810.
- [148] *Webvision: The Organization of the Retina and Visual System*, **1995**.
- [149] F. Müller, U. B. Kaupp, *Naturwissenschaften* **1998**, 85, 49–61.
- [150] Y. Koutalos, T. G. Ebrey, *Photochem. Photobiol.* **1986**, 44, 809–817.
- [151] K. Werner, PhD Thesis, **2007**.
- [152] O. P. Ernst, F. J. Bartl, *Chembiochem* **2002**, 3, 968–974.
- [153] R. S. Molday, *Invest. Ophthalmol. Vis. Sci.* **1998**, 39, 2491–513.
- [154] M. Chabre, *Comptes rendus l'Académie des Sci. Série III, Sci. la vie* **1992**, 314, 1–5.
- [155] U. Wilden, S. W. Hall, H. Kühn, *Proc. Natl. Acad. Sci. U. S. A.* **1986**, 83, 1174–1178.
- [156] H. Shichi, R. L. Somers, *J. Biol. Chem.* **1978**, 253, 7040–7046.
- [157] K. Palczewski, J. H. McDowell, S. Jakes, T. S. Ingebritsen, P. A. Hargrave, *J. Biol. Chem.* **1989**, 264, 15770–15773.
- [158] M. E. Burns, V. Y. Arshavsky, *Neuron* **2005**, 48, 387–401.
- [159] K. Palczewski, *Science (80-)*. **2000**, 289, 739–745.
- [160] D. Salom, D. T. Lodowski, R. E. Stenkamp, I. L. Trong, M. Golczak, B. Jastrzebska, T. Harris, J. A. Ballesteros, K. Palczewski, *Proc. Natl. Acad. Sci. U.S.A.* **2006**, 103, 16123–16128.
- [161] H. Nakamichi, T. Okada, *Angew. Chem. Int. Ed. Engl.* **2006**, 45, 4270–3.
- [162] J. H. Park, P. Scheerer, K. P. Hofmann, H.-W. Choe, O. P. Ernst, *Nature* **2008**, 454, 183–187.
- [163] M. Murakami, T. Kouyama, *Nature* **2008**, 453, 363–367.
- [164] T. Warne, M. J. Serrano-Vega, J. G. Baker, R. Moukhametzianov, P. C. Edwards, R. Henderson, A. G. W. Leslie, C. G. Tate, G. F. X. Schertler, *Nature* **2008**, 454, 486–491.
- [165] E. C. Y. Yan, M. A. Kazmi, Z. Ganim, J.-M. Hou, D. Pan, B. S. W. Chang, T. P. Sakmar, R. A. Mathies, *Proc. Natl. Acad. Sci. U. S. A.* **2003**, 100, 9262–9267.
- [166] E. Getmanova, A. B. Patel, J. Klein-Seetharaman, M. C. Loewen, P. J. Reeves, N. Friedman, M. Sheves, S. O. Smith, H. G. Khorana, *Biochemistry* **2004**, 43, 1126–1133.
- [167] H. R. Bourne, E. C. Meng, *Science* **2000**, 289, 733–734.
- [168] T. Mirzadegan, G. Benkő, S. Filipek, K. Palczewski, *Biochemistry* **2003**, 42, 2759–2767.
- [169] X. Periole, M. A. Ceruso, E. L. Mehler, *Biochemistry* **2004**, 43, 6858–6864.
- [170] O. Fritze, S. Filipek, V. Kuksa, K. Palczewski, K. P. Hofmann, O. P. Ernst, *Proc. Natl. Acad. Sci. U. S. A.* **2003**, 100, 2290–2295.
- [171] B. König, A. Arendt, J. H. McDowell, M. Kahlert, P. A. Hargrave, K. P. Hofmann, *Proc. Natl. Acad. Sci. U. S. A.* **1989**, 86, 6878–6882.
- [172] A. B. Patel, E. Crocker, P. J. Reeves, E. V. Getmanova, M. Eilers, H. G. Khorana, S. O. Smith, *J. Mol. Biol.* **2005**, 347, 803–812.

- [173] M. Chabre, J. Breton, *Photochem. Photobiol.* **1979**, *30*, 295–299.
- [174] C. N. Rafferty, C. G. Muellenberg, H. Shichi, *Biochemistry* **1980**, *19*, 2145–2151.
- [175] T. A. Nakayama, H. G. Khorana, *J. Biol. Chem.* **1990**, *265*, 15762–15769.
- [176] T. A. Nakayama, H. G. Khorana, *J. Biol. Chem.* **1991**, *266*, 4269–4275.
- [177] T. Ebrey, M. Tsuda, G. Sassenrath, J. L. West, W. H. Waddell, *FEBS Lett.* **1980**, *116*, 217–219.
- [178] A. J. Rader, G. Anderson, B. Isin, H. G. Khorana, I. Bahar, J. Klein-Seetharaman, *Proc. Natl. Acad. Sci. U. S. A.* **2004**, *101*, 7246–7251.
- [179] H.-W. Choe, Y. J. Kim, J. H. Park, T. Morizumi, E. F. Pai, N. Krauss, K. P. Hofmann, P. Scheerer, O. P. Ernst, *Nature* **2011**, *471*, 651–655.
- [180] P. Scheerer, J. H. Park, P. W. Hildebrand, Y. J. Kim, N. Krauss, H.-W. Choe, K. P. Hofmann, O. P. Ernst, *Nature* **2008**, *455*, 497–502.
- [181] C. Altenbach, A. K. Kusnetzow, O. P. Ernst, K. P. Hofmann, W. L. Hubbell, *Proc. Natl. Acad. Sci. U. S. A.* **2008**, *105*, 7439–7444.
- [182] T. D. Dunham, D. L. Farrens, *J. Biol. Chem.* **1999**, *274*, 1683–1690.
- [183] H. Nakamichi, T. Okada, *Proc. Natl. Acad. Sci. U. S. A.* **2006**, *103*, 12729–12734.
- [184] F. J. Bartl, R. Vogel, *Phys. Chem. Chem. Phys.* **2007**, *9*, 1648.
- [185] S. T. Menon, M. Han, T. P. Sakmar, *Physiol. Rev.* **2001**, *81*, 1659–1688.
- [186] A. Mendez, M. E. Burns, A. Roca, J. Lem, L.-W. Wu, M. I. Simon, D. A. Baylor, J. Chen, *Neuron* **2000**, *28*, 153–164.
- [187] E. Ritter, M. Elgeti, F. J. Bartl, *Photochem. Photobiol.* **2008**, *84*, 911–920.
- [188] M. Heck, S. A. Schädel, D. Maretzki, K. P. Hofmann, *Vision Res.* **2003**, *43*, 3003–3010.
- [189] J. W. Lewis, F. J. van Kuijk, J. A. Carruthers, D. S. Kliger, *Vision Res.* **1997**, *37*, 1–8.
- [190] R. G. Matthews, R. Hubbard, P. K. Brown, G. Wald, *J. Gen. Physiol.* **1963**, *47*, 215–240.
- [191] K. Zimmermann, E. Ritter, F. J. Bartl, K. P. Hofmann, M. Heck, *J. Biol. Chem.* **2004**, *279*, 48112–48119.
- [192] R. Vogel, F. Siebert, X.-Y. Zhang, G. Fan, M. Sheves, *Biochemistry* **2004**, *43*, 9457–9466.
- [193] K. J. Rothschild, J. Gillespie, W. J. DeGrip, *Biophys. J.* **1987**, *51*, 345–350.
- [194] T. J. Melia, C. W. Cowan, J. K. Angleson, T. G. Wensel, *Biophys. J.* **1997**, *73*, 3182–3191.
- [195] R. Vogel, F. Siebert, *J. Biol. Chem.* **2001**, *276*, 38487–38493.
- [196] O. P. Ernst, F. J. Bartl, *ChemBiochem* **2002**, *3*, 968–974.
- [197] C. D. Strader, T. M. Fong, M. R. Tota, D. Underwood, R. A. Dixon, *Annu. Rev. Biochem.* **1994**, *63*, 101–132.
- [198] T. Ebrey, Y. Koutalos, *Prog. Retin. Eye Res.* **2001**, *20*, 49–94.
- [199] M. Mahalingam, R. Vogel, *Biochemistry* **2006**, *45*, 15624–15632.
- [200] M. Heck, S. A. Schädel, D. Maretzki, F. J. Bartl, E. Ritter, K. Palczewski, K. P. Hofmann, *J. Biol. Chem.* **2003**, *278*, 3162–3169.
- [201] J. Liu, Y. Itagaki, S. Ben-Shabat, K. Nakanishi, J. R. Sparrow, *J. Biol. Chem.* **2000**, *275*, 29354–29360.
- [202] F. Haeseleer, J. Huang, L. Lebioda, J. C. Saari, K. Palczewski, *J. Biol. Chem.* **1998**, *273*, 21790–21799.
- [203] A. H. Bunt-Milam, J. C. Saari, *J. Cell Biol.* **1983**, *97*, 703–712.
- [204] T. I. Okajima, B. Wiggert, G. J. Chader, D. R. Pepperberg, *J. Biol. Chem.* **1994**, *269*, 21983–21989.
- [205] Q. Wu, L. R. Blakeley, M. C. Cornwall, R. K. Crouch, B. N. Wiggert, Y. Koutalos, *Biochemistry* **2007**, *46*, 8669–8679.
- [206] J. C. Saari, D. L. Bredberg, *J. Biol. Chem.* **1989**, *264*, 8636–8640.
- [207] G. Moiseyev, R. K. Crouch, P. Goletz, J. Oatis, T. M. Redmond, J. Ma, *Biochemistry* **2003**, *42*, 2229–2238.

- [208] T. M. Redmond, S. Yu, E. Lee, D. Bok, D. Hamasaki, N. Chen, P. Goletz, J. X. Ma, R. K. Crouch, K. Pfeifer, *Nat. Genet.* **1998**, *20*, 344–351.
- [209] M. Jin, S. Li, W. N. Moghrabi, H. Sun, G. H. Travis, *Cell* **2005**, *122*, 449–459.
- [210] C. A. Driessen, B. P. Janssen, H. J. Winkens, A. H. van Vugt, T. L. de Leeuw, J. J. Janssen, *Invest. Ophthalmol. Vis. Sci.* **1995**, *36*, 1988–1996.
- [211] R. K. Crouch, E. S. Hazard, T. Lind, B. Wiggert, G. Chader, D. W. Corson, *Photochem. Photobiol.* **1992**, *56*, 251–255.
- [212] P. Ala-Laurila, A. V Kolesnikov, R. K. Crouch, E. Tsina, S. A. Shukolyukov, V. I. Govardovskii, Y. Koutalos, B. Wiggert, M. E. Estevez, M. C. Cornwall, *J. Gen. Physiol.* **2006**, *128*, 153–169.
- [213] R. A. Radu, N. L. Mata, A. Bagla, G. H. Travis, *Proc. Natl. Acad. Sci. U. S. A.* **2004**, *101*, 5928–5933.
- [214] J. R. Sparrow, N. Fishkin, J. Zhou, B. Cai, Y. P. Jang, S. Krane, Y. Itagaki, K. Nakanishi, *Vision Res.* **2003**, *43*, 2983–2990.
- [215] A. Wenzel, C. Grimm, M. Samardzija, C. E. Remé, *Prog. Retin. Eye Res.* **2005**, *24*, 275–306.
- [216] M. E. Sommer, W. C. Smith, D. L. Farrens, *J. Biol. Chem.* **2005**, *280*, 6861–6871.
- [217] K. Palczewski, J. P. Van Hooser, G. G. Garwin, J. Chen, G. I. Liou, J. C. Saari, *Biochemistry* **1999**, *38*, 12012–12019.
- [218] K. P. Hofmann, A. Pulvermüller, J. Buczyłko, P. Van Hooser, K. Palczewski, *J. Biol. Chem.* **1992**, *267*, 15701–15706.
- [219] M. E. Sommer, K. P. Hofmann, M. Heck, *Nat. Commun.* **2012**, *3*, 995.
- [220] S. A. Vishnivetskiy, M. M. Hosey, J. L. Benovic, V. V Gurevich, *J. Biol. Chem.* **2004**, *279*, 1262–1268.
- [221] J. Granzin, U. Wilden, H. W. Choe, J. Labahn, B. Krafft, G. Büldt, *Nature* **1998**, *391*, 918–921.
- [222] J. A. Hirsch, C. Schubert, V. V Gurevich, P. B. Sigler, *Cell* **1999**, *97*, 257–269.
- [223] R. B. Sutton, S. A. Vishnivetskiy, J. Robert, S. M. Hanson, D. Raman, B. E. Knox, M. Kono, J. Navarro, V. V Gurevich, *J. Mol. Biol.* **2005**, *354*, 1069–1080.
- [224] M. Han, V. V Gurevich, S. A. Vishnivetskiy, P. B. Sigler, C. Schubert, *Structure* **2001**, *9*, 869–880.
- [225] S. K. Milano, H. C. Pace, Y.-M. Kim, C. Brenner, J. L. Benovic, *Biochemistry* **2002**, *41*, 3321–3328.
- [226] J. Granzin, A. Stadler, A. Cousin, R. Schlesinger, R. Batra-Safferling, *Sci. Rep.* **2015**, *5*, 15808.
- [227] S. A. Vishnivetskiy, C. L. Paz, C. Schubert, J. A. Hirsch, P. B. Sigler, V. V Gurevich, *J. Biol. Chem.* **1999**, *274*, 11451–11454.
- [228] M. E. Sommer, D. L. Farrens, J. H. McDowell, L. A. Weber, W. C. Smith, *J. Biol. Chem.* **2007**, *282*, 25560–25568.
- [229] S. M. Hanson, D. J. Francis, S. A. Vishnivetskiy, E. A. Kolobova, W. L. Hubbell, C. S. Klug, V. V. Gurevich, *Proc. Natl. Acad. Sci. U. S. A.* **2006**, *103*, 4900–4905.
- [230] K. Palczewski, J. Buczyłko, H. Ohguro, R. S. Annan, S. A. Carr, J. W. Crabb, M. W. Kaplan, R. S. Johnson, K. A. Walsh, *Protein Sci.* **1994**, *3*, 314–324.
- [231] W. C. Smith, A. H. Milam, D. Dugger, A. Arendt, P. A. Hargrave, K. Palczewski, *J. Biol. Chem.* **1994**, *269*, 15407–15410.
- [232] W. C. Smith, a H. Milam, D. Dugger, a Arendt, P. a Hargrave, K. Palczewski, *J. Biol. Chem.* **1994**, *269*, 15407–15410.
- [233] J. Granzin, A. Cousin, M. Weirauch, R. Schlesinger, G. Büldt, R. Batra-Safferling, *J. Mol. Biol.* **2012**, *416*, 611–618.
- [234] Y. J. Kim, K. P. Hofmann, O. P. Ernst, P. Scheerer, H.-W. Choe, M. E. Sommer, *Nature* **2013**, *497*, 142–146.
- [235] K. Schröder, A. Pulvermüller, K. P. Hofmann, *J. Biol. Chem.* **2002**, *277*, 43987–43996.
- [236] S. E. Feuerstein, A. Pulvermüller, R. Hartmann, J. Granzin, M. Stoldt, P. Henklein,

- O. P. Ernst, M. Heck, D. Willbold, B. W. Koenig, *Biochemistry* **2009**, *48*, 10733–10742.
- [237] A. Claing, S. A. Laporte, M. G. Caron, R. J. Lefkowitz, *Prog. Neurobiol.* **2002**, *66*, 61–79.
- [238] S. J. Perry, R. J. Lefkowitz, *Trends Cell Biol.* **2002**, *12*, 130–138.
- [239] K. S. Nair, S. M. Hanson, A. Mendez, E. V Gurevich, M. J. Kennedy, V. I. Shestopalov, S. A. Vishnivetskiy, J. Chen, J. B. Hurley, V. V Gurevich, et al., *Neuron* **2005**, *46*, 555–567.
- [240] S. M. Hanson, E. V Gurevich, S. A. Vishnivetskiy, M. R. Ahmed, X. Song, V. V Gurevich, *Proc. Natl. Acad. Sci. U. S. A.* **2007**, *104*, 3125–3128.
- [241] S. A. Laporte, R. H. Oakley, J. A. Holt, L. S. Barak, M. G. Caron, *J. Biol. Chem.* **2000**, *275*, 23120–23126.
- [242] K. L. Pierce, R. J. Lefkowitz, *Nat. Rev. Neurosci.* **2001**, *2*, 727–733.
- [243] P. Tsao, T. Cao, M. von Zastrow, *Trends Pharmacol. Sci.* **2001**, *22*, 91–96.
- [244] K. L. Pierce, R. T. Premont, R. J. Lefkowitz, *Nat. Rev. Mol. Cell Biol.* **2002**, *3*, 639–950.
- [245] T. B. Kirkwood, S. N. Austad, *Nature* **2000**, *408*, 233–238.
- [246] D. Harman, *J. Gerontol.* **1956**, *11*, 298–300.
- [247] R. Pearl, *The Rate of Living*, A. A. Knopf, Inc., New York, **1928**.
- [248] H. Prillinger, K. Esser, *Mol. Gen. Genet.* **1977**, *156*, 333–45.
- [249] S. W. Stumpferl, O. Stephan, H. D. Osiewacz, *Eukaryot. Cell* **2004**, *3*, 200–11.
- [250] C. Kenyon, J. Chang, E. Gensch, A. Rudner, R. Tabtiang, *Nature* **1993**, *366*, 461–464.
- [251] V. J. Thannickal, B. L. Fanburg, *Am. J. Physiol. Lung Cell. Mol. Physiol.* **2000**, *279*, L1005–L1028.
- [252] E. R. Stadtman, *Curr. Med. Chem.* **2004**, *11*, 1105–1112.
- [253] D. Trachootham, J. Alexandre, P. Huang, *Nat. Rev. Drug Discov.* **2009**, *8*, 579–591.
- [254] B. Halliwell, J. M. Gutteridge, *Biochem. J.* **1984**, *219*, 1–14.
- [255] T. F. Slater, *Biochem. J.* **1984**, *222*, 1–15.
- [256] J. M. McCord, *N. Engl. J. Med.* **1985**, *312*, 159–163.
- [257] Y.-R. Chen, C.-L. Chen, L. Zhang, K. B. Green-Church, J. L. Zweier, *J. Biol. Chem.* **2005**, *280*, 37339–37348.
- [258] S. Dröse, U. Brandt, *J. Biol. Chem.* **2008**, *283*, 21649–21654.
- [259] S. M. Schieke, D. Phillips, J. P. McCoy, A. M. Aponte, R.-F. Shen, R. S. Balaban, T. Finkel, *J. Biol. Chem.* **2006**, *281*, 27643–27652.
- [260] D. H. Flint, J. F. Tuminello, M. H. Emptage, *J. Biol. Chem.* **1993**, *268*, 22369–22376.
- [261] J. M. Gutteridge, P. G. Winyard, D. R. Blake, J. Lunec, S. Brailsford, B. Halliwell, *Biochem. J.* **1985**, *230*, 517–523.
- [262] G. Agullo, L. Gamet-Payraastre, S. Manenti, C. Viala, C. Rémésy, H. Chap, B. Payraastre, *Biochem. Pharmacol.* **1997**, *53*, 1649–1657.
- [263] J. R. Hoult, M. A. Moroney, M. Payá, *Methods Enzymol.* **1994**, *234*, 443–454.
- [264] M. J. Loughton, P. J. Evans, M. A. Moroney, J. R. Hoult, B. Halliwell, *Biochem. Pharmacol.* **1991**, *42*, 1673–1681.
- [265] G. Lolli, G. Cozza, M. Mazzorana, E. Tibaldi, L. Cesaro, A. Donella-Deana, F. Meggio, A. Venerando, C. Franchin, S. Sarno, et al., *Biochemistry* **2012**, *51*, 6097–6107.
- [266] M. A. Moroney, M. J. Alcaraz, R. A. Forder, F. Carey, J. R. Hoult, *J. Pharm. Pharmacol.* **1988**, *40*, 787–792.
- [267] I. Morel, G. Lescoat, P. Cillard, J. Cillard, *Methods Enzymol.* **1994**, *234*, 437–443.
- [268] N. R. Perron, J. L. Brumaghim, *Cell Biochem. Biophys.* **2009**, *53*, 75–100.
- [269] I. M. C. M. Rietjens, M. G. Boersma, H. van der Woude, S. M. F. Jeurissen, M. E. Schutte, G. M. Alink, *Mutat. Res.* **2005**, *574*, 124–138.

- [270] D. Metodiewa, A. K. Jaiswal, N. Cenas, E. Dickançaitė, J. Segura-Aguilar, *Free Radic. Biol. Med.* **1999**, *26*, 107–116.
- [271] A. Robaszkiewicz, A. Balcerczyk, G. Bartosz, *Cell Biol. Int.* **2007**, *31*, 1245–1250.
- [272] J. E. Brown, H. Khodr, R. C. Hider, C. A. Rice-Evans, *Biochem. J.* **1998**, *330* (Pt 3), 1173–1178.
- [273] T. Bakır, I. Sönmezoğlu, F. Imer, R. Apak, *Int. J. Food Sci. Nutr.* **2014**, *65*, 226–234.
- [274] E. V Schmalhausen, E. B. Zhlobek, I. N. Shalova, O. Firuzi, L. Saso, V. I. Muronetz, *Food Chem. Toxicol.* **2007**, *45*, 1988–1993.
- [275] G. Cao, E. Sofic, R. L. Prior, *Free Radic. Biol. Med.* **1997**, *22*, 749–760.
- [276] C. I. Cook, B. P. Yu, *Mech. Ageing Dev.* **1998**, *102*, 1–13.
- [277] P. Zatta, D. Drago, P. Zambenedetti, S. Bolognin, E. Nogara, A. Peruffo, B. Cozzi, *J. Chem. Neuroanat.* **2008**, *36*, 1–5.
- [278] H. Decker, K. E. van Holde, in *Oxyg. Evol. Life*, Springer Berlin Heidelberg, Berlin, Heidelberg, **2011**, pp. 43–59.
- [279] U. Stahl, P. A. Lemke, P. Tudzynski, U. Kück, K. Esser, *Mol. Gen. Genet.* **1978**, *162*, 341–343.
- [280] C. Q. Scheckhuber, N. Erjavec, A. Tinazli, A. Hamann, T. Nyström, H. D. Osiewacz, *Nat. Cell Biol.* **2007**, *9*, 99–105.
- [281] B. Kunstmann, H. D. Osiewacz, *Ageing Cell* **2008**, *7*, 651–662.
- [282] B. Kunstmann, H. D. Osiewacz, *Ageing (Albany. NY)*. **2009**, *1*, 328–334.
- [283] G. L. Cantoni, *J. Biol. Chem.* **1951**, *189*, 203–216.
- [284] C. P. Joshi, V. L. Chiang, *Plant Mol. Biol.* **1998**, *37*, 663–674.
- [285] R. M. Kagan, S. Clarke, *Arch. Biochem. Biophys.* **1994**, *310*, 417–427.
- [286] J.-L. Ferrer, *PLANT Physiol.* **2005**, *137*, 1009–1017.
- [287] X. Hou, Y. Wang, Z. Zhou, S. Bao, Y. Lin, W. Gong, *J. Struct. Biol.* **2007**, *159*, 523–528.

Acknowledgments

The help and support of many people has inspired me to achieve my goals throughout the work on this thesis.

First and foremost, I would like to express my sincere appreciation and gratitude to **Prof. Dr. Harald Schwalbe** for his excellent supervision during my PhD. His support and inspiring suggestions have been precious for the development of this thesis content. Dear Harald, you have always shown trust in my competencies and provided me the freedom and opportunity to grow as a research scientist. I thank you from the bottom of my heart for motivating me even during the tough times of my Ph.D. years.

I am sincerely grateful to our secretary **Anna Paulus** for helping me for innumerable time right from my first day in Frankfurt. Whatever may be the problem (non-scientific), I went straight to Anna and she came out with a solution. Thank you Anna for bearing with me and my disturbances for so many years.

At this point, I want to thank another person, **Dr. Sridhar Sreeramulu** without whom I would not have survived my Frankfurt days. On one hand, he was a very tough and strict mentor and on other hand he was like a loving and caring elder brother to me. Dear Sridhar, thank you for all your support and encouragement during my research days. And **Dr. Santosh Gande**, how can I forget your contribution. You and Sridhar have not only helped me in my research work but also guided me to become a better person.

And when I talk about mentorship, another name straightaway comes to my mind and that is **Dr. Krishna Saxena**. I will be always grateful to you for not only teaching me all the tricks about molecular biology and biochemistry but also for so many fruitful discussions related to my research.

On similar note, I would like to express my gratitude towards few more persons who have taught me different aspects of science. First, I would like to thank **Dr. Raja K. Muruga Poopathi** for introducing me to the world of NMR. **Dr. Christian Richter** carried forward from there and given me the basic training of NMR starting from recording spectra to analyzing it. I know I had given you hard times at the spectrometer but you were always patient and delivered me the required knowledge. Thank you Christian for sharing your vast NMR experience with me and I wish you all the best. Next, I would like to express my sincere gratitude to **Dr. Boris Fürtig**, who had helped me to set up the laser coupled NMR experiments. Without you I would have been still trapped under the black cloth (you know which one I am talking about) asking for help. I would also like to thank our very

own **Dr. Henry Jonker** for all his useful tips about recording NMR experiments and insightful discussion on my projects. I will always remember each and every one of those funny moments we shared along with Irene, Hanna, Robert and Anna in Lyon and Warsaw.

I would like to thank **Prof. Dr. Josef Wachtveitl**, **Prof. Dr. Charles R. Sanders**, **Prof. Dr. Vsevolod V. Gurevich**, **Prof. Dr. Judith Klein-Seetharaman**, **Prof. Dr. Jens Wöhnert**, **PD Dr. Rupert Abele**, **Dr. Vladimir V. Rogov**, **Prof. Dr. Volker Dötsch**, **Prof. Dr. Clemens Glaubitz** and **Prof. Dr. Heinz D. Osiewacz** for their scientific collaborations and useful advice. A special thanks to Prof. Dr. Josef Wachtveitl for agreeing to be my “Zweitgutachter”.

And if I talk about collaboration, how could I forget about “**Charles**” **Elias Eckert**. Thank you for sharing your knowledge about UV/Vis flash photolysis and in return I hope I was able to transfer some of my NMR and cell biology knowledge to you. Without you and **Dr. Chavdar Slavov**, I could not have finished the arrestin-rhodopsin project.

Special thanks go to **Verena Linhard** for her crystallizing effort and **Dr. Denis Kudlinzki** for determining the structure of PaMTH1. Dear Denis, thank you for also sharing your vast knowledge about proteins.

I would like to thank **Dr. Ulrich Schieborr**, **Dr. Robert Silvers**, **Dr. Jochen Stehle**, **Dr. Kai Schlepckow**, **Dr. Alexey Cherepanov**, **Dr. Jitendra Kumar** and **Florian Buhr** for their timely help during my doctoral study. I would specially like to mention about Dr. Jochen Stehle who not only introduced me to the world of rhodopsins but also taught me how to grow HEK cells and shared my pain in maintaining them for days and months.

I am grateful to all the present and past members of the AK Schwalbe for providing me an excellent working atmosphere. I would like to thank **Laurie Lannes** and **Isam Elamri** in particular, for fruitful exchange of scientific ideas.

Big thanks to **Dr. Martin Hähnke** and **Fabian Hiller** for their invaluable tech support. In absence of them, most of us would not have survived our PhD with that primitive knowledge about computers and software.

I also want to thank **Elke Stirnal** for taking care about ordering chemicals and other laboratory materials for us.

My deepest gratitude I owe to all the secretaries of AK Schwalbe, in particular **Anna Paulus**, **Elena Hartmann** and **Kerstin Dathe** for their continuous support and all those daunting paper works that has made our life much easier.

Many thanks to **Dr. Sridhar Sreeramulu, Dr. Krishna Saxena, Dr. Boris Fürtig** and **Dr. Denis Kudlinzki** for reading this thesis and providing useful suggestions. Special thanks to Krishna and Denis for translating the summary of this thesis in German.

At this moment, I would like to thank all the previous and current members of “girls room”, my second home away from home: **Dr. Muruga Poopathi Raja, Dr. Janina Buck, Dr. Anna Lena Lieblein, Dr. Gerd Nielsen, Dr. Anke Reining, Dr. Hanna Steinert, Irene Bessi, Anna Niesteruk, Florian Lehner, Nusrat Qureshi, Nina Kubatova** and **Sven Warhaut**.

A special thank goes to **Irene** who had been my constant support right from the starting day. Her encouragement and motivation has helped me to complete my thesis. Dear Irene, I hope we can continue of friendship in the same way in future. Thanks **Anna** for not only sharing some excellent scientific ideas with me but also introducing me to the “Vodka Bar”. And **Flo** and **Sven**, I hope you should not stop the fight to gain our fundamental rights in the girls room. Just joking!!! I will always cherish all the lively and funny moments I share in the past years with all the members of girls room.

Outside our group, there are so many other people I would like to extend my heartfelt thanks. To start with my school and university teachers who have encourage me to pursue my career in science. To my german course mates (**Marta, Pete, Irene, Laurie, Serdar** and **Alex**) for some wonderful moments. To all my Indian and non-Indian friends here, for supporting me and my wife during our stay in Frankfurt, in particular **Abhishek Acharya** and **Dr. Rana Nandi** for their timely support and immense help. And also to all those friends out there in India, you have still stayed in touch with me and shared news about my beloved country.

My deepest thanks go to my parents, my elder and younger brother, without whom I would not have made it this far. I am deeply indebted to them for their unconditional love and support. Special thanks to my beloved wife **Arpita** and her wonderful family who all have been very supportive and caring. These past several years have not been an easy ride, but Arpita has always stood by my side, even when I was irritable and annoying. I can't thank you enough for encouraging me throughout this journey. I feel that what we have learned about life had strengthened our commitment towards each other and helped us to live life to the fullest.

Curriculum vitae

Personal Data

<i>Name</i>	Deep Chatterjee
<i>Nationality</i>	Indian
<i>Date of birth</i>	07 December 1984
<i>Place of birth</i>	Kolkata (India)
<i>Marital status</i>	Married

School

<i>03/1991-05/2001</i>	Primary education (Nava Nalanda High School)
<i>07/2001-07/2003</i>	High school (Kalidhan institution)

University Education

<i>08/2003-08/2006</i>	Bachelor Degree in Microbiology University of Calcutta (India).
<i>08/2006-09/2008</i>	Master Degree in Microbiology University of Calcutta (India).
<i>12/2009-today</i>	PhD student in Prof. Harald Schwalbe group, Center for Biomolecular Magnetic Resonance (BMRZ), Frankfurt Goethe University (Germany).

Academic Teachers

Mrs. Jayanti Majumdar, Mrs. Barthi, Dr. Ashish K Das, Dr. Parthasarathi Chakraborty, Dr. Dipak K. Kar, Dr. Soma Halder, Mr. Nirmalya Chakraborty, Dr. Subhas C. Jana, Dr. Arabinda Das, Dr Anup K. Guin, Dr. Anil K. Ghosh, Dr. Sridhar Sreeramulu, Dr. Krishna Saxena, Dr. Raja K. M. Poopathi, Dr. Christian Richter, Dr. Boris Fürtig, Prof. Dr. Josef Wachtveitl, Prof. Dr. Harald Schwalbe.

Complete list of publications

1. Influence of Arrestin on the Photodecay of Bovine Rhodopsin. Chatterjee D*, Eckert CE*, Slavov C, Saxena K, Fürtig B, Sanders CR, Gurevich VV, Wachtveitl J, Schwalbe H. *Angew Chem Intl Ed Engl.* **2015**, 54, 13555-13560.*Equal contribution
2. Structure and Biophysical Characterization of the S-Adenosylmethionine-dependent O-Methyltransferase PaMTH1, a Putative Enzyme Accumulating during Senescence of *Podospira anserina*. Chatterjee D, Kudlinzki D, Linhard V, Saxena K, Schieborr U, Gande SL, Wurm JP, Wöhnert J, Abele R, Rogov VV, Dötsch V, Osiewacz HD, Sreeramulu S, Schwalbe H. *J Biol Chem.* **2015**, 290, 16415-16430.
3. Design of photocaged puromycin for nascent polypeptide release and spatiotemporal monitoring of translation. Buhr F, Kohl-Landgraf J, tom Dieck S, Hanus C, Chatterjee D, Hegelein A, Schuman EM, Wachtveitl J, Schwalbe H. *Angew Chem Intl Ed Engl.* **2015**, 54, 3717-3721.
4. Characterization of the Simultaneous Decay Kinetics of Metarhodopsin States II and III in Rhodopsin by Solution-State NMR Spectroscopy. Stehle J, Silvers R, Werner K, Chatterjee D, Gande S, Scholz F, Dutta A, Wachtveitl J, Klein-Seetharaman J, Schwalbe H. *Angew Chem Intl Ed Engl.* **2014**, 53, 2078-2084.